creative commons
COMMONS DEED

저작자표시-비영리-변경금지 2.0 대한민국

이용자는 아래의 조건을 따르는 경우에 한하여 자유롭게

- 이 저작물을 복제, 배포, 전송, 전시, 공연 및 방송할 수 있습니다.

다음과 같은 조건을 따라야 합니다:

저작자표시. 귀하는 원저작자를 표시하여야 합니다.

비영리. 귀하는 이 저작물을 영리 목적으로 이용할 수 없습니다.

변경금지. 귀하는 이 저작물을 개작, 변형 또는 가공할 수 없습니다.

- 귀하는, 이 저작물의 재이용이나 배포의 경우, 이 저작물에 적용된 이용허락조건을 명확하게 나타내어야 합니다.
- 저작권자로부터 별도의 허가를 받으면 이러한 조건들은 적용되지 않습니다.

저작권법에 따른 이용자의 권리는 위의 내용에 의하여 영향을 받지 않습니다.

이것은 이용허락규약(Legal Code)을 이해하기 쉽게 요약한 것입니다.

Disclaimer

dCollection

이학박사 학위논문

Selections of High Redshift Quasars with Multi-wavelength Data

다파장 관측 자료를 이용한 초기 우주 퀘이사 탐사

2015년 8월

서울대학교 대학원
물리·천문학부 천문학전공
전 이 슬

Selections of High Redshift Quasars with Multi-wavelength Data

by

Yiseul Jeon
(ysjeon@astro.snu.ac.kr)

A dissertation submitted in partial fulfillment of the requirements for the degree of

Doctor of Philosophy

in

Astronomy

in

Astronomy Program
Department of Physics and Astronomy
Seoul National University

Committee:

Professor	Myung Gyoon Lee
Professor	Myungshin Im
Professor	Hyung Mok Lee
Professor	Jong-Hak Woo
Professor	Minjin Kim

To my mother

ABSTRACT

High redshift quasars (z $>$ 5) hold keys to understanding the evolution of the universe in its early stage. Yet, the number of high redshift quasars uncovered from previous studies is relatively small (70 or so), and are concentrated mostly in a limited redshift range (z $\sim$ 6). To understand the early mass growth of supermassive black holes and the final stage of the cosmic reionization, it is important to find a statistically meaningful sample of quasars with various physical properties. Here we present a survey for high redshift quasars, which is divided into three sub-surveys: quasar selections at z $\sim$ 5, 6, and 7.

We conducted a quasar survey at z $\sim$ 5 using SDSS and UKIDSS LAS data and supporting observations using the CQUEAN instrument. The search for quasars in this redshift range is known to be challenging due to limitations of filter sets used in previous studies. We adopted custom-designed filters, Is and Iz, and carried out imaging follow-up observations with CQUEAN. Additional data, such as WISE catalogs, were used to assign priorities to candidates. Using these new filters and a new selection technique, we were able to reduce the number of interlopers. After optical spectroscopy, we discovered six new quasars. We obtained NIR spectra of 3 of these 6 quasars and measured their physical properties. We constructed the completeness distribution to derive the selection efficiency.

The quasar survey at z $\sim$ 6 also used SDSS and UKIDSS LAS data, to select relatively bright quasars over a wide survey area. We developed a new selection method to eliminate contamination, and found that our new selection method reduced interloper efficiently. After conducting imaging and spectroscopic follow-up observations, we confirmed two new quasars. For future works, IMS data can be used for selection of additional z $\sim$ 6 quasars, searching for relatively faint sources.

To select quasars at z $\sim$ 7, we carried out an NIR imaging survey, the Infrared

Medium-deep Survey (IMS), covering a $\sim$120 deg^2 area with 5σ depths of $Y = 22.3$ Vega and $J = 22.0$ Vega using UKIRT and WFCAM for 5 years. Seven extragalactic fields with deep optical data were imaged. We conducted data reduction, detection, and photometry on these data, and created catalogs of these IMS fields, which contain photometric information of $\sim 7\times10^6$ sources. We used two selection methods for the z $\sim$ 7 quasar selection, adopting Y-band or infrared band data, SWIRE data, in addition to deep J-band data (IMS and UKIDSS DXS) and optical data. This survey covered $\sim$110 deg^2 area and found $\sim$30 candidates, but we have not yet spectroscopically identified any quasars at z $\sim$ 7. Spectroscopic follow-ups are still ongoing.

We estimated black hole masses and Eddington ratios from the observed optical and NIR spectra, and found that the newly discovered quasars are growing via accretion more vigorous than those of their lower redshift counterparts. We estimated the quasar number densities from our discoveries for each redshift range, and compared them to those expected from the quasar luminosity functions in literature. We found that the number density at z $\sim$ 5, estimated from our discovered quasars, shows values similar to those estimated in literature. However the observed number density of quasars at z $\sim$ 7 shows values lower than what is expected, even after considering an extrapolated number density evolution. We conclude that the quasar number density at z $\sim$ 7 declines toward higher redshift, steeper than the empirically expected evolution.

Since we were unable to find quasars at $5.5 <$ z < 6.0 due to the low selection efficiency, we present an alternative selection method for this redshift range, using medium-band filters attached to SQUEAN. The χ^2 fitting of SEDs from these medium-band filters estimates photometric redshifts with a 1σ error of 0.15. Therefore we suggest that the medium-band observations can be used for a powerful selection method for robust candidates at z $\sim$ 5.5.

Keywords: catalogs – observations – quasars: emission lines – quasar: general – quasar: supermassive black holes – surveys

Student Number: 2007-20438

Contents

Abstract **i**

List of Figures **xvii**

List of Tables **xxi**

1 Introduction **1**

1.1 AGNs and SMBHs 1

1.1.1 General Properties 1

1.1.2 Black Hole – Host Galaxy Correlation 5

1.2 Origin of the SMBHs 5

1.3 Quasars 7

1.4 Physical Properties of AGNs 8

1.4.1 Mass of SMBH 8

1.4.2 Eddington Ratio 10

1.5 AGN Selection Method via Multi-wavelength Data 11

1.6 Quasar Selection Method using UV/optical Continua 12

1.7 High Redshift Quasar Surveys 14

1.8 IMS Quasar Survey 14

1.9 Outline of this Thesis 17

2 Infrared Medium-deep Survey using UKIRT **19**

2.1 Introduction 19

2.2 Survey Design 20

2.2.1 Field Selection 20

2.2.2 Multi-wavelength Data 22

2.3 Observation 24

2.3.1 UKIRT and WFCAM 24

2.3.2 Planning Observation 28

2.3.3 Observing Schedule 28

2.4 Data Reduction 30

2.4.1 Preprocessing and Astrometry from CASU 30

2.4.2 Photometric Calibration and Construction of One Stacked Array 30

2.4.3 Detection and Photometry 32

2.5 Catalog Properties 34

2.5.1 Crosstalk Flagging 34

2.5.2 Limiting Magnitude and Seeing 37

2.5.3 Catalog Format 39

2.6 Summary 40

3 Quasar Selection at z $\sim$ 5 **43**

3.1 Introduction 43

3.2 Selection Method 46

3.2.1 Definition of Color-color Diagrams 46

3.2.2 Multi-wavelength Data 51

3.2.3 Color Selection with SDSS and UKIDSS LAS 53

3.2.4 Color Selection with Is and Iz-bands of CQUEAN 54

3.2.5 Other Selection Criteria 54

3.2.6 Priority for Imaging Follow-up Observations 61
3.3 Optical Imaging Follow-up Observations with CQUEAN 62
3.3.1 Observations 62
3.3.2 Data Reduction 63
3.4 Optical Spectroscopic Follow-up Observations 64
3.4.1 Observations 64
3.4.2 Data Reduction 67
3.5 NIR Spectroscopic Observation 67
3.5.1 Observations 67
3.5.2 Data Reduction 68
3.6 Photometric Properties of IMS Quasars at z $\sim$ 5 68
3.7 Spectral Properties of IMS Quasars at z $\sim$ 5 69
3.7.1 Optical and NIR Spectra 69
3.7.2 Physical Properties on Spectra 78
3.7.3 Individual Properties of Quasars 80
3.8 Quasar Selection Efficiency 81
3.8.1 Color Selection Completeness 81
3.8.2 Contamination by Interlopers 83
3.8.3 Low Selection Efficiency due to Quasar Variability 88
3.9 Summary 88

4 Quasar Selection at z $\sim$ 6 **89**
4.1 Introduction 89
4.2 Selection Method 91
4.2.1 Definition of Color-color Diagrams 91
4.2.2 Multi-wavelength Data 92
4.2.3 Flag Checking 94
4.2.4 Color Selection with SDSS and UKIDSS LAS 95

4.2.5 Previously Discovered Quasars in Literature 99
4.3 Optical and NIR Imaging Follow-up Observations 99
4.4 Optical Spectroscopic Follow-up Observations 102
4.5 Spectral Properties of IMS Quasars at z $\sim$ 6 104
4.5.1 Optical Spectra 104
4.5.2 Physical Properties on Spectra 104
4.5.3 Individual Properties of Quasars 107
4.6 Quasar Selection Efficiency 110
4.7 Summary 111

5 Quasar Selection at z $\sim$ 7 **113**
5.1 Introduction 113
5.2 Selection Method 117
5.2.1 Definition of Color-color Diagrams 117
5.2.2 Multi-wavelength Data 119
5.2.3 Color Selections with IR/Y bands 123
5.2.4 Survey Area 125
5.3 Quasar Selection Efficiency 125
5.4 Summary 129

6 Properties of High Redshift Quasars **131**
6.1 Introduction 131
6.2 Spectral Model for Continuum Components 132
6.3 Spectral Model for Emission Line Components 133
6.4 Spectral Modeling 134
6.5 Results on the Continuum and Emission Lines Modeling 134
6.6 UV Continuum Luminosity 135
6.7 Black Hole Mass 141

6.8 Eddington Ratio 143
6.9 Summary 144

7 Discussion **149**
7.1 Expected Quasar Number from Our Surveys 149
7.2 Quasar Number Density Evolution and Black Hole Accretion Activities 157
7.3 Search for Quasars using Other Datasets 159
7.3.1 Selection of Quasars at z $\sim$ 6 with IMS and UKIDSS DXS . 159
7.3.2 Selection of Quasars at z $\sim$ 6 with the *AKARI* NEP-Wide Survey 159

8 New Selection Strategy Using Medium-Band Observation **163**
8.1 Introduction 163
8.2 Observations 166
8.2.1 SQUEAN Medium-band Filters 166
8.2.2 Quasar and Dwarf Star Samples 166
8.2.3 SQUEAN Medium-band Observations and Data Reduction . 168
8.2.4 Photometric Calibration 170
8.3 Results 175
8.3.1 Filter Response Curves with Quasar Spectra 175
8.3.2 Magnitude and Colors of Targets 175
8.3.3 SEDs 180
8.3.4 Color-color Diagrams 180
8.3.5 Photometric Redshifts of Quasars from SED Fitting 183
8.3.6 χ^2 Fitting with Different Filter Sets 187
8.4 Observation Strategy 188
8.5 Discussion and Summary 188

9 Conclusion **191**

Bibliography **194**

A Optical Images and Source Catalog of *AKARI* NEP-Wide Survey Field **205**

A.1 INTRODUCTION 206

A.2 OBSERVATIONS 208

A.3 DATA REDUCTION 217

A.3.1 Preprocessing 217

A.3.2 Astrometry 219

A.3.3 Photometric Calibration 220

A.4 CATALOGS 223

A.4.1 Object Detection and Photometry 223

A.4.2 Star-Galaxy Separation 226

A.4.3 Catalog Format 229

A.4.4 Completeness 230

A.4.5 Reliability 233

A.5 PROPERTIES OF THE DATA 235

A.5.1 Galaxy Number Counts 235

A.5.2 Color-Magnitude Diagram 237

A.6 DISCUSSION 241

A.7 SUMMARY 244

B *J* and *H*-band Imaging of *AKARI* North Ecliptic Pole Survey Field **253**

B.1 INTRODUCTION 254

B.2 OBSERVATIONS 257

B.3 DATA REDUCTION 264

B.3.1 Preprocessing 264
B.3.2 Astrometry 268
B.3.3 Photometric Calibration 270
B.4 CATALOGS 274
B.4.1 Object Detection and Photometry 274
B.4.2 Crosstalk Flagging 277
B.4.3 Data from Imai et al. (2007) 278
B.4.4 Star-Galaxy Separation 278
B.4.5 Catalog Format 280
B.4.6 Completeness 284
B.4.7 Reliability 286
B.5 PROPERTIES OF THE DATA 288
B.5.1 Source Number Counts 288
B.5.2 Color-Magnitude Diagram 292
B.6 SUMMARY 292

List of Figures

1.1 A sketch of an AGN according to the description of the unification model 2

1.2 Average unobscured radio-quiet AGN spectrum from far-IR to hard X-ray 4

1.3 Spectra of model quasars with the SDSS filter curves 15

1.4 Redshift tracks of quasars on color-color diagrams 16

2.1 Locations of IMS fields 22

2.2 Quasar luminosity function of z $\sim$ 6 23

2.3 Focal plane layout of WFCAM 26

2.4 An example of an image and a confidence map of WFCAM 27

2.5 Transmission curves for the WFCAM filter set 27

2.6 The elements within the MSB 29

2.7 Locations of the cross-talks on the array 35

2.8 Three examples of cross-talks generated from various magnitude sources 36

2.9 The total exposure times, seeing, and limiting magnitudes for the ELAIS-N2 field 37

2.10 The total exposure times, seeing, and limiting magnitudes for the entire Y-band field 38

2.11 The total exposure times, seeing, and limiting magnitudes for the entire J-band field 38

3.1 Mass distribution of the SMBHs along the redshifts 47
3.2 Two color-color diagrams adopted by Fan et al. (1999) and Willott et al. (2009) 48
3.3 Filter transmission curves of CQUEAN 49
3.4 SEDs of dwarf stars and a quasar spectrum at z = 5 with filter response curves of z, J, and K-bands 51
3.5 Two color-color diagrams for quasar selection at $5 < z < 6$ 52
3.6 Two color-color diagrams using Is and Iz-bands 55
3.7 SEDs of dwarf stars and a quasar spectrum at z = 5 with filter response curves of K, $W1$, and $W2$-bands 56
3.8 Quasar SEDs with WISE photometry 59
3.9 Two color-color diagrams with WISE photometry 60
3.10 Our new quasars at $z \sim 5$ on $r-i-z-J-K$ color-color diagrams 72
3.11 Our new quasars at $z \sim 5$ on $K-W1-W2-W3$ color-color diagrams 73
3.12 Our new quasars at $z \sim 5$ with the Is and Iz photometry 74
3.13 Optical spectra of our new quasars at $z \sim 5$ 76
3.14 NIR spectrum of ID0085 from Magellan/FIRE 77
3.15 NIR spectrum of ID0099 from the Magellan/FIRE 77
3.16 NIR spectrum of ID0106 from the Magellan/FIRE 78
3.17 Completeness as a function of redshift and M_{1450} 84
3.18 Similar to Figure 3.5 85
3.19 z-band magnitude differences between SDSS DR7 and Stripe 82 catalogs 86

4.1 Two color-color diagrams we adopted for quasar selection at $z \sim 6$. 93
4.2 An example of before and after the imaging follow-up observations . 103

4.3 Optical spectra of ID0615 from Magellan/MagE and Magellan/LDSS3 105
4.4 Optical spectrum of ID0176 from HET/LRS 106
4.5 Similar to Figure 3.17 109

5.1 Color-color diagram adapted from Mortlock et al. (2011) 115
5.2 $Z - Y$ vs. $Y - J$ color-color diagram adapted from Venemans et al. (2013) 116
5.3 SEDs of dwarf stars and a quasar spectrum at z = 7 119
5.4 Two color-color diagrams for quasar selection at z > 6.5 using IR bands 120
5.5 Two color-color diagrams for quasar selection at z > 6.5 using Y-band 121
5.6 Astrometric differences between two catalogs before the adjustment . 124
5.7 Similar to Figures 3.17 and 4.5 126
5.8 Similar to Figure 5.7 127

6.1 Continuum and emission line modeling for the C IV of ID0085 136
6.2 Continuum and emission line modeling for the Mg II of ID0085 . . . 137
6.3 Continuum and emission line modeling for the C IV of ID0099 138
6.4 Emission line modeling for the C IV of ID0106 139
6.5 Continuum and emission line modeling for the Mg II of ID0106 . . . 140
6.6 $M_{\rm BH}$ for the objects with error bars for each estimator 142
6.7 $M_{\rm BH}$ as a function of the $L_{\rm Bol}$ 145

7.1 Luminosity functions of quasars at z = 5, 6, and 7 154
7.2 Plots similar to Figure 7.1 155
7.3 Evolution of quasar number density per $\rm Gpc^3$ as a function of redshift 156
7.4 Quasar number density evolution as a function of redshift 158
7.5 Completeness as a function of redshift and M_{1450} using the IMS and UKIDSS DXS data 160

7.6 Completeness as a function of redshift and M_{1450} using the *AKARI* NEP-Wide survey data 161

8.1 QE of the camera and filter response functions 167
8.2 Detection limits for each filter of CQUEAN 170
8.3 Examples of the χ^2 fitting of SDSS stars 173
8.4 Zp calculations for ID0719 174
8.5 Filter response curves with quasar spectra 176
8.6 Filter response curves with dwarf spectra 177
8.7 Three color composition images of the quasars 177
8.8 Photometry from the SDSS $r/i/z$ and the medium-band filters . . . 181
8.9 Color-color diagrams from combinations of nine medium-band filters 184
8.10 Color-color diagrams of nine medium-band filters including SDSS and UKIDSS LAS filters 185
8.11 Reduced χ^2 distributions when we use Filterset1 186
8.12 Reduced χ^2 distributions for the ID0719 and DW0120 with Filterset4 and Filterset5 189

A.1 Field coverage of the NEP-Wide optical survey 211
A.2 FWHMs and the 5σ detection limits for each subfield 212
A.3 Distribution of the astrometry differences between our catalog and USNO-B1 catalog 220
A.4 Several measures of the image quality and the depth of each subfield 224
A.5 $B-H$ vs. $H-N2$ color-color diagrams 231
A.6 SExtractor stellarity distribution and the photometric error distribution 232
A.7 Completeness for $B-$, $R-$, and $I-$band 234
A.8 False detection rate for $B-$, $R-$, and $I-$band 236
A.9 Galaxy and stellar number counts of $B-$, $R-$, and $I-$band 239

A.10 Color-magnitude diagrams of R vs. $B-R$ 242
A.11 I vs. $R-I$ color-magnitude diagrams 245
A.12 Color-color diagrams of $B-R$ vs. $R-I$ 246

B.1 Filter response curves of multi-wavelength data covering the NEP field 260
B.2 Field coverage of the *AKARI* NEP multi-wavelength data 263
B.3 Seeing and 5σ detection limits for each subfield 266
B.4 Several measures of the image quality and depth of each subfield . . 267
B.5 Distribution of the differences in position between our sources and 2MASS sources 269
B.6 Photometric difference between our sources and 2MASS sources . . . 271
B.7 $B-H$ versus $H-N2$ color-color diagram 279
B.8 The photometric error distribution and the stellarity distribution . . 281
B.9 Completeness for J and $H-$bands 284
B.10 False detection rate for J and $H-$bands 287
B.11 Galaxy and stellar number counts of J and $H-$bands 289
B.12 Color-magnitude diagrams of J versus $J-H$ 291

List of Tables

2.1 Summary of IMS fields 25
2.2 Seeing and limiting magnitudes for all fields 39
2.3 Catalog format 41

3.1 Priorities for CQUEAN imaging follow-up observations 62
3.2 Observation summary of discovered quasars from optical spectroscopic observations 65
3.3 Targets turned out to be stars or galaxies from optical spectroscopic observations 66
3.4 Observation summary for NIR spectroscopic observations 68
3.5 Optical photometric information of IMS quasars 70
3.6 NIR photometric information of IMS quasars 71
3.7 Photometric Properties of IMS Quasars at z $\sim$ 5 74
3.8 Information of the discovered quasars at z $\sim$ 5 79

4.1 `PHOTO` Flags used by candidate selection 94
4.2 Candidate list selected from UKIDSS LAS DR8 96
4.2 Candidate list selected from UKIDSS LAS DR8 97
4.3 Candidate list selected from UKIDSS LAS DR9 98
4.3 Candidate list selected from UKIDSS LAS DR9 100
4.4 Quasars in Literature 101

4.5 Information of the quasars discovered at z $\sim$ 6 108

5.1 Quasar Survey Area 125

6.1 Power-law slopes, line widths, and continuum luminosities estimated from the NIR spectra 146

6.2 Black hole masses estimated from the different mass estimators and relations 146

6.3 $L_{\rm Bol}$, $L_{\rm Edd}$, and $L_{\rm Bol}/L_{\rm Edd}$ estimated from the different mass estimators and relations 147

6.4 Eddington ratios estimated from the different mass estimators and relations 147

7.1 Summary of our Survey 153

7.2 IMS and UKIDSS DXS fields available for quasar selection at z $\sim$ 6 160

8.1 Information of the targets 169

8.2 Filter characteristic 171

8.3 SDSS and UKIDSS LAS photometric information of the targets . . . 178

8.4 Medium band photometric information of the targets 179

A.1 Names of each subfield in Figure A.1 and their central positions. . . 213

A.2 Observation summary. 214

A.3 Photometric zero-point, seeing, 5σ detection limit, magnitude of the completeness 50%, and magnitude of the reliability 99% for each subfield. 215

A.3 Photometric zero-point, seeing, 5σ detection limit, magnitude of the completeness 50%, and magnitude of the reliability 99% for each subfield. 216

A.3 Photometric zero-point, seeing, 5σ detection limit, magnitude of the completeness 50%, and magnitude of the reliability 99% for each subfield. 218
A.4 $B-, R-$, and $I-$ band merged catalog. 227
A.5 Galaxy and stellar number counts. 238

B.1 Information of the multi-wavelength survey for the optical, NIR and MIR bands in NEP-Wide survey. 258
B.2 Same as Table B.1 but in NEP-Deep survey. 259
B.3 Names of each subfield in Figure B.1 and their central positions. . . 262
B.3 Names of each subfield in Figure B.1 and their central positions. . . 264
B.4 Observation summary. 265
B.5 Photometric zeropoint, seeing, 5σ detection limit, magnitude of 50% completeness, and magnitude of 99% reliability for each subfield. . . 272
B.5 Photometric zeropoint, seeing, 5σ detection limit, magnitude of 50% completeness, and magnitude of 99% reliability for each subfield. . . 273
B.5 Photometric zeropoint, seeing, 5σ detection limit, magnitude of 50% completeness, and magnitude of 99% reliability for each subfield. . . 275
B.6 J and $H-$band merged catalog. 283
B.6 J and $H-$band merged catalog. 285
B.7 Galaxy and stellar number counts. 290

Chapter 1

Introduction

1.1 AGNs and SMBHs

1.1.1 General Properties

A supermassive black hole (SMBH) is a type of black hole with mass $M_{\rm BH} \geq 10^6\,{\rm M}_\odot$. For example, the SMBH at the center of the Milky Way is a $2.6 \times 10^6\,{\rm M}_\odot$ black hole (Ghez et al. 1998). Also it is known that every massive galaxies harbor SMBHs. When material falling into the central SMBH fuels the activity of the SMBH, it is called an active galactic nucleus (AGN). AGNs are one of the most luminous objects in the universe with a typical bolometric luminosity $L_{\rm Bol} \sim 10^{45-48}$ erg s^{-1}, that is emitted over a very wide range of wavelengths from gamma-rays to radio.

Many different types of AGNs have been observed, for example, Seyfert 1, Seyfert 2, quasars, blazars, etc. They are grouped into a wide variety of phenomenological subclasses that share many similar properties. The unification model (Urry & Padovani 1995) is an attempt to explain these various classes of AGNs with a simple model. It proposes that the observational differences between different types of AGNs are due to their different orientations to the observers and that all AGNs are

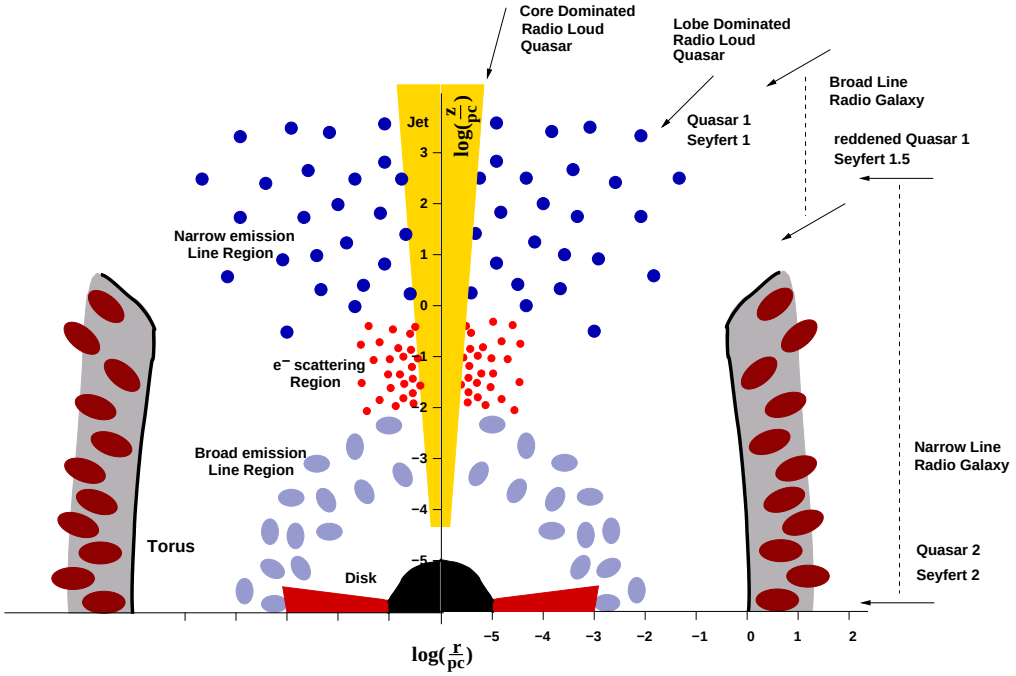

Figure 1.1 A sketch of an AGN according to the description of the unification model. A central black hole, along with the surrounding accretion disk, BLR, NLR, torus, and jet are shown. This figure is adapted from Zier & Biermann (2002).

intrinsically the same. In this model, the AGNs consist of several parts. Figure 1.1 shows each part of an AGN, adapted from Zier & Biermann (2002). An accretion disk, a central engine that is close to the black hole, emits lots of energy at a scale of a few hundred to thousand AU, via dissipative processes on the disk while transporting matter into the black hole. In addition, a corona forms above the accretion disk. Dense gas clouds with high velocity at distances from the accretion disk of a few tenths of a pc, so-called broad line regions (BLRs), rotate around the black hole, producing broad emission lines that have full width at half maximum (FWHM) of $\sim$ 1,500 – 10,000 km s^{-1}. This accretion disk and the BLRs are embedded in a Compton-thick dust torus. In addition, another type of gas clouds with low velocity and density, narrow line regions (NLRs), rotate around the black hole at the scale of the torus, producing narrow emission lines that have FWHM $\leq$ 300 – 800 km s^{-1}. A relativistic jet is extended outward to a scale of $\sim$10 kpc – $\sim$10 Mpc.

According to this model, the orientation is the only factor that determines the types we see, so all AGNs are intrinsically Seyfert 1. They are observed with spectral properties with broad and narrow emission lines on the optical and ultraviolet (UV) continuum. The nucleus emits soft and hard X-rays and the dust torus emits the infrared (IR) emission. Seyfert 2 AGNs are believed to be Seyfert 1 AGNs that are hidden by the torus, and thus, only show the narrow emission lines. Blazars are AGNs with the jets close to our line of sight.

Figure 1.2 shows an AGN spectrum from the far-IR to hard X-rays, adapted from Treister & Urry (2012). The radio emission corresponds to a strong, non-thermal component originating from a collimated relativistic jet (Begelman et al. 1984). The UV/optical emission are associated with the thermal radiation with T$\sim$30,000K originating from the accretion disk (Malkan & Sargent 1982). Radiation coming from the accretion disk are absorbed by the dust torus and re-emitted at IR wavelengths of $\sim$ 2 – 3 (hot component of T $\sim$ 1,000 – 1,500 K; Kim et al. 2015)

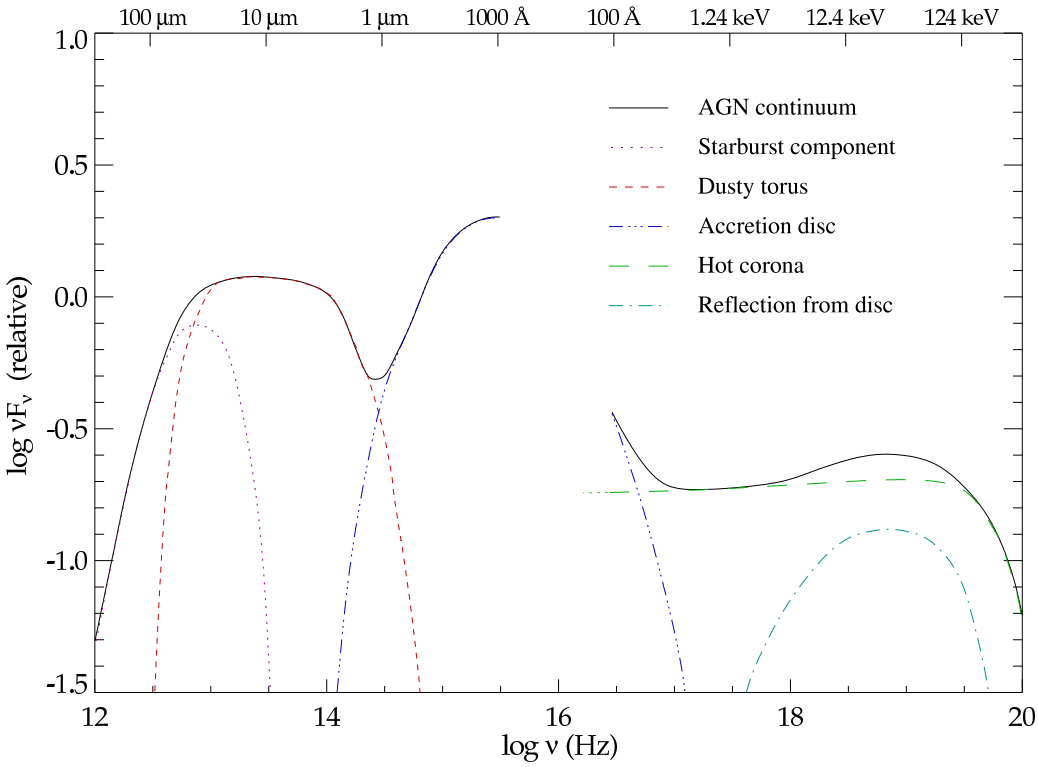

Figure 1.2 Average unobscured radio-quiet AGN spectrum from far-IR to hard X-ray. This figure is adapted from Treister & Urry (2012).

to $\sim$100μm (a cold component of T$\sim$50 K) (Leipski et al. 2014). X-ray emission is attributed to inverse-Compton scattering due to high energy electrons in the hot corona that surroundings the disk.

1.1.2 Black Hole – Host Galaxy Correlation

It is well known that AGNs play a crucial role in the formation and evolution of galaxies. The AGNs' host galaxies are influenced via powerful radiative and mechanical feedback from the AGNs (Croton et al. 2006), and this causes the two to co-evolve. Therefore they both grow with close relations. Many studies have established a correlation between the masses of the central SMBHs and properties of their host galaxies, such as stellar mass (Marconi & Hunt 2003), luminosity (Magorrian et al. 1998), velocity dispersion (Gebhardt et al. 2000; Ferrarese & Merritt 2000), and dark matter halo mass (Ferrarese 2002). These correlations suggest that there exists a fundamental relation between SMBHs and their host galaxies, even though the masses of the SMBHs are less than 1% of the stellar mass of their host galaxies. Also, literature (e.g., Springel et al. 2005; Hopkins et al. 2006; Menci et al. 2006; Croton et al. 2006) have shown that the black hole growth influences the star formation history of its host galaxy, for example, star formation quenching by the black hole (Bower et al. 2006), although the precise mechanism is unclear.

1.2 Origin of the SMBHs

How the initial seed black hole formed, and how the seed mass grew rapidly to $M_{\rm BH} \sim 10^{10}\,{\rm M}_{\odot}$ in less than 1 Gyr, are currently unknown, but there are scenarios for the mechanism (Volonteri 2010, 2012; Volonteri & Bellovary 2012). One such theory is that the compact remnants of the first generation stars, so-called population III stars (Madau & Rees 2001) with typical masses of $10^2 - 10^3\,{\rm M}_{\odot}$, become seeds

for the first black holes and the growth started at z $\sim$ 20. Another theory is that the first black holes formed directly through the gravitational collapse of metal-free gas clouds, leading to seed masses of $10^4 - 10^6\,\mathrm{M}_\odot$ at z $\sim$ 10 – 15 (Djorgovski et al. 2008; Devecchi & Volonteri 2009; Bromm & Loeb 2003; Lodato & Natarajan 2006; Latif et al. 2013).

The origin of the seeds can give constraints on the formation processes of SMBHs in the early universe. The final mass of a black hole, starting from an initial mass M_0 without considering feedback mechanisms from the black hole, is (Shapiro 2005)

$$M(t) = M_0 \exp\Big(f\frac{1-\epsilon}{\epsilon}\frac{t-t_0}{t_{\mathrm{Edd}}}\Big), \tag{1.1}$$

where M_0 is the mass at t_0, f is the Eddington ratio, ϵ is the radiative efficiency, and t_{Edd} is the Eddington limited timescale of 0.45 Gyr.

Recent observations (Jiang et al. 2007; Netzer et al. 2007; Kurk et al. 2007; Vestergaard et al. 2008; Shen et al. 2008; Mortlock et al. 2011; De Rosa et al. 2014) have reported that extremely massive black holes up to $M_{\mathrm{BH}} \sim 10^{10}\,\mathrm{M}_\odot$ already exist at z $\sim$ 6, which corresponds to less than 1 Gyr after the Big Bang. Considering the expected redshift of the first seed assuming that the seed originated from population III stars at z $\sim$ 15, a seed with $10^2\,\mathrm{M}_\odot$ needs $\sim$ 0.9 Gyr to grow to a mass of $10^{10}\,\mathrm{M}_\odot$, which is too short for the seed to accrete and grow to this M_{BH}. To explain the extreme M_{BH} at high redshift, several works have suggested that more massive black hole seeds started their growth earlier (e.g., Bromm & Loeb 2003; Begelman et al. 2006; Lodato & Natarajan 2006; Bellovary et al. 2011; Fan 2006c; Volonteri 2010), or the seeds experienced super-Eddington accretion rates (e.g., Volonteri & Rees 2005; Wyithe & Loeb 2012; Madau et al. 2014).

1.3 Quasars

Quasars are defined as unobscured AGNs from the perspective of the unification model. The first quasar was discovered by M. Schmidt in 1963.

– Luminous, distant quasars are a powerful tool to study the early universe. They are unique probes of the high redshift intergalactic medium (IGM) and the early growth of massive galaxies and black holes. After the first discovery of z $\sim$ 6 quasars by the Sloan Digital Sky Survey (SDSS), many physical properties of these quasars have been studied.

– The hypothesis of the rapid growth of central black holes in the early universe is supported by multiple lines of evidence, such as their high luminosities ($M_{1450} < -26$ mag), black hole masses of $\sim 10^9\,M_\odot$ (e.g., Jun et al. 2015), and Eddington limit luminosities ($\log(L_{\rm Bol}/L_{\rm Edd}) \geq -0.35 \pm 0.25$; e.g., Jiang et al. 2007; Kurk et al. 2007).

– Their nuclear emission lines show that their host galaxies experienced vigorous star formation and metal enrichment, even when the age of the universe was less than 1 Gyr, and since then, the metallicity does not evolve over cosmic time (e.g., Jiang et al. 2007; Kurk et al. 2007; Juarez et al. 2009; De Rosa et al. 2011, 2014).

– Spectra at wavelengths shorter than Lyman α (Lyα) indicate the ionization state of the IGM, and the lack of flux at these wavelengths for z $>$ 6 demonstrate that the last stage of the reionization is at this epoch (e.g., Fan et al. 2006b; Carilli et al. 2010; McGreer et al. 2011).

– Galaxies at high redshifts can be found using bright quasars that they host, and their star formation has been studied through mid-IR – radio observations (e.g., Walter et al. 2009; Jiang et al. 2010; Wang et al. 2011, 2013).

Therefore, high redshift quasars are important probes for understanding the black hole mass growth, galaxy evolution, and the IGM status at the early universe.

1.4 Physical Properties of AGNs

1.4.1 Mass of SMBH

There are several ways to constrain the mass of SMBHs; (i) via stellar kinematics around the black hole at the center of the Milky Way galaxy (e.g., Gillessen et al. 2009) (ii) via Doppler broadening due to the motion of stars close to the nucleus for the black hole of other local galaxies (iii) via the high velocity of the gas surrounding the black hole.

The case of (iii) is particularly powerful because it does not rely on spatial resolution, high enough to observe the sphere of influence of the black hole. For unobscured, Type 1 AGNs, if we assume that the surrounding gas is in virial motion for the black hole potential, we estimate the black hole masses using broad emission lines of AGN spectra through

$$M_{\rm BH} = \frac{f v_{\rm BLR}^2 R_{\rm BLR}}{G}, \tag{1.2}$$

where f is a geometric factor, $R_{\rm BLR}$ is distance of the broad line region, $v_{\rm BLR}$ is the velocity width of the line and G is the gravitational constant.

The $R_{\rm BLR}$ can be measured by reverberation mapping (Blandford & McKee 1982; Peterson 1993). The time lag between the continuum and the broad emission line flux variabilities is an indicator of $R_{\rm BLR}$. The $R_{\rm BLR}$'s of luminous sources increase the time lag by an order of magnitudes or more. This correlation between the AGN continuum luminosity and the $R_{\rm BLR}$ ($R_{\rm BLR} - L$ relation) scales typically as $R \sim L^{0.5}$.

A correlation between $R_{\rm BLR}$ and the continuum or emission line luminosity has been found from the reverberation mapping (e.g., Kaspi et al. 2000; Peterson et al. 2004; Bentz et al. 2010; Barth et al. 2011; Grier et al. 2012), and this relation has been applied to estimate masses of high redshift AGNs, because the UV emission lines such as C IV or Mg II are available for the high redshift AGNs. After calibrating the Hβ emission line using $R_{\rm BLR} - L$ relation, Mg II (McLure & Jarvis 2002) and

C IV (Vestergaard & Peterson 2006) emission lines have been used as mass estimators via empirical mass-scaling relations; this is the so-called single epoch reverberation mapping. Although the reliability of the black hole mass estimates based on the Mg II or the C IV emission lines is still controversial compared to the hydrogen Balmer line based estimates (Baskin & Laor 2005; Netzer et al. 2007; Trakhtenbrot & Netzer 2012), this method has been applied to large AGN surveys such as SDSS and has provided masses for more than a million AGNs including the most distant AGN at z = 7. Studies have compared the black hole masses estimated using reverberation mapping and single epoch reverberation mapping, and the low scatters demonstrate that this single epoch reverberation mapping is one of the most powerful techniques for the black hole mass estimation.

For mass estimates based on C IV , there is an empirical $M_{\rm BH}$ calibration obtained by Vestergaard & Peterson (2006)

$$\frac{M_{\rm BH,CIV}}{\rm M_\odot} = 4.24 \left[\frac{\rm FWHM_{CIV}}{\rm km\ s^{-1}}\right]^2 \left[\frac{\lambda L_\lambda(1350)}{10^{44}\ \rm erg\ s^{-1}}\right]^{0.53}, \tag{1.3}$$

and the Mg II , McLure & Jarvis (2004) provide

$$\frac{M_{\rm BH,MgII}}{\rm M_\odot} = 2.55 \left[\frac{\rm FWHM_{MgII}}{\rm km\ s^{-1}}\right]^2 \left[\frac{\lambda L_\lambda(3000)}{10^{44}\ \rm erg\ s^{-1}}\right]^{0.62}, \tag{1.4}$$

where $\rm FWHM_{CIV}$ and $\rm FWHM_{MgII}$ are the line widths of C IV and Mg II , and $\lambda L_\lambda(1350)$ and $\lambda L_\lambda(3000)$ are the continuum fluxes at the rest-frame wavelengths of $1350\mathring{A}$ and $3000\mathring{A}$. The 1σ scatter is 0.36 dex for Eq. 1.3 and 0.41 dex for Eq. 1.4.

Jun et al. (2015) provide the updated $M_{\rm BH}$ estimators from C IV and Mg II emission lines including an extended scaling relation between the rest-frame optical continuum and the line luminosity of AGNs to the high luminosity, high redshift regime,

$$\frac{M_{\rm BH,CIV}}{\rm M_\odot} = (4.72 \pm 1.63) \times 10^6 \left[\frac{\rm FWHM_{CIV}}{1,000 \rm km\ s^{-1}}\right]^{(2.11\pm0.11)} \left[\frac{\lambda L_\lambda(1350)}{10^{44}\ \rm erg\ s^{-1}}\right]^{(0.547\pm0.037)} \tag{1.5}$$

for C IV , and

$$\frac{M_{\rm BH,MgII}}{\rm M_\odot} = (4.19 \pm 1.19) \times 10^6 \left[\frac{\rm FWHM_{MgII}}{\rm km\ s^{-1}}\right]^{(2.45\pm0.06)} \left[\frac{\lambda L_\lambda(3000)}{10^{44}\ \rm erg\ s^{-1}}\right]^{(0.548\pm0.035)} \tag{1.6}$$

for Mg II . The intrinsic scatters are 0.40 and 0.09 dex for $M_{\rm BH,CIV}$ and $M_{\rm BH,MgII}$, respectively.

Previous studies compared the $M_{\rm BH}$ estimators using these UV emission lines to those using optical emission lines, and suggested that the $M_{\rm BH}$ from the Mg II are in general more reliable than C IV -based estimates, and the uncertainty of the latter is less than 1 dex (e.g., Netzer et al. 2007; Shen & Liu 2012).

For the virial factor in these black hole mass estimators, we adopt $f = 5.1 \pm 1.3$ from Woo et al. (2013).

1.4.2 Eddington Ratio

The quasar Eddington ratio is defined as the ratio between the AGN bolometric luminosity ($L_{\rm Bol}$) and the Eddington luminosity ($L_{\rm Edd}$).

$L_{\rm Bol}$ is obtained by applying the bolometric correction computed by Shen et al. (2008) to $\lambda L_\lambda(1350)$ or $\lambda L_\lambda(3000)$,

$$L_{\rm Bol} = 3.81 \lambda L_\lambda(1350) \tag{1.7}$$

and

$$L_{\rm Bol} = 5.15 \lambda L_\lambda(3000). \tag{1.8}$$

The typical error in bolometric corrections is ∼0.1 dex for optically selected SDSS quasars (Richards et al. 2006), and may be slightly larger for the correction from $\lambda L_\lambda(1350)$.

$L_{\rm Edd}$ is defined as the maximum luminosity attainable when the radiation pressure force is equal to the gravitational force,

$$L_{\rm Edd} = 1.26 \times 10^{38}\ (M_{\rm BH}/\ \rm M_\odot)\ erg\ s^{-1}. \tag{1.9}$$

For objects whose luminosities are dominated by accretion, the luminosity is proportional to the accretion rate,

$$L \propto \dot{M} = \epsilon \dot{M} c^2 \tag{1.10}$$

where ϵ is the accretion efficiency. Therefore, $L_{\rm Edd}$ can be described by the maximum accretion rate, $L_{\rm Edd} \sim \dot{M}_{\rm Edd}$, and expressing $L_{\rm Bol}$ as a function of the accretion rate of the black hole ($\dot{M}_{\rm BH}$), the Eddington ratio $L_{\rm Bol}/L_{\rm Edd}$ is equivalent to $\dot{M}_{\rm BH}/\dot{M}_{\rm Edd}$. In other words, the Eddington ratio of one is the accretion rate in units of the maximum possible accretion rate.

1.5 AGN Selection Method via Multi-wavelength Data

Since AGNs emit radiation over a wide range of wavelengths, they can be selected using a variety of wavelength regimes. However, each selection method has its own strengths and weaknesses.

a) Radio: The first AGN, 3C 273, was discovered using the radio wavelengths (Schmidt 1963). However, since radio-quiet AGNs are typically ∼3 orders of magnitude fainter in radio than radio-loud AGNs, and constitute roughly 90% of luminous type-1 AGNs, the radio-selected samples are biased towards the radio-loud sources. In the case of the high redshift AGNs at z > 5.7, only ∼7% shows radio-loud properties (Frey et al. 2012; Bañados et al. 2015).

b) UV/optical continuum: This method uses differences in SED shapes between AGNs and other sources at these wavelengths. It is very efficient, such that 3×10^6 AGNs have been discovered through many surveys (see Chap. 1.6). However, since these wavelengths are strongly affected by extinction and stellar light from host galaxies, which contaminate the power-law properties of the AGN continuum for low luminous sources, it misses obscured AGNs, which are thought to occupy ∼75% of the overall AGN population, or relatively faint AGNs.

c) Optical emission lines: Baldwin et al. (1981) reported that AGN spectra have very different emission line intensity ratios compared to those of star forming galaxies. Therefore this method is more complete, in terms of selecting obscured or low luminosity AGNs. However this selection is restricted to AGNs with relatively bright emission lines. Furthermore, since these lines are redshifted to longer wavelengths ($\lambda > 7000\mathring{A}$, where the atmosphere emission is bright, or $\lambda > 1\mu$m, where the atmosphere is opaque), this method can be used only up to z $\sim$ 1.

d) X-ray: AGNs are typically $\sim$ 1 – 5 orders of magnitude more luminous in X-ray than normal galaxies. However the most obscured sources can be missed, and the detection limits of X-ray detectors are difficult to reach by high redshift AGNs.

Among these selection methods, we used the UV/optical continuum selection methods. A survey for the photometric data of several filters over a large area provides the SED shape of each source, and we can separate sources of interest from the other contaminants. This method is currently the most popular method for quasar surveys.

1.6 Quasar Selection Method using UV/optical Continua

Selection of quasars at high redshift generally use the drastic magnitude difference between two nearby broadbands, caused by a sharp drop in flux blueward of the Lyα emission line. We call this large break between two bands 'dropout' or 'drop'. Due to extinction by the IGM, high redshift quasars at z $\gtrsim$ 6 have almost zero flux at $\lambda < 1216\mathring{A}$ (Gunn-Peterson effect; Gunn & Peterson 1965). Since the Lyα emission line is redshifted to longer wavelengths at high redshifts, quasars at 0 < z < 6 can be selected using optical broadbands. Figure 1.3 shows three spectra of quasars from a quasar template from Vanden Berk et al. (2001), redshifted to z = 3.6, z = 4.7,

and z = 5.9, with the SDSS filter curves overplotted. We can see that the r-drop starts at z = 3.6, i-drop at z = 4.7, and z-drop at z = 5.9. Figure 1.4 shows redshift tracks of quasars at various redshift ranges on color-color diagrams. We can see that the $r - i$ color of a quasar becomes redder for higher redshifts, showing the r-dropouts ((a)). At z > 4.7, the quasar shows red $i - z$ colors up to z = 5.9 ((b)). Selection of higher redshift quasars need longer wavelengths since the Lyα emission line is redshifted to the end of the optical wavelengths and beyond. Fan et al. (2001) introduced a color-color diagram including NIR bands for selection of quasars at z $\sim$ 6. The quasar redshift track in Figure 1.4 (c) shows that quasars at z > 5.7 have extremely red $z - J$ colors.

As will be explained in the next paragraph, these drastic colors of high redshift quasars allow them to be selected using these color-color diagrams. Since stars and low redshift galaxies have SEDs different from those of quasars, specific filter sets can be used to separate quasars from other sources via color-color diagrams. Explicitly, the sharp dropouts of quasar SEDs result in extremely red colors, and thus isolate quasars to the edge of color-color diagrams. Fan et al. (1999) found specific filter sets to distinguish quasars from other sources on various color-color diagrams according to their redshifts. They used the ugr bands to find quasars at 0.0 < z < 3.6, gri bands for 3.6 < z < 4.6, and riz bands for 4.6 < z < 5.1. Including the NIR wavelengths, izJ bands are used for finding quasars at 5.7 < z < 6.4. The current SDSS filter system cannot discover quasars at 5.1 < z < 5.7: selection of these quasars is illustrated in Chap. 3, 4 and 5. Recently, employing the Y-band, selection of quasars at z > 6.4 has become available. The drastic $Y - J$ colors of z > 6.4 quasars cause them to be located at positions distant from other interlopers on color-color diagrams. Quasar selection at 5 < z < 7 in literature used three color-color diagrams using the riz, izJ, or zYJ bands for quasars at 4.6 < z < 5.1, 5.7 < z < 6.4, and z > 6.4, respectively. Since photometry from large area

surveys in optical and NIR wavelengths are available, about 3×10^6 quasars were found using UV/optical continua (SDSS DR12 Quasar Catalog; Paris et al. 2015, in preparation).

1.7 High Redshift Quasar Surveys

Since luminous, distant ($z > 5.7$) quasars are rare (an estimated source density of $\sim$1 per Gpc^3, for example Fan et al. 2004; Willott et al. 2010a), surveys covering a large area of the sky are required to discover the high redshift quasars. Recently, more than 70 quasars at $z \geq 5$ have been discovered through large area surveys such as SDSS, Canada-France High-z Quasar Survey (CFHQS; Willott et al. 2005), United Kingdom Infrared Telescope (UKIRT) Infrared Deep Sky Survey (UKIDSS; Lawrence et al. 2007), Panoramic Survey Telescope and Rapid Response System 1 (Pan-STARRS1) survey, and Visible and Infrared Survey Telescope for Astronomy (VISTA) Kilo-degree Infrared Galaxy survey (VIKING). SDSS has discovered $\sim$40 quasars (e.g., Fan et al. 2000, 2001, 2003, 2006a; Jiang et al. 2008, 2009, 2015), CFHQS has provided relatively faint quasars (Willott et al. 2007, 2009, 2010a,b), UKIDSS has found several quasars (Venemans et al. 2007; Mortlock et al. 2009, 2011), Pan-STARRS1 survey has published >10 quasars (Morganson et al. 2012; Bañados et al. 2014; Venemans et al. 2015), and VIKING has discovered 3 quasars at $z > 6.5$ (Venemans et al. 2013). These surveys are still on-going and the number of discovered high redshift quasars is constantly increasing. Details of these quasar surveys are illustrated in Chap. 3, 4 and 5.

1.8 IMS Quasar Survey

We have conducted a survey of quasars in the early universe beyond $z = 5$, which is one of the main sciences of the Infrared Medium-deep Survey (IMS) performed by

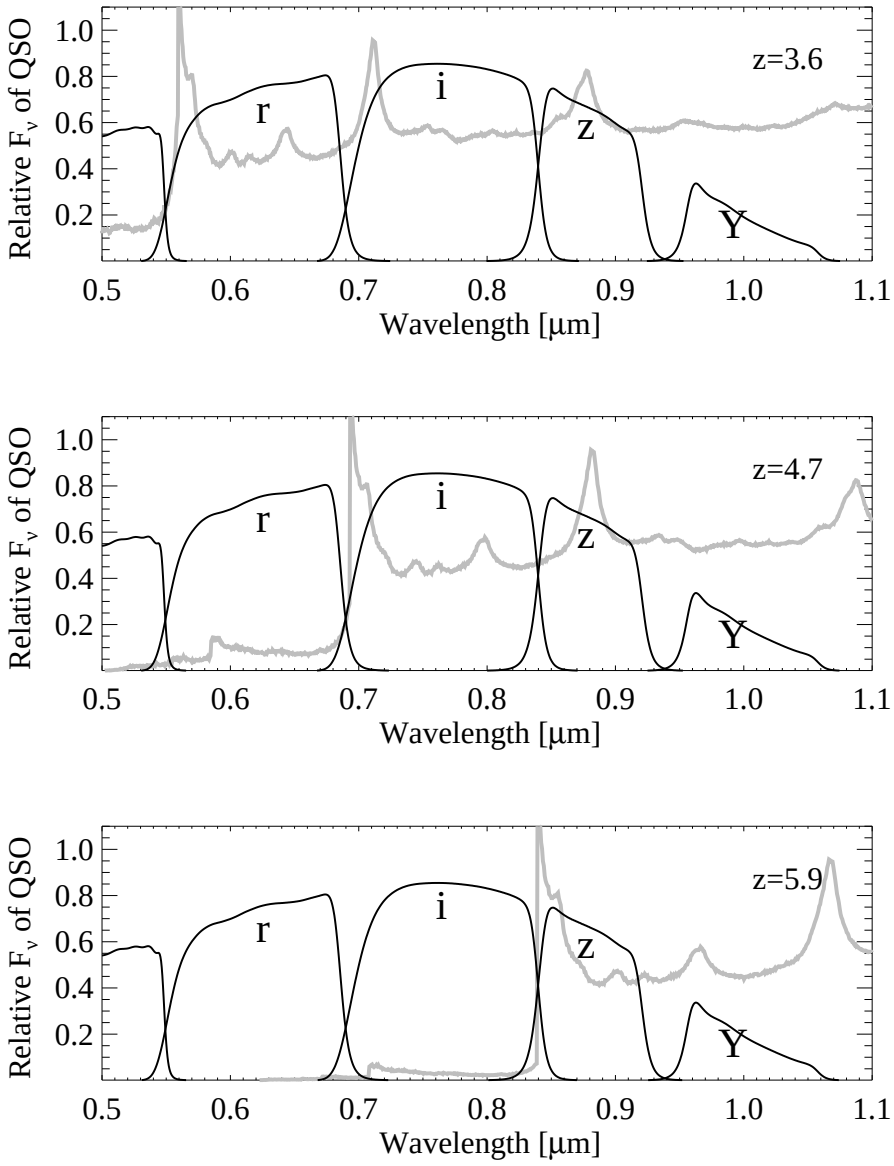

Figure 1.3 Spectra of model quasars redshifted to z = 3.6, z = 4.7, and z = 5.9, with the SDSS filter curves overplotted. The original quasar spectrum is from Vanden Berk et al. (2001).

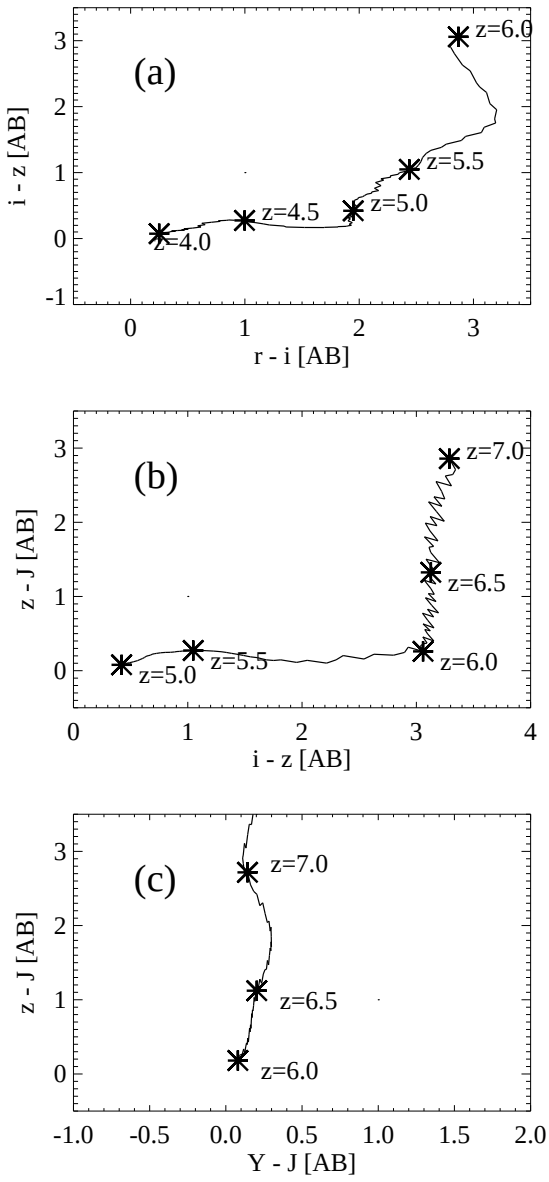

Figure 1.4 Redshift tracks of quasars at various redshift ranges on color-color diagrams.

the Center for the Exploration of the Origin of the Universe (CEOU). We use multi-wavelength data for the quasar color selection from wide field optical/IR surveys. In addition, we carried out a J-band imaging survey at UKIRT with a depth of ∼23 AB and survey area of ∼120 deg^2. Our selection uses the sharp drop in flux blueward of Lyα due to IGM absorption as dropouts, pioneered by Fan et al. (2001), preventing contamination by L and T dwarf stars (Kirkpatrick et al. 1999). Also, for the quasar candidates at $5 < z < 6$, we are carrying out imaging follow-up observations with the Camera for QUasars in EArly uNiverse (CQUEAN; Park et al. 2012), installed on the 2.1-m telescope at McDonald observatory, for candidates selected from the multi-wavelength data. We developed new quasar selection methods using multi-wavelength data from optical to IR to reduce contamination to a very low level. After performing spectroscopic observations in optical, we have confirmed 8 quasars at $4.7 < z < 6.1$ so far.

1.9 Outline of this Thesis

As explained above, AGNs, co-evolving with their host galaxies, are important objects for studying the early universe. The origin of the SMBHs is unclear and their masses are inconsistent with the possible models of their origins. Also, due to their high luminosities, luminous quasars are a powerful tool to investigate the early universe, such as the reionization status of the IGM and their host galaxy properties, as well as the mass growth history of AGNs.

Many studies have found quasars and their physical properties, such as their black hole masses and Eddington ratio, up to $z = 7$. However only ∼70 quasars at $z > 5$ have been discovered until now (∼0.02% of discovered quasars, mostly at $z \sim 5$ or $z \sim 6$.). Although these quasars are used to interpret many physical phenomena, it is important to find a statistically meaningful sample of quasars with various physical properties.

In this thesis, we describe our quasar survey with new data and techniques. Chap. 2 introduces our NIR imaging survey, which provides data necessary for our high redshift quasar selection. Our selection methods are classified into three sub-surveys according to the redshift ranges for each available dataset; surveys for z $\sim$ 5, 6, and 7. From Chap. 3 to 5, we introduce these three surveys and their results. Data described in Chap. 2 and other archival data were used for these selection methods using our new technique. In Chap. 6, we present physical properties of our discovered quasars. We discuss our results in Chap. 7, and suggest a new selection technique for high redshift quasars in Chap. 8. We summarize this study and present our conclusion in Chap. 9. Additionally, in Appendices A and B, we introduce new datasets in optical and NIR bands of the *AKARI* North Ecliptic Pole Wide survey field, which can be used as data for high redshift object selection.

Chapter 2

Infrared Medium-deep Survey using UKIRT

2.1 Introduction

In this chapter, we present the Infrared Medium-deep Survey (IMS) using the United Kingdom Infra-Red Telescope (UKIRT) and Wide Field Camera (WFCAM; Casali et al. 2007). Considering various multi-wavelength data such as the Canada-France-Hawaii Telescope Legacy Survey (CFHTLS[1]), the UKIRT Infrared Deep Sky Survey (UKIDSS[2]) Deep Extragalactic Survey (DXS) and the Spitzer Wide-Area Infrared Extragalactic Survey (SWIRE[3]), we designed a near-infrared (NIR) imaging survey with Y and J filters, covering $\sim$120 deg^2 up to detection magnitudes of $\sim$23 AB, and carried out UKIRT observations over 7 extragalactic fields: the XMM-Newton Large-Scale Structure (XMM-LSS) field, the CFHTLS Wide 2 (CFHTLS-W2) field, the Lockman-Hole field, the Extended Groth Strip (EGS) field, the European Large

[1] http://www.cfht.hawaii.edu/Science/CFHTLS/

[2] http://www.ukidss.org/

[3] http://swire.ipac.caltech.edu//swire/swire.html

Area ISO Survey North 1 (ELAIS-N1) field, ELAIS North 2 (ELAIS-N2) field, and SA22 field (Chap. 2.2). Data observed from UKIRT and WFCAM are preprocessed by the Cambridge Astronomical Survey Unit (CASU[4]) at Cambridge in the United Kingdom and is downloaded from the WFCAM Science Archive (WSA[5]). We conducted processesing including flux calibration and stacking (Chap. 2.3 and 2.4). After detection and photometry, we provide 7 merged catalogs for each field, and show the properties of these catalogs as well as information about the survey qualities (Chap. 2.5). Detailed information can be found on our web page[6]. We summarize this survey in the final chapter (Chap. 2.6). We use the AB system for SDSS *ugriz* filters and the Vega system for UKIDSS $ZYJHK$ filters.

2.2 Survey Design

2.2.1 Field Selection

Before planning an NIR survey using UKIRT, we selected our survey fields among many extragalactic fields considering the conditions below. First, there should be multi-wavelength data in order to obtain as much information about the targets as possible. The information are crucial for selecting objects with specific physical properties and the available data can increase the selection efficiency. Second, we need deep optical data, especially z-band data. Because the z $\sim$ 7 quasar selection uses the z-dropout technique, the z-band data should be sufficiently deep for employing the dropout technique. For a $J = 22.5$ AB object, z-band should be as deep as $z \sim$24 mag or so. Third, the fields should cover a wide area. Considering the small number of high redshift quasars, the large selection area raises the probability of finding high redshift objects. From the second and third conditions, we selected the area

[4]http://casu.ast.cam.ac.uk/

[5]http://surveys.roe.ac.uk/wsa/

[6]http://astro.snu.ac.kr/~exact/dokuwiki4/doku.php

observed with CFHT MegaCam. CFHTLS data using MegaCam is on-going with the z-band depth of $z = 23.9$ for the CFHTLS Wide field with a 80% completeness limit, providing deep z-band data, ∼3 magnitude deeper than SDSS. Since CFHT provides the other MegaCam data through the CFHT MegaPipe Archive, there also exist some fields with deep z-band data, not belonging to CFHTLS. Fourth, since UKIDSS DXS has a depth similar to that of IMS, we did not cover their survey area in order to avoid the duplication. Therefore we chose famous extragalactic fields that UKIDSS DXS does not cover, but for which CFHT MegaCam data exists. (We also include the DXS area for our analysis just as we do for IMS covered area.) As a result, we set up the list of our survey field using UKIRT: XMM-LSS, CFHT-W2, Lockman-Hole, EGS, ELAIS-N1, ELAIS-N2, and SA22. The field locations are shown in Figure 2.1.

The depth of our survey was decided from the luminosity function of quasars at z ∼ 6. Figure 2.2 shows the luminosity function of z ∼ 6 quasars from Willott et al. (2010a). We can see that the slope of the bright end is steeper than that of the faint end. The steeper slope of the luminosity function at the bright end results more quasars than the faint end slope if we increase a depth using a limited integration time. For example, increasing the integration time by a factor of 10 makes the survey depth 1.25 mag deeper. The number of quasars with $M_{1450} < -28.00 + 1.25$ is ∼8 times more than that for $M_{1450} < -28.00$, whereas the number of quasars with $M_{1450} < -22.00 + 1.25$ is ∼2 times more than that for $M_{1450} < -22.00$. The dotted line of Figure 2.2 indicates the median depth of our IMS ($M_{1450} < -24$) and the dashed line is for UKIDSS LAS ($M_{1450} < -26$). As explained above, we can see that our survey covers $M_{1450} \lesssim M^*_{1450}$, where the M^*_{1450} is the break magnitude; hence 'Medium-deep'.

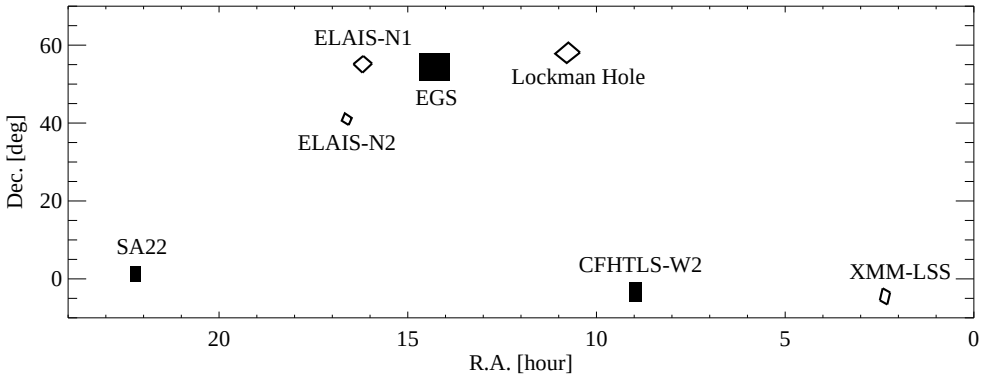

Figure 2.1 Locations of IMS fields. The empty boxes indicate fields with SWIRE data and the filled boxes are for fields with CFHTLS data. The CFHTLS-W1 (XMM-LSS) field has both CFHTLS and SWIRE data.

2.2.2 Multi-wavelength Data

Table 2.1 lists the summary of our IMS fields. All of our fields have multi-wavelength data from X-ray to radio, which make IMS fields one of the most popular extra-galactic regions. These fields are covered by CFHT MegaCam data in *ugriz* bands with the z-band limiting magnitude of 23.9 mag. There are four CFHTLS-Wide fields; CFHTLS-W1 covering a part of XMM-LSS, CFHTLS-W2, CFHTLS-W3 covering the entire EGS, and CFHTLS-W4 covering SA22. In addition Lockman Hole, ELAIS-N1 and ELAIS-N2 have CFHT MegaPipe archive data. 5 fields have the UKIRT DXS data in J and K-bands with J-band depths of 20.9 – 22.4 mag. Also, although literature generally used optical and NIR wavelengths for the quasar selections, wavelengths longer than NIR can play an important role in z $\sim$ 7 quasar selections. Here we used SWIRE data, covering XMM-LSS, Lockman Hole, ELAIS-N1, and ELAIS-N2 fields in MIR and FIR wavelengths. They provide IRAC data

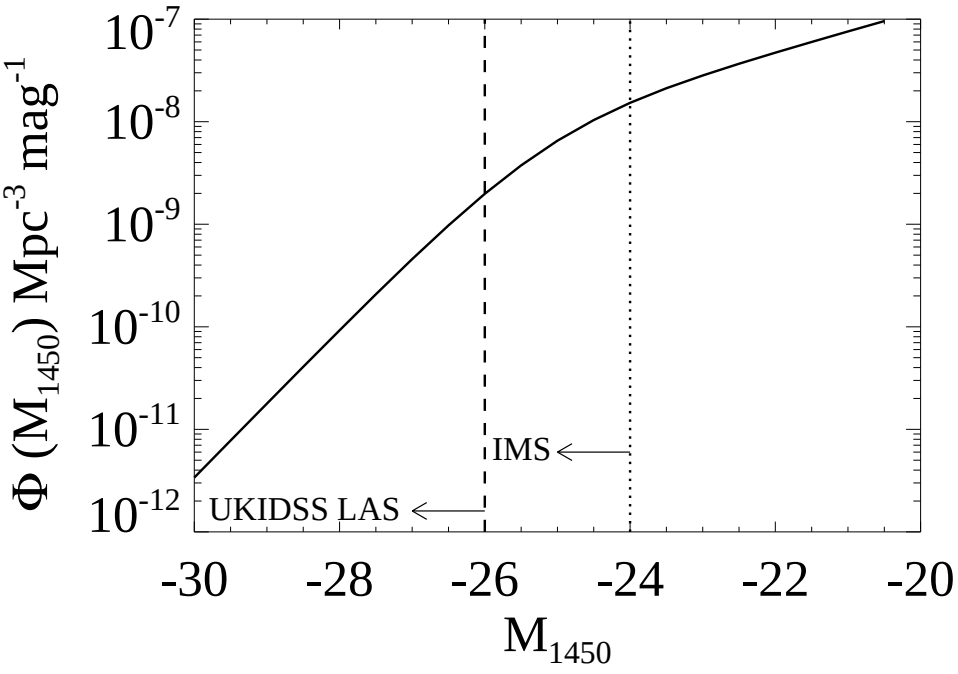

Figure 2.2 Quasar luminosity function of z $\sim$ 6 quasars from Willott et al. (2010a). The dotted line indicates the median depth of our IMS ($M_{1450} < -24$) and the dashed line is for the UKIDSS LAS ($M_{1450} < -26$).

with depths of 3.7 μJy at 3.6 μm and 5.4 μJy at 4.5 μm. Our web page[7] contains detailed descriptions of the surveyed fields. These multi-wavelength data is also described in Chap. 5.2.2.

2.3 Observation

2.3.1 UKIRT and WFCAM

UKIRT is a 3.8-m telescope governed by the Joint Astronomy Centre (JAC). WFCAM is an NIR wide field camera mounted on UKIRT. WFCAM is designed to carry out large-scale survey observations. Most of the WFCAM observing time was devoted to UKIDSS.

The camera consists of 4 Rockwell Hawaii-II (HgCdTe 2048×2048) 'arrays'. Figure 2.3 shows the focal plane layout adapted from Dye et al. (2006). Each array has a size of $13.7' \times 13.7'$ with $0.4''$ per pixel. A set of 4 'observations' are united together into a 'tile' to cover a contiguous image of 0.75 deg^2 area. The gaps between the arrays in one observation are filled by another observation. Therefore if we want a depth corresponding to a 1 hour integration time per pixel per tile, we need 4 hours of exposure time to complete 4 observations. An auto-guider CCD is installed in the center. The left panel of Figure 2.4 shows an example image taken by WFCAM. The transmission curves of the broadband filters available in WFCAM are shown in Figure 2.5.

The raw data are transferred to CASU for full off-line processing, and finally to the WSA, from where we can download the calibrated data.

[7] http://astro.snu.ac.kr/∼exact/dokuwiki4/doku.php?id=start:fields

Table 2.1. Summary of IMS fields

Field	RA / Dec	Area (deg^2)	X-ray	Optical (mag in AB)	NIR (mag in Vega)	IR	Radio
XMM-LSS	02 : 18 : 00 −07 : 00 : 00	72	XMM-Newton	CFHTLS-W1 (u25.2 g25.5 r25.0 i/y24.8 z23.9, 72 deg^2) Subaru Suprime-Cam W-S-I+ No INT data	UKIDSS DXS+UDS IMS (Y22.8 J22.4, 7 deg^2)	SWIRE (9.2)	GMRT VLA
CFHTLS-W2	08 : 57 : 49 −03 : 19 : 00	25	N/A	CFHTLS-W2 (u25.2 g25.5 r25.0 i/y24.8 z23.9, 25 deg^2)	IMS (Y22.4 J21.7, 27 deg^2)	N/A	VLA
Lockman Hole	10 : 45 : 00 +58 : 00 : 00	15	XMM-Newton Chandra	CFHT Megapipe Archive (15 deg^2) Subaru (i27.2) Mayall Ugri (i24.98)	UKIDSS DXS IMS (J22.4, 6 deg^2)	SWIRE (11)	GMRT, VLA Allen, WSRT VLBA, MERLIN 10C survey
EGS	14 : 17 : 54 +54 : 30 : 31	49	XMM-Newton Chandra	CFHTLS-W3 (u25.2 g25.5 r25.0 i/y24.8 z23.9, 49 deg^2)	IMS (Y22.2 J21.7, 40 deg^2)	N/A	VLA SCUBA2
ELAIS-N1	16 : 11 : 00 +55 : 00 : 00	11	XMM-Newton Chandra	CFHT Megapipe Archive (11 deg^2) Subaru i/Zr INT ugriz	UKIDSS DXS IMS (J22.2, 5 deg^2)	SWIRE (9.2)	VLA GMRT DRAO ST
ELAIS-N2	16 : 36 : 48 +41 : 01 : 45	5	Chandra	CFHT Megapipe Archive (5 deg^2) INT ugriz	IMS (J22.6, 5 deg^2)	SWIRE (4.8)	VLA, GMRT SCUBA, MAMBO
SA22	22 : 13 : 18 +01 : 19 : 00	25	XMM-Newton Chandra	CFHTLS-W4 (u25.2 g25.5 r25.0 i/y24.8 z23.9, 25 deg^2)	UKIDSS DXS IMS (Y22.9 J22.4, 16 deg^2)	N/A	VLA SCUBA

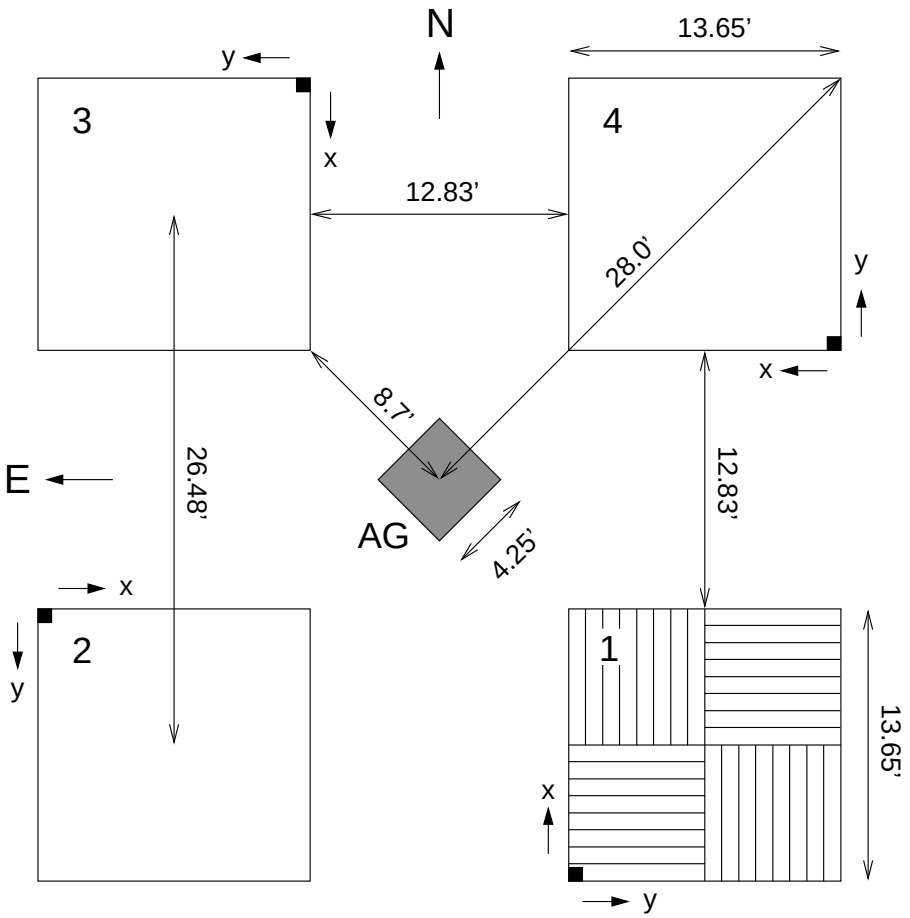

Figure 2.3 Focal plane layout of WFCAM, adapted from from Dye et al. (2006).

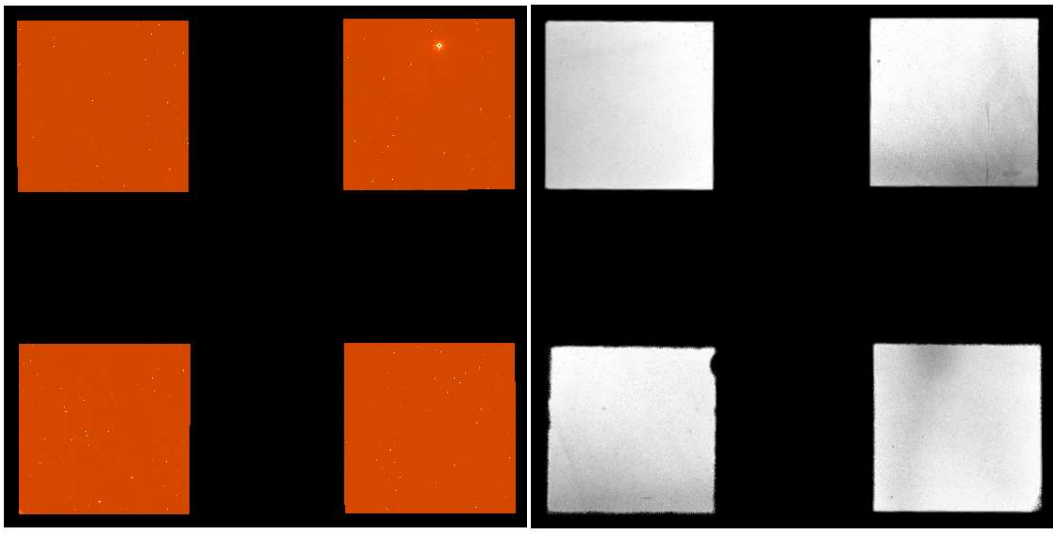

Figure 2.4 An example of an image (left) and a confidence map (right) of WFCAM.

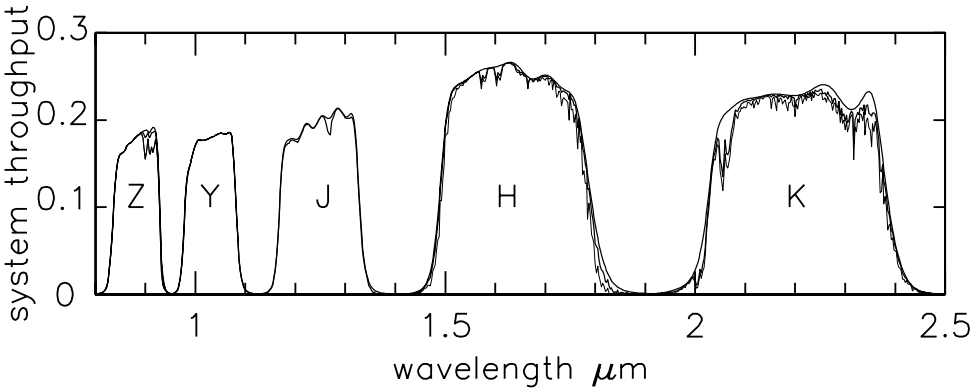

Figure 2.5 Transmission curves for the WFCAM filter set, adapted from Hewett et al. (2006).

2.3.2 Planning Observation

A minimum schedulable block (MSB) is an ordered list of observations, which are prepared using the Observing Tool. Figure 2.6 shows each element within the MSB adapted from Irwin et al. (2004). For each tile, 4 MSBs were created in order to content the aim with one hour integration time per pixel explained in Chap. 2.3.1. Each MSB contains information of pointing coordinates for 4 observations, their guide star positions, jitter mode, readout mode, filter, exposure time, and microstep pattern. We adopted 20 seconds exposure time for a single image to reduce the overhead from readout and prevent high background value due to the sky, `NDR_1.0` as the readout mode which is suitable for a long exposure time, `9 jitter with 3.2/6.4 arcsec diamond` as the offset pattern to reduce the overhead caused by telescope offsets, and `2×2 small 1` as the microstepping.

The pixel scale of the WFCAM array is $0.4''$ per pixel, which does not critically sample the specific shape of the point spread function (PSF) due to the large pixel size. To obtain critical sampling of the PSF, we adopted a technique known as microstepping. Among the available options, we choose the `2×2 small` sequence, dividing one pixel into half, resulting in a pixel scale of $0.2''$ per pixel. Its number of pointing is 4 with the offset size of $1.41''$. The 4 MSBs for each tile was executed with different orders of observations. For example, if the first MSB has a pointing order of North-East, South-East, North-West, and South-West, the second MSB has a pointing order of North-East, North-West, South-East, and South-West. The difference between the orders of 4 observations can prevent afterimages in the detector if there is a very bright star.

2.3.3 Observing Schedule

From the first observation in 2009 May, we used ∼130 nights for general observations and a few nights for query observations. The sky extinction were up to ∼0.2 mag

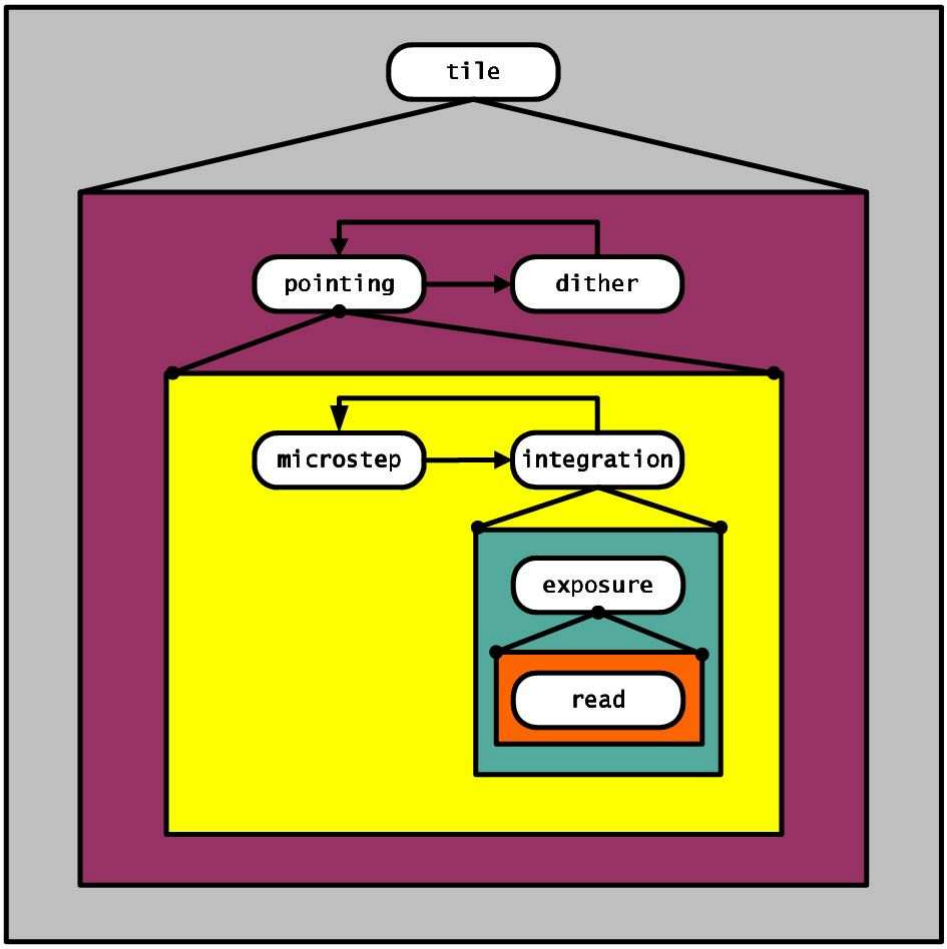

Figure 2.6 The elements within the MSB, adapted from Irwin et al. (2004).

for the J-band, and $\sim$0.1 mag for the Y-band (1σ confidence level). The seeing condition were $\sim 0.9''$ for J-band and $\sim 1.0''$ for Y-band. The total integration time for the J-band imaging observation is about 1300 hours and 800 hours for the Y-band. These observations continued until 2013A. The whole UKIRT schedule is listed in the our web page[8].

2.4 Data Reduction

2.4.1 Preprocessing and Astrometry from CASU

The raw WFCAM data are preprocessed by an automated pipeline provided by CASU. The pipeline conducts preprocessing including flat fielding, dark subtraction, sky background subtraction, and astrometric calibration. Then 36 images after the 9 ditherings $\times$ 4 microsteppings are combined as one array. These four arrays from one observation are written as multi-extension FITS (MEF) files consisting of 4 extensions, and each extension contains a combined, single array image. Therefore 4 FITS data are created from one MSB. The pipeline also provides catalogs containing source detections and photometry. The preprocessed images and catalogs can be downloaded from WSA.

2.4.2 Photometric Calibration and Construction of One Stacked Array

After downloading the FITS files, the data were split into single extensions. Usually we had 2 – 5 observations for each pixel and thus, 2 – 5 images covered the same region. To stack the images from one pointing, first, the zero points of each image were calculated, then, the images were combined through flux calibration.

For the zero point calibration of each image, we used the 2MASS Point Source

[8] http://astro.snu.ac.kr/~exact/dokuwiki4/doku.php?id=start:observation

Catalog (PSC). CASU provides images which contain zero point information in their headers, but since it is known that the flux calibration from the CASU pipeline can be wrong, we conducted the flux calibration ourselves. For the 2 – 5 arrays covering one pointing, the zero-points of each array can be different due to a rapidly deteriorating weather. The zero point difference is larger if the observations were carried out on different nights. Therefore we calculated the zero points for each array and combined the arrays with flux scaling.

To calculate the zero point of an array, we used stellar objects in the 2MASS PSC satisfying the following conditions: $0 < J_{\rm 2MASS} - K_{\rm 2MASS} < 1$ and the photometric error less than 0.1 mag for all bands. The WFCAM magnitudes from the 2MASS photometry were calculated from these formulae[9]:

$$Y_{\rm WFCAM} = J_{\rm 2MASS} + 0.50 \times (J_{\rm 2MASS} - H_{\rm 2MASS}) + 0.08$$
$$J_{\rm WFCAM} = J_{\rm 2MASS} - 0.065 \times (J_{\rm 2MASS} - H_{\rm 2MASS}).$$

We derived the difference between 2MASS and instrumental magnitudes of each source in a field and computed the average value of the difference to define the zero point. The zero point error was determined from the standard deviation of the scatters. The average zero point error is less than 0.05 mag. These zero point values were used for the flux calibration. We set the DN for each images satisfying $M = 28.00 - 2.5\log({\rm DN})$.

To adjust the zero point of each array and combine all images for an array to one stacked array, we used the SWarp (Bertin et al. 2002) software with the `FSCALE` option. We compared the zero points of each array to a fixed value 28.0 and calculated the differences as a flux calibration factor. During resampling of SWarp, the intensity of each array was scaled according to these flux calibration factors. On average, 1.3 to J-band and 1.6 to Y-band were multiplied to each array to adjust the zero points to 28.0 Each array was background subtracted with `BACK_SIZE` 300 and

[9]http://casu.ast.cam.ac.uk/surveys-projects/wfcam/technical/photometry

combined in average. This background size is suitable to calculate local background values, not affected by the size of bright stars or nearby galaxies. We input confidence map data from CASU (right panel in Figure 2.4) for each science data and a single weight-map data is created during the combining processes. For convenience, we also constructed mosaicked images of whole 0.75 $\deg^2$ corresponding to one tile, using SWarp.

Although we can use the deep stack images provided by CASU, we conducted our own combining procedures. It is because CASU does not weed out low quality images when stacking, although sky condition such as seeing sizes and extinctions varies for each observation. Before combining, we checked the images and excluded the images with low qualities, for example, images with seeing larger than $2''$ or extinction greater than about 1 magnitude. The seeing values were obtained from the value recorded in the header. We confirm that these values are reliable by checking the seeing condition in the images by ourselves. Removing files of bad condition can provide better full width at half maximum (FWHM) values and low photometric errors in a stacked image, preventing the decline of the image quality caused by some low quality images.

2.4.3 Detection and Photometry

For the detection and photometry, we used SExtractor (SE; Bertin & Arnouts 1996). We created photometric catalogs from each stacked array, not from the mosaicked images. Also we adopt weight-maps created during the SWarp procedure. After many trials of SE parameter sets, we chose a set of 0.7 for `DETECT_THRESH`, 4 connected pixels for `DETECT_MINAREA`, `DEBLEND_NTHRESH` of 32, `DEBLEND_MINCONT` of 0.005, 256 for `BACK_SIZE`, and 3 for `BACK_FILTERSIZE` as the optimal set of detection parameters. We used `gauss_5.0_9×9.conv`, `gauss_4.0_7×7.conv`, or `gauss_3.0_5×5.conv` (where, for example, `gauss_3.0_5×5.conv` indicates the 5×5

convolution mask of a gaussian PSF with FWHM = 3.0 pixels) as a convolution filter for detection depending on the seeing condition for each stacked array. The adopted detection limit corresponds to the S/N of about 1.4. This value was decided using false detection rates, which is taken as a reliability of detections. The false detection rate is defined as the ratio of the number of objects detected in a negative image (multiplied by -1 to the original image) to the number of objects detected in the original image. The false detection rate drops below 0.1 at the adopted detection limit.

We derived aperture magnitudes using aperture diameters of 5.00, 7.07, 10.00, 14.14, 20.00, 28.28, 40.00, 50.00, and 60.00 pixels. These aperture sizes are similar to those of the DXS catalog from `Aper_flux_1` to `Aper_flux_9`, corresponding to $1/2\times$`RCORE`, $1/\sqrt{2}\times$`RCORE`, $1\times$`RCORE`, $\sqrt{2}\times$`RCORE`, $2\times$`RCORE`, $2\sqrt{2}\times$`RCORE`, $4\times$`RCORE`, $5\times$`RCORE`, and $6\times$`RCORE` with a core radius of `RCORE`=5 pixels, where this core radius is defined as a fixed value corresponding to $1.0''$ for convenience. Also the `MAG_AUTO` using Kron-like elliptical aperture, `MAG_ISO` for isophotal magnitude, and `MAG_PETRO` using Petrosian-like elliptical aperture were estimated. We calculated the aperture correction values of these apertures for each stacked array and included the values in the header of each catalog. The magnitude errors are computed by combining the standard SE estimates and the zero point errors.

Finally, we merged the catalogs from each individual array. Objects that exits on two or more fields in the overlapping areas, and are matched within a $1''$ separation, were considered to be the same. An object that had the smallest auto magnitude error from SE was included in the final catalog. These catalogs contain Y and/ or J-band photometric information of total $\sim 7 \times 10^6$ sources. The final catalogs for each IMS field can be downloaded at our web page[10] as a format of fits table.

[10]http://astro.snu.ac.kr/∼exact/dokuwiki4/doku.php?id=start:data

2.5 Catalog Properties

2.5.1 Crosstalk Flagging

WFCAM shows many spurious sources caused by bright stars. One of them is the cross-talk. The cross-talk artifacts occur at multiples of ±128 pixels (256 pixels for our case due to the 2×2 microstepping) away from a bright star in the readout channel direction. The crosstalk signals can be identified as doughnut-shaped signals and their strength are stronger for a brighter source. Figure 2.7 illustrates the expected cross-talk positions[11] and Figure 2.8 shows examples of cross-talks generated from sources with three different magnitudes.

We examined the magnitude of the source that generates crosstalks and predicted expected positions of cross-talks from each bright star. After many trials of expecting cross-talk positions and checking sources on these positions by eyes, we set the farthest cross-talk position from each star to define the region where the cross-talks lie within. When a star is brighter, it produces brighter cross-talks and, therefore, the cross-talks are visible even when the position from the star is far. We divided the bright stars into two classes; stars brighter than 14 mag and stars between 14 and 16 mag. For the brightest class (magnitude < 14), cross-talks continue to the end of an array. For the other case ($14 <$ magnitude < 16), cross-talks up to the ±2nd positions are observed and cross-talks after the 3rd positions start to disappear on the array. These magnitude cuts were decided using the stacked image of the deepest field in ELAIS-N2. The fraction of objects located on the expected cross cross-talk positions is high if these cross-talks are generated from bright sources, and the fraction decreases as the magnitudes of the source increases. Then, at around 15 magnitude sources, this fraction continue to a fixed value, 17%, which is the fracion of objects detected on the random positions. Therefore we confirm see that

[11] http://casu.ast.cam.ac.uk/surveys-projects/wfcam/technical/crosstalk

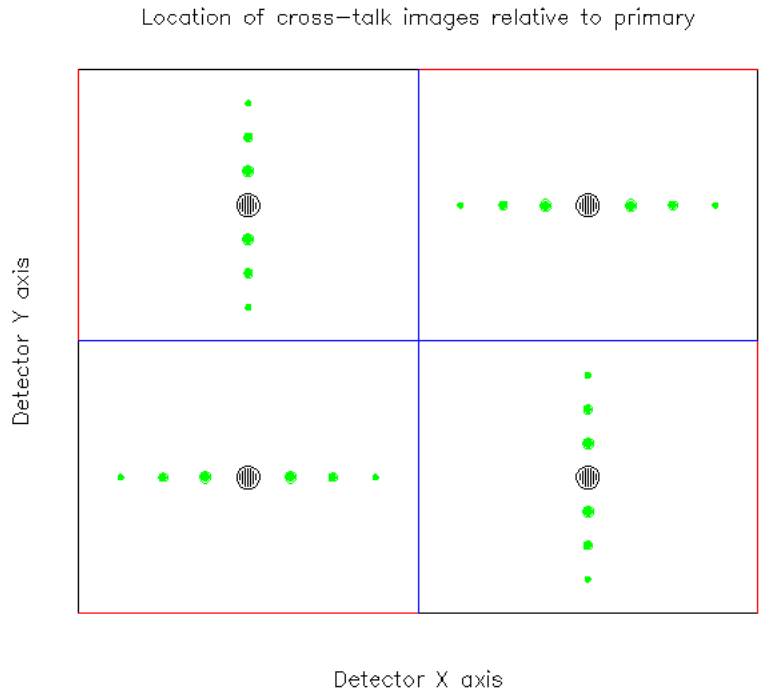

Figure 2.7 Locations of the cross-talks on the array.

the cross-talks generated from objects fainter than 16 mag are not detectable. From this observation, we decided 16 mag as a limit for objects generating cross-talks. This cut was estimated from the deepest image, and ,therefore, also applied to other fields as al lower limit.

We included the flag information for objects at the crosstalk positions in our merged catalog, to indicate that either the object is a potential crosstalk signal or its photometry is affected by the crosstalk.

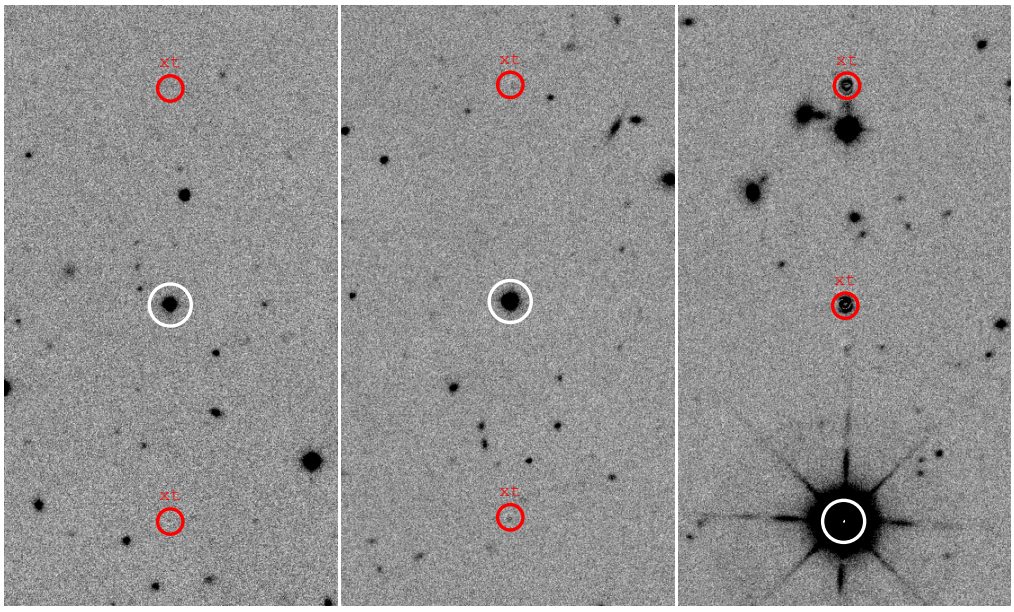

Figure 2.8 Three examples of cross-talks generated from various magnitude sources (white circles) of J=15.7 (left), 14.7 (middle), and 10.5 (right) mag. The expected cross-talk positions are denoted with black circles. We can see that the brightest sources with J=10.5 mag (right panel) generates noticeable cross-talks, whereas the source with J=15.7 mag (left panel) does not generate detectable cross-talks. The faint cross-talk signal in the middle panel can be confused as a real object.

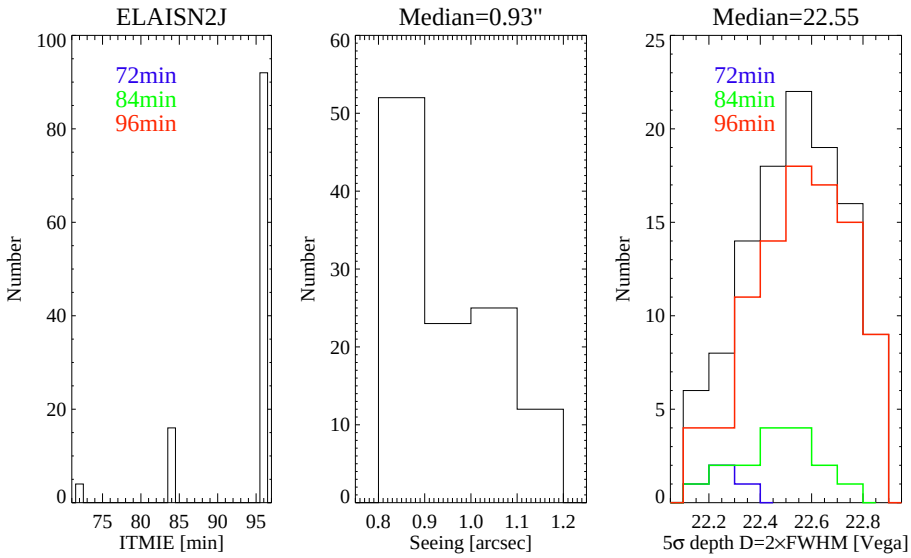

Figure 2.9 Distributions of the total exposure times, seeing, and limiting magnitudes for the ELAIS-N2 field.

2.5.2 Limiting Magnitude and Seeing

The seeing values were determined for each stacked array, as the median values of FWHM of non-saturated point sources with magnitude between 13 and 18 mag. The seeing values of arrays are determined to be $\sim$0.97″ and $\sim$0.93″ for Y and J-band, respectively. To determine the limiting magnitudes, we used the aperture size corresponding to a diameter of the FWHM. Figure 2.9 shows an example of the distributions of the total exposure times, seeing, and limiting magnitudes for the ELAIS-N2 field, and Figure 2.10 and 2.11 is for the whole Y and J-band, respectively. Table 2.2 shows the seeing and limiting magnitudes for all fields. Considering the aperture correction values, we can actually detect sources of $\sim$0.3 mag fainter than the 5σ detection limits in Table 2.2, in their aperture magnitudes with 2×FWHM diameter.

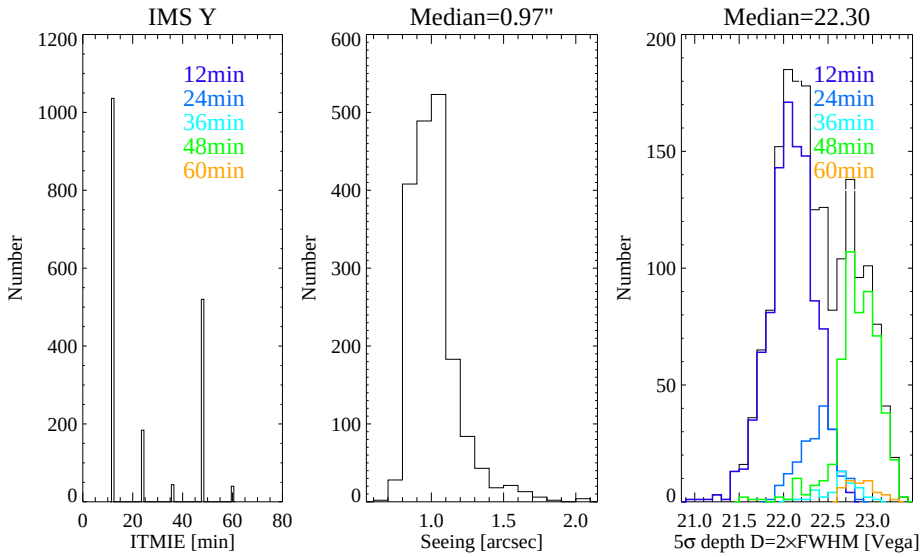

Figure 2.10 Distributions of the total exposure times, seeing, and limiting magnitudes for the entire Y-band field.

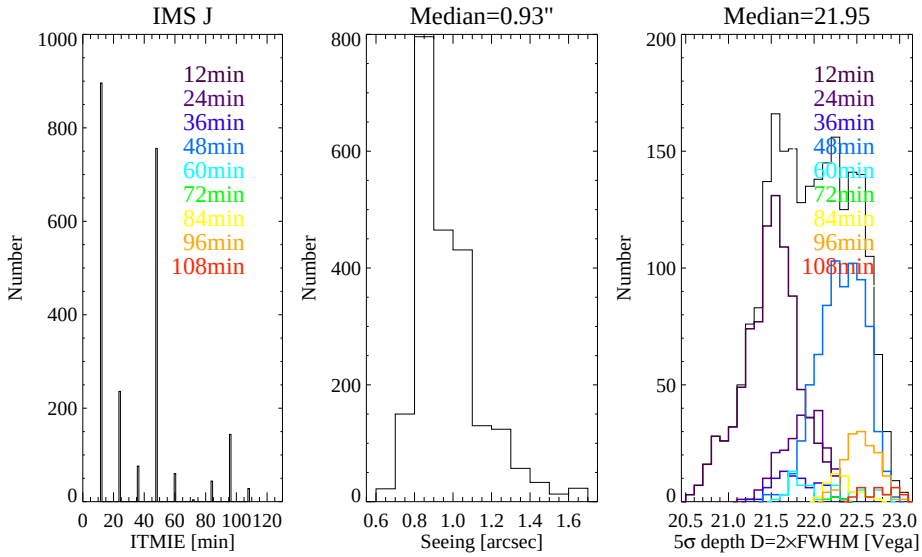

Figure 2.11 Distributions of the total exposure times, seeing, and limiting magnitudes for the entire J-band field.

Table 2.2. Seeing and limiting magnitudes for all fields

Field	Y-band		J-band	
	Seeing [″]	Depth [Vega]	Seeing [″]	Depth [Vega]
XMM-LSS	1.0	22.8	0.9	22.4
CFHTLS-W2	1.0	22.2	1.0	21.7
Lockman Hole	···	···	1.0	22.4
EGS	1.0	22.1	0.9	21.7
ELAIS-N1	···	···	0.8	22.2
ELAIS-N2	···	···	0.9	22.5
SA22	0.9	22.9	0.8	22.4

2.5.3 Catalog Format

Table 2.3 lists the contents of our merged catalogs. Each catalog contains 39 columns: identification number (ID) for the global ID (field_filter_xxxxxxxx; e.g. EN1_J_00000001, EN1_J_00000002 and EN1_J_00000003), NUMBER for the object number (field_tile_array_xxxxx; e.g. EN1_01_B.A_4462, EN1_01_B.A_4458, and EN1_01_A.A_3), right ascension (R. A. in degree, J2000), declination (Dec. in degree, J2000), X and Y position on the array, magnitudes and errors, Kron aperture radius, Petrosian aperture radius, FWHM size in pixel, ellipticity, position angle (east of north in degree), stellarity, extraction flags from SE, number of matched objects from different arrays, and cross-talk information (0: Source, 1: Cross-talk). We provide three kinds of total magnitudes; `MAG_AUTO` using Kron-like elliptical aperture, `MAG_ISO` for isophotal magnitude, and `MAG_PETRO` using Petrosian-like elliptical aperture. For aperture magnitudes, we estimated them for 9 different aperture size;

aperture magnitude within 5.0-pixel (1.00″) diameter, 7.1-pixel (1.42″) diameter, 10.0-pixel (2.00″) diameter, 14.1-pixel (2.82″) diameter, 20.0-pixel (4.00″) diameter, 28.3-pixel (5.66″) diameter, 40.0-pixel (8.00″) diameter, 50.0-pixel (10.0″) diameter, and 60.0-pixel (12.0″) diameter. The aperture correction values were estimated from all aperture sizes. The magnitude errors are computed from the square root sum of the Poisson noise from the source and the zeropoint error from the photometric calibration. The zeropoint errors have values less than 0.05 mag. The stellarities have values between zero (extended source) and one (point source). The Galactic extinction values were calculated from the extinction map of Schlegel et al. (1998) and, we obtained ratio of total to selective extinctions R, $R = A_\lambda / E(B-V)$, where the A_λ is extinction at a given wavelength λ and $E(B-V)$ is the color excess, as 1.193 for Y and 0.902 for J-bands from Cardelli et al. (1989). Note that the magnitudes in the final catalog are not corrected for the Galactic extinction. Also the aperture correction was not applied for aperture magnitudes. The conversion formulae from Vega to AB magnitudes are as follows (Hewett et al. 2006):

$$Y_{\rm Vega} = Y_{\rm AB} - 0.634$$
$$J_{\rm Vega} = J_{\rm AB} - 0.938.$$

2.6 Summary

We conducted an NIR imaging survey covering $\sim$120 deg^2 with detection limits of $Y = 22.3$ and $J = 22.0$, using UKIRT and WFCAM. Seven extragalactic fields, which have multi-wavelength data (including deep optical z-band data) and cover wide area, were selected: XMM-LSS, CFHT-W2, Lockman-Hole, EGS, ELAIS-N1, ELAIS-N2, and SA22. Considering the detector properties, we designed and executed the observations from 2009A to 2013A. We carried out data reduction including flux calibration and stacking to obtain the best quality data. After detection and photometry, we merged catalogs created from each tile and generated catalogs

Table 2.3. Catalog format

Column	Name	Description
1	ID	Global ID [field_filter_xxxxxxxx]
2	NUMBER	Object number [field_tile_array_xxxxx]
3	RA	Right ascension (J2000) [deg]
4	DEC	Declination (J2000) [deg]
5	X_IMAGE	Object position along the x-axis in the detection image [pixel]
6	Y_IMAGE	Object position along the y-axis in the detection image [pixel]
7	MAG_AUTO	Kron-like elliptical aperture magnitude [mag]
8	MAGERR_AUTO	RMS error for AUTO magnitude [mag]
9	MAG_ISO	Isophotal magnitude [mag]
10	MAGERR_ISO	RMS error for isophotal magnitude [mag]
11	MAG_PETRO	Petrosian-like elliptical aperture magnitude [mag]
12	MAGERR_PETRO	RMS error for PETROsian magnitude [mag]
13	MAG_APER_1	Aperture magnitude within 5.0-pixel (1.00″) diameter [mag]
14	MAG_APER_2	Aperture magnitude within 7.1-pixel (1.42″) diameter [mag]
15	MAG_APER_3	Aperture magnitude within 10.0-pixel (2.00″) diameter [mag]
16	MAG_APER_4	Aperture magnitude within 14.1-pixel (2.82″) diameter [mag]
17	MAG_APER_5	Aperture magnitude within 20.0-pixel (4.00″) diameter [mag]
18	MAG_APER_6	Aperture magnitude within 28.3-pixel (5.66″) diameter [mag]
19	MAG_APER_7	Aperture magnitude within 40.0-pixel (8.00″) diameter [mag]
20	MAG_APER_8	Aperture magnitude within 50.0-pixel (10.0″) diameter [mag]
21	MAG_APER_9	Aperture magnitude within 60.0-pixel (12.0″) diameter [mag]
22	MAGERR_APER_1	RMS error for the aperture mag 1 [mag]
23	MAGERR_APER_2	RMS error for the aperture mag 2 [mag]
24	MAGERR_APER_3	RMS error for the aperture mag 3 [mag]
25	MAGERR_APER_4	RMS error for the aperture mag 4 [mag]
26	MAGERR_APER_5	RMS error for the aperture mag 5 [mag]
27	MAGERR_APER_6	RMS error for the aperture mag 6 [mag]
28	MAGERR_APER_7	RMS error for the aperture mag 7 [mag]
29	MAGERR_APER_8	RMS error for the aperture mag 8 [mag]
30	MAGERR_APER_9	RMS error for the aperture mag 9 [mag]
31	KRON_RADIUS	Kron aperture
32	PETRO_RADIUS	Petrosian aperture
33	FWHM_IMAGE	FWHM assuming a gaussian core [pixel]
34	ELLIPTICITY	1 - B_IMAGE/A_IMAGE
35	PA	Position angle (east of north) (J2000) [deg]
36	CLASS_STAR	Star/Galaxy classifier output
37	FLAGS	Extraction flags from SExtractor
38	NM	Number of matched objects from different arrays
39	xtfl	Cross-talk information (0 : Source, 1 : Cross-talk)

Note. — The aperture correction was not applied for aperture magnitudes. The Galactic extinction was not corrected. All magnitudes are given in the Vega system.

for each field. Our catalogs contain photometric data of $\sim 7 \times 10^6$ sources including cross-talk information. This IMS data is being used for various studies including our high redshift quasar selection.

Chapter 3

Quasar Selection at z $\sim$ 5

3.1 Introduction

In recent years, more than 70 quasars at z $\geq$ 5 have been discovered from large area surveys (e.g., Fan et al. 2003, 2006a; Willott et al. 2007, 2010a; Jiang et al. 2008, 2009, 2015; Mortlock et al. 2009, 2011). These high redshift quasars enable us to study the evolution of supermassive black holes (SMBHs; e.g., Jiang et al. 2007; Kurk et al. 2007; Jun et al. 2015) and the metal enrichment history of the early universe when the age of the universe was less than 1 Gyr (e.g., Jiang et al. 2007; Kurk et al. 2007; Juarez et al. 2009; De Rosa et al. 2011, 2014). In addition, they allow us to examine the line-of-sight condition of the intergalactic medium (IGM), such as the re-ionization state (e.g., Fan et al. 2006b; Carilli et al. 2010; McGreer et al. 2011).

Observations have shown that quasars with M $\sim 10^{10}$ $M_{\odot}$ are found at z $\sim$ 4.5, but at z $>$ 6, the average mass of SMBHs seem to be $\sim 10^{9}$ $M_{\odot}$ and they appear to be vigorously evolving (Shen et al. 2011; Jiang et al. 2010; Im 2009; Jun et al. 2015). However, there are not enough quasars whose masses have been estimated to investigate how they evolved at 5 $<$ z $<$ 6 (yellow shaded region on Figure 3.1

or Figure 16 in Jun et al. 2015). Measuring the black hole masses for a fair number of objects at this redshift range allows us to do the following: (1) they can be used to derive the Eddington luminosities, and consequently, the Eddington ratios, to see how vigorously these quasars are growing. One might expect the growth to slow down at this epoch; (2) the construction of the black hole mass function can help us understand how rapidly the most massive quasars have grown since z $\sim$ 6; (3) the spectral energy distribution (SED) shapes of quasars can be investigated to see if quasars with very massive black holes have a lower accretion disk temperature, as suggested by Laor & Davis (2011) and Wang et al. (2014).

However, there exist redshift gaps in current high redshift quasar surveys, especially at $4.8 < z < 5.7$. Although some quasar surveys have been performed at z $\sim$ 5 or z $\sim$ 6 (e.g., Zheng et al. 2000; Sharp et al. 2001; Schneider et al. 2001; Fan et al. 2003, 2006a; Mahabal et al. 2005; Cool et al. 2006; Willott et al. 2007, 2010a; Jiang et al. 2008, 2009, 2015; Wu & Jia 2010; Matute et al. 2013; McGreer et al. 2013), they could not detect all quasars at $5 < z < 6$ efficiently (yellow shaded region on Figure 3.1). This is due to limitations of current filter systems employed by these surveys as described below.

Most of the quasars at z $\sim$ 5 were discovered by the Sloan Digital Sky Survey (SDSS; Richards et al. 2002; McGreer et al. 2013) using the $r-i$ color for r-dropouts and the $i-z$ color for removing dwarf stars. However their filter system cannot observe quasars at z $>$ 5.1. Also Ikeda et al. (2012) used the $r-i$ vs. $i-z$ color-color diagram and discovered only one type-2 quasar at z = 5.07. In the case of Wu & Jia (2010), to find quasars with redshift up to 5.3, they adopted new color cuts, $J-K$ vs. $i-Y$, and conducted a χ^2 fitting of SEDs for high redshift quasars, but the SED fitting was done only on the color selected candidates, which is incapable of selecting quasars at z $>$ 5. Therefore, these studies were unsuccessful in finding z $>$ 5 quasars. For quasar surveys at z $\sim$ 6, most surveys for z $\sim$ 6 are limited to z

> 5.7.

This low efficiency is because the late type stars or dwarf stars have colors similar to those of quasars at $5 < z < 6$. Figure 3.2 shows two color-color diagrams generally used for the high redshift quasar selection. The black solid lines with asterisks are quasar redshift tracks redshifted from a quasar template from Vanden Berk et al. (2001), the triangles are for model colors of dwarf stars from Burrows et al. (2006), the squares are for model colors of stars by Hewett et al. (2006) from Bruzual-Persson-Gunn-Stryker (BPGS) atlas, and the crosses are point-like sources from the SDSS Star Catalog. Fan et al. (1999) used the $r - i$ vs. $i - z$ color-color diagram for quasars at $z > 4.5$ (Figure 3.2 (a); r-dropout quasars) and Willott et al. (2009) used the $i - z$ vs. $z - J$ color-color diagram for quasars at $z \sim 6$ (Figure 3.2 (b); i-dropout quasars). The solid boxes indicate their quasar selection boxes. We can see that r-dropout quasars at $z > 5.1$ (Figure 3.2 (a)) and i-dropout quasars at $z < 5.7$ (Figure 3.2 (b)) are mixed with the late type stars or dwarf stars on these color-color diagrams. Therefore the r-dropout technique alone cannot be used for $z \sim 5.5$ quasar selection. As can be seen from above, any configuration of colors from SDSS and UKIDSS filters cannot separate quasars at $5.1 < z < 5.7$ from stars effectively; a new filter system which exploits the wavelength range between classic filters is necessary to find these quasars.

Therefore we searched for and studied such high redshift quasars at $5 < z < 6$ using new, additional datasets and performing follow-up observations. First, we designed a new filter set, Is and Iz, to supplement the previous filter systems for selecting quasars at this redshift range. Since the central wavelengths of these filters are located between r and i, and between i and z, respectively, we can select high redshift quasars at this redshift gap, where the SDSS or other filter sets cannot explore. Second, we needed a special optical detector which has better sensitivity than previous CCDs, leading to the higher efficiency of observation with Is and

Iz filters. Considering the requirements of a new system, we developed a CCD camera system, Camera for QUasars in EArly uNiverse (CQUEAN; Park et al. 2012). Equipping a deep-depletion CCD chip to provide high quantum efficiency (QE) at 0.7 – 1 μm, we conducted follow-up imaging observations of quasar candidates with Is and Iz filters and narrowed down the quasar candidates. CQUEAN was installed on the 2.1-m Otto Struve Telescope at McDonald Observatory in August 2010, and it has obtained photometric data for many scientific programs including our high redshift quasar survey. The filter transmission curves of Is and Iz (black solid lines), and the SDSS gri and LSST zY bands (colored dashed lines) installed on CQUEAN are shown in Figure 3.3 including the QE of the CCD (gray solid line).

Chap. 3.2 describes our quasar selection algorithm including color cuts, multi-wavelength data we used, and design for follow-up observations. Then we explain the optical imaging follow-up observations (Chap. 3.3), optical spectroscopic follow-up observations (Chap. 3.4), and NIR spectroscopic observations (Chap. 3.5). The photometric and spectroscopic properties of our newly discovered quasars are shown in Chap. 3.6 and 3.7. We discussed our quasar selection efficiency in Chap. 3.8. We summarize this survey in the final chapter (Chap. 3.9). Throughout this paper, we use a cosmology with $\Omega_M = 0.3, \Omega_\Lambda = 0.7$, and $H_0 = 70$ km s^{-1}Mpc^{-1}. We use the AB magnitude system.

3.2 Selection Method

3.2.1 Definition of Color-color Diagrams

To select quasar candidates from the broadband photometry, we used the dropout feature at the Lyα emission line and the power-law continuum. The Lyα dropouts can be identified using the $r - i$ color for $3.6 < z < 4.7$ and $i - z$ color for $4.7 < z < 5.8$. To exploit the differences of continuum properties between stars and quasars, we

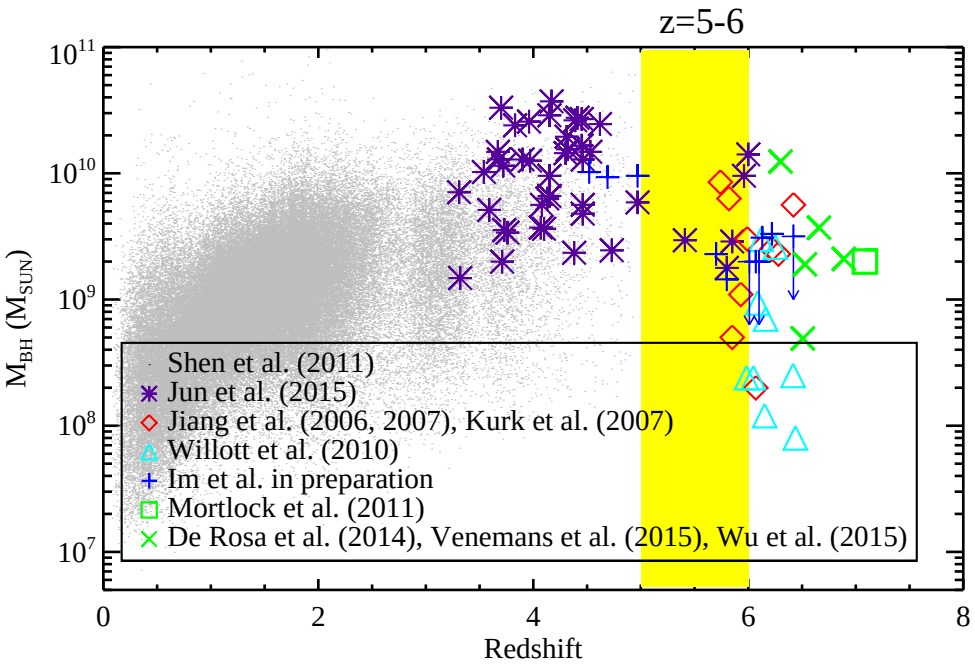

Figure 3.1 Mass distribution of the SMBHs along the redshifts from the literature (symbols). The yellow shaded region indicates the redshift gap at $5 < z < 6$.

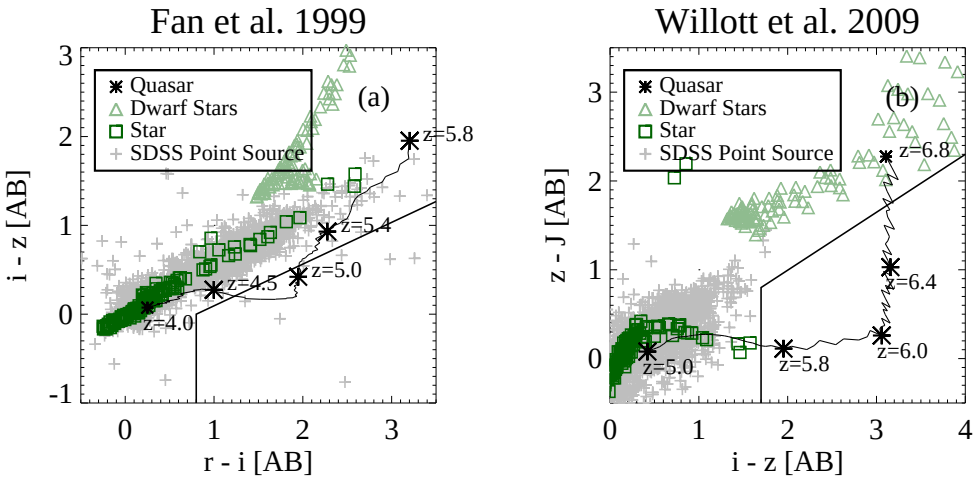

Figure 3.2 Two color-color diagrams adopted by Fan et al. (1999) and Willott et al. (2009). The black solid lines with asterisks are quasar redshift tracks, the triangles are for models of dwarf stars, the squares are for models of stars, and the crosses are point-like sources from the SDSS Star Catalog. We can see that the position of the redshift track from z = 5.1 to z = 5.7 coincides with those of late type stars or dwarf stars. The solid boxes indicate their quasar selection boxes.

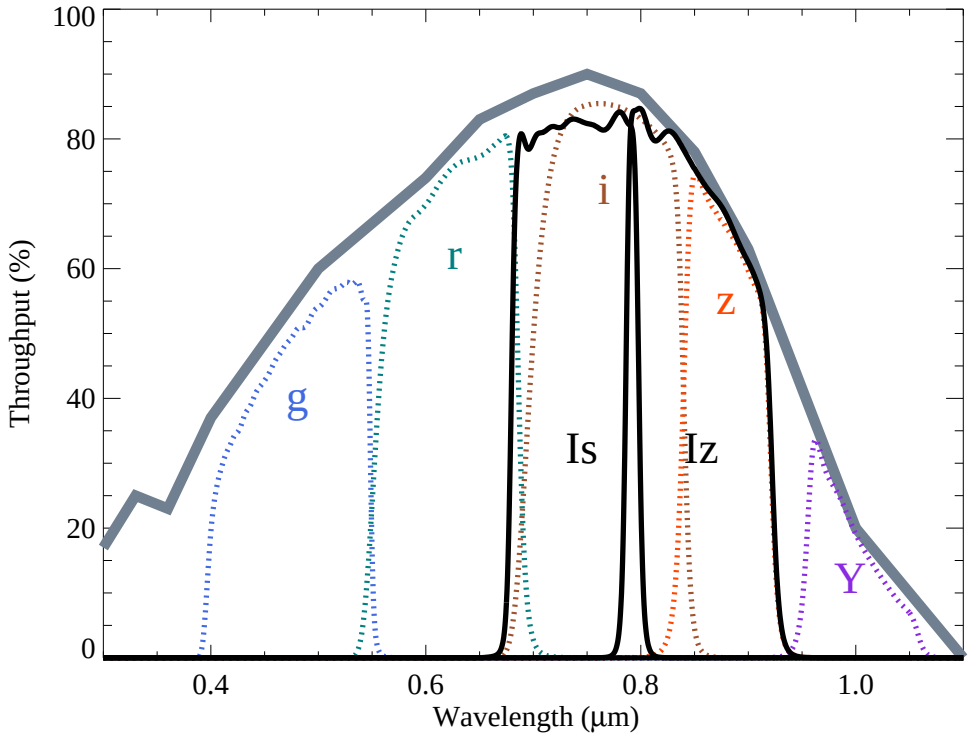

Figure 3.3 Filter transmission curves of Is and Iz (black solid lines), SDSS gri, and LSST zY bands (colored dashed lines), and the QE of the CCD (gray solid line) of CQUEAN.

plotted color-color diagrams employing various combinations of colors, for example, $i-z$, $z-Y$, $Y-J$, $J-H$, and $H-K$. Comparing color differences between the quasar redshift track and other interlopers, we decided to use two color-color diagrams: $r-i$ vs. $i-z$ and $z-J$ vs. $J-K$. We plotted SEDs of model dwarf stars from Burrows et al. (2006) and a quasar spectrum at z = 5 using a quasar template from Vanden Berk et al. (2001), with filter response curves of z, J, and K-bands in Figure 3.4. These SEDs indicate that the $z-J$ color of the quasar is bluer than that of the dwarf stars. Therefore the dwarf stars, which cannot be excluded using $r-i$ cut, can be excluded using the $z-J$ color.

Figure 3.5 shows two color-color diagrams with model dwarf stars from Burrows et al. (2006) (triangles), observed dwarf stars from Patten et al. (2006) and Zhang et al. (2009) (squares), and sources from the SDSS catalog (filled gray circles, ∼10,000 randomly selected sources). The black circles in (b) indicate SDSS sources with $r-i > 1.5$. To verify the position of quasars at $4 < z < 6$, we also plotted previously discovered quasars from the SDSS DR7 quasar catalog and from Leipski et al. (2014) (crosses; the color of each symbol indicates its redshift shown on the color bar in (b)). The quasar redshift tracks at $4 < z < 6$, are plotted by assuming a quasar template from Vanden Berk et al. (2001). The thick solid lines indicate the selection boxes for our quasar selection and the dotted box in (a) is from Fan et al. (1999) for comparison. The selection boxes are defined as below:

`Cut1`) $r-i > 1.5$

`Cut2`) $0 < J-K < 1 \ \cap \ -1 < z-J < 0.5 \ \cap \ (z-J) < (J-K) + 0.2$,

`Cut1` is for selecting the r and i-dropout objects and `Cut2` is for weeding out the late type and dwarf stars. Since a part of the stellar locus (filled circles) is still located inside `Cut1`, and the selection box of `Cut2` is close to the stellar locus (filled circles), there will be contamination by late type stars.

Using SDSS DR7 quasar catalog, we find that about 55% (80%, 90%) of quasars

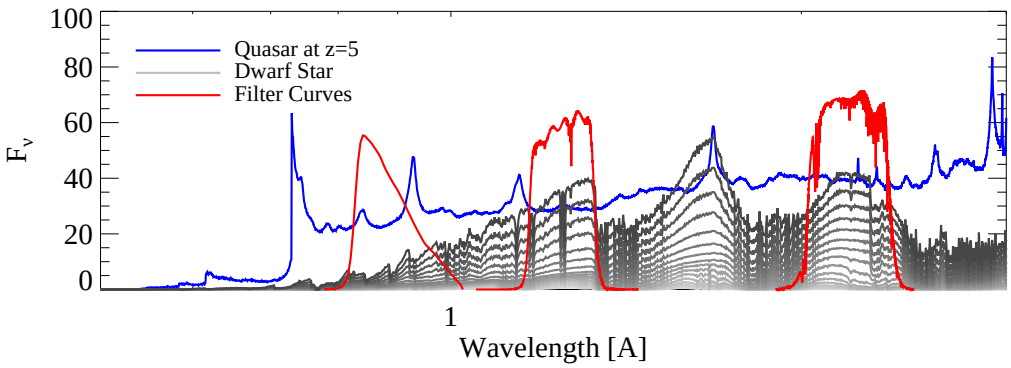

Figure 3.4 SEDs of dwarf stars and a quasar spectrum at z = 5 with filter response curves of z, J, and K-bands overplotted.

satisfy `Cut1` among 392 (223, 56) quasars at z > 4.5 (4.7, 5.0). Also from the catalog of Leipski et al. (2014), which contains quasars at 5.00 < z < 6.43, about 95% (100%) quasars satisfy `Cut2` among 21 (20) quasars at z < 6.0 (5.7). These two diagrams were the most efficient in separating quasars from other interlopers among various color-color diagrams.

3.2.2 Multi-wavelength Data

The cross-matched sources from SDSS DR7 and UKIDSS LAS DR8 were used for the selection, covering an area of ∼2,700 deg^2. The merged catalog of these two surveys were downloaded from the WSA[1]. The conditions for the matching query include sources of $u > 22.3$, $g > 23.0$, and $r - i > 1.5$ with `sdssPrimary`=1 and UKIDSS LAS detection within a 2″ distance. We initially adopted the 5σ detection limits for u and g-band magnitudes. We selected catalog information as below: R.A. and Dec. for each source, UKIDSS 2″ aperture magnitudes with aperture correction (`yAperMag3`, `j_1AperMag3`, `hAperMag3`, `kAperMag3`) and their errors, SDSS

[1]http://surveys.roe.ac.uk/wsa/

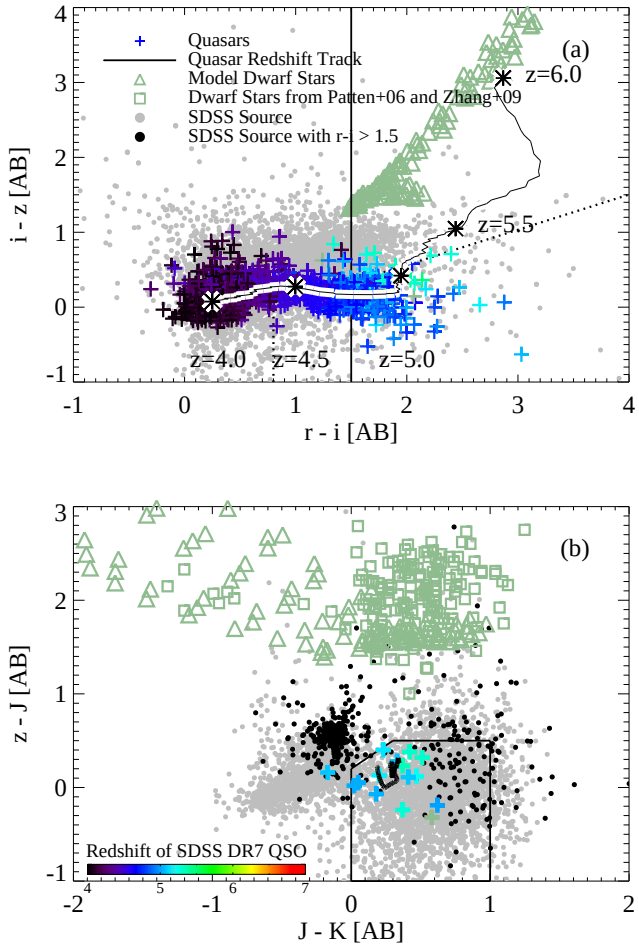

Figure 3.5 Two color-color diagrams we adopted for quasar selection at $5 < z < 6$. The model dwarf stars (triangles), observed dwarf stars from Patten et al. (2006) and Zhang et al. (2009) (squares), sources from SDSS (filled gray circles), previously discovered quasars (crosses) with their color bar in (b), and the redshift tracks of quasars at $4 < z < 6$ (black solid line with asterisks in (a) and black solid line in (b)) are plotted. The solid lines indicate the selection boxes for our quasar selection and the dotted box in (a) is from Fan et al. (1999) for comparison. The black circles in (b) are SDSS sources with $r - i > 1.5$, showing high contamination rate.

PSF magnitudes (`psfMag_u`, `psfMag_g`, `psfMag_r`, `psfMag_i`, `psfMag_z`) and their errors, and information about the stellarity (`mergedClass`, `pStar`, `pGalaxy`, `pNoise`, `pSaturated`, `type_z`). The result of the query contains $\sim 2.8 \times 10^6$ sources.

After the release of UKIDSS LAS DR10, we extended the survey area to ∼3,400 deg^2, and cross-matched sources from SDSS DR8. The query result contains $\sim 3.1 \times 10^6$ sources, with a limiting magnitude cut of $z < 19.5$.

3.2.3 Color Selection with SDSS and UKIDSS LAS

The criteria for the candidate selection are given below:

`Cond_a`) u, g magnitudes fainter than the 3σ detection limits for each band ($u > 22.85$ mag and $g > 23.55$ mag)

`Cond_b`) $r - i > 1.5$

`Cond_c`) $0 < J - K < 1 \bigcap -1 < z - J < 0.5 \bigcap (z - J) < (J - K) + 0.2$

`Cond_d`) $z < 19.5$ mag

From the entire sample of $\sim 2.8 \times 10^6$ sources from the query with UKIDSS LAS DR8, $\sim 2.0 \times 10^6$ sources satisfy `Cond_a`. Among them, $\sim 1.5 \times 10^6$ sources satisfy `Cond_b` and `Cond_c`, and 3,486 of those satisfy `Cond_d`.

These 3,486 candidates still contain contamination considering that the expected number of quasars at z ∼ 5 in 3,400 deg^2 is ∼30 (Chap. 7.1). It is because the selected candidates from these two color-color diagram are still contaminated by interlopers, showing that some of contamination selected with $r - i$ cuts are located in the selection box of the second selection cuts in Figure 3.5. Details are discussed in Chap. 3.8.2. Therefore, we need additional selection methods to eliminate these contaminants.

We checked the number of sources which were classified as quasars at z > 4.7 from the SDSS DR7 quasar catalog and found that 24 sources were included in the quasar catalog, with their redshifts distributed in the range of z = 4.69 – 5.29; these

sources were eliminated from our final candidate list.

3.2.4 Color Selection with Is and Iz-bands of CQUEAN

Since the contamination rate is still too high even after the $z - J - K$ cuts, the candidates selected in Chap. 3.2.3 were conducted optical imaging follow-up observations to eliminate the contamination, using the Is and Iz-bands of CQUEAN. The color cuts were defined using quasar redshift tracks. The most robust candidates for spectroscopic follow-up observations were selected using $r - Is$ vs. $Is - Iz$ or $Is - Iz$ vs. $Iz - J$ color-color diagrams. The criteria for the selections are as below:

`CCD1` ($r - Is$ vs. $Is - Iz$ for $4.7 < \mathrm{z} < 5.4$):

$$r - Is > 1.2 \ \cap \ Is - Iz < 1.2 \ \cap \ Is - Iz < 1.5 \times (r - Is) - 1.2$$

`CCD2` ($Is - Iz$ vs. $Iz - J$ for $5.4 < \mathrm{z} < 6.1$):

$$s - Iz > 1.8 \ \cap \ Iz - J < 1.5.$$

Figure 3.6 shows these two color-color diagrams with quasar redshift tracks (black lines; from Vanden Berk et al. 2001), model dwarf stars (triangles; from Burrows et al. 2006), a star forming galaxy redshift track (blue line; model colors from M51), and a passive galaxy redshift track (red line; model colors from the Bruzual & Charlot (2003) model of a passively evolving 5 Gyr-old galaxy with spontaneous burst, metallicity of Z=0.02, and the Salpeter IMF) on these two color-color diagrams. The two selection boxes for these two color cuts are denoted.

3.2.5 Other Selection Criteria

We set additional criteria for setting priorities of our candidates. These priorities were used for the imaging or spectroscopic follow-up observations.

a) WISE detection

The Wide-field Infrared Survey Explorer (WISE) catalog was released after our candidate selection; the $W1$ and $W2$-band data were matched to our candidate list

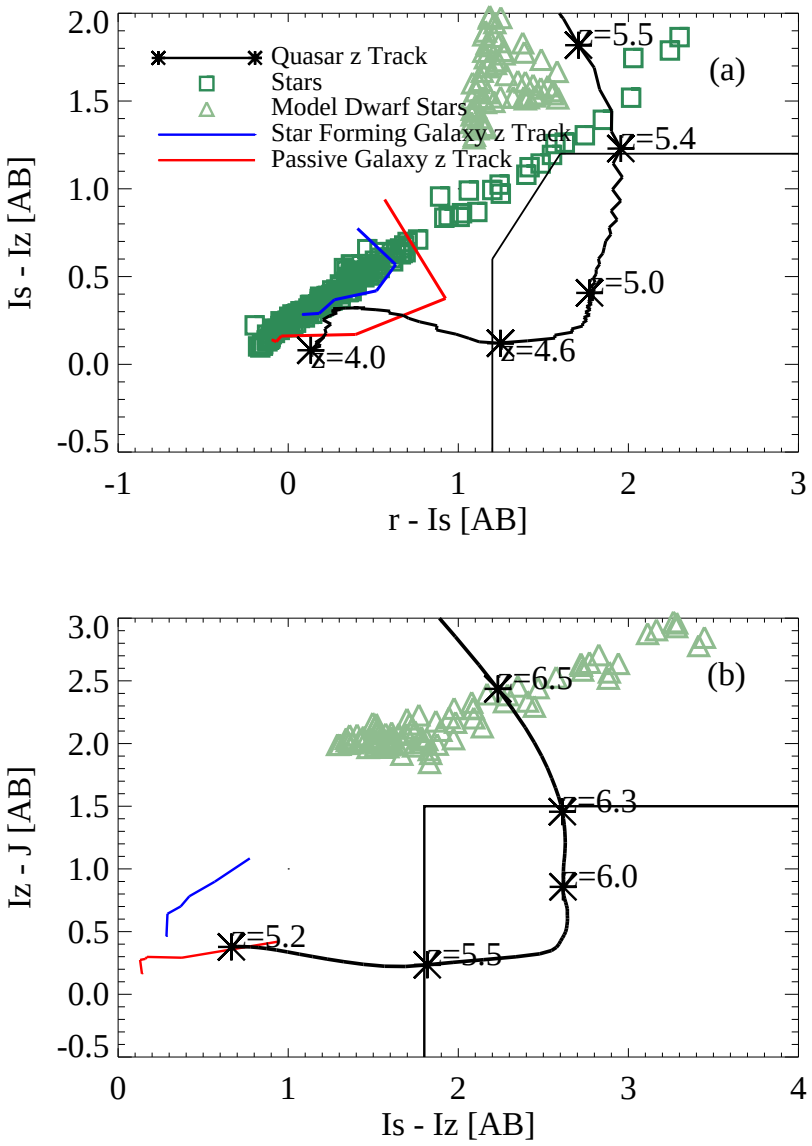

Figure 3.6 Two color-color diagrams using Is and Iz-bands. Quasar redshift tracks (black lines), model dwarf stars (triangles), star forming galaxy redshift tracks (blue lines), passive galaxy redshift tracks (red lines), and the two selection boxes are plotted.

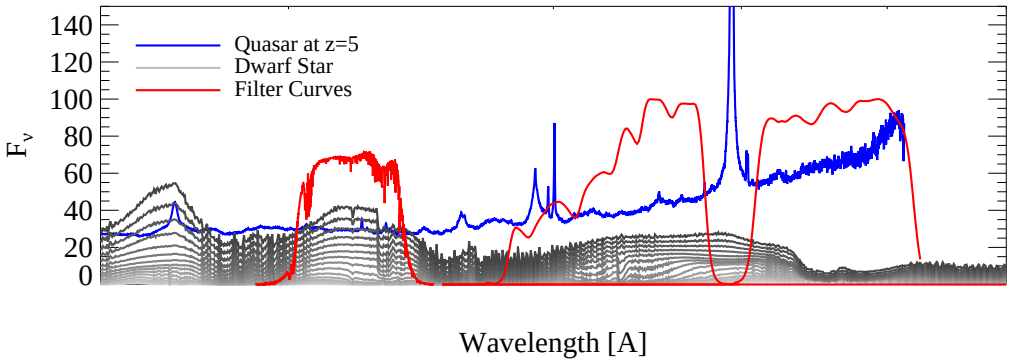

Figure 3.7 SEDs of dwarf stars and a quasar spectrum at z = 5 with filter response curves of K, $W1$, and $W2$-bands overplotted.

to select sources that are bright in the $W1$-band. We assigned high priorities to these sources for the imaging or spectroscopic follow-up observations.

We initially used the WISE Preliminary Release Source Catalog for the WISE detection query. The list of our candidates was used to find WISE sources within a $10''$ radius. Among the 3,486 candidates from UKIDSS LAS DR8, 1,142 were located inside the WISE survey area, but only 871 sources had WISE detections within $10''$. Also, from the WISE All-Sky Source Catalog, all 3,486 of our candidates were located inside the WISE survey area, and 2,660 of them had WISE detections within $10''$. Considering the distribution of distances between our targets and WISE detections, we decided the matching radius to be $2''$. We plotted SEDs of dwarf stars from Burrows et al. (2006) and a quasar spectrum at z = 5 using a quasar template from Vanden Berk et al. (2001), with filter response curves of K, $W1$, and $W2$-bands in Figure 3.7. We expect that the quasars at z $\sim$ 5 have red $K - W1$ and $W1 - W2$ colors whereas the dwarf stars do not.

We downloaded information such as `w1mpro` – `w4mpro` (instrumental profile-fit photometry magnitudes of bands 1 – 4), `w1sigmpro` – `w4sigmpro` (instrumental

profile-fit photometry flux uncertainty in mag units of bands 1 – 4), `nb` (number of blend components used in each fit), `cc_flags` (prioritized artifacts affecting the source in each band), and `ext_flg` (probability that source morphology is not consistent with single PSF). We checked the credibility of the photometric information of each WISE source by visually inspecting the WISE images and their SEDs, and we gave low priorities to WISE sources which had `nb` > 1, `ext_flg` $\neq 0$, and `cc_flags` $\neq 0000$. The final number of candidates within a matching radius of $2''$ and with high priorities is 1,880 from the WISE All-Sky Source Catalog.

Our color cut criteria on the color-color diagrams with the WISE colors were decided using the observed and model magnitudes of high redshift quasars. 5 of the 24 previously discovered quasars had WISE detections from the WISE Preliminary Release Source catalog. Figure 3.8 shows their SEDs including WISE photometry and the redshifted quasar templates from Vanden Berk et al. (2001) (gray lines). All of them satisfy the conditions for the `nb`, `ext_flg`, and `cc_flags`. From these SEDs, we found that the power-law continuum induces a constant SED slope between $W1$ and $W2$ or $W1$ and $W3$-bands. Plotting various combinations of these bands on color-color diagrams, we decided the color cuts for the high redshift quasar selection.

We used $K - W1$ vs. $W1 - W2$ and $K - W1$ vs. $W1 - W3$ color-color diagrams (Figure 3.9) to give high proprieties for candidates with specific color ranges. We plotted the observed colors of the 5 quasars (squares) and model dwarf stars (triangles; from Burrows et al. 2006), as well as a quasar redshift track at $5 < z < 6$ (black line; from Vanden Berk et al. 2001), a star forming galaxy redshift track (blue line; model colors from M51), and a passive galaxy redshift track (red line; model colors from the Bruzual & Charlot (2003) model of a passively evolving 5 Gyr-old galaxy with spontaneous burst, metallicity of Z=0.02, and the Salpeter IMF) on these two color-color diagrams. The two selection boxes for these two color cuts are denoted. Since the quasar template from Vanden Berk et al. (2001) redshifted to $z \sim$

5 does not extend to the $W3$-band, only Figure 3.9 (a) has the quasar redshift track. Due to the power-law continuum of quasars at this observed wavelength range, they have almost identical $K - W1$ and $W1 - W2$ colors, and thus cover a small region on the color-color diagram. From the colors of the observed quasars on these two color-color diagrams, we decided `Cut1` (purple boxes). Also, the criteria of `Cut2` (green boxes) were selected considering the position of the quasar redshift track. The candidates inside these color cuts were assigned high priorities. We defined our color cuts (purple boxes for `Cut1` and green boxes for `Cut2`) as below:

`Cut1`: $W1 - W2 > -0.6 \cap -0.6 < K - W1 < 2$

and/or $W1 - W3 > -0.6 \cap -0.6 < K - W1 < 2$

`Cut2`: $W1 - W2 > 0 \cap K - W1 > -0.5$

and/or $W1 - W3 > 0 \cap K - W1 > -0.5$.

b) Color cuts from McGreer et al. (2013)

McGreer et al. (2013) discovered 71 quasars at $4.7 < z < 5.1$ over the area covered by SDSS, including Stripe 82. We gave high priorities to our candidates that are inside the color cuts used in their work. Their color cuts are defined as below:

`Cut1`) $r - i > 1.2$

`Cut2`) $(i - z) < 0.625 \times (r - i - 1.0)$

`Cut3`)$i - z < 0.55$

`Cut4`) $i - J < (r - i - 1.0) + 0.56$.

158 of our candidates satisfied the above conditions, with 10 of them being previously discovered as high redshift quasars. We assigned high priorities to the other 148 candidates. Sources predicted from these color cuts, but not included in our color cuts, are also added additionally to our candidate list.

c) *H-K* color cut

From the SEDs of the SDSS quasars, we found that quasars at $5 < z < 6$ tend to

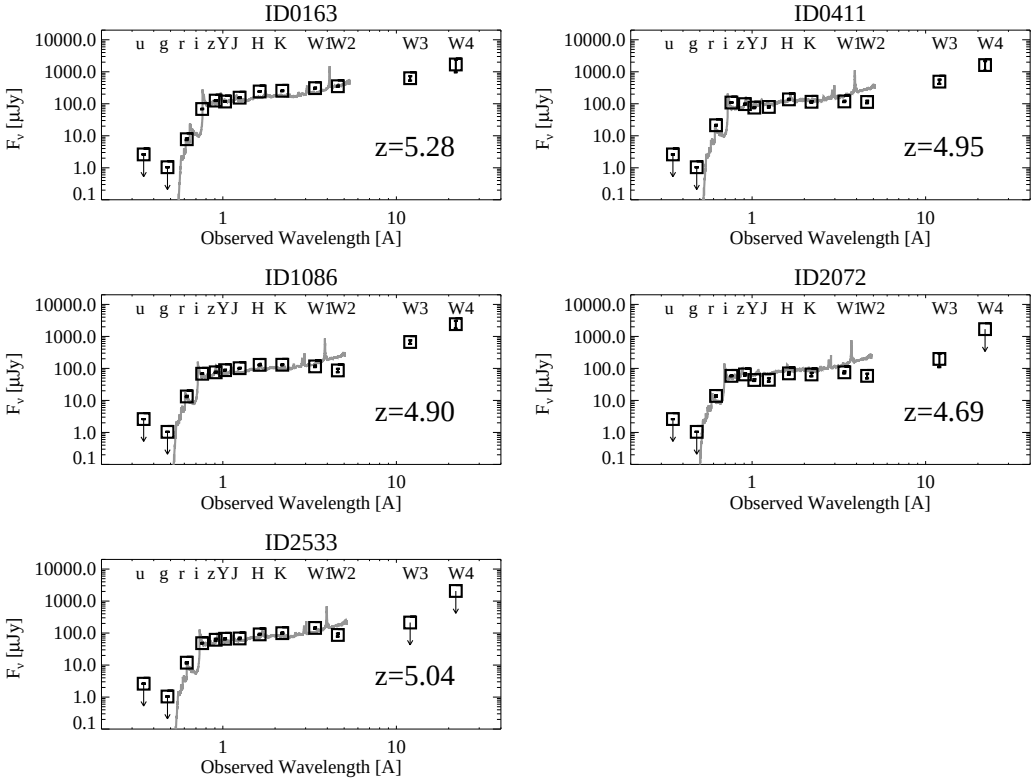

Figure 3.8 SEDs of quasars that are also candidates of our survey, and that are included in the WISE Preliminary Release Source Catalog. The gray lines are the quasar templates from Vanden Berk et al. (2001), redshifted to each redshift of sources.

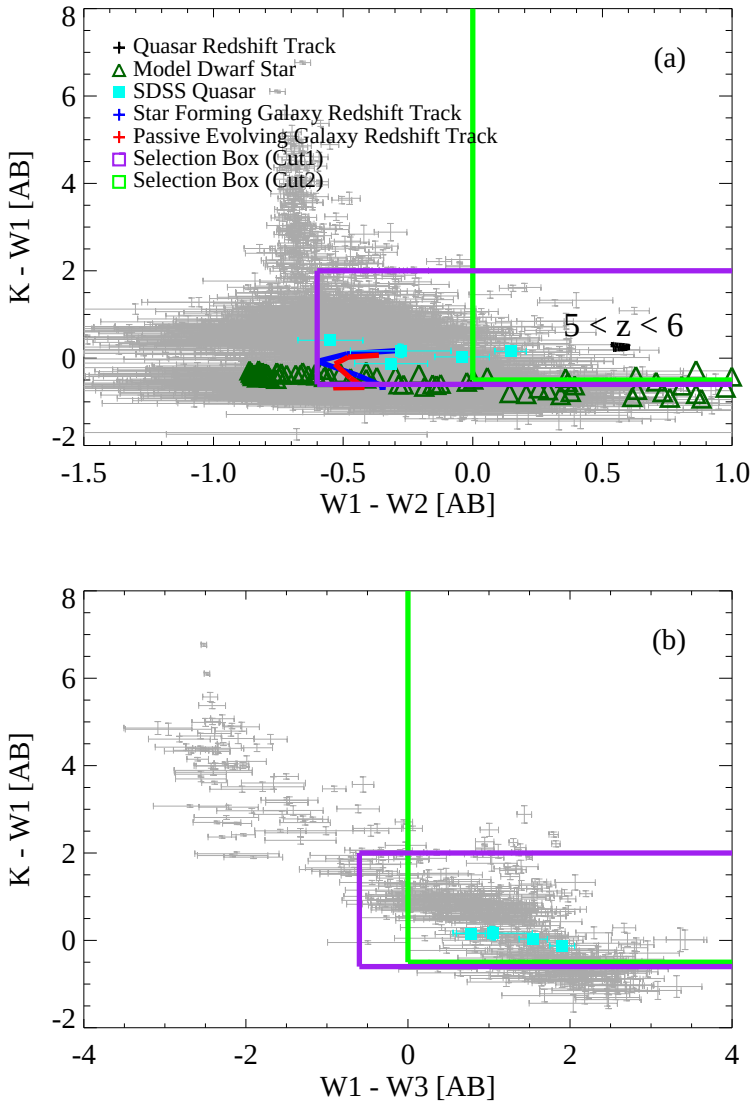

Figure 3.9 Two color-color diagrams with WISE photometry and our selection boxes. We plotted the observed colors of the 5 quasars (squares) and model dwarf stars (triangles), and redshift tracks of a quasar for $5 < z < 6$ (black line), a star forming galaxy for $0 < z < 1$ (blue line), and a passive galaxy for $0 < z < 1$(red line).

have $H-K$ colors redder than those of dwarf stars due to the power-law continuum of quasars. Therefore we gave higher priorities to sources that have $H-K+0.1>0$. The 0.1 mag is included to take the photometric errors into consideration.

d) Candidates from Polsterer et al. (2013)

Polsterer et al. (2013) provide a quasar candidate catalog containing 121,909 sources with their photometric redshifts at $2.558 \leq z \leq 6.131$. 10 sources are included in our candidate list and we gave higher priorities to these sources.

e) Stellarity

We use `mergedClass` for UKIDSS LAS and `type` for SDSS to distinguish point sources from extended sources. We defined that a source with `mergedClass` $= -1$ or -2, or `type` $= 6$, is a point source, and gave higher priorities to these sources. We did not exclude the extended sources because 17% of the discovered quasars from McGreer et al. (2013) are classified as extended sources, meaning that some quasars may be observed as extended sources.

3.2.6 Priority for Imaging Follow-up Observations

We set priorities of our candidates for the imaging follow-up observations considering the stellarity, the WISE detection, the color cuts from McGreer et al. (2013), and the $H-K$ color cut. The high priority candidates from Polsterer et al. (2013) are for spectroscopic follow-up observations. Objects showing point-like shapes with WISE detections and red $H-K$ color as well as satisfying the color cuts from McGreer et al. (2013) were classified as the most important candidates. Table 3.1 lists the priority for each case, with smaller numbers indicating higher priorities. We conducted the Is and Iz imaging for the high priority objects.

Table 3.1. Priorities for CQUEAN imaging follow-up observations

Priority	Stellarity	WISE	McGreer	$H-K$
0	yes	yes	yes	yes
1	yes	no	yes	yes
2	yes	yes	no	yes
3	yes	no	no	yes
4	yes or yes or yes			no
5	no		yes	
10	others			

3.3 Optical Imaging Follow-up Observations with CQUEAN

3.3.1 Observations

Follow-up observations of our high redshift quasar candidates using CQUEAN started in August 2010 and are still on-going. About 1,400 among 3,486 candidates with high priorities were observed by CQUEAN until now.

We used short single exposure times of 30s for Iz and 60s for Is filters, respectively, considering sky variations due to thin cirrus. After many trials, we decided the total exposure time depending on the sky conditions, such as seeing conditions and extinction. If the peak value of a target is greater than 80 ADU after a 30s exposure with Iz, 2.5 (30s $\times$ 5) and 5 (60s $\times$ 5) min were used as the integration times with the Iz and Is filters, respectively. If the signal is lower than the criterion, we exposed 5 (30s $\times$ 10) and 10 (60s $\times$ 10) min with Iz and Is, respectively.

3.3.2 Data Reduction

Preprocessing, such as bias subtraction, dark subtraction and flat fielding, were conducted with the usual data reduction procedure using the IRAF `noao.imred.ccdred` package. Since the bias values may change with time (Park et al. 2012), we used bias images that are closest, time-wise, to each target image to make a bias frame. We combined images of each field and filter in average. We used the `ccmap` task of IRAF and SCAMP (Bertin 2006) to derive astrometric solutions. SExtractor (SE; Bertin & Arnouts 1996) was used for the source detection and photometry. We derived auto-magnitudes which are taken as the total magnitudes.

For the photometric calibration, we used stellar objects, for which SDSS photometry is available, inside each target field. Using the r, i, and z-band magnitudes of a neighborhood object, we did a χ^2 fitting to the SED of the object to find a best-fitted spectral template among stellar spectral templates. We used template from Gunn & Stryker (1983), containing 175 spectra with various stellar types. From the best-fit template, we calculated model magnitudes for Is and Iz filters using their filter transmission curves, and defined the values as their standard magnitudes (M_{std}) of each filter. Then, the standard magnitudes of the neighborhood stars were compared with their instrument magnitudes (m_{ins}; $m_{ins} = -2.5\log(\mathrm{DN})$), and the differences between the M_{std} and the m_{ins} were used to estimate the zero-point (Zp). We defined the Zp as the average value of the magnitude difference and the zero-point error as the standard deviation of the scatters. The average zero-point error is about 0.05 mag. During the calculation, objects with large χ^2 values were rejected for the estimation. The standard magnitude of our sources for each filter was calculated with a formula of $M_{std} = Zp + m_{ins}$.

3.4 Optical Spectroscopic Follow-up Observations

3.4.1 Observations

We observed our candidates using the Kitt Peak National Observatory (KPNO) 4-m Mayall telescope or European Southern Observatory (ESO) New Technology Telescope (NTT). The KPNO observations were scattered over three runs[2] for 10 nights from January to September 2013, and the ESO observation[3] was done for 3 nights at May 2013.

For the observations at KPNO, we used the 4-m Ritchey-Chrétien Focus Spectrograph in a longslit mode (RCSPL) with a LB1A CCD, the BL400 grating of R $\sim$ 500 for a $2''$ slit, and OG400 filter. LB1A uses a thick CCD chip, therefore it does not suffer much from fringing, and provides a good sensitivity in the longer optical wavelengths than previous CCDs. For the observation at the ESO telescope, we used the ESO New Technology Telescope with the ESO Faint Object Spectrograph and Camera v.2 (EFOSC2) at La Silla observatory. The EFOSC2 was used with Gr#2 of R $\sim$ 135 for a $1''$ slit.

We took calibration frames including bias, dark, flat, and arc. Standard stars such as G191B2B, GD153, CD-32d9927, LTT7379, LTT3864, Feige110, and HR7596 were observed for the flux calibration. The slit widths were variously set from $1.0''$ to $3.0''$, depending on the seeing conditions . We observed 47 candidates and 6 of them turned out to be high redshift quasars. ID0308 was observed with both the KPNO 4-m telescope and NTT. We combined two spectra in average for this object. Table 3.2 shows the observational summary of the discovered quasars, namely the total integration time and the slit width for each target. Table 3.3 lists targets turned out to be stars or galaxies.

[2]NOAO 2012B-0537, 2013A-0506, and 2013B-0534 by PI: Y. Jeon

[3]ESO 091.A-0878(A) by PI: Y. Jeon

Table 3.2. Observation summary of discovered quasars from optical spectroscopic observations

Date	Telescope	Target	Int. Time [min]	SlitWidth [″]
16 Jan. 2013	KPNO 4-m	ID0654	80	3.0
6 May 2013	NTT	ID0719	40	1.2
6 May 2013	NTT	ID0308	90	1.0
7 May 2013	NTT	ID0719	60	1.0
27 Sep. 2013	KPNO 4-m	ID0106	45	1.5
28 Sep. 2013	KPNO 4-m	ID0099	60	1.5
28 Sep. 2013	KPNO 4-m	ID0085	45	1.5
29 Sep. 2013	KPNO 4-m	ID0308	60	1.5
29 Sep. 2013	KPNO 4-m	ID0106	45	1.5

Table 3.3. Targets turned out to be stars or galaxies from optical spectroscopic observations

Date	Telescope	Target	R.A.	Dec.
Jan. 2013	KPNO 4-m	ID0695	13 : 37 : 30.69	−00 : 47 : 21.9
Jan. 2013	KPNO 4-m	ID0941	03 : 30 : 09.15	+00 : 14 : 04.3
Jan. 2013	KPNO 4-m	ID1526	09 : 19 : 08.53	+30 : 59 : 25.8
Jan. 2013	KPNO 4-m	ID2295	01 : 09 : 18.18	+13 : 49 : 04.6
May 2013	NTT	ID0063	14 : 35 : 21.94	+01 : 06 : 15.1
May 2013	NTT	ID0077	08 : 50 : 03.85	+00 : 30 : 13.5
May 2013	NTT	ID0125	15 : 02 : 08.64	+01 : 05 : 33.0
May 2013	NTT	ID0340	14 : 07 : 24.65	+12 : 31 : 36.3
May 2013	NTT	ID0348	02 : 41 : 13.57	−00 : 38 : 48.9
May 2013	NTT	ID0484	15 : 47 : 02.32	+06 : 42 : 18.7
May 2013	NTT	ID0752	22 : 25 : 10.10	+00 : 57 : 36.5
May 2013	NTT	ID0924	15 : 46 : 17.02	+01 : 22 : 50.4
May 2013	NTT	ID0931	12 : 01 : 16.55	+12 : 39 : 51.5
May 2013	NTT	ID0931	12 : 01 : 16.55	+12 : 39 : 51.5
May 2013	NTT	ID1741	13 : 01 : 03.02	+12 : 07 : 05.9
May 2013	NTT	ID1913	22 : 21 : 40.39	+00 : 21 : 53.0
May 2013	NTT	ID2063	15 : 44 : 47.43	+05 : 28 : 45.6
May 2013	NTT	ID2907	21 : 18 : 17.18	−00 : 31 : 33.0
May 2013	NTT	ID2940	21 : 33 : 55.12	−00 : 05 : 51.3
May 2013	NTT	ID3045	10 : 15 : 42.50	+10 : 21 : 38.4
May 2013	NTT	ID3048	10 : 43 : 51.47	+00 : 06 : 46.1
May 2013	KPNO 4-m	ID0122	00 : 18 : 32.51	+07 : 42 : 24.7
May 2013	KPNO 4-m	ID0172	14 : 35 : 44.10	−00 : 00 : 56.6
May 2013	KPNO 4-m	ID0297	13 : 56 : 14.66	+08 : 35 : 43.7
May 2013	KPNO 4-m	ID2152	16 : 35 : 54.49	+29 : 34 : 40.8
May 2013	KPNO 4-m	ID2173	15 : 39 : 09.11	+05 : 42 : 07.4
May 2013	KPNO 4-m	ID3099	07 : 50 : 43.54	+28 : 22 : 42.6
Sep. 2013	KPNO 4-m	ID0025	09 : 41 : 28.12	+00 : 32 : 03.7
Sep. 2013	KPNO 4-m	ID0120	14 : 06 : 09.66	+13 : 56 : 41.9
Sep. 2013	KPNO 4-m	ID0148	15 : 03 : 53.32	+11 : 53 : 17.2
Sep. 2013	KPNO 4-m	ID0231	11 : 01 : 10.42	+06 : 06 : 33.0
Sep. 2013	KPNO 4-m	ID0320	15 : 34 : 56.50	+04 : 24 : 10.2
Sep. 2013	KPNO 4-m	ID0326	16 : 39 : 43.89	+31 : 22 : 39.0
Sep. 2013	KPNO 4-m	ID0490	02 : 06 : 32.12	−00 : 48 : 05.5
Sep. 2013	KPNO 4-m	ID0727	21 : 09 : 50.94	+00 : 30 : 44.7
Sep. 2013	KPNO 4-m	ID1589	16 : 41 : 07.20	+31 : 04 : 13.3
Sep. 2013	KPNO 4-m	ID1604	22 : 58 : 41.59	−00 : 00 : 16.7
Sep. 2013	KPNO 4-m	ID2050	23 : 22 : 51.23	+06 : 38 : 30.1
Sep. 2013	KPNO 4-m	ID2738	22 : 14 : 32.58	−00 : 59 : 21.4
Sep. 2013	KPNO 4-m	ID3091	21 : 45 : 56.77	+00 : 26 : 01.0
Sep. 2013	KPNO 4-m	ID3234	21 : 02 : 27.71	−00 : 46 : 46.4

3.4.2 Data Reduction

The steps for the preprocessing were conducted with usual methods including bias subtraction, dark subtraction, and flat fielding, for each science image, standard star image and arc image using the `noao.imred.ccdred` package of IRAF. The spectra were extracted using the `noao.imred.kpnoslit` or the `noao.twodspec.apextract` package for each single image. We used the optimal aperture size for each image where the S/N is highest. After this, wavelength and flux calibrations were conducted. The spectra were flux calibrated using spectra of the observed standard stars from Massey & Gronwall (1990) and Hamuy et al. (1992, 1994). Considering the light loss due to various seeing conditions, we scaled the spectra extracted from each image using broadband photometry. We chose i-band for this calibration, since we get the highest S/N in this band for the observed spectra. The flux calibrated spectra were combined using the `scombine` task in median. The spectra were corrected for Galactic extinction using values from Cardelli et al. (1989) and Schlegel et al. (1998).

3.5 NIR Spectroscopic Observation

3.5.1 Observations

To measure the physical properties such as the black hole masses, we observed 3 out of all 6 targets in September 2014 using Magellan/FIRE. Table 3.4 lists the name, coordinates, integration time, and observation date of each target.

We used a slit width of $1.00''$ with Echelle mode (R = 3,600). The ABBA pointing method was used for the sky subtraction between exposures. We observed standard stars for each target. Data for the flat fielding and the wavelength calibration were also taken.

Table 3.4. Observation summary for NIR spectroscopic observations

Target	R.A. & Dec.	Integration Time	Date
ID0106	01:22:47.3 +12:16:24	900s × 4	06 Oct. 2014
ID0099	01:55:33.3 +04:15:07	900s × 2	07 Oct. 2014
ID0085	03:24:07.7 +04:26:13	900s × 4	06 Oct. 2014

3.5.2 Data Reduction

The data reduction was conducted using the IDL suite, `FIREHOSE`, for each frame. This pipeline conducts the preprocessing, object extraction, telluric correction, and flux calibration. The package excludes spectral regions that were significantly contaminated by telluric absorption. The spectra were corrected for Galactic extinction using information of Cardelli et al. (1989) and Schlegel et al. (1998).

3.6 Photometric Properties of IMS Quasars at z ∼ 5

From this survey, we discovered six new quasars at z ∼ 5. We list the photometric information from SDSS and UKIDSS LAS of them in Table 3.5 with their names and coordinates. Table 3.6 lists the photometric information from WISE and CQUEAN and Table 3.7 shows their photometric properties. All of them have WISE detections and most of them are located inside the WISE color cuts ($K - W1 - W2$ or $K - W1 - W3$), except IMSJ2225+0330 and IMSJ0155+0415, since they do not have $W3$ detection. IMSJ0324+0426, IMSJ0122+1216, and IMSJ1437+0708 satisfy the color cuts from McGreer et al. (2013), which is incapable of selecting z > 5.1 quasars. Polsterer et al. (2013) provided a photometric redshift for IMSJ1437+0708

of z=4.961±0.127, which is in agreement with our redshift estimated from its Lyα emission line (Chap. 3.7.2).

We plotted the positions of these IMS quasars in the $r-i-z-J-K$ (Figure 3.10) and the $K-W1-W2-W3$ (Figure 3.11) color-color diagrams. In Figure 3.10 (a), one object, IMSJ0324+0426, does not satisfy our $r-i$ color cut since it was discovered from the color cuts of McGreer et al. (2013). Figure 3.12 shows the colors of 2 IMS quasars with the Is and Iz photometry in the $r-Is-Iz$ color-color diagram.

Only 2 quasars among ∼1,400 sources with the Is and Iz photometry were identified as high redshift quasars with the $r-Is-Iz$ color-color diagram, and none of our candidates were discovered with the $Is-Iz-J$ color-color diagram. The other quasars were selected as candidates using the WISE photometry or the color cuts from McGreer et al. (2013). The expected numbers of quasars for each selection method are ∼30 from $r-Is-Iz$ color selection and ∼5 from $Is-Iz-J$ color selection (Chap. 7.1). This low efficiency of the quasar selection is discussed in Chap. 3.8.

3.7 Spectral Properties of IMS Quasars at z ∼ 5

3.7.1 Optical and NIR Spectra

First, we present the optical spectra of 6 new quasars at z ∼ 5 in Figure 3.13. We plotted spectra smoothed with resolution of each instrument (black lines) to increase the S/N per resolution element, comparing to the original spectra (gray lines). The blue lines denote the errors of the spectra.

These quasars show diverse shapes of Lyα emission lines. For example, ID0085, ID0106, and ID0719 have strong Lyα emission, while the other three show smoother shapes. These weak Lyα lines are fairly common at high redshift. Jiang et al. (2009)

Table 3.5. Optical photometric information of IMS quasars

ID	Name	R.A. & Dec	u	g	r	i	z	Is	Iz
ID0085	IMSJ0324+0426	03:24:07.7+04:26:13.25	25.50±0.72	23.95±0.39	20.39±0.04	19.03±0.03	19.15±0.06	···	···
ID0106	IMSJ0122+1216	01:22:47.3+12:16:23.94	23.43±0.59	24.29±0.37	22.35±0.14	19.37±0.03	19.27±0.06	···	···
ID0719	IMSJ1437+0708	14:37:04.8+07:08:08.30	23.87±1.03	25.02±0.72	20.71±0.04	19.20±0.02	19.10±0.06	19.17±0.11	19.01±0.09
ID0308	IMSJ2225+0330	22:25:14.4+03:30:12.58	24.06±1.02	25.67±0.68	22.01±0.14	20.02±0.05	19.47±0.10	···	···
ID0654	IMSJ1022+0801	10:22:01.9+08:01:22.10	23.89±1.10	25.23±0.64	21.27±0.06	19.74±0.02	19.07±0.05	19.74±0.13	19.20±0.18
ID0099	IMSJ0155+0415	01:55:33.3+04:15:06.78	24.59±1.04	24.07±0.38	21.81±0.10	19.98±0.03	19.26±0.06	···	···

Table 3.6. NIR photometric information of IMS quasars

ID	Name	$W1$	$W2$	$W3$	$W4$	Y	J	H	K
ID0085	IMSJ0324+0426	19.39±0.05	19.23±0.05	18.96±0.05	18.83±0.05	18.47±0.05	18.45±0.09	16.74±0.31	15.27±0.38
ID0106	IMSJ0122+1216	19.12±0.04	18.92±0.04	18.56±0.04	18.50±0.04	18.28±0.05	18.36±0.09	16.67±0.17	99.00±9.00
ID0719	IMSJ1437+0708	19.40±0.05	19.39±0.08	19.01±0.06	18.99±0.08	18.99±0.07	19.12±0.13	18.10±0.46	99.00±9.00
ID0308	IMSJ2225+0330	19.48±0.06	19.33±0.06	19.04±0.10	18.99±0.08	19.44±0.12	19.28±0.22	99.00±9.00	99.00±9.00
ID0654	IMSJ1022+0801	19.21±0.05	19.06±0.05	18.82±0.06	18.71±0.05	18.23±0.05	18.26±0.10	17.01±0.36	99.00±9.00
ID0099	IMSJ0155+0415	19.66±0.07	19.28±0.06	19.00±0.06	18.91±0.06	18.98±0.08	18.68±0.11	99.00±9.00	99.00±9.00

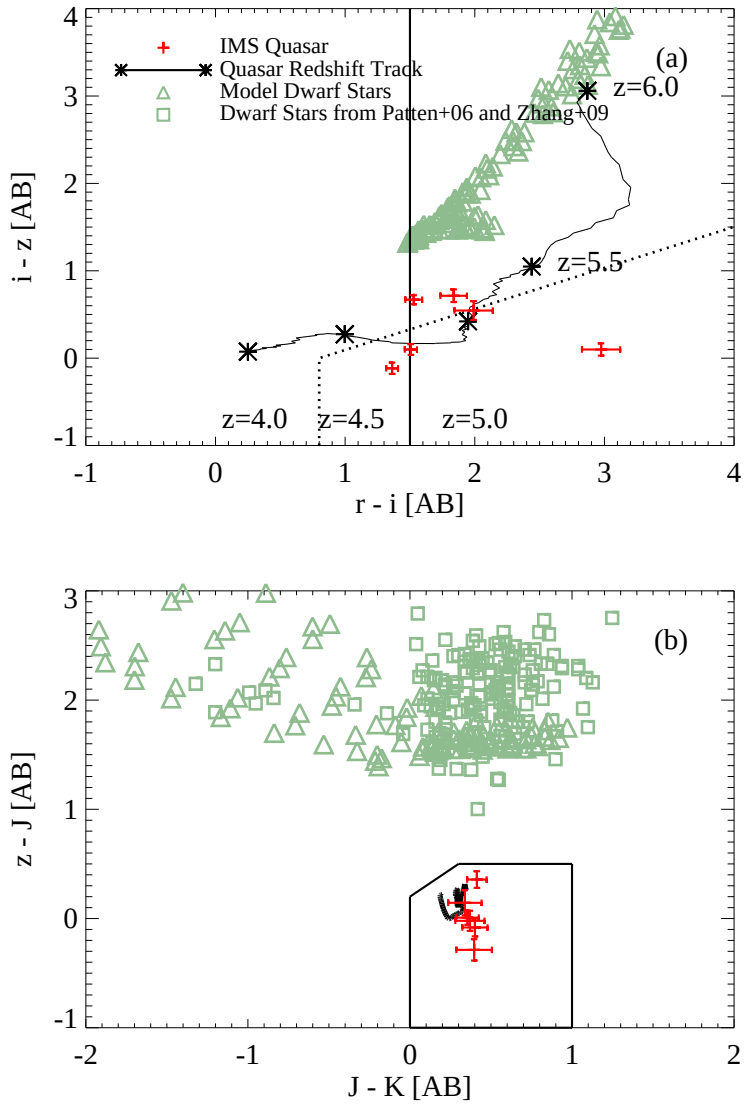

Figure 3.10 Similar to Figure 3.5. We plotted our 6 new quasars at z $\sim$ 5 on these color-color diagrams and all of them are within the selection boxes. One exception in the $r - i - z$ color-color diagram is IMSJ0324+0426, which was discovered from the color cuts of McGreer et al. (2013).

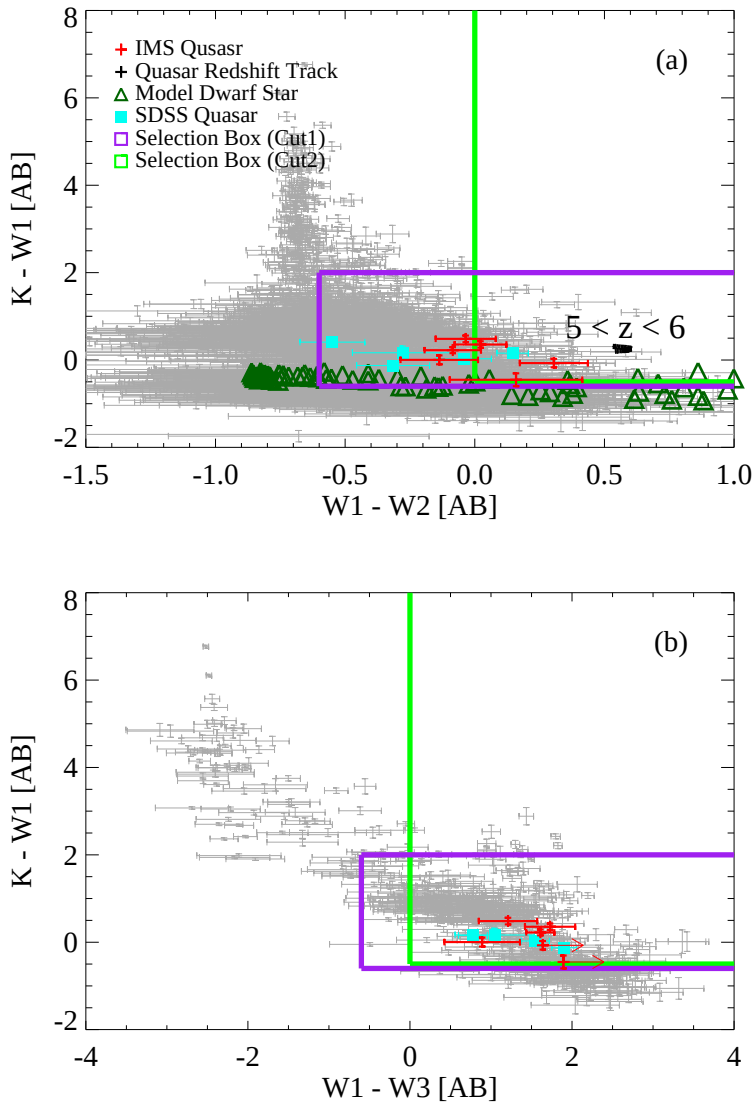

Figure 3.11 Similar to Figure 3.9. All 6 quasars at z 5 satisfy the color cuts within the error bars.

Table 3.7. Photometric Properties of IMS Quasars at z ∼ 5

ID	Name	WISE[a] $(K-W1-W2)$	WISE[b] $(K-W1-W3)$	McGreer et al. (2013)[c]	Polsterer et al. (2013)[d]
ID0085	IMSJ0324+0426	yes	yes	yes	no
ID0106	IMSJ0122+1216	yes	yes	yes	no
ID0719	IMSJ1437+0708	yes	yes	yes	yes
ID0308	IMSJ2225+0330	yes	no	no	no
ID0654	IMSJ1022+0801	yes	yes	no	no
ID0099	IMSJ0155+0415	yes	no	no	no

[a] Does it satisfy the color cut of $K-W1-W2$?

[b] Does it satisfy the color cut of $K-W1-W3$?

[c] Does it satisfy the color cuts from McGreer et al. (2013)?

[d] Is it contained in the candidate list from Polsterer et al. (2013)?

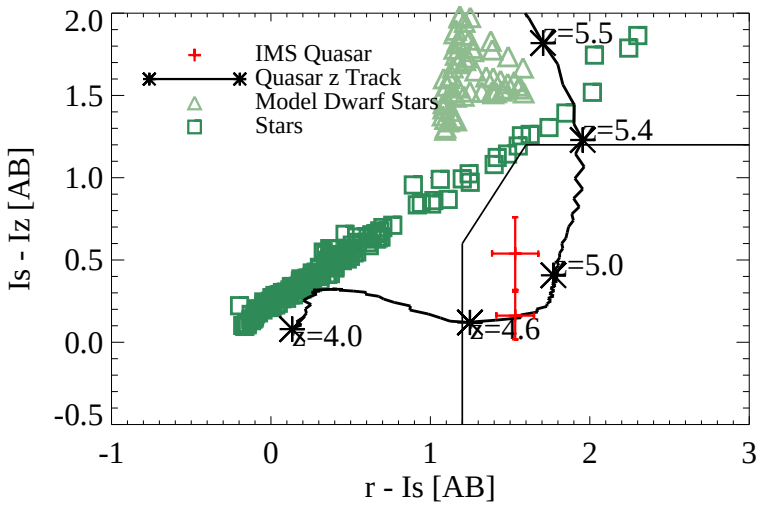

Figure 3.12 Similar to Figure 3.6 (a). We plotted our 2 new quasars with the Is and Iz photometry on the color-color diagram.

and Bañados et al. (2014) show that a significant fraction of these weak emission line quasars at high redshift have weak Lyα. Most of the other emission lines with the exception of Lyα, are difficult to verify, due to the low QE and the imperfection of the sky emission line subtraction at wavelengths longer than 0.8 μm. This can provide significant uncertainties for the continuum flux estimations such as flux at 1350$\mathring{A}$ for the black hole mass estimation and at 1450$\mathring{A}$ for absolute magnitudes of the continuum at rest-frame 1450$\mathring{A}$ (M_{1450}). For instance, bumps that look like broad emission lines may not be actual emission or absorption lines. They were produced due to the insufficient sky emission line subtraction and the low S/N ratio at these wavelengths. However, ID0106 shows significant deep absorption features: this is because ID0106 is a broad absorption line (BAL) quasars. This property can be noticed in its NIR spectrum more clearly.

Second, we present NIR spectra of three objects, ID0085, ID0099, and ID0106 in Figures 3.14, 3.15, and 3.16, respectively. To increase the S/N per resolution element, we binned the reduced spectra to the spectral resolution of each instrument. Using the median statistics for the binning process, we can exclude noise peaks and residuals from telluric absorption corrections. Errors on the smoothed spectra were calculated from the errors on the original spectra via standard error propagation. Since the typical widths of the broad emission lines are FWHM $>$ 1000km s^{-1}, the process binning to R = 3,600 does not affect our results for the continuum and broad emission lines. The regions at $\lambda < 0.9\mu$m can be affected by the flux calibrations from standard stars due to the low quantum efficiency at these wavelengths. Since the observed wavelengths of the C IV emission lines for ID0085 and ID0106 are located at these wavelengths, measurements of continuum slopes can be affected by these incorrect flux calibrations.

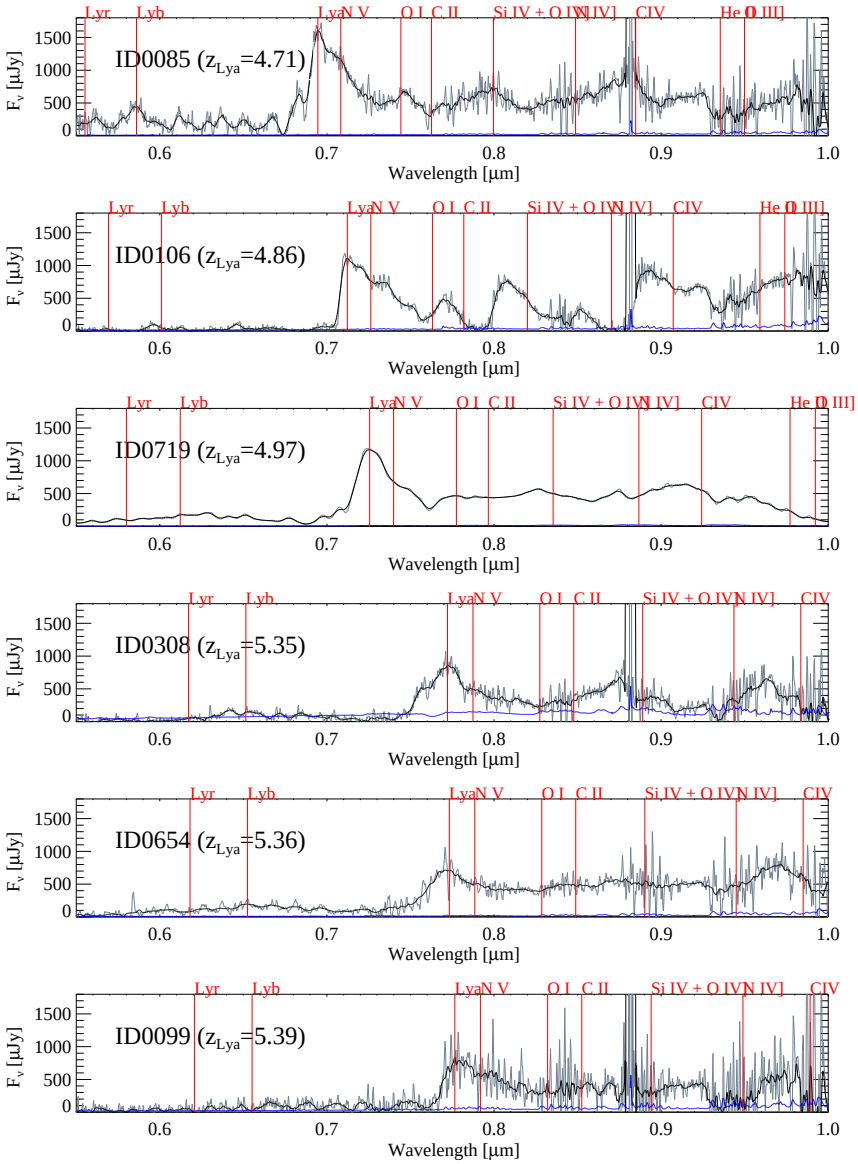

Figure 3.13 Optical spectra of 6 quasars at $4.7 < z < 5.4$ from KPNO 4-m telescope/RCSPL and NTT/EFOCS2. The gray lines are the original spectra and the black lines are spectra smoothed with their instrumental resolutions. The blue lines denote the errors of each spectrum and the red vertical lines indicate general quasar emission lines.

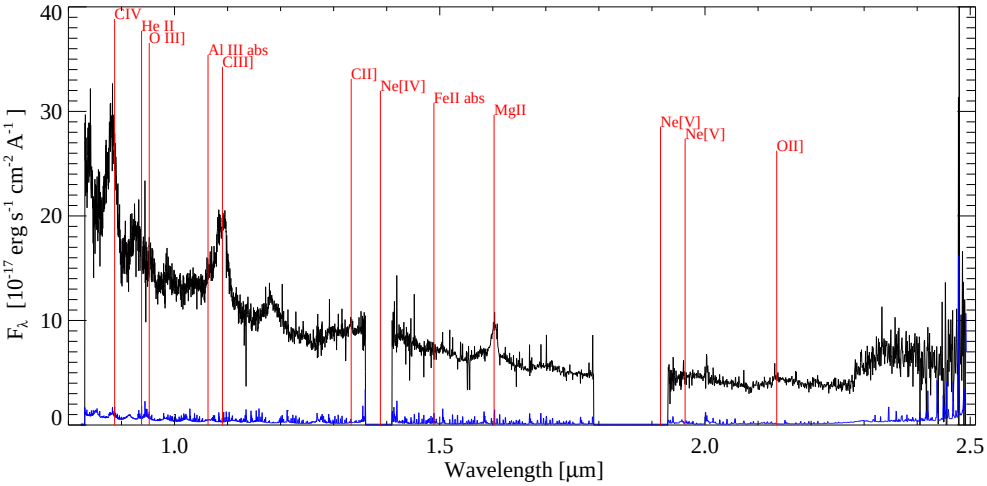

Figure 3.14 NIR spectrum of ID0085 from Magellan/FIRE, binned by its instrumental resolution. The blue line denotes the errors of the spectrum and the red vertical lines indicate general quasar emission lines.

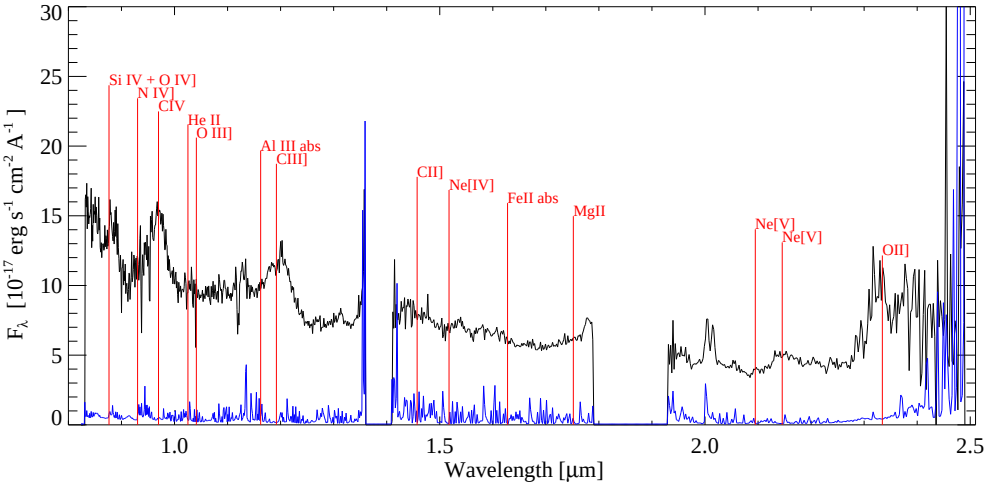

Figure 3.15 NIR spectrum of ID0099 from the Magellan/FIRE, binned by its instrumental resolution. The blue line denotes the errors of the spectrum and the red vertical lines indicate general quasar emission lines.

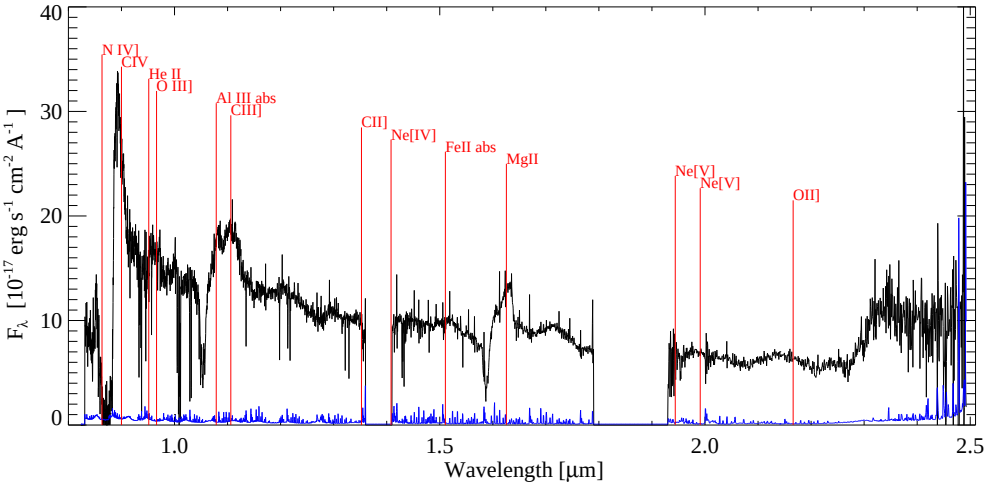

Figure 3.16 NIR spectrum of ID0106 from the Magellan/FIRE, binned by its instrumental resolution. The blue line denotes the errors of the spectrum and the red vertical lines indicate general quasar emission lines.

3.7.2 Physical Properties on Spectra

Table 3.8 lists the identification number (ID), name, coordinates, z magnitude, redshift, and M_{1450} of the quasars.

The redshifts of ID0308 and ID0654 were measured from the Lyα emission lines by fitting a Gaussian profile. However other spectra show sharp declinations bluewards of Lyα. In these cases, their redshifts were measured using the peak positions of each spectrum after smoothing spectra with the resolution of each instrument. The redshift errors contain the uncertainties from the spectral resolution of each instrument, because one of the most dominant uncertainty of the redshift measurement is caused by the low spectral resolution. Larger errors are caused by an ambiguous Lyα shape, which can be heavily affected by the Lyα forest and the blending with the N v emission line. Low resolution spectra suffer more from such problems. However we could not assign appropriate uncertainties resulting from the attenuated

Table 3.8. Information of the discovered quasars at z $\sim$ 5

ID	Name	R.A. & Dec.	z	$z_{Ly\alpha}$	M_{1450}
ID0085	IMSJ0324+0426	03:24:07.7+04:26:13.25	19.145±0.060	4.712±0.039	−27.21±0.29
ID0106	IMSJ0122+1216	01:22:47.3+12:16:23.94	19.274±0.063	4.857±0.039	−26.47±0.68
ID0719	IMSJ1437+0708	14:37:04.8+07:08:08.30	19.100±0.059	4.967±0.049	−27.14±0.09
ID0308	IMSJ2225+0330	22:25:14.4+03:30:12.58	19.474±0.097	5.350±0.049	−26.47±0.29
ID0654	IMSJ1022+0801	10:22:01.9+08:01:22.10	19.072±0.046	5.359±0.079	−27.38±0.10
ID0099	IMSJ0155+0415	01:55:33.3+04:15:06.78	19.261±0.065	5.386±0.039	−26.85±1.09

Lyα emission lines.

The values of M_{1450} are listed in Table 3.8. We calculated the values from the average flux at 1440$\AA$ – 1460$\AA$ on the optical spectra. The uncertainties were estimated from the rms continuum flux density. The observed wavelengths of the rest-frame 1450$\AA$ are located at 8700$\AA$ for z = 5.0 quasars, where the sky emission lines are significant. Due to the difficulty of subtracting the sky from the relatively low S/N spectra, these values are crude and the actual magnitude uncertainties are higher than the error estimates.

In the NIR spectra, the C IV and C III] emission lines of ID0085 ($z_{CIV} = 4.672 \pm 0.003$ and $z_{CIII]} = 4.715 \pm 0.002$) present blueshifts with respect to the Mg II emission line; $\Delta v_{CIV} = -2907 \pm 150$ km s^{-1} and $\Delta v_{CIII]} = -620 \pm 122$ km s^{-1}. The C III] emission line of ID0099 ($z_{CIII]} = 5.249 \pm 0.002$) is blueshifted with respect to the C IV emission line; $\Delta v_{CIII]} = -569 \pm 111$ km s^{-1}. This is similar to the spectra of other high redshift quasars (e.g., Richards et al. 2002; De Rosa et al. 2014). Mortlock et al. (2011) reports a similar blueshifted C IV emission line with respect to the Mg II ($\Delta v_{CIV} = -2800 \pm 500$ km s^{-1}) for the quasar at z=7.085.

3.7.3 Individual Properties of Quasars

These are individual properties of the spectra for each quasar.

ID0085 ($z_{Ly\alpha}$=4.71): It has a strong Lyα emission line. It also shows relatively strong Lyman β, O I , Si IV+O IV], and C IV emission lines and a weak N V emission line. In the NIR spectrum, C IV , C III] , and Mg II emission lines are prominent.

ID0106 ($z_{Ly\alpha}$=4.86): It is a BAL quasar showing deep drops on the continuum. It has a strong Lyα emission line. It also shows a weak Lyman β emission line. We cannot figure out other emission lines due to these deep absorptions. In the NIR spectrum, the C IV , C III] , and Mg II have strong emissions. The left side of these lines are severely affected by absorptions.

ID0719 ($z_{Ly\alpha}$=4.97): Its spectrum was obtained from NTT/EFOSC2 with R $\sim$ 130 with a long integration time ($\sim$1.5 hours), so, it has the highest S/N ratio among other optical spectra. However it does not show any prominent emission line except the Lyα due to the low resolution.

ID0308 ($z_{Ly\alpha}$=5.35): Its spectra were observed by two telescopes, KPNO 4-m telescope and NTT, and were combined in average. It has a smooth Lyα line and does not show any other line emission.

ID0654 ($z_{Ly\alpha}$=5.36): It has the weakest Lyα emission line among the spectra. Other emission lines cannot be determinded.

ID0099 ($z_{Ly\alpha}$=5.39): It also has a weak Lyα emission line and other emission lines cannot be determinded. In the NIR spectrum, it has prominent Si IV+O IV], C IV , and C III] emission lines. We could not find a feature of Mg II emission line where the rest frame wavelength is 2800Å. It might be caused from the low S/N near the spectral region that were contaminated by telluric absorption.

3.8 Quasar Selection Efficiency

To calculate the expected quasar number for each quasar selection method, we derived the quasar selection efficiency which can be affected by various reasons. The quasar selection efficiency is defined as the number of discovered quasars among the number of candidates. Meanwhile, completeness from color selection is defined as the number of quasar models inside specific color cuts among the number of quasar model with specific redshift and magnitude. First, we calculated the completeness from our color cuts. The fraction of selected quasars for a specific redshift is determined by the sizes and positions of color selection boxes and magnitude limits of surveys. Applying various quasar templates, we calculated the completeness using the fraction of quasars that fall within each selection box, as a function of redshift and M_{1450} (Chap. 3.8.1). Another effect on the quasar selection is the contamination from other sources. The selection efficiency of quasars with magnitudes close to survey depths is affected by the photometric uncertainties of sources and the separation between the selection boxes and the contaminants (Chap. 3.8.2). Finally, although the color cut boxes need to be small in order to avoid contamination, this also results in low selection efficiency. Especially, if multi-band data of quasars showing variability were not observed simultaneously, these quasars may lie outside of the selection boxes. Since some quasars have large variability (> 0.1 mag in extreme cases), this effect is considerable for small selection boxes (Chap. 3.8.3).

3.8.1 Color Selection Completeness

We tested the completeness of our color selection. Then we apply this completeness to our quasar surveys and predict the expected quasar number of each survey in Chap. 7.1.

To measure the fraction of quasars missed due to our color cuts, we follow approaches from previous studies (e.g., Willott et al. 2005; Venemans et al. 2013). The

composite quasar template from Vanden Berk et al. (2001) is redshifted to various redshift ranges, assuming that the spectral properties of quasars do not evolve significantly with redshift (e.g., Kuhn et al. 2001; Fan et al. 2004; Jun et al. 2015), except wavelengths blueward of the Lyα line. Flux in these wavelengths are absorbed by neutral hydrogen (H I) in the IGM, and the absorption becomes strong toward higher redshift because the fraction of H I increases with redshift (Gunn-Peterson effect; Gunn & Peterson 1965). We applied this attenuation effect to our redshifted spectra using Madau et al. (1996). We redshifted the spectrum to $4 \leq$ z ≤ 8 with steps of Δz = 0.05 and changed M_{1450} to $-30 < M_{1450} < -20$ with steps of $\Delta M_{1450} = 0.5$. Then we calculated model magnitudes for each band using their transmission curves.

The most important effect on colors is the continuum slope of quasars. We modeled each redshifted spectrum into 13 cases, which have continuum slopes of $-1.3 \leq \alpha_\nu \leq -0.1$ (where $F_\nu \propto \nu^{\alpha_\nu}$) with steps of $\Delta\alpha_\nu = 0.1$. This range was derived using α_ν values from the SDSS DR12 quasar catalog (Paris et al. 2015, in preparation), among about 230,000 quasars which have measured α_ν: the mean value of α_ν is -0.7 with a 1σ dispersion of 0.6 (68.3% confidence level). De Rosa et al. (2014) analyzed a sample of 4 quasars at z > 6.5 and 3 of these 4 quasars (75%) satisfy this α_ν range. Note that our estimated completeness can be overestimated because the α_ν values depend on their bolometric luminosities (Xie et al. 2015).

Figure 3.17 (a) shows the completeness distribution as a function of redshift and M_{1450}, for the selection using $r - i - z - J - K$ ($r - i$ vs. $i - z$ and $z - J$ vs. $J - K$ color-color diagrams) and $r - Is$ vs. $Is - Iz$ color-color diagrams, and (c) shows the completeness distribution when using $r - i - z - J - K$ and $Is - Iz$ vs. $Iz - J$ color-color diagrams. In Figure 3.17 (b) and (d), we plotted the completeness as a function of redshift for the two methods, for case of $M_{1450} = -29$. The completeness in Figure 3.17 (b) rises steeply from 0% to 100% between z = 4.60

and z = 4.70, remains a contant 100% up to z = 5.15, and drops below 80% for z > 5.35. In the case of Figure 3.17 (d), the slopes of the completeness distribution at the borderline redshift values are more gradual than those in (b). The redshift ranges of the completeness greater than 80% are $4.60 < z < 5.40$ for (b) and $5.55 < z < 6.05$ for (d), which represents the expected redshift ranges of selected quasars from the two color-color diagrams using the Is and Iz-bands. The completeness of the two selection methods drop to below 50% at $M_{1450} > -27.0$ at fixed z = 4.90 and z = 5.80 for (a) and (c), respectively, where the M_{1450} limit was estimated from our magnitude cut, $z < 19.5$ mag. We also plotted the redshifts and M_{1450} of our six new discovered quasars, IMSJ0324+0426, IMSJ0122+1216, IMSJ1437+0708, IMSJ2225+0330, IMSJ1022+0801, and IMSJ0155+0415 (Table 3.8), with red boxes in (a). Since the continuum flux at $\lambda_{\rm rest} = 1450\mathring{A}$ of our spectra locate where the sky emission lines are significant, the errors in the M_{1450} estimates are high. We calculated the completeness when we used only $r - i - z - J - K$ photometry, and found that the adoption of Is and Iz photometry has no effect on the completeness.

3.8.2 Contamination by Interlopers

One factor causing the efficiency to decrease is contamination by other sources. In the case of the quasar selection at z $\sim$ 5, we adopted $r - i$ and $z - J$ color cuts to remove contaminants such as late type stars or dwarf stars. Although the dwarf stars can be rejected relatively efficiently using these color cuts (color differences between the dwarf stars and the selection box are $\geq$ 1 mag), the late type stars still prevail, even with an additional $J - K$ cut. This is because the color differences between the late type stars and the selection box are too small (barely few tenths of magnitude). Selection with the Is and Iz filters also shows small color differences between the stellar locus and the selection box, indicating that the Is and Iz-bands are also incapable of removing the stellar sources perfectly. Furthermore, sources

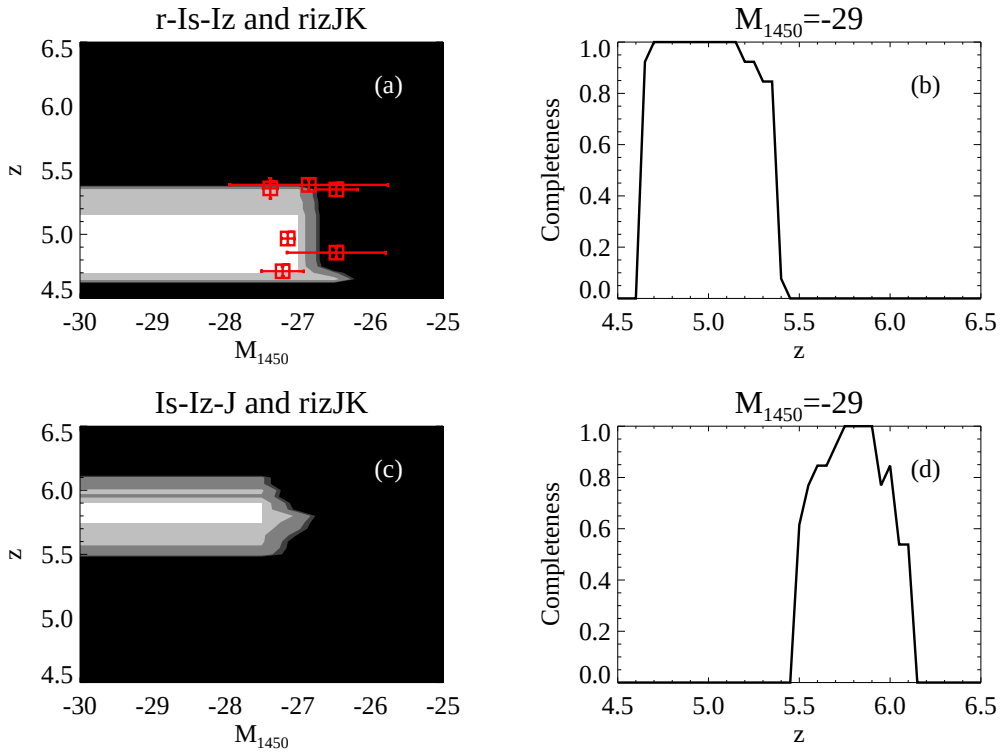

Figure 3.17 (a): Completeness as a function of redshift and M_{1450} for $r-i-z-J-K$ and $r-Is$ vs. $Is-Iz$ selection. The red boxes indicate the redshift and M_{1450} of our six new quasars. (b): Completeness as a function of redshift from (a) when $M_{1450}=-29$. (c): Completeness for $r-i-z-J-K$ and $Is-Iz$ vs. $Iz-J$ selection. (d): Completeness from (c) when $M_{1450}=-29$. The colors of the contours indicate 0% and 100% completeness for black and white, respectively.

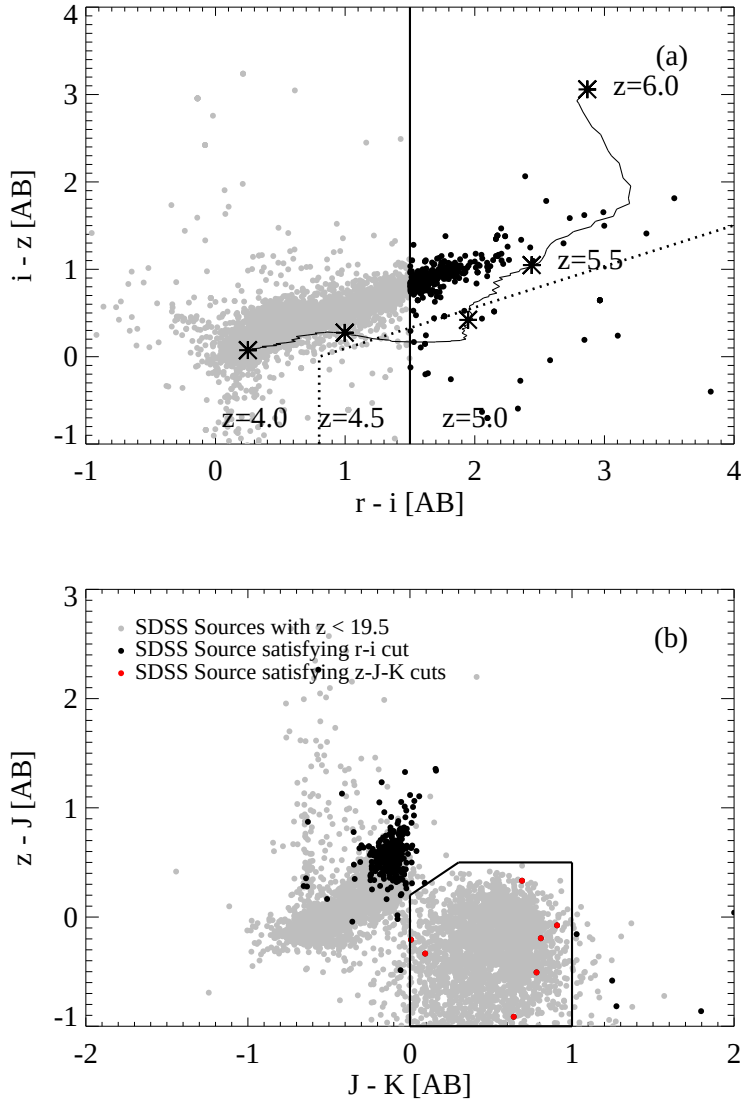

Figure 3.18 Similar to Figure 3.5. We plotted sources from the SDSS and UKIDSS LAS catalog, with a condition of $z < 19.5$, with gray circles. Only 10^4 sources are plotted for convenience. Sources satisfying the $r-i$ cut are plotted with black circles and sources satisfying both $r-i$ cut and $z-J-K$ selection box are plotted with red circles.

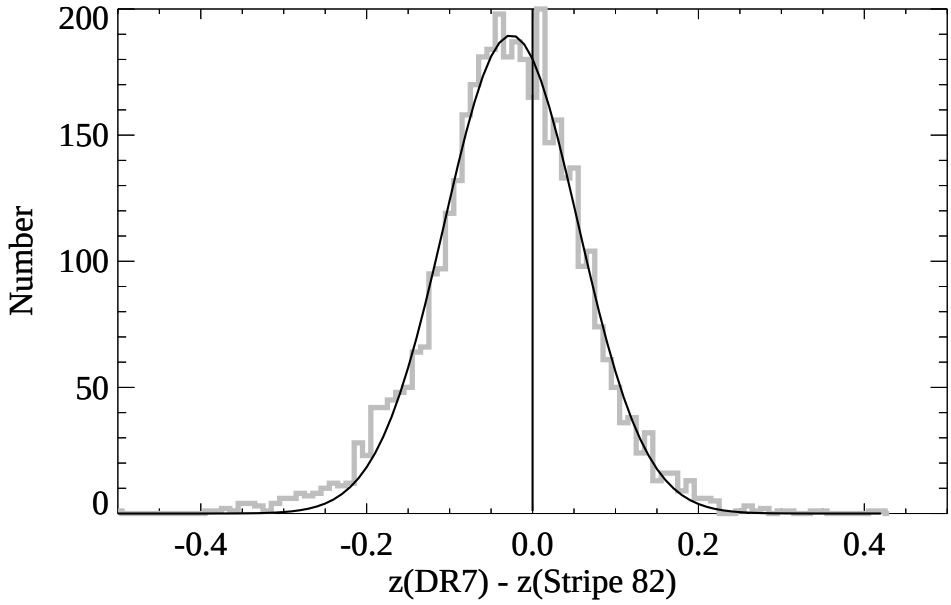

Figure 3.19 z-band magnitude differences between SDSS DR7 and Stripe 82 catalogs (gray histogram) and its Gaussian fitting (black solid line).

with magnitudes near the survey depth contaminate the quasar selection boxes with more easy due to their large uncertainties in the magnitudes.

Figure 3.18 shows a similar plot to Figure 3.5. We plotted sources (gray circles) merged from the SDSS and UKIDSS LAS catalog, with a condition of $z < 19.5$, which is our magnitude cut for the quasar selection of z $\sim$ 5. Only 10^4 sources are plotted for convenience. From these sources, we estimated the contamination rate. Sources satisfy the $r - i$ cut is 449 (black circles) and 7 sources (red circles; 1.6%) are located in the $z - J - K$ selection box. If we query the merged catalog of SDSS and UKIDSS LAS DR10, with a condition of $z < 19.5$ and $r - i$ color cut, $\sim 10^6$ sources are contained in the query result, and 98.4% sources are rejected from the $z - J - K$ cuts. However, $\sim 10^4$ sources still belong to the candidate list. Considering that the expected number of quasars for the survey area of 3,400 deg^2 is $\sim$30, more than 99.5% of these $\sim 10^4$ sources will be interlopers.

These interlopers can be increase due to the inaccuracy of the z-band photometry. Since the z-band of SDSS shows low QE, the z-band photometry have uncertainties larger than those expected from Poission noise by sky background fluctuations. To check these photometric uncertainties, we compared two catalogs, SDSS DR7 and Stripe 82 catalogs. Objects in the Stripe 82 catalog are detected and cataloged about 2 magnitudes deeper than those in the DR7 catalog. Figure 3.19 shows the magnitude differences of these two catalogs (gray histogram). We used $\sim$4,000 sources with $19.0 < z < 19.5$. We fitted this distribution using the Gaussian function (black solid line). These magnitude difference shows a systematic offset (z-band photometry from the DR7 catalog is 0.03 magnitude brighter than those from the Stripe 82 catalog) and 32% of these sources have magnitude differences greater than 0.08 mag. These magnitude differences between a catalog and a catalog deeper than the former indicate the critical photometric uncertainties, and sources with inaccurate photometry can be mis-classified as quasar candidates.

Also this contamination increases if we consider the variability of the late type stars. Hartman et al. (2011) reported that some of variable K and M dwarf stars they discovered have large variability (> 0.13 mag in extreme cases). This variability of the late type stars increases the probability that the contaminants are incorrectly selected as high redshift quasars.

3.8.3 Low Selection Efficiency due to Quasar Variability

Similar to the variability of the late type stars, the variability of quasars also affects the selection efficiency. Quasars, whose variability can be observed 0.1 mag in extreme cases (MacLeod et al. 2012), can be located outside selection boxes in color-color diagrams, or near the boundary of selection boxes. In the former case, the quasar will be rejected from the candidate list, and in the latter case, low priority will be assigned to the target, and spectroscopy will not be conducted.

3.9 Summary

We conducted the quasar selection at z $\sim$ 5 using data from wide area surveys, SDSS and UKIDSS LAS, with a new selection technique that we developed. Candidates were selected from our $r-i-z-J-K$ color cuts. The candidates were observed with CQUEAN Is and Iz filters for optical imaging follow-up observations. Then we carried out optical spectroscopic observations to identify quasars and discovered six new quasars. Three of them were observed by NIR spectroscopy to measure their physical properties. Our survey shows a low selection efficiency, because the $r-i-z-J-K$ color cuts we adopted are not sufficient to remove interlopers even with the additional Is and Iz photometry. Therefore, to discover quasars at z $\sim$ 5, we need another selection technique, and a new selection strategy is suggested in Chap. 8.

Chapter 4

Quasar Selection at z $\sim$ 6

4.1 Introduction

In recent years, more than 50 quasars at z $\sim$ 6 have been discovered. These quasars are a key probe to investigate the physical conditions of the intergalactic medium (IGM). Quasars at z $\sim$ 6 show highly absorbed spectra at wavelength shorter than Lyman α (e.g., Fan et al. 2006b). This Gunn-Peterson (GP; Gunn & Peterson 1965) absorption trough indicates that the optical depth increases toward the high redshift, causing a debate of whether the rapid evolution is a continuous process or an abrupt transition (e.g., Fan et al. 2006b; Becker et al. 2007).

After the Sloan Digital Sky Survey (SDSS) started the quasar survey at z $\sim$ 6 (Fan et al. 1999), the Canada-France High-z Quasar Survey (CFHQS) and the UKIRT Infrared Deep Sky Survey (UKIDSS) have followed their studies. They adopted the dropout selection method in the i-band, so called i-dropouts. After selecting i-dropouts, follow-up J-band photometry is conducted on these candidates, and the blue $z-J$ colors are used to exclude dwarf stars (e.g., Fan et al. 2001, 2003, 2004, 2006a; Jiang et al. 2008, 2009; Willott et al. 2007, 2009, 2010a,b). After near-infrared (NIR) photometry become available from large area surveys, quasar

selection can be conducted without the follow-up observations (Venemans et al. 2007; Mortlock et al. 2009; Morganson et al. 2012; Bañados et al. 2014; Jiang et al. 2015).

The largest survey for z ∼ 6 quasars is SDSS with a survey area of more than 8,000 deg^2 with a limiting magnitude of $z \sim 20$ mag, and the Stripe 82 area over 300 deg^2. They have discovered ∼30 quasars (e.g., Fan et al. 2001, 2003, 2004, 2006a; Jiang et al. 2008, 2009). CFHQS has provided relatively faint quasars (e.g., Willott et al. 2007, 2009, 2010a,b), also the quasar luminosity function down to the faint end. UKIDSS has found several quasars (e.g., Venemans et al. 2007; Mortlock et al. 2009). The Panoramic Survey Telescope & Rapid Response System 1 (Pan-STARRS1, PS1; Kaiser et al. 2002, 2010) survey, covering more than 20,000 deg^2, provided about 10 quasars (Morganson et al. 2012; Bañados et al. 2014).

The quasar luminosity function at z ∼ 6 was constructed from these quasars. Willott et al. (2010a) derived the luminosity function of quasars at z ∼ 6 using a sample of 40 quasars at z ∼ 6 from various surveys. They show the evolution of the luminosity function, decreasing the number density toward higher redshift, compared to those of quasars at $3 < z < 6$ (Fan et al. 2001). McGreer et al. (2013) and Venemans et al. (2013) suggested a similar trend of the number density evolution using z ∼ 5 quasars and $z > 6.5$ quasars, respectively. This luminosity function at z ∼ 6 is used to study the source of the IGM ionization at this redshift. At z ∼ 10, the first stars mainly caused the re-ionization (Kashlinsky et al. 2005), and at z ∼ 6, quasars and star forming galaxies supplied photons to ionize the IGM (e.g., Willott et al. 2005; Jiang et al. 2008). Willott et al. (2010b) calculated the $z = 6$ quasar intergalactic ionizing flux using their luminosity function and found that it is 20 – 100 times lower than what is necessary for reionization.

As a pilot study for high redshift quasar survey, we designed a bright quasar survey at z ∼ 6, using data with a relatively shallow depths but large area coverage. Due to the restriction on resources for follow-up observations, we developed a new

selection criterion with multi-wavelength data to reduce contaminants. We explain this in Chap. 4.2. Then Chap. 4.3 and 4.4 show the follow-up observations in optical and NIR wavelengths, and we present their results in Chap. 4.5. In Chap. 4.6, we discussed our quasar selection efficiency. We summarize this survey in the final chapter (Chap. 4.7). Throughout this paper, we use a cosmology with $\Omega_M = 0.3, \Omega_\Lambda = 0.7$, and $H_0 = 70$ km s^{-1}Mpc^{-1}. We use the AB system for SDSS *ugriz* filters and the Vega system for UKIDSS $ZYJHK$ filters.

4.2 Selection Method

In this section, we present details of our candidate selection method. The selection procedure is similar to those of previous studies (e.g., Fan et al. 2001, 2003; Jiang et al. 2008, 2009). Since the filter response profiles and CCD sensitivities for the previous quasars surveys are not identical to those of our quasar survey, we calculated the expected colors of quasars from different filter sets we used. Also we adopted another selection criterion to increase the selection efficiency. This new method we developted reduced contamination efficiently from our candidate list.

4.2.1 Definition of Color-color Diagrams

There is a traditional method to select quasars at z $\sim$ 6 using the Lyα drop from the i, z, and J photometry. In our case, we tried another color cut to reduce the contamination, using the differences of continuum properties between quasars and stars. We attempted many combinations of $YJHK$ filters to find the best color boxes to separate quasars from other sources. Figure 4.1 shows two color-color diagrams with quasar redshift tracks from Vanden Berk et al. (2001) (solid lines with asterisks), model dwarf stars from Burrows et al. (2006) (triangles), stars from Hewett et al. (2006) from BPGS atlas (green squares), point-like sources from the

SDSS Star Catalog (gray points; ∼6,000 randomly selected sources with $15 < z < 20$), redshift tracks of a star forming galaxy (blue line; model colors from M51), and redshift tracks of a passive galaxy (red line; model colors from the Bruzual & Charlot (2003) and a passively evolving 5 Gyr-old galaxy with spontaneous burst, metallicity of Z=0.02, and a Salpeter IMF). To verify the position of quasars at z ∼ 6, we also plotted colors of previously discovered quasars with UKIDSS LAS photometry (red boxes with error bars).

Comparing distances between the quasar redshift track and other interlopers in the color-color diagrams, we decided to use two color-color diagrams, $i-z$ vs. $z-J$ and $Y-J$ vs. $J-K$, and indicated the selection boxes for quasar selection in Figure 4.1. The color cuts we defined are as below:

`Cut1`: $i-z > 2.2 \cap z-J < 2.5 \cap (z-J) < (i-z)+0.5$

`Cut2_small`: $0.2 < Y-J < 0.6 \cap 1.2 < J-K < 1.5$

`Cut2_large`: $0.0 < Y-J < 0.6 \cap 1.0 < J-K < 2.0$

We determined the criteria of `Cut2_small` from the quasar redshift track on Figure 4.1 (b). We used another larger cut, `Cut2_large`, that contains most of the discovered quasars, with the exception of a BAL quasar, which may have irregular colors.

4.2.2 Multi-wavelength Data

We used UKIDSS LAS DR8 and SDSS DR7, covering an area of ∼2,700 deg^2 for the quasar selection. The merged catalog of these two surveys was downloaded from the WSA[1]. The conditions for the matching query include sources of $u > 22.3$, $g > 23.0$ and $r > 23.1$, with `sdssPrimary`=1 and UKIDSS LAS detection within a $2''$ distance. We initially adopted the 5σ detection limits for the u, g, and r-band magnitudes. Also we adopted color cuts of $i-z > 2.2$, and

[1] http://surveys.roe.ac.uk/wsa/

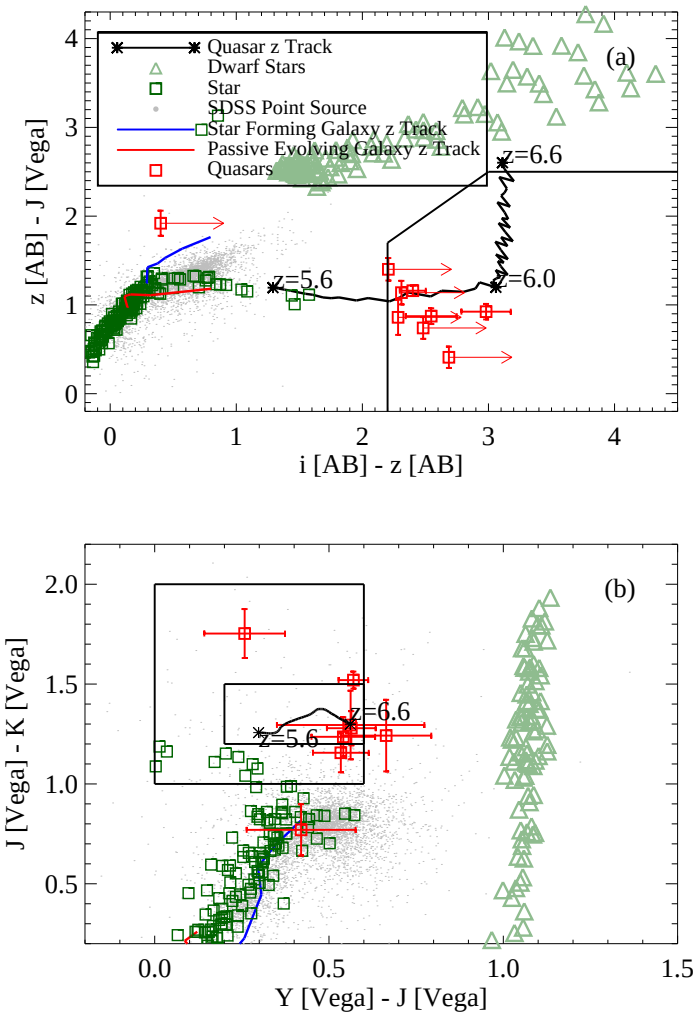

Figure 4.1 Two color-color diagrams we adopted for quasar selection at z $\sim$ 6. Model dwarf stars (triangles), stars from Hewett et al. (2006) (squares), point-like sources from the SDSS Star Catalog (gray points), previously discovered quasars (red boxes with error bars), redshift tracks of a quasar at 5.6 $<$ z $<$ 6.6 (black solid line with asterisks), redshift tracks of a star forming galaxy (blue line), and redshift tracks of a passive galaxy (red line) are plotted. The solid lines indicate the selection boxes for our quasar selection.

Table 4.1. PHOTO Flags used by candidate selection

Flag Name	Hex Bit	Description
BRIGHT	0×2	Object was detected in first, "bright" object-finding step; generally brighter than $r^* = 17.5$
EDGE	0×4	Object was too close to edge of frame
BLENDED	0×8	Object had multiple peaks detected within it; was thus a candidate to be a deblending parent
CHILD	0×10	Object is the product of an attempt to deblend a BLENDED object.
SATUR	0×40000	The object contains one or more saturated pixels

$z - J < 2.5$, similar to Cut1. We selected catalog information as below: R.A. and Dec. for each source, UKIDSS 2″ aperture magnitudes with aperture correction (yAperMag3, j_1AperMag3, hAperMag3, kAperMag3) and their errors, SDSS PSF magnitudes (psfMag_u, psfMag_g, psfMag_r, psfMag_i, psfMag_z) and their errors, information about the stellarity (mergedClass, pStar, pGalaxy, pNoise, pSaturated, type_z), and PHOTO flags information (flags, flags_z). The total number of sources from the query was 10,705. After the release of UKIDSS LAS DR9, we expanded the survey area to ∼3,400 deg^2, and combined this with the SDSS DR7.

4.2.3 Flag Checking

To reduce spurious sources resulting from incorrect photometric information of SDSS z-band, we used a set of flags for each object from PHOTO Flags (Stoughton et al. 2002). We rejected candidates with the flags in Table 4.1, similar to the criteria of Richards et al. (2002).

4.2.4 Color Selection with SDSS and UKIDSS LAS

We selected quasar candidates from UKIDSS LAS DR8, using the color cuts explained in Chap. 4.2.1 with the 5σ detection limits for u, g, and r-bands and a magnitude limit of J < 19.2 (In the case of UKIDSS LAS DR9, we extended the magnitude cut to J < 19.6). Beyond this magnitude cut, the number of contaminants in the i-dropout selection increases dramatically. The second color cut, $Y - J - K$, eliminated 94% of interlopers selected from the first color cut, $i - z - J$, indicating that the second cut we developted is essential to reduce contamination. We checked the overlap of previously discovered quasars with our candidates and found 3 quasars at z > 5. For the UKIDSS LAS DR9 catalog, the number increases to 8. There is no detection of all of our candidates with FIRST, within $5''$ radii, in both UKIDSS LAS DR8 and 9. Although distant quasars are expected to appear as a point source, faint point-like objects can be classified as extended objects due to their low S/N. Thus we did not reject extended objects in the candidate list.

We found 82 candidates using these color and magnitude cuts from the UKIDSS LAS DR8 catalog, and 394 candidates from UKIDSS LAS DR9. We rejected unreliable sources using the following criteria:

i) Object with a detection on the r-band image.

ii) Blended object in the z-band or NIR bands.

iii) Object on the expected cross-talk positions in the NIR bands.

After the rejections, we finally listed 42 targets with J < 19.2 from the UKIDSS LAS DR8 and 43 targets with J < 19.6 from the UKIDSS LAS DR9. These candidates are listed in Table 4.2 and 4.3. Since the expected number of quasars at z ~ 6 in 3,400 deg^2 is $\sim$15 and at most 50 (Chap. 7.1), we can see that these candidates are still contaminated from interlopers, mostly due to their low S/N ratio at z-band (See Chap. 3.8.2). Therefore we need follow-up imaging observations to improve photometry and remove contamination (Chap. 4.3).

Table 4.2. Candidate list selected from UKIDSS LAS DR8

ID	R.A & Dec.	$z_{\rm SDSS}$	$J_{\rm UKIDSS}$	CQUEAN i	CQUEAN z	UKIRT Z	UKIRT J
LASDR8_ID029	00 : 20 : 58.32 + 00 : 41 : 11.28	20.17±0.19	19.80±0.14	···	21.14± 0.07	99.53±99.00	18.84± 0.05
LASDR8_ID020	00 : 44 : 54.98 + 13 : 52 : 12.80	20.15±0.20	19.72±0.11	···	21.17± 0.08	99.53±99.00	···
LASDR8_ID038	01 : 02 : 44.83 + 00 : 00 : 58.37	20.08±0.19	19.91±0.11	···	21.29± 0.09	99.53±99.00	···
LASDR8_ID055	01 : 38 : 20.72 + 15 : 02 : 09.21	20.41±0.17	20.01±0.15	21.41± 0.05	···	20.69± 0.16	···
LASDR8_ID015[a]	01 : 59 : 07.32 − 00 : 25 : 06.33	20.06±0.10	19.63±0.10	23.06± 0.25	···	19.61± 0.08	···
LASDR8_ID069	03 : 28 : 28.47 − 01 : 02 : 46.28	20.25±0.16	20.09±0.09	···	20.98± 0.08	99.53±99.00	···
LASDR8_ID081	07 : 52 : 26.22 + 25 : 56 : 31.92	20.46±0.19	20.13±0.09	29.15± 0.27	20.78± 0.05	99.53±99.00	···
LASDR8_ID073	07 : 58 : 11.06 + 23 : 23 : 46.85	20.46±0.16	20.10±0.08	22.15± 0.08	21.28± 0.11	99.53±99.00	···
LASDR8_ID022	08 : 40 : 29.73 − 01 : 13 : 33.69	20.03±0.21	19.76±0.11	21.89± 0.05	20.96± 0.05	99.53±99.00	18.75± 0.08
LASDR8_ID032	08 : 47 : 11.03 + 06 : 06 : 18.76	19.71±0.18	19.85±0.07	···	21.97± 0.12	99.53±99.00	···
LASDR8_ID026	09 : 02 : 54.45 + 01 : 18 : 19.37	19.55±0.18	19.80±0.12	···	···	20.68± 0.14	···
LASDR8_ID048	09 : 20 : 53.48 + 31 : 11 : 27.00	20.11±0.16	19.99±0.08	29.73± 0.15	···	20.56± 0.05	···
LASDR8_ID082	09 : 32 : 28.65 + 31 : 10 : 30.84	20.44±0.19	20.13±0.08	···	···	21.01± 0.06	···
LASDR8_ID023	09 : 58 : 13.71 + 10 : 51 : 19.92	20.15±0.16	19.76±0.11	···	21.15± 0.09	99.53±99.00	18.72± 0.04
LASDR8_ID068	10 : 01 : 41.56 + 07 : 47 : 29.19	20.01±0.16	20.09±0.12	21.52± 0.07	20.76± 0.04	99.53±99.00	···
LASDR8_ID046	10 : 05 : 11.09 + 10 : 01 : 59.83	20.00±0.20	19.97±0.11	···	21.71± 0.15	99.53±99.00	···
LASDR8_ID072	10 : 18 : 41.15 + 06 : 31 : 52.26	20.36±0.19	20.10±0.20	···	···	21.42± 0.07	···
LASDR8_ID034	10 : 24 : 55.42 + 01 : 17 : 19.93	19.70±0.15	19.87±0.09	···	21.11± 0.07	99.53±99.00	···
LASDR8_ID031	11 : 18 : 05.58 + 01 : 32 : 27.77	20.24±0.14	19.85±0.14	···	21.12± 0.08	99.53±99.00	···
LASDR8_ID080	11 : 21 : 29.99 + 10 : 57 : 28.26	20.16±0.18	20.12±0.15	···	···	20.90± 0.05	···
LASDR8_ID066	11 : 28 : 46.19 + 09 : 19 : 42.22	19.73±0.17	20.09±0.15	···	···	20.91± 0.04	···
LASDR8_ID052	11 : 49 : 00.42 + 11 : 04 : 39.46	20.43±0.21	20.00±0.08	···	···	21.23± 0.05	···
LASDR8_ID030	11 : 53 : 09.53 + 01 : 57 : 00.15	20.33±0.17	19.83±0.14	···	···	21.33± 0.06	···
LASDR8_ID058	12 : 09 : 14.67 − 01 : 48 : 52.88	20.19±0.27	20.02±0.14	···	···	20.93± 0.07	···
LASDR8_ID057	12 : 12 : 16.30 + 11 : 53 : 04.45	20.49±0.15	20.02±0.14	···	···	21.21± 0.08	···
LASDR8_ID077	12 : 14 : 15.12 + 03 : 51 : 25.07	20.38±0.19	20.12±0.15	···	···	20.98± 0.04	···
LASDR8_ID025	12 : 22 : 08.71 + 13 : 00 : 09.69	20.27±0.13	19.77±0.11	···	···	20.79± 0.03	···
LASDR8_ID044	12 : 31 : 28.38 + 13 : 24 : 57.23	20.30±0.16	19.96±0.14	···	···	20.88± 0.12	···
LASDR8_ID062	12 : 33 : 31.90 + 12 : 31 : 04.21	20.42±0.19	20.04±0.12	···	···	21.18± 0.05	···
LASDR8_ID060	13 : 17 : 44.03 − 01 : 30 : 58.39	20.58±0.21	20.04±0.14	···	21.33± 0.10	99.53±99.00	···
LASDR8_ID078	13 : 28 : 59.19 + 09 : 53 : 31.21	17.13±0.15	20.12±0.11	···	21.42± 0.08	99.53±99.00	19.20± 0.04

Table 4.2 (cont'd)

ID	R.A & Dec.	$z_{\rm SDSS}$	$J_{\rm UKIDSS}$	CQUEAN i	CQUEAN z	UKIRT Z	UKIRT J
LASDR8_ID075	14 : 03 : 19.13 + 09 : 02 : 51.07	20.21±0.15	20.11±0.10	21.49± 0.10	20.30± 0.06	99.53±99.00	19.21± 0.04
LASDR8_ID028	14 : 05 : 17.59 − 00 : 17 : 52.86	20.22±0.14	19.80±0.10	···	20.81± 0.12	99.53±99.00	18.90± 0.06
LASDR8_ID027	14 : 07 : 21.61 + 01 : 29 : 53.13	19.15±0.06	19.80±0.16	···	20.75± 0.06	99.53±99.00	18.79± 0.03
LASDR8_ID067	14 : 22 : 53.11 − 01 : 28 : 02.39	20.10±0.21	20.09±0.11	···	20.78± 0.10	99.53±99.00	18.97± 0.03
LASDR8_ID035	14 : 31 : 58.32 − 00 : 34 : 03.14	20.19±0.14	19.88±0.13	···	20.51± 0.08	99.53±99.00	18.83± 0.03
LASDR8_ID079	14 : 39 : 26.37 + 05 : 33 : 06.65	20.34±0.16	20.12±0.16	···	21.15± 0.11	99.53±99.00	···
LASDR8_ID054	15 : 19 : 44.36 + 04 : 38 : 12.24	20.22±0.14	20.00±0.15	···	21.09± 0.11	99.53±99.00	18.84± 0.04
LASDR8_ID053	16 : 25 : 35.82 + 30 : 36 : 54.08	20.46±0.20	20.00±0.11	···	21.30± 0.09	99.53±99.00	18.93± 0.03
LASDR8_ID033	22 : 46 : 22.11 − 00 : 20 : 30.77	20.36±0.16	19.86±0.12	···	···	21.07± 0.04	18.68± 0.02
LASDR8_ID051	22 : 49 : 08.91 + 00 : 54 : 24.01	20.45±0.15	19.99±0.12	···	···	21.30± 0.06	18.89± 0.03
LASDR8_ID007	23 : 42 : 56.22 + 14 : 05 : 36.47	19.60±0.10	19.13±0.08	···	···	···	18.11± 0.02

[a] This object was identified as a high redshift quasar at z = 6.0.

Table 4.3. Candidate list selected from UKIDSS LAS DR9

ID	R.A & Dec.	$z_{\rm SDSS}$	$J_{\rm UKIDSS}$	CQUEAN i	CQUEAN z	UKIRT Z	UKIRT J	WISE cut
LASDR9_ID020	01 : 26 : 22.99 + 15 : 39 : 16.42	19.03±0.07	18.13±0.03	20.23± 0.11	···	19.80± 0.02	17.25± 0.04	···
LASDR9_ID036	01 : 02 : 02.01 + 07 : 37 : 27.72	19.34±0.11	18.49±0.03	···	···	20.38± 0.04	17.65± 0.04	···
LASDR9_ID037	22 : 26 : 02.17 + 05 : 35 : 04.59	19.27±0.07	18.51±0.04	21.62± 0.25	···	20.12± 0.02	17.68± 0.09	···
LASDR9_ID063	10 : 46 : 25.79 + 04 : 24 : 40.28	19.69±0.07	18.80±0.03	···	20.26± 0.04	···	···	···
LASDR9_ID068	08 : 38 : 47.12 + 09 : 27 : 59.99	19.61±0.06	18.85±0.04	22.18± 0.18	···	20.65± 0.03	17.85± 0.07	···
LASDR9_ID081	08 : 05 : 45.87 + 22 : 32 : 32.28	19.74±0.12	18.98±0.03	22.32± 0.33	···	21.01± 0.05	17.83± 0.08	···
LASDR9_ID085	10 : 28 : 59.89 + 11 : 51 : 21.54	19.89±0.12	19.00±0.04	22.42± 0.19	···	20.53± 0.03	18.03± 0.04	×
LASDR9_ID098	03 : 32 : 56.11 + 05 : 05 : 28.35	19.91±0.17	19.06±0.06	···	20.25± 0.08	21.07± 0.04	18.09± 0.05	···
LASDR9_ID099	11 : 26 : 19.86 + 11 : 34 : 13.63	19.90±0.11	19.07±0.05	···	···	21.04± 0.03	18.16± 0.08	···
LASDR9_ID106	12 : 32 : 36.86 + 10 : 14 : 57.95	19.85±0.16	19.10±0.04	···	···	21.02± 0.07	18.14± 0.06	···
LASDR9_ID108	11 : 43 : 25.63 + 11 : 23 : 08.82	19.91±0.10	19.11±0.06	···	···	···	···	×
LASDR9_ID109	14 : 10 : 24.01 + 04 : 06 : 53.36	19.97±0.14	19.12±0.03	···	···	20.70± 0.05	18.24± 0.07	···
LASDR9_ID114	01 : 58 : 16.23 + 07 : 17 : 37.46	19.83±0.10	19.14±0.06	···	···	···	···	×
LASDR9_ID115	10 : 47 : 32.50 + 01 : 44 : 00.14	19.89±0.12	19.15±0.04	···	···	21.01± 0.06	18.46± 0.06	···
LASDR9_ID116	12 : 27 : 05.14 + 02 : 18 : 04.91	19.88±0.12	19.16±0.05	22.15± 0.09	20.74± 0.03	···	···	···
LASDR9_ID117	08 : 57 : 55.62 + 02 : 04 : 41.53	20.00±0.13	19.16±0.06	···	···	···	···	×
LASDR9_ID119	02 : 32 : 24.53 + 05 : 39 : 01.66	19.88±0.12	19.18±0.06	···	20.78± 0.08	···	···	×
LASDR9_ID121	02 : 07 : 22.62 + 12 : 27 : 09.90	19.80±0.15	19.19±0.07	···	···	21.21± 0.06	18.01± 0.08	···
LASDR9_ID123	12 : 19 : 53.59 + 11 : 03 : 57.91	20.00±0.17	19.21±0.06	···	···	21.29± 0.08	18.02± 0.11	···
LASDR9_ID130	08 : 00 : 25.13 + 22 : 04 : 58.52	19.98±0.13	19.25±0.04	···	···	···	···	×
LASDR9_ID134	10 : 58 : 04.64 + 10 : 57 : 11.51	19.96±0.17	19.26±0.05	···	···	21.24± 0.05	18.28± 0.05	···
LASDR9_ID137	11 : 50 : 25.06 + 05 : 07 : 35.97	19.92±0.15	19.28±0.05	···	···	21.02± 0.05	18.28± 0.09	×
LASDR9_ID139	12 : 32 : 27.68 + 10 : 21 : 47.66	20.07±0.19	19.29±0.05	···	20.67± 0.05	···	···	···
LASDR9_ID146	10 : 37 : 55.46 − 01 : 38 : 59.74	19.96±0.14	19.32±0.04	···	···	···	···	×
LASDR9_ID147	10 : 46 : 54.64 + 02 : 25 : 32.39	19.99±0.15	19.33±0.05	···	···	21.17± 0.04	18.44± 0.05	···
LASDR9_ID150	09 : 55 : 33.32 − 02 : 08 : 41.26	20.04±0.15	19.34±0.07	22.33± 0.16	21.06± 0.05	···	···	···
LASDR9_ID165	23 : 35 : 08.51 + 06 : 52 : 20.94	19.87±0.10	19.39±0.06	23.06± 0.25	20.62± 0.03	···	···	×
LASDR9_ID170	09 : 28 : 17.19 + 10 : 36 : 05.06	20.09±0.10	19.42±0.04	···	···	21.05± 0.06	18.38± 0.08	···
LASDR9_ID171	23 : 31 : 10.30 + 10 : 23 : 48.32	20.04±0.13	19.43±0.08	···	···	21.36± 0.05	18.47± 0.06	×
LASDR9_ID179	12 : 13 : 47.22 + 10 : 21 : 33.77	19.94±0.20	19.48±0.07	···	···	21.39± 0.07	18.63± 0.08	···
LASDR9_ID183	00 : 29 : 02.15 + 13 : 59 : 39.69	20.04±0.16	19.50±0.07	22.41± 0.48	···	21.01± 0.06	18.44± 0.11	···

4.2.5 Previously Discovered Quasars in Literature

We found 8 quasars that were previously discovered from our candidate list. These quasars are summarized in Table 4.4. One of these quasars, LASDR8_143 (IMSJ0148+0600) was also discovered by us, using $r-i$ color from SDSS Sloan Extension for Galactic Understanding and Exploration (SEGUE) data during our independent attempt to search for high redshift quasars in the SEGUE dataset. We conducted follow-up Z and J-band imaging observations using UKIRT/WFCAM, and discovered it as a high redshift quasars at z $\sim$ 6 through spectroscopy (Chap 4.4). Recently, it was noted by Jiang et al. (2015).

4.3 Optical and NIR Imaging Follow-up Observations

We carried out a series of imaging follow-up observations in the optical and NIR bands to improve photometry, remove contamination, and identify quasars. For the candidates, we obtained deeper i, z, or J-band images using i and z-bands of McDonald 2.1m/CQUEAN, or Z and J-bands of UKIRT/WFCAM. The follow-up imaging observations were conducted during April 2011 – June 2012. Also we included new detection and photometry conducted by ourselves using SDSS and UKIDSS LAS images. Additionally, we introduced the Wide-field Infrared Survey Explorer (WISE) photometry and rejected candidates with small $K-W1$ colors ($K-W1 \lesssim -0.5$), since the model color of quasars at z = 6 is $K-W1 = 0.2$. Table 4.2 and 4.3 show the candidate lists selected from UKIDSS LAS DR8 and 9, respectively. These tables contain the photometry from SDSS and UKIDSS ($z_{\rm SDSS}$ and $J_{\rm UKIDSS}$), and the improved photometry from the imaging follow-up observations or our new detection (CQUEAN i, CQUEAN z, UKIRT Z, and UKIRT J).

We conducted the z-band observations to confirm their flux with higher S/N data. We used i and z-band of McDonald 2.1m/CQUEAN or Z-band of UKIRT/WFCAM,

Table 4.3 (cont'd)

ID	R.A & Dec.	$z_{\rm SDSS}$	$J_{\rm UKIDSS}$	CQUEAN i	CQUEAN z	UKIRT Z	UKIRT J	WISE cut
LASDR9_ID189	15 : 23 : 21.81 + 30 : 31 : 20.98	20.09±0.16	19.52±0.06	···	···	21.24± 0.08	18.40± 0.10	···
LASDR9_ID193	12 : 58 : 26.39 + 03 : 38 : 24.01	20.10±0.27	19.53±0.08	···	···	20.96± 0.06	18.37± 0.10	···
LASDR9_ID195	14 : 05 : 36.68 − 01 : 19 : 32.89	20.00±0.13	19.53±0.08	···	20.85± 0.09	···	···	···
LASDR9_ID196	15 : 38 : 24.81 + 06 : 23 : 00.71	20.00±0.24	19.54±0.08	22.97± 0.32	···	21.40± 0.09	18.71± 0.11	···
LASDR9_ID202	16 : 48 : 18.28 + 29 : 19 : 59.95	20.00±0.16	19.55±0.06	22.38± 0.09	···	···	···	×
LASDR9_ID205	10 : 50 : 59.54 + 11 : 39 : 52.88	19.86±0.16	19.58±0.09	21.14± 0.17	···	20.83± 0.07	18.69± 0.07	···
LASDR9_ID208	00 : 00 : 03.71 + 08 : 35 : 02.53	19.99±0.22	19.58±0.08	···	···	21.56± 0.09	18.68± 0.13	···
LASDR9_ID217	09 : 48 : 08.50 + 01 : 50 : 03.36	19.94±0.12	19.64±0.06	···	···	21.41± 0.07	18.65± 0.09	···
LASDR9_ID223	09 : 21 : 30.97 + 09 : 02 : 51.02	20.03±0.15	19.66±0.06	···	···	21.03± 0.07	18.36± 0.08	···
LASDR9_ID232	09 : 13 : 21.95 + 02 : 51 : 35.96	19.38±0.08	19.72±0.08	···	···	21.27± 0.05	18.61± 0.08	···
LASDR9_ID255	13 : 32 : 32.15 + 09 : 55 : 19.33	20.07±0.19	19.85±0.07	21.67± 0.21	···	21.12± 0.04	18.95± 0.11	···

Table 4.4. Quasars in Literature

ID[a]	R.A. Dec.	redshift	z [AB]	J [Vega]	Reference
LASDR8_143[b]	01 : 48 : 37.63 + 06 : 00 : 20.1	5.92	19.29±0.06	18.36±0.06	Jiang et al. (2015)
LASDR9_289	08 : 41 : 19.52 + 29 : 05 : 04.6	5.96	19.82±0.08	19.08±0.09	Goto (2006)
LASDR9_243	10 : 30 : 27.12 + 05 : 24 : 55.1	6.31	19.99±0.10	18.85±0.08	Fan et al. (2001)
LASDR8_009	10 : 44 : 33.05 − 01 : 25 : 01.9	5.74	19.07±0.07	18.31±0.05	Fan et al. (2000)
LASDR9_259	12 : 50 : 51.93 + 31 : 30 : 21.9	6.13	19.52±0.08	18.92±0.11	Fan et al. (2006a)
LASDR9_214	13 : 19 : 11.29 + 09 : 50 : 51.4	6.13	20.09±0.12	18.69±0.05	Mortlock et al. (2009)
LASDR9_306	14 : 11 : 11.28 + 12 : 17 : 37.3	5.93	19.61±0.08	19.20±0.09	Fan et al. (2004)
LASDR8_070	16 : 23 : 31.81 + 31 : 12 : 00.5	6.22	19.77±0.14	19.16±0.11	Fan et al. (2004)

[a] Identification number from our candidate list.

[b] We also selected this quasar as a candidate using SDSS SEGUE data, and conducted follow-up imaging observations using UKIRT/WFCAM. Through optical spectroscopy, we confirmed it as a high redshift quasar (IMSJ0148+0600).

and also observed the candidates using J-band of UKIRT/WFCAM. Data from CQUEAN data were reduced in a standard method. In the case of WFCAM data, we used preprocessed images and catalogs from the Cambridge Astronomical Survey Unit (CASU).

With the improved i, z, Z and J-band photometry, we rejected objects outside our selection box. As an example, Figure 4.2 shows a color-color diagram of a subset of candidates before (gray crosses) and after (red boxes) the follow-up observations. We can see that the gray crosses in the selection boxes move outside the box after the accurate photometry, except two candidates: LASDR8_015 and LASDR8_143. We conducted spectroscopy for these 2 candidates, explained in the next section. Through these imaging follow-up observations, we rejected 99% of contamination, which is very efficient. As we can see in Chap. 3.8.2, the z-band photometry from SDSS show very large photometric uncertainties.

The expected number of quasars at z $\sim$ 6 is $\sim$17 in 3,400 deg^2 (Chap. 7.1). Since the uncertainties of the luminosity function at z $\sim$ 6 is high, the range of the expected quasars is 4 – 50 considering the 1σ confidence level. Our selection

identified 9 quasars including newly discovered 2 quasars and this number is in agreement with the expected number from the luminosity function.

4.4 Optical Spectroscopic Follow-up Observations

In this section, we present details of our optical spectroscopic identification. We have taken spectra of 2 high priority candidates which were not rejected after the follow-up imaging observations, as shown in section 4.3. The results of the spectroscopic follow-up observations are summarized in Chap 4.5.

ID0176 (LASDR8_143) was discovered using Hobby-Eberly Telescope (HET) and Low Resolution Spectrograph (LRS). With g1 (300l/mm) and a $2''$ longslit, the spectral resolution is $16\mathring{A}$. Two observations in December 2010 and January 2011 were conducted. Bias, flat, arc, and standard star data were taken.

ID6015 (LASDR8_015) was discovered using Magellan telescope and Magellan Echellette Spectrograph (MagE) in September 2011. We obtained bias, arc, flat images for calibrations with a $1''$ slit width (R=4,100). Standard stars were observed for flux calibrations. We exposed 1,800s on source. Processing of the data were done by a pipeline designed for the Magellan/MagE.

Then ID6015 was observed again using Magellan telescope and Low Dispersion Survey Spectrograph 3 (LDSS3) in July 2014. The flat, arc, standard star images and the two science images were obtained with VPH-Red grism, OG-590 filter, and a slit width of $0.75''$ (R=1,810). The total integration time was 30 min. The data were processed via bias subtraction using overscan area and flat fielding from dome flat images using the `noao.imred.ccdred` package of IRAF. The aperture extraction was done using the `noao.twodspec.apextract` package for each image and the spectra were combined using the `scombine` task in average. We obtained the wavelength and flux calibration solutions using the arc images and standard star images, respectively.

The spectra of these two quasars were scaled to an absolute flux scale using

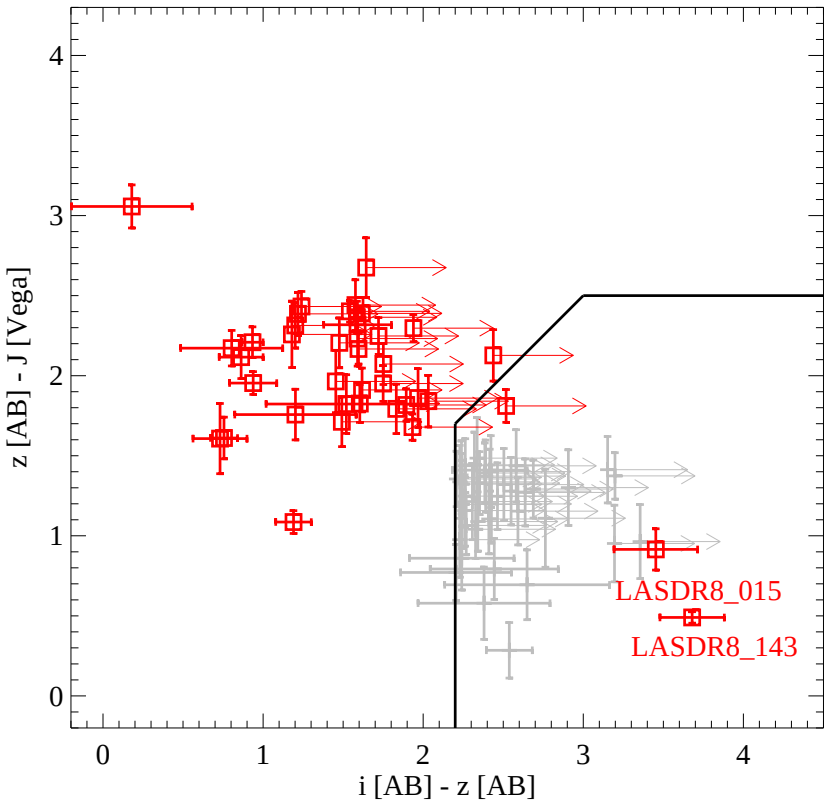

Figure 4.2 An example of colors of our candidates before (gray crosses) and after (red boxes) the imaging follow-up observations. The two sources, LASDR8_015 and LASDR8_143, within the selection box was confirmed as quasars via spectroscopic observations.

z-band photometry from SDSS. The spectra were corrected for Galactic extinction using information of Cardelli et al. (1989) and Schlegel et al. (1998).

4.5 Spectral Properties of IMS Quasars at z ∼ 6

4.5.1 Optical Spectra

We present the optical spectra of 2 new quasars at z ∼ 6 in Figure 4.3 and 4.4. Figures 4.3 shows spectra of ID0615 at z = 6.0 from the Magellan/MagE (gray line) and Magellan/LDSS3 (black line), and Figure 4.4 is for ID0176 at z = 5.9 from the HET/LRS. In Figure 4.3, we plot two spectra obtained from different instruments, Magellan/MagE and Magellan/LDSS3, which show small differences in their shapes. It could be caused by various reasons, for example, slit losses due to the seeing variation or the uncertainty of flux calibrations. In Figure 4.4, we plotted spectra smoothed with resolutions of each instrument (black lines) to increase the S/N per resolution element, compared to the original spectra (gray lines). The blue lines denote the errors of the spectra. In the case of ID0176, it was independently discovered by Jiang et al. (2015).

4.5.2 Physical Properties on Spectra

Table 4.5 lists the identification number (ID), name, coordinates, z magnitude, redshift, and M_{1450} of the quasars.

Since both objects show a sharp declination bluewards of Lyα, we measured their redshifts using the peak positions of each spectrum after smoothing spectra with the resolution of each instrument. The redshift errors contain the uncertainties from the spectral resolution of each instrument, as explained in Chap. 3.7.2. ID0176 shows an ambiguous Lyα shape. Jiang et al. (2015) reports the redshift of ID0176 as $z_{CII} = 5.923 \pm 0.003$ that is estimated from the C II emission line, using a spectrum

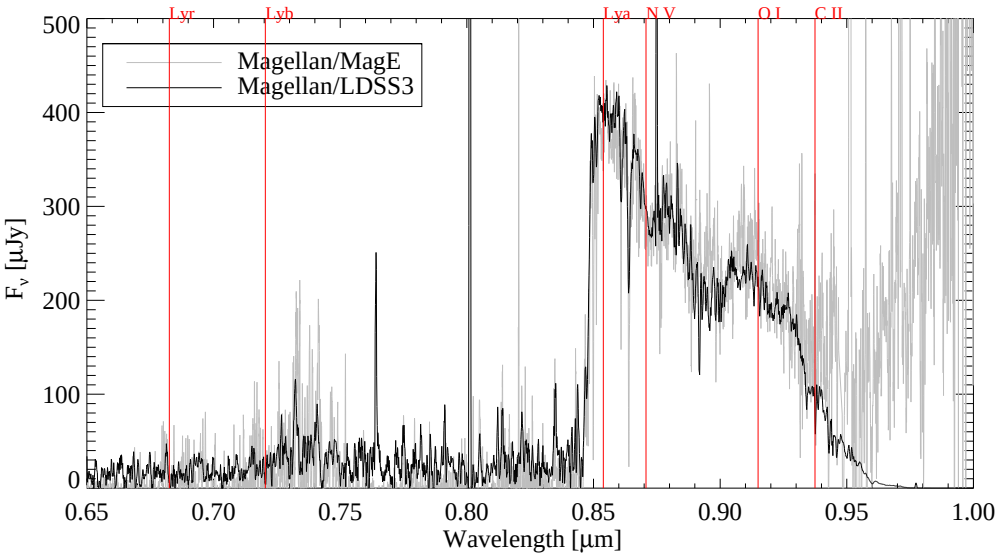

Figure 4.3 Optical spectra of ID0615 from Magellan/MagE (gray line) and Magellan/LDSS3 (black line). The red vertical lines indicate general quasar emission lines.

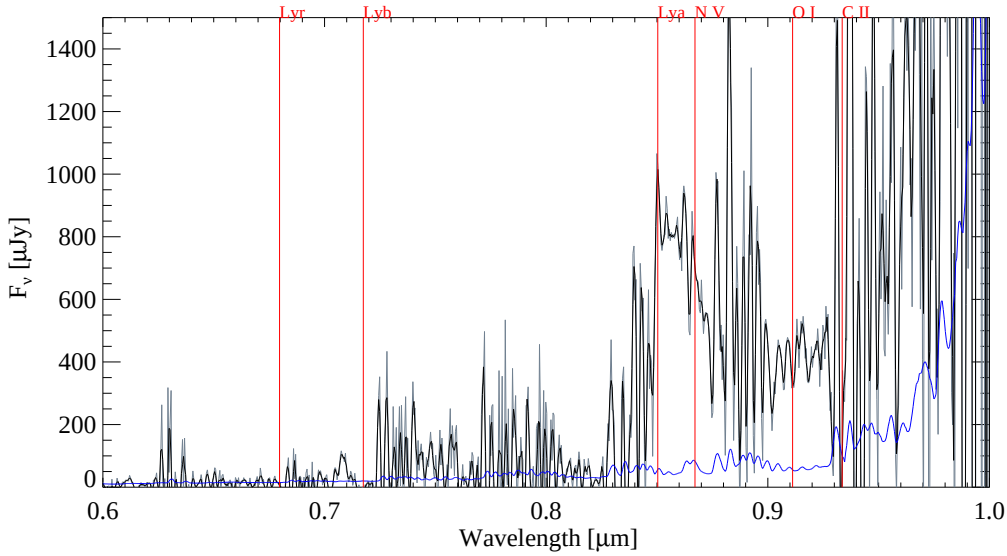

Figure 4.4 Optical spectrum of ID0176 from HET/LRS. The gray line is the original spectrum and the black line is the spectrum smoothed by its instrumental resolution. The blue line denotes the errors, showing the low S/N ratio of the spectrum. The red vertical lines indicate general quasar emission lines.

taken from MMT/Red Channel Spectrograph with resolution $\sim 10\mathring{A}$. This redshift does not agree with our result, $z_{Ly\alpha} = 5.993 \pm 0.013$, within the error range. Since its Lyα emission line is observed to be strongly altered shape from the higher resolution spectrum of Jiang et al. (2015) (they reported that it is likely a BAL quasar), our redshift measured from the Lyα emission line is incorrect by miscalculating the peak position of the Lyα emission line.

Absolute magnitudes of the continua at rest-frame $1450\mathring{A}$ (M_{1450}) are listed in Table 4.5. In the case of two quasars at z $\sim$ 6, the rest-frame $1450\mathring{A}$ is located at the observed wavelength $\sim$1.0 μm, where our optical spectra cannot access. To estimate M_{1450} for these cases, we scaled a redshifted spectrum from the SDSS composite spectrum of Vanden Berk et al. (2001) to the z-band magnitude for each target. Then the flux at $1450\mathring{A}$ was estimated from this redshifted and flux-scaled spectrum (Leipski et al. 2014), using the average flux in $1440\mathring{A}$ – $1460\mathring{A}$ on the spectra. The uncertainties were estimated from the rms continuum flux density. These uncertainties are smaller than those of the quasars at z $\sim$ 5 in Chap 3.7.2, because the S/N of the model spectra are higher than those of the observed spectra of quasars at z $\sim$ 5.

4.5.3 Individual Properties of Quasars

These are individual properties of the spectra for each quasar.

ID0615 ($z_{Ly\alpha}$=6.02): Its spectra were observed by two instruments of Magellan telescope, MagE and LDSS3. It shows a strong Lyα emission line.

ID0176 ($z_{Ly\alpha}$=5.99): It has a strong Lyα emission line, but we cannot figure out the other emission lines due the low S/N ratio. It was independently discovered by Jiang et al. (2015).

Table 4.5. Information of the quasars discovered at z ∼ 6

ID	Name	R.A. & Dec.	z	$z_{Ly\alpha}$	M_{1450}
ID0615 (LASDR9_015)	IMSJ0159−0025	01:59:07.3−00:25:06.33	20.063±0.100	6.022±0.002	−26.60±0.01
ID0176 (LASDR9_143)	IMSJ0148+0600	01:48:37.6+06:00:19.90	19.289±0.058	5.993±0.013[a]	−27.34±0.01

[a]Jiang et al. (2015) provides a more accurate redshift, $z_{CII} = 5.923 \pm 0.003$

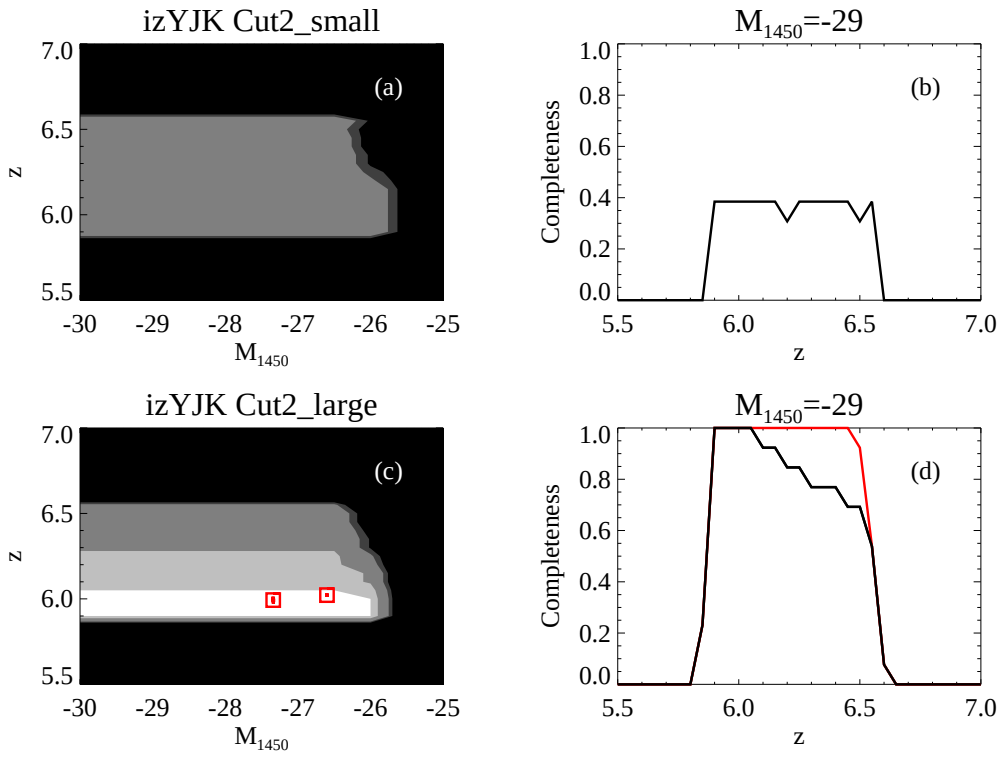

Figure 4.5 Similar to Figure 3.17, but (a) and (b) are for the selection using the $i-z-J$ color-color diagram and the small selection box of the $Y-J-K$ color-color diagram, and (c) and (d) are for the selection using the $i-z-J$ color-color diagram and the large selection box of the $Y-J-K$ color-color diagram. The red boxes in (c) indicate the redshifts and M_{1450} of our two new quasars. The red line in (d) shows the completeness when we do not adopt the second color-color diagram, $Y-J$ vs. $J-K$. The colors of the contours indicate 0% and 100% completeness for black and white, respectively.

4.6 Quasar Selection Efficiency

To calculate the expected quasar number for each quasar selection method, we derived the quasar selection efficiency using the completeness from our color cuts. The quasar selection efficiency is defined as the number of discovered quasars among the number of candidates, and completeness from color selection is defined as the number of quasar models inside specific color cuts among the number of quasar models with specific redshift and magnitude. We calculated the completeness from our color cuts using the same method described in Chap. 3.8.1. Then we apply this completeness to our quasar surveys and predict the expected quasar number of each survey in Chap. 7.1.

Figure 4.5 shows plots similar to Figure 3.17, but (a) and (b) are for the selection using the $i - z - J$ selection and the small selection box of the $Y - J - K$ color-color diagram, and (c) and (d) are for the selection using the $i - z - J$ and the large selection box of the $Y - J - K$ color-color diagram. We can see that the completeness including the small selection box (Figure 4.5 (b)) is less than 50% for all redshifts and M_{1450}. The completeness from the large selection box (black line in Figure 4.5 (d)) shows a steep increase at z = 5.85 and a steady decrease after z = 6.10. The redshift range with the completeness greater than 70% (80%) in Figure 4.5 (d) is $5.85 < z < 6.45$ ($5.85 < z < 6.30$). At z = 6, the completeness in Figure 4.5 (c) drops below to 50% for $M_{1450} > -26.0$, where the M_{1450} limit was estimated from our magnitude cut, $J < 19.6$ mag. We also plotted the redshift and M_{1450} for our two new quasars, IMSJ0159-0025 and IMSJ0148+0600 (Table 4.5), with red boxes in Figure 4.5 (c). The red line in Figure 4.5 (d) shows the completeness distribution when we do not adopt the second color-color diagram, $Y - J$ vs. $J - K$, indicating that the low completeness at $z > 6.05$ is directly caused by the second color-color diagram. Although the second color-color diagram decreases the completeness from 100% to 88% for $6.05 < z < 6.50$, the second color-color diagram is essential because

the second color-color diagram eliminats 94% of the contaminants selected from the first color-color diagram, $i - z$ vs. $z - J$.

4.7 Summary

We conducted a quasar survey at z $\sim$ 6 using multi-wavelength data covering a wide area. We developed a new selection criteria in addition to the currently used selection method, and found that the new method eliminated 94% of contamination. We conducted optical and NIR imaging follow-up observations and these data reduced contaminants efficiently. Finally, we discovered two new quasars at z = 5.9 and 6.0 from optical spectroscopy. We estimated the completeness distribution of our survey and found that, although the second color cut ($Y - J - K$) reduces the completeness by 12%, it is critically essential to decrease the contamination rate. The quasar selection at z $\sim$ 6 can also be conducted using deeper datasets, such as the IMS data in Chap. 2, which is illustrated in detail in Chap. 7.3.1.

Chapter 5

Quasar Selection at z $\sim$ 7

5.1 Introduction

High redshift quasars are very useful objects to study the cosmic reionization history at the end of the reionization and the formation and growth of structures including the supermassive black holes (SMBHs). It is because high S/N spectra required for these studies are only available for these luminous quasars. Previous studies have discovered high redshift galaxies at z $>$ 6 through deep surveys (e.g., Stark et al. 2011). However, high redshift galaxies are too faint to provide the high S/N spectra although the number density of galaxies at z $\sim$ 7 is a factor of 10^6 higher than that of quasars at z $\sim$ 7. On the other hand, gamma ray bursts are the brightest objects in the universe and have been used to study the early universe (e.g., Jang et al. 2011). However their brightness only continue for a few days (Gehrels et al. 2009).

Historically, most of the quasar color selection at z $<$ 5 are basically based on data at the optical wavelengths (e.g., Richards et al. 2002), and selection methods are available for z $\sim$ 6 quasars by adopting near-infrared (NIR) information such as the J-band (e.g., Fan et al. 2001, 2003, 2004, 2006a; Jiang et al. 2008, 2009; Willott et al. 2007, 2009, 2010a,b). However quasars at z $>$ 6.5 are undetectable in

optical wavelengths since their Lyα emission lines are redshifted to the z-band and the shorter wavelengths are absorbed by the intergalactic medium (IGM; Gunn & Peterson 1965). Therefore more information from the NIR wavelengths are needed for the z $\sim$ 7 quasar selection. Additionally imaging surveys covering a wide area are required in both optical and NIR bands, because these high redshift quasars are rare ($\sim$1 quasars per Gpc^{-3} at z $\sim$ 7).

The number of known z $>$ 6.5 quasars is 7, and all of them were discovered from large area surveys. The first z-dropout quasar was discovered by Mortlock et al. (2011), the most distant quasar up to date at z=7.085. They used the UKIRT Infrared Deep Sky Survey Large Area Survey (UKIDSS LAS) DR8, with a combination of $i - Y - J$ (Figure 5.1). Venemans et al. (2015) found 3 quasars at 6.5 $<$ z $<$ 6.7 as their first results from the Panoramic Survey Telescope & Rapid Response System 1 (Pan-STARRS1, PS1; Kaiser et al. 2002, 2010) survey. The PS1 survey covers 20,000 deg^2 with five filters, g_{P1}, r_{P1}, i_{P1}, z_{P1}, and y_{P1}. Mortlock et al. (2011) and Venemans et al. (2015) measured the neutral hydrogen fraction of the IGM in front of their quasars along our line-of-sight. Since high redshift quasars ionize magaparsec-scale near zones around them, ones can calculate the size of these ionized zones ($R_{\rm NZ}$), using their transmission profiles. They shows that the $R_{\rm NZ}$ evolves with redshift: the $R_{\rm NZ}$ of quasars at z $\sim$ 7 is a factor of three smaller than those of quasars at 6.0 $<$ z $<$ 6.4. Venemans et al. (2013) reported 3 quasars at z $>$ 6.5 in 332 deg^2 among the VISTA Kilo-degree Infrared Galaxy (VIKING) survey, using the color cuts in Figure 5.2. They present the quasar luminosity function at z $>$ 6.5. All of these discoveries were conducted i) using large area surveys: UKIDSS has NIR imaging survey of $\sim$4,000 deg^2, VIKING will cover 1,500 deg^2, and PS1 covers over more than 20,000 deg^2, and ii) including Y-band data.

We designed a survey for z $\sim$ 7 quasar selection using our own IMS and other archival data. We developed a new selection technique using IR wavelength infor-

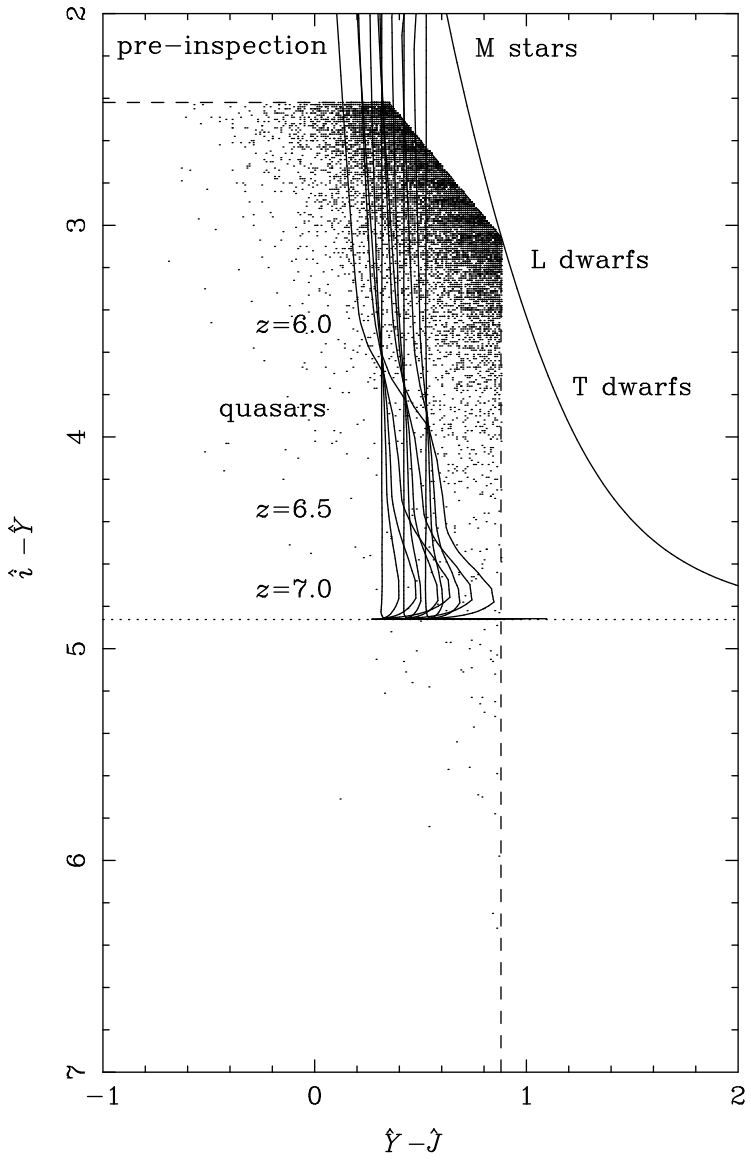

Figure 5.1 Color-color diagram adapted from Mortlock et al. (2011). They show sources from UKIDSS LAS DR8 LAS (points), the stellar locus, and the quasar models. The dashed lines denote the their selection cuts.

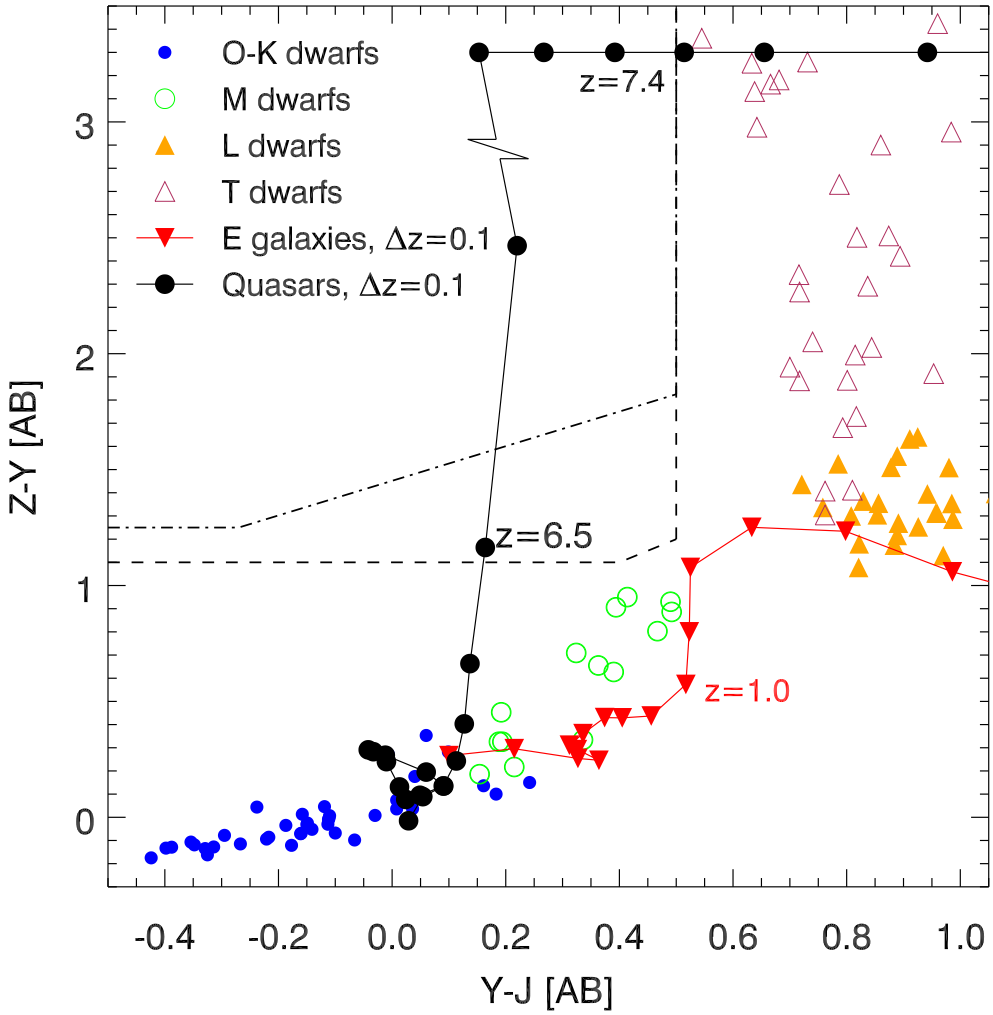

Figure 5.2 $Z - Y$ vs. $Y - J$ color-color diagram adapted from Venemans et al. (2013). The dashed and dash-dotted lines show their color cuts. The simulated colors of main sequence stars (small, blue dots), M dwarfs (green, open circles), L dwarfs (yellow, solid triangles), T dwarfs (open, maroon triangles), elliptical galaxies (red, upside-down triangles), and quasars (black, solid points) from Hewett et al. (2006) are plotted.

mation as well as the previous method adopting the Y-band photometry. In Chap. 5.2, we show the definition of our color cuts, multi-wavelength data we used, and our color selections. Chap. 5.3 shows the completeness distribution of this survey. We summarize this survey in the final chapter (Chap. 5.4). Throughout this paper, we use a cosmology with $\Omega_M = 0.3, \Omega_\Lambda = 0.7$, and $H_0 = 70$ km s^{-1}Mpc^{-1}. We use the AB magnitude system.

5.2 Selection Method

5.2.1 Definition of Color-color Diagrams

Selection methods of z > 6.5 quasars used the Y-band photometry combined with other bands, for example, $z - Y - J$ or $I - Z - Y - J$ (e.g., Choi et al. 2012). We adopted this Y-band selection method for IMS fields observed with the Y-band: EGS, SA22, CFHTLS-W2, and XMM-LSS fields.

In many fields, Spitzer Infrared Array Camera (IRAC) mid-infrared band images are available. In such fields, the addition of Y-band is not critical and we derived a new selection method using IR bands. We plotted SEDs of dwarf stars from Burrows et al. (2006) and a quasar spectrum at z = 7 using the quasar template from Vanden Berk et al. (2001), with filter response curves of J, $Ch1$, and $Ch2$-bands in Figure 5.3, where the $Ch1$ and $Ch2$ are bands of Spitzer IRAC. From this figure, we can see that the IR selection is possible since SEDs of high redshift quasars at $\lambda > 2\mu m$ are different from SEDs of dwarf stars. Venemans et al. (2015) discovered 3 quasars at $6.5 <$ z < 6.7 in Pan-STARRS1 using the WISE $W1$ and $W2$ bands combined with optical and NIR bands, indicating that the color selection using mid-infrared bands can be applied to find quasars at z ~ 7.

The Spitzer Wide-area InfraRed Extragalactic (SWIRE) survey provides IRAC data for 6 fields: ELAIS-N1, ELAIS-N2, Lockman Hole, XMM-LSS, ELAIS-S1, and

CDF-S with a depth of 3.7 μJy at 3.6 μm. Combining with the CFHT MegaCam data, we selected 4 fields, ELAIS-N1, ELAIS-N2, Lockman Hole, and XMM-LSS for the IR color selection.

We plotted various color-color diagrams and checked their positions on the color-color diagrams. Figures 5.4 and 5.5 show the color-color diagrams we used, for the IR selection, and for the Y-band selection, respectively. To define color cuts, we plotted position of i) quasar redshift tracks (black lines with asterisks from Vanden Berk et al. 2001), ii) dwarf stars from model spectra of Burrows et al. (2006) (triangles) or observed dwarf stars from Patten et al. (2006) and Zhang et al. (2009) (rectangles), iii) a star forming galaxy redshift track (blue lines, from M51), and a passive galaxy redshift track (red lines, from the Bruzual & Charlot (2003) model of a passively evolving 5 Gyr-old galaxy with spontaneous burst, metallicity of Z=0.02, and the Salpeter IMF). Also we plotted $z-Y$ and $Y-J$ colors of 7 quasars at z > 6.5 from Mortlock et al. (2011), Venemans et al. (2013), and Venemans et al. (2015) in Figure 5.5 with red crosses. The solid lines in Figures 5.4 and 5.5 indicate the selection boxes.

We defined the color cuts as below:

For the IR bands selection,

`Cut1` $z-J > 1.5 \ \cap \ J-Ch1 > 0 \ \cap \ z-J > 7.5(J-Ch1)-4.5$

`Cut2_small` $0.2 < Ch1-Ch2 < 1.0 \ \cap \ 0.2 < J-Ch1 < 0.9$

`Cut2_large` $Ch1-Ch2 > 0 \ \cap \ 0 < J-Ch1 < 1$

and for the Y-band selection,

`Cut1_small` $z-Y > 1.4 \ \cap \ -0.1 < Y-J < 0.5$

`Cut1_large` $z-Y > 1.4 \ \cap \ Y-J < 0.6$

We set a conservative color cuts of $J-Ch1$ and $Ch1-Ch2$ to reduce contamination. Barnett et al. (2015) provided the $Ch1$ and $Ch2$ photometry of the quasar at z = 7.084, ULAS J1120+0641, and we plotted its colors on Figure 5.4. Although

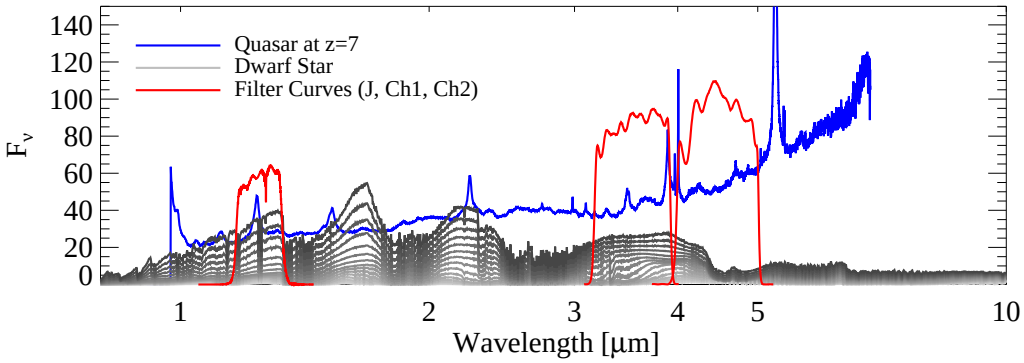

Figure 5.3 SEDs of dwarf stars and a quasar spectrum at z = 7 with filter response curves of J, $Ch1$, and $Ch2$-bands overplotted.

this object satisfies the color cuts on the $z - J$ vs. $J - Ch1$ color-color diagram, it has a blue $Ch1 - Ch2$ color, which is different from our prediction. We did not consider this blue color of the continuum when we constructed our color cuts. Since the Spitzer photometric information of the other 6 quasars at z $\sim$ 7, except ULAS J1120+0641, is unknown, we were unable to discuss the trend of the continuum slopes at high redshift. If the continuum slopes of quasars at z $\sim$ 7 are bluer than those of low redshift quasars, our color cuts should be modified.

5.2.2 Multi-wavelength Data

For these two color selection methods, we gathered available archival multi-wavelength data including the UKIDSS DXS and IMS, and cross-matched them. During the matching processes, we adjusted astrometric differences between catalogs from various surveys. We calculated the differences in R.A. and Dec. directions using the matched catalogs, and applied the offset values to each catalog. Figure 5.6 shows astrometric differences between two catalogs (in this case, from a small area in the EGS field between IMS Y-band and CFHT i-band catalogs (upper panels), and a

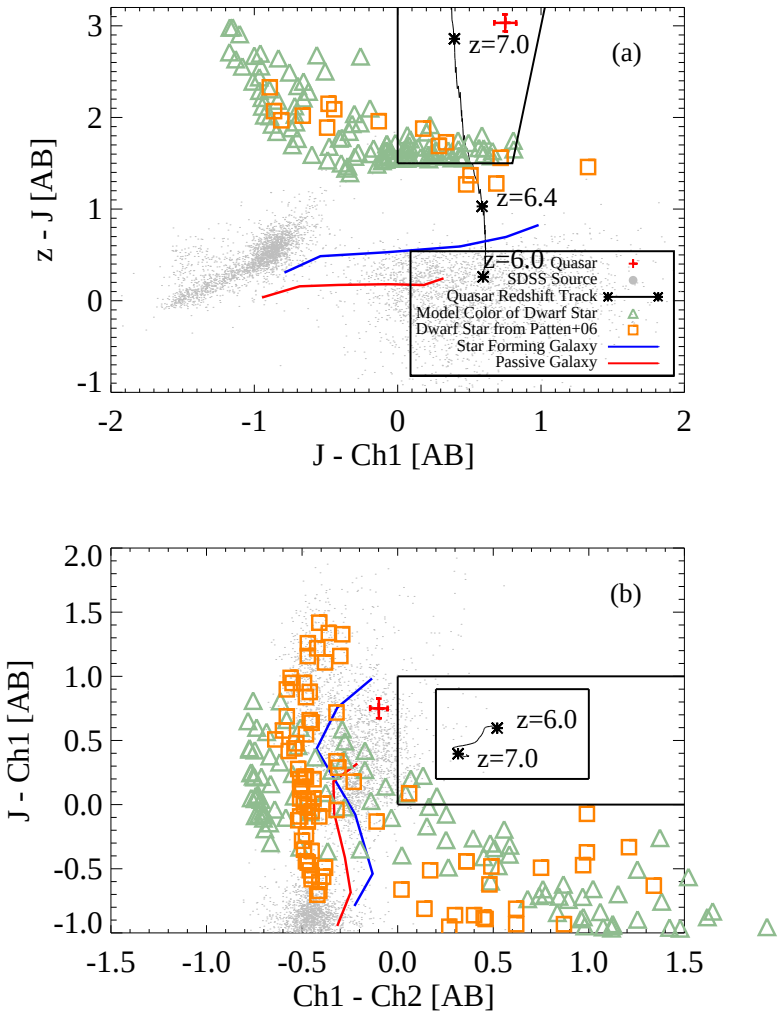

Figure 5.4 Two color-color diagrams we adopted for quasar selection at z > 6.5 using IR bands. Quasar redshift tracks (black lines), model dwarf stars (triangles), observed dwarf stars from Patten et al. (2006) (rectangles), a star forming galaxy redshift track (blue lines), and a passive galaxy redshift track (red lines) are plotted with SDSS sources (gray points). We include the observed quasar at z = 7 with a red cross. The solid lines indicate the selection boxes for our quasar selection.

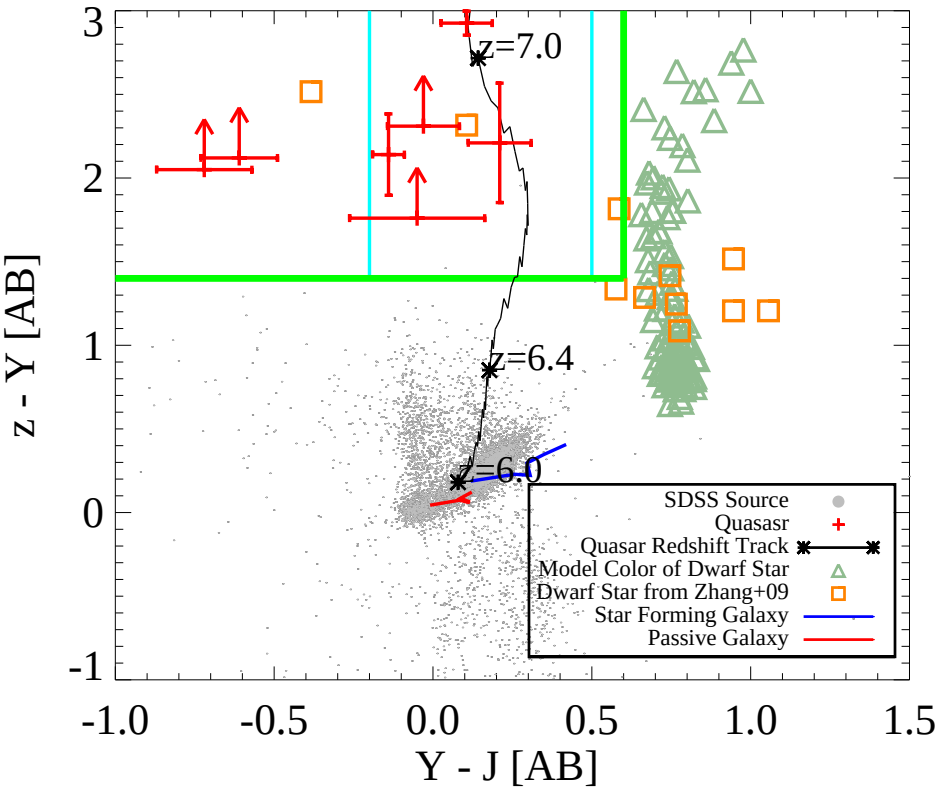

Figure 5.5 Two color-color diagrams we adopted for quasar selection at z > 6.5 using the Y-band. The symbols are similar to Figure 5.4. We include the observed quasars with red crosses and observed dwarf stars from Zhang et al. (2009) with boxes. The cyan and green lines indicate the selection boxes for our quasar selection.

small area in the ELAIS-N1 field between IMS J-band and SWIRE catalogs (lower panels)) before the adjustment. The distributions of R.A and Dec. offsets were fitted with Gaussian functions and the offsets were estimated. The differences are from $-0.3''$ to $0.1''$ between NIR and optical bands, and from $-0.2''$ to $0.3''$ between NIR and SWIRE data. The 1σ dispersion from these Gaussian fitting is $0.13''$. We compared these systematic differences in the positions between IMS YJ, CFHT iz, and SWIRE to other catalogs. we used the Two Micron All Sky Survey (2MASS) Point Source Catalog (PSC) for a NIR reference catalog and the USNO-B1.0 Catalog for a optical reference catalog. Although the position between IMS and 2MASS has no systematic difference, CFHT vs. USNO-B1.0, SWIRE vs. USNO-B1.0, or SWIRE vs. 2MASS have systematic differences larger than their position uncertainties, without any particular direction in their offsets.

We used the optical data taken by CFHT MegaCam, Subaru Suprime-Cam, INT and KPNO 4-m telescope, the NIR data from IMS and UKIDSS DXS, and the IR data from SWIRE survey. We summarize these IMS fields in Table 2.1.

a) CFHT MegaCam data

CFHTLS provides optical data at $ugriz$ bands with the z-band limiting magnitude of 23.9 mag. Also we used CFHT MegaPipe data with z-band depth similar to that of CFHTLS.

b) Subaru Suprime-Cam

We downloaded Suprime-Cam data through the SMOKA Archive SUP Search[1] with r, i, and Zr-bands covering ELAIS-N1, Lockman Hole, XMM-LSS fields. The data were reduced using SDFRED2. We found astrometric solutions using SCAMP (Bertin 2006). The limiting magnitude of the i-band is $\sim$26 mag. For a z = 7 quasar, the $i - J$ color is 4.4 when we estimate this color using a quasar template from Vanden Berk et al. (2001). Therefore these i-band data are useful to reject

[1] http://smoka.nao.ac.jp/SUPsearch.jsp

objects that have the i-band detections.

c) Optical data observed with INT and KPNO 4-m telescope

SWIRE conducted optical imaging follow-up observations in five optical bands ($UgriZ$) for these SWIRE fields: Lockman Hole, ELAIS-N1, and ELAIS-N2. The i-band depths of these data are about 23.7 mag. Although these i-band data are not as deep as those of the Subaru Suprime-Cam data, many candidates were rejected after checking the i-band detections from these data.

d) IMS and UKIDSS DXS

IMS (Chap. 2) covering $\sim$120 deg^2 with depths of 22.0 – 24.0 mag for Y-band and 21.5 – 24.0 mag for J-band, and the UKIDSS DXS with J-band depths of 21.8 – 23.3 mag were used as reference catalogs.

e) SWIRE

SWIRE surveyed $\sim$49 deg^2 with the MIPS far-infrared camera and IRAC mid-infrared camera. They provide IRAC data with depths of 3.7 μJy at 3.6 μm and 5.4 μJy at 4.5 μm. We conducted new detections and photometry from the image data and used them as the IR catalogs, in addition to the catalogs they provide.

5.2.3 Color Selections with IR/Y bands

Since the two IR data, IMS and DXS, show various depths for each field, we decided the magnitude cut using photometric errors, $J_{err} < 0.1$ mag for the IR bands selection and $Y_{err} < 0.143$ mag for the Y-band selection. Using the color cuts described in Chap. 5.2.1, we selected objects located in the selection boxes. i-band detected sources from various optical surveys explained in Chap 5.2.2 were rejected as z-dropouts.

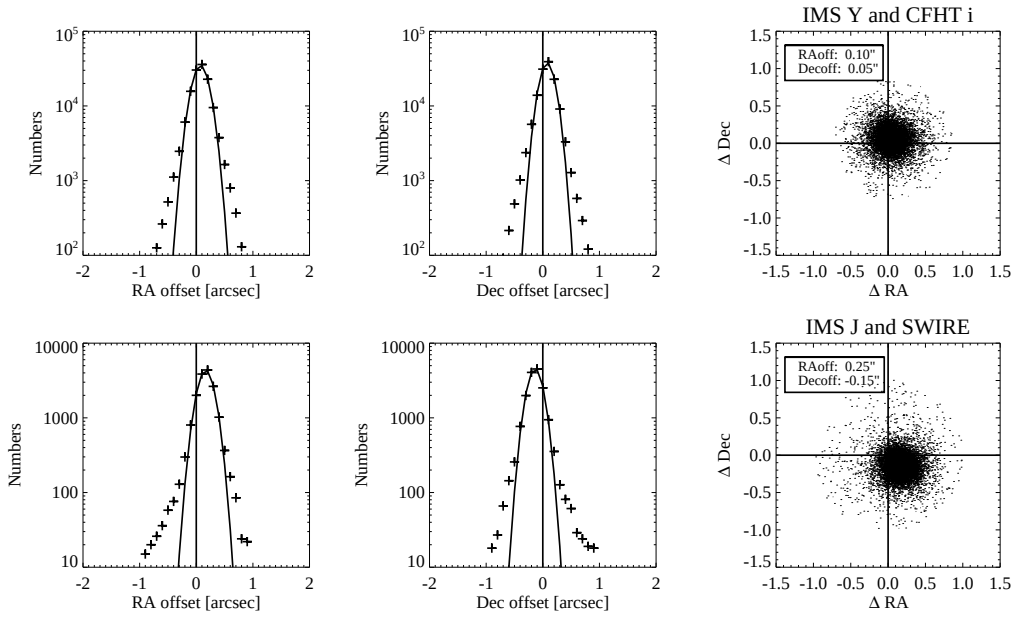

Figure 5.6 Astrometric differences between two catalogs before the adjustment, for a small area in the the EGS field between IMS Y-band and CFHT i-band catalogs (upper panels), and a small area in the ELAIS-N1 field between IMS J-band and SWIRE catalogs (lower panels) as examples.

Table 5.1. Quasar Survey Area

Field	Selection with IR bands		Selection with Y-band
	DXS	IMS	IMS
	(DXS+SWIRE+CFHT)	(IMS-J+SWIRE+CFHT)	(IMS-Y+CFHT)
XMM-LSS	3.0	3.1	4.4
CFHTLS-W2	···	···	23.1
Lockman Hole	7.0	3.5	···
EGS	···	···	36.6
ELAIS-N1	7.8	3.6	···
ELAIS-N2	···	4.1	···
SA22	···	···	14.1
Total	17.7	14.3	78.3

Note. — The unit is $\deg^2$.

5.2.4 Survey Area

The area used in each selection method are listed in Table 5.1. The IMS and DXS area covered with other multi-wavelength data all together were used for the selections. The DXS or IMS area with J-band as well as the CFHT and SWIRE data were used for the IR selection, and the IMS area with Y-band as well as the CFHT data were used for the Y-band selection.

5.3 Quasar Selection Efficiency

To calculate the expected quasar number for each quasar selection method, we derived the quasar selection efficiency using the completeness from our color cuts. The quasar selection efficiency is defined as the number of discovered quasars among the number of candidates, and completeness from color selection is defined as the num-

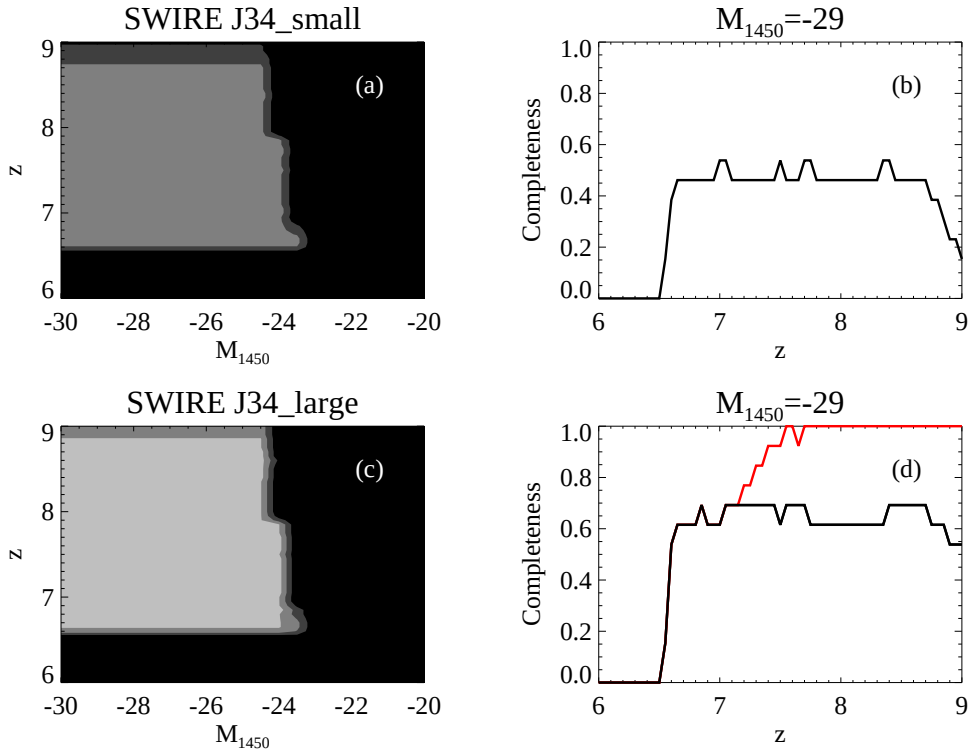

Figure 5.7 Similar to Figures 3.17 and 4.5, but for the quasar selection at z $\sim$ 7 using $z - J - Ch1 - Ch2$ cuts, with the small ((a) and (b)) and large ((c) and (d)) selection boxes in the second color-color diagram, $J - Ch1$ vs. $Ch1 - Ch2$. The red line in (d) indicates the completeness when we do not adopt the second color-color diagram. The colors of the contours indicate 0% and 100% completeness for black and white, respectively.

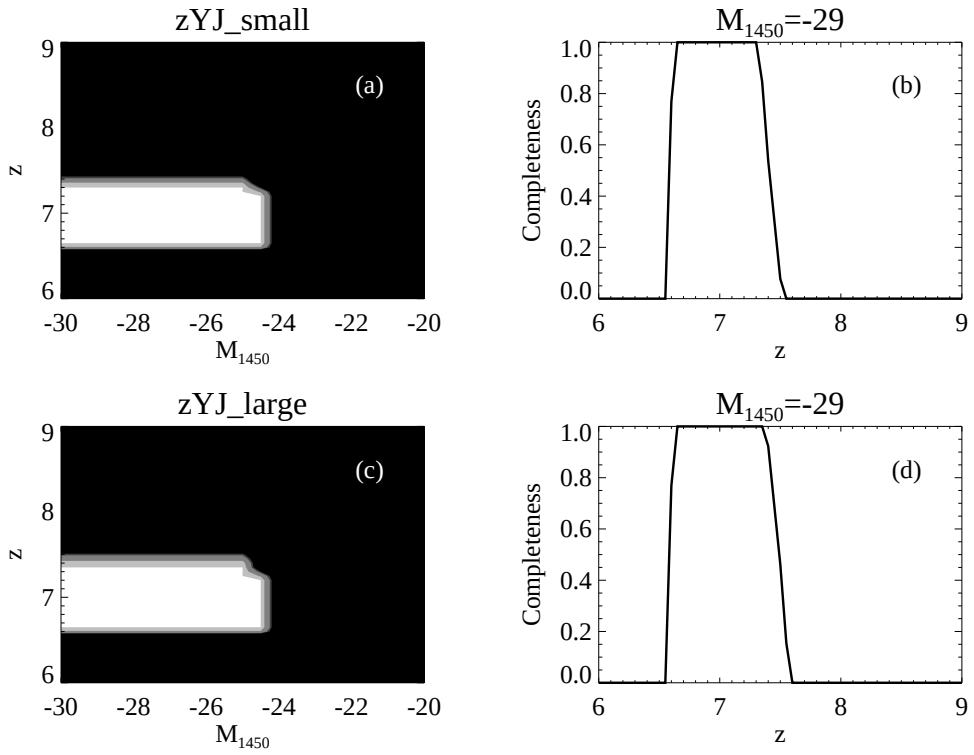

Figure 5.8 Similar to Figure 5.7, but for the quasar selection at z $\sim$ 7 using Y-band. (a) and (b) use the small selection box in the $z - Y - J$ color-color diagram, while (c) and (d) use the large selection box. The colors of the contours indicate 0% and 100% completeness for black and white, respectively.

ber of quasar models inside specific color cuts among the number of quasar models with specific redshift and magnitude. We calculated the completeness using the same method explained in Chap. 3.8.1 and 4.6. Then we apply this completeness to our quasar surveys and predict the expected quasar number of each survey in Chap. 7.1.

Figures 5.7 and 5.8 show plots similar to Figures 3.17 and 4.5. In Figure 5.7, we plotted the completeness distribution for the selection using the $z-J-Ch1-Ch2$ ($z-J$ vs. $J-Ch1$ and $J-Ch1$ vs. $Ch1-Ch2$) color-color diagrams, with the small ((a) and (b)) and large ((c) and (d)) selection boxes in the second color-color diagram, $J-Ch1$ vs. $Ch1-Ch2$. Figure 5.8 (a) and (b) are for the selection using the small selection box in $z-Y-J$ color-color diagram, and (c) and (d) are for the selection using the large selection box in the $z-Y-J$ color-color diagram. The completeness distribution for the selection using the $z-J-Ch1-Ch2$ color-color diagrams (black line in Figure 5.7 (b) and (d)) is less than 80% for all redshifts and M_{1450}, which demonstrates the low selection efficiency resulting from these selection boxes. The redshift coverage with the completeness greater than 60% in Figure 5.7 (d) is $6.60 < z < 8.90$. The red line in Figure 5.7 (d) indicates the completeness distribution when we do not adopt the second color-color diagram, $J-Ch1$ vs. $Ch1-Ch2$. We can see that the second color cut decreases the completeness for $z > 7.10$. The completeness distribution from the selection using the $z-Y-J$ color-color diagram show wide redshift coverages in both small (Figure 5.8 (b)) and large (Figure 5.8 (d)) selection boxes, $6.60 < z < 7.40$ and $6.55 < z < 7.45$ with the completeness greater than 80%, respectively. At $z = 7$, the completeness from the two selection methods (Figure 5.7 (c) and 5.8 (c)) drop to below 50% at $M_{1450} > -24.0$, where the M_{1450} limit was estimated from our magnitude cuts, $J < 22.1$ and $Y < 22.6$ for the IR bands selection and the Y-band selection, respectively. None of quasars at $z \sim 7$ was discovered, constraining the upper limits on the quasar number density.

From this completeness, we estimate the upper limits of quasar number density at z $\sim$ 7 and compare these values to the luminosity function at z $\sim$ 7 (Chap. 7.1).

5.4 Summary

We are conducting a survey for quasars at z $\sim$ 7 using our Y and J-band imaging data from IMS and archival data from optical to IR wavelengths. From the IMS Y-band data covering $\sim$80 deg^2, we selected quasars using a method similar to previous studies. Also we developed a new selection technique adopting IR bands for IMS fields where SWIRE provides the IRAC data. Within the entire $\sim$110 deg^2 area, we found no quasars at z $\sim$ 7. The upper limits of the quasar number density, estimated from this result, is discussed in Chap. 7.1.

Chapter 6

Properties of High Redshift Quasars

6.1 Introduction

In this chapter, we present the physical properties of three IMS quasars based on the spectroscopic data obtained with optical and near infrared (NIR) spectroscopy. In our NIR spectra, we identify both C IV and Mg II lines for ID0085 and ID0101, and only C IV line for ID0099. After modeling continuum (Chap. 6.2) and emission lines of C IV and Mg II (Chap. 6.3), we estimate continuum slopes α_ν (where α_ν is for $F(\nu) \propto \nu^{\alpha_\nu}$), line widths (full width at half maximum; FWHM), continuum flux at the rest-frame wavelength 1350$\mathring{A}$ and 3000$\mathring{A}$ ($\lambda L_\lambda(1350)$ and $\lambda L_\lambda(3000)$) for each emission line (Chap. 6.5 and 6.6). From these measurements, we calculate the black hole mass from the C IV emission line ($M_{\rm BH,CIV}$) or from the Mg II emission line ($M_{\rm BH,MgII}$) through different relations from McLure & Jarvis (2004), Vestergaard & Peterson (2006), and Jun et al. (2015) (Chap. 6.7) using the Eq. 1.3, 1.4, 1.5, and 1.6. The bolometric luminosity ($L_{\rm Bol}$), Eddington luminosity ($L_{\rm Edd}$), and the ratio between two values ($L_{\rm Bol}/L_{\rm Edd}$) are calculated from the continuum flux and

the black hole masses, using the Eq. 1.7, 1.8, and 1.9 (Chap. 6.8) . For the virial factor in these black hole mass estimators, we adopt $f = 5.1 \pm 1.3$ from Woo et al. (2013).

6.2 Spectral Model for Continuum Components

We modeled the quasar continuum assuming two components, a power law component and a component that describes Fe II emission lines as given below:

$$F(\lambda) = a \times \lambda^{\alpha_\lambda} + b \times \mathrm{FeII}(\lambda, v)$$

where α_λ is the continuum slope (in this case, $\alpha_\nu = -\alpha_\lambda - 2$ for $F(\lambda) \propto \lambda^{\alpha_\lambda}$), and v and b are the width and strength of Fe II templates. We used two Fe II templates from Vestergaard & Wilkes (2001) and Tsuzuki et al. (2006). Although the Fe II template from Vestergaard & Wilkes (2001) has been popularly used (e.g., Fine et al. 2008; Vestergaard & Osmer 2009; Shen et al. 2011), it contains no information of Fe II line undernearth the Mg II line, since it was directly made from the observed spectrum of the narrow line Seypert 1 galaxy, I Zwicky 1. In contrast, Tsuzuki et al. (2006) provides another template of the original I Zwicky 1 template adding with the Fe II emissions undernearth the Mg II line, which were calculated with the one-dimensional photoionzation model, CLOUDY (Ferland et al. 1998). We used both templates and compared the results. A scaled and broadened Fe II template was used for modeling the Fe II emissions with our spectra. In the case of the C IV emission line, only Vestergaard & Wilkes (2001) provide the Fe II template in this wavelength range. We modeled the two components simultaneously.

The quality of the continuum subtraction depends on the determination of the continuum fitting ranges. We selected narrow fitting windows which minimize the contributions by other emission components. In the case of ID0085 and ID0099, we used continuum windows of 1490$\mathring{A}$ – 1520$\mathring{A}$ and 1590$\mathring{A}$ – 1620$\mathring{A}$ for C IV , and 2500$\mathring{A}$ – 2750$\mathring{A}$ and 2850$\mathring{A}$ – 3090$\mathring{A}$ for Mg II after trying various fitting ranges. Since the

quality of ID0085 spectrum around the C IV emission line is not sufficiently good to constrain the Fe II emissions, we failed to find the Fe II component for the C IV emission line of ID0085. Since ID0106 shows significant broad absorptions blueward of the C IV and Mg II emission lines, we changed the fitting window ranges of the Mg II emission line as 2500$\mathring{A}$ – 2650$\mathring{A}$ and 2850$\mathring{A}$ – 3000$\mathring{A}$. For the C IV line of ID0106, we cannot set the continuum window at the blue side of ID0106 due to the significant broad absorption and, thus, we failed the continuum subtraction for the C IV line of ID0106.

Since most of the uncertainties in the continuum slope or the line width result from the fitting range of the continuum modeling, we varied the fitting ranges into 36 cases within the given wavelength windows and conducted model fitting for each different sub wavelength range to calculate the uncertainties. Since we cannot determine the continuum fitting range of C IV emission line of ID0106, we set the uncertainty of this line width as 5% of the line width instead of the uncertainty derived from the various continuum ranges, because, for other lines, the uncertainty of their line widths is 5% of their line widths.

6.3 Spectral Model for Emission Line Components

After subtracting the modeled continuum from each spectrum, we fitted C IV and Mg II emission lines. We used a single- and a double-Gaussian profiles considering presence of asymmetric profiles characterized by red or blue wings. For the fitting ranges, we set 1500$\mathring{A}$ – 1600$\mathring{A}$ for C IV lines of ID0085 and ID0099, and 2700$\mathring{A}$ – 2900$\mathring{A}$ for Mg II of ID0085 and ID0106. In the case of the C IV emission line of ID0106 which is affected by a broad absorption line, we set the fitting range to 1350$\mathring{A}$ – 1590$\mathring{A}$. The Mg II lines of ID0085 and ID0106 are well fitted by double-Gaussian profiles due to their asymmetric shapes, whereas the C IV lines can be fitted using a single-Gaussian profile. We did not model narrow emission line components of C IV

and Mg II if there is no significant feature (Park 2012).

To obtain the line width FWHM, the measured $\mathrm{FWHM_{obs}}$ was corrected for the instrumental resolution $\mathrm{FWHM_{ins}}$:

$$\mathrm{FWHM}= \sqrt{(\mathrm{FWHM_{obs}})^2 - (\mathrm{FWHM_{ins}})^2}.$$

The effects due to the instrumental resolution are less than 0.1% for these R = 3,600 spectra.

6.4 Spectral Modeling

We used an IDL procedure, `mpfit.pro` to find the best-fitted models to the observed spectra using the method of the χ^2 minimization for both continuum and emission line. We included the 1σ errors of the spectra for each fitting. From the best-fit model, we can obtain the best-fit estimates for each parameter such as a power-law slope and a line width. The uncertainties for each parameter were calculated with a method described below. The vast majority of the uncertainties come from uncertainties in the best fitting ranges of the continuum modeling. To calculate the uncertainty resulted from the different continuum fitting ranges, we compared best-fit parameters for each try described in Chap. 6.2 and we set the average and standard deviation of the values as the best-fit parameter and its error.

6.5 Results on the Continuum and Emission Lines Modeling

From Figures 6.1 to 6.5, the best-fit continuum and line models are shown for each emission line. In Table 6.1 we list the best-fit estimates of the power-law slopes ($\alpha_{\nu,\mathrm{CIV}}$ and $\alpha_{\nu,\mathrm{MgII}}$) and line widths ($\mathrm{FWHM_{CIV}}$ and $\mathrm{FWHM_{MgII}}$) parameters and their errors for each emission line.

In literature, the power-law slopes vary significantly between sources. For example, Davis et al. (2007) presents the distributions of $-1.5 < \alpha_\nu < 0.5$ for both case of 2200$\AA$ – 4000$\AA$ and 1450$\AA$ – 2200$\AA$ among quasars at $0.76 < z < 1.26$ and $1.67 < z < 2.07$, respectively. At high redshift, quasars at $4 < z < 6.5$ from De Rosa et al. (2011) show $-4 < \alpha_\nu < 0.7$, and quasars at $z > 6.5$ from De Rosa et al. (2014) show $-0.67 < \alpha_\nu < 0.56$. The slope coefficients from our results are in agreement with the literature.

The FWHMs for each emission line of our quasars show similar values to other quasars at high redshift. For example, De Rosa et al. (2014) reported that the $\mathrm{FWHM_{MgII}}$ of 4 quasars at $z > 6.5$ has a range of 3,000 km s^{-1} < $\mathrm{FWHM_{MgII}}$ < 5,000 km s^{-1}. Although De Rosa et al. (2011) present quasars of $\mathrm{FWHM_{MgII}}$ < 3,000 km s^{-1} among quasars at $4 < z < 6.5$, $\mathrm{FWHM_{MgII}}$ of ID0085 shows somewhat a small value comparing to the result from De Rosa et al. (2014). The Mg II emission lines of ID0085 and ID0106 show a double-Gaussian shape. ID0085 has a narrow emission line component with FWHM = 797±43 km s^{-1} (purple line at the last panel of Figure 6.2). Therefore the $\mathrm{FWHM_{MgII}}$ of ID0085 was calculated from the broad component. ID0106 also has a component with FWHM=818±56 km s^{-1}. However these two components are needed to fit the asymmetric shape of this emission line due to the broad absorption, thus, we do not consider this component as a narrow line component.

There is no significant difference in the derived power-law slope and line width parameters when using different Fe II templates (Vestergaard & Wilkes 2001; Tsuzuki et al. 2006).

6.6 UV Continuum Luminosity

The $\lambda L_\lambda(1350)$ and $\lambda L_\lambda(3000)$ were calculated from the optical or NIR spectra. For ID0085, we used the optical and NIR spectra for the $\lambda L_\lambda(1350)$ and $\lambda L_\lambda(3000)$,

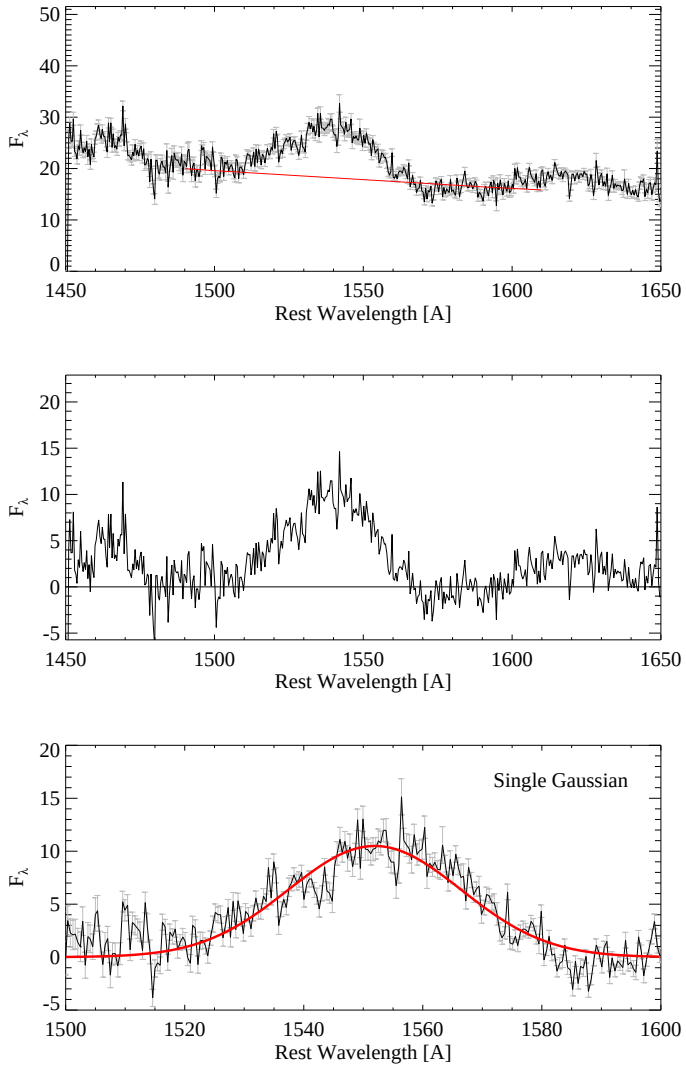

Figure 6.1 An example of continuum and emission line modeling for the C IV emission line of ID0085. Upper two panels show spectra before and after continuum subtraction. Since we cannot find a solution for the Fe II template fitting, only the power-law component is plotted (thin red line) The lower panel shows an example of the line modeling. A single-Gaussian function is suitable for the fitting.

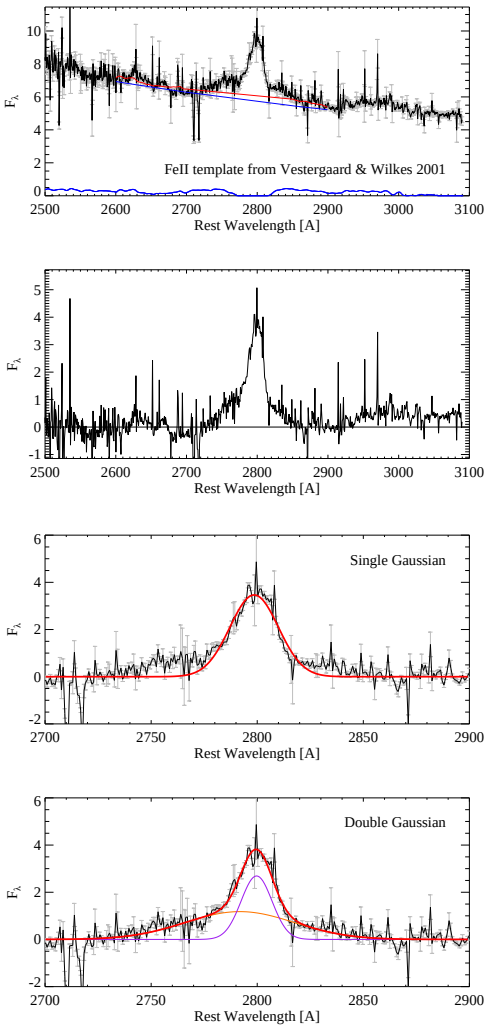

Figure 6.2 An example of continuum and emission line modeling for the Mg II emission line of ID0085. Upper two panels show spectra before and after continuum subtraction. The blue lines denote the best-fit Fe II template and the power-law component, and the thin red line is the composite spectrum for these two components. We used Fe II template from Vestergaard & Wilkes (2001) as an example. The two lower two panels show an example of the line modeling, both case of a single and double-Gaussian fitting. One of the double-Gaussian components is a narrow line (violet line) with FWHM = 797±43km s^{-1}.

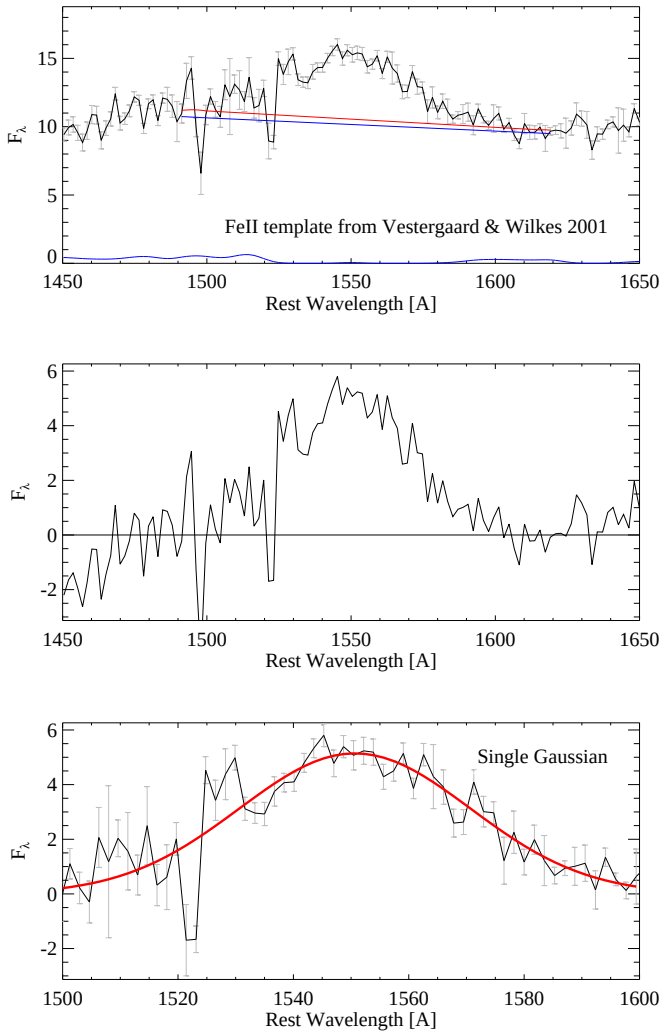

Figure 6.3 An example of continuum and emission line modeling for the C IV emission line of ID0099. Upper two panels show spectra before and after continuum subtraction. The blue lines denote the best-fit Fe II template and the power-law component, and the thin red line is the composite spectrum for these two components. We used Fe II template from Vestergaard & Wilkes (2001) as an example. The two lower panel shows an example of the line modeling. A single-Gaussian function is suitable for the fitting.

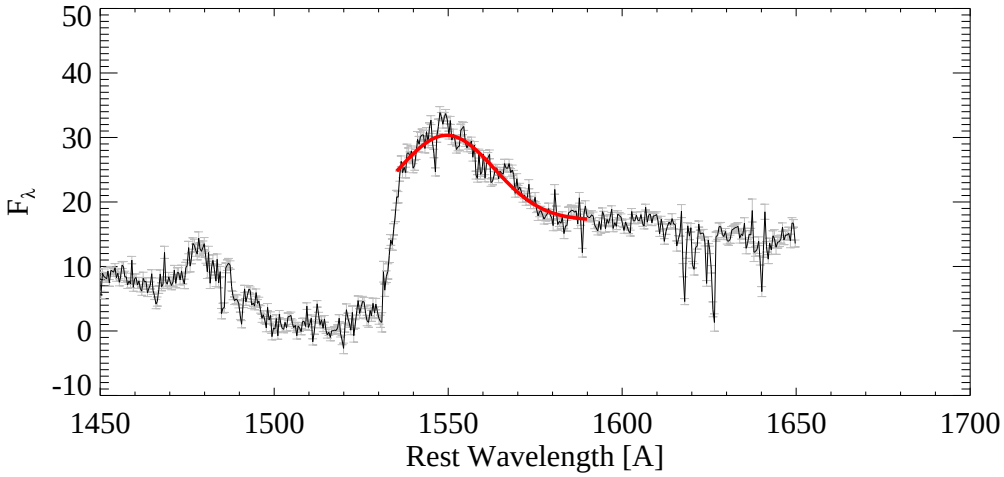

Figure 6.4 Emission line modeling for the C IV emission line of ID0106. Since we cannot find a solution for a continuum modeling, a single-Gaussian function is used for the emission line fitting with in a specific range of the spectrum.

respectively. The $\lambda L_\lambda(1350)$ of ID0099 and the $\lambda L_\lambda(3000)$ of ID0106 were estimated from their NIR spectra. In the case of the $\lambda L_\lambda(1350)$ of ID0106, the continuum near the 1350A shows deep drops in its optical spectrum. Therefore, we used a redshifted and flux-scaled spectrum from the SDSS composite spectrum from Vanden Berk et al. (2001) to the i-band magnitude of ID0106 and estimated the continuum flux from this redshifted and flux-scaled spectrum. The $\lambda L_\lambda(1350)$ and $\lambda L_\lambda(3000)$ were calculated from the average flux in the $1340\mathring{A}$ – $1360\mathring{A}$ and $2950\mathring{A}$ – $3050\mathring{A}$, respectively. The uncertainty in the continuum luminosity was estimated from the scatters on the continuum flux. The $\lambda L_\lambda(1350)$ and $\lambda L_\lambda(3000)$ are listed in Table 6.1.

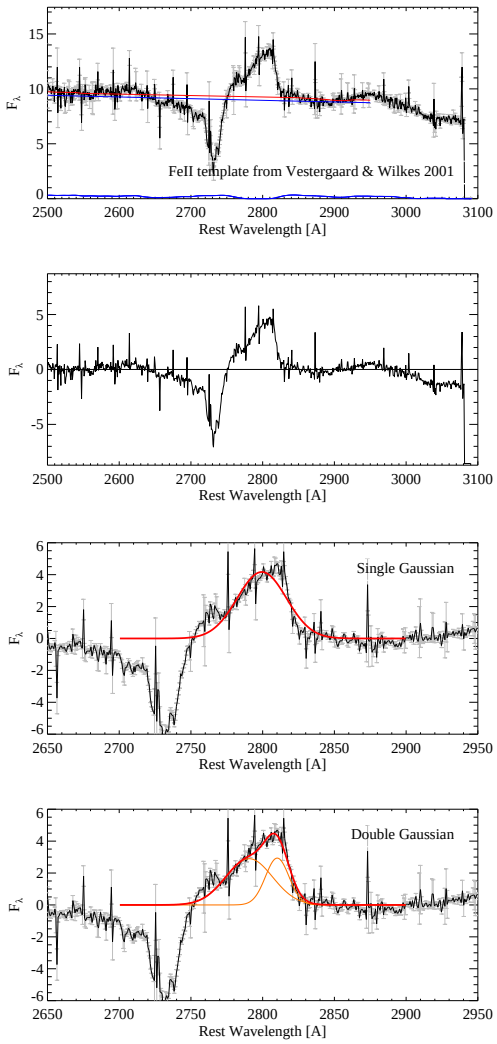

Figure 6.5 An example of continuum and emission line modeling for the Mg II emission line of ID0106. Upper two panels show spectra before and after continuum subtraction. The blue lines denote the best-fit Fe II template and the power-law component, and the thin red line is the composite spectrum for these two components. We used Fe II template from Vestergaard & Wilkes (2001) as an example. The two lower panel shows an example of the line modeling. Two Gaussian components are used to fit the line shape.

6.7 Black Hole Mass

In Table 6.2, we list the black hole mass estimates obtained from C IV and Mg II emission lines ($M_{\rm BH,CIV}$ and $M_{\rm BH,MgII}$), using equations of McLure & Jarvis (2004), Vestergaard & Peterson (2006), and Jun et al. (2015). The uncertainties of the masses propagate from the uncertainties of the FWHM and the continuum luminosity. Note that these uncertainties were underestimated due to the low S/N spectra. Figure 6.6 shows these masses with error bars for each object and estimator.

Comparing two mass estimators, $M_{\rm BH,CIV}$ and $M_{\rm BH,MgII}$, emission lines, for ID0085 and ID0106, the average value between different relations of $M_{\rm BH,CIV}$ is larger than those of $M_{\rm BH,MgII}$, 0.8 dex for ID0085 and 0.2 dex for ID0106. We note that $M_{\rm BH}$ values from C IV line have a large scatter with respect to $M_{\rm BH}$ from Mg II or Hβ/Hα (the intrinsic scatters of the $M_{\rm BH,CIV}$ from Jun et al. (2015) is 0.40 dex and the $M_{\rm BH,MgII}$ from Jun et al. (2015) is 0.09 dex), therefore the large discrepancy between $M_{\rm BH,CIV}$ and $M_{\rm BH,MgII}$ can be understood as a result of the large scatter in $M_{\rm BH,CIV}$ estimators. Hence, we take the Mg II based values to be more reliable.

Considering the black hole masses calculated from the two relations for each C IV and Mg II emission lines, the relations of Jun et al. (2015) lead higher values than that of McLure & Jarvis (2004) or Vestergaard & Peterson (2006). Comparing the intrinsic scatter in the relations to our derived uncertainties, where $\sim$0.1 dex for ID0085 and ID0099, the intrinsic scatter in the $M_{\rm BH,CIV}$ estimator (0.40 dex) is larger than the uncertainties we derived, and that in the $M_{\rm BH,MgII}$ estimator (0.09 dex) is comparable to our uncertainties. Therefore, we can see that the uncertainties we estimated are arisen from intrinsic scatter in the scaling relations.

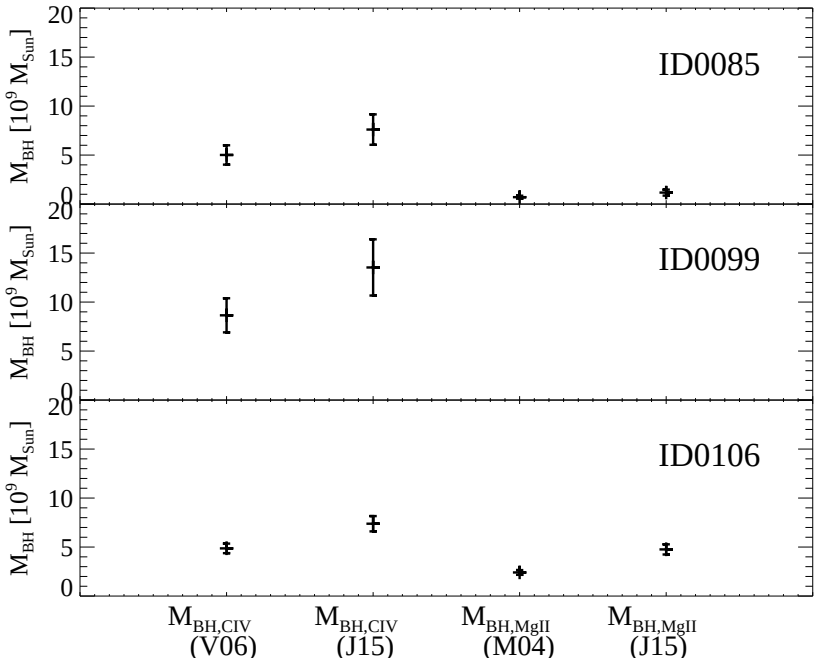

Figure 6.6 $M_{\rm BH}$ for the objects with error bars for each estimator.

6.8 Eddington Ratio

We computed the Eddington ratios using Eq. 1.7, 1.8, and 1.9. We computed $L_{\rm Bol}$ from $\lambda L_{\lambda}(1350)$ and $\lambda L_{\lambda}(3000)$, and $L_{\rm Edd}$ from $M_{\rm BH,CIV}$ and $M_{\rm BH,MgII}$. In Table 6.3, we list $L_{\rm Bol}$, $L_{\rm Edd}$, and $L_{\rm Bol}/L_{\rm Edd}$ for each case.

The $L_{\rm Bol}$ values that are calculated from $\lambda L_{\lambda}(1350)$ and $\lambda L_{\lambda}(3000)$ are not agreed for ID0106, although the error of the $L_{\rm Bol}(1350)$ of ID0085 is large. The $\lambda L_{\lambda}(1350)$ of ID0106 estimated from the redshifted and flux-scaled model spectrum provides crude continuum flux value because we assume that the genuine spectrum has a same spectral shape with the modeled spectrum. In the case of ID0085, because the C IV emission line is located at the observed wavelength $\sim 0.8\mu$m, where the sky emission lines are significant, the continuum flux measurement is affected by the imperfection of the sky subtraction. Therefore, the $L_{\rm Bol}(1350)$ has a larger uncertainty than the error of ID0106 estimated from the modeled spectrum. In the case of ID0099, $\lambda L_{\lambda}(1350)$ can be affected by the uncertain flux calibration from standard star observations for its NIR spectrum. Considering that the typical error in bolometric corrections is $\sim$0.1 dex, and slightly higher for the correction from $\lambda L_{\lambda}(1350)$, our estimated uncertainties (0.01 – 0.05 dex) is smaller than the intrinsic error from the bolometric correction, except ID0085 (which have 0.2 dex uncertainties based on $\lambda L_{\lambda}(1350)$). Therefore, we can see that the uncertainties we estimated are arisen from intrinsic scatter in the bolometric correction.

In Table 6.4, we find that the Eddington ratios from $M_{\rm BH,CIV}$ and $\lambda L_{\lambda}(1350)$ are smaller by a factor of a few than the Eddington ratios using $M_{\rm BH,MgII}$ and $\lambda L_{\lambda}(3000)$. The discrepancy is most likely caused by the difference in the derived $M_{\rm BH}$ values. As we mentioned earlier, C IV-based $M_{\rm BH}$ values are in general more uncertain than Mg II-based values, and therefore we consider that Mg II-based Eddington ratios to be more reliable.

Figure 6.7 shows $M_{\rm BH}$ as a function of the $L_{\rm Bol}$. To compare our sources with

low redshift quasars, we used a sample of SDSS quasars (Shen et al. 2011). Quasars with $M_{\rm BH,MgII}$ information were selected and they covers a redshift range of 0.35 $<$ z $<$ 2.25. These low redshift quasars are plotted with the gray points and black contours. As a sample of high redshift, we used quasars at z $\sim$ 5 (Trakhtenbrot et al. 2011, purple crosses), z $\sim$ 6 (Jiang et al. 2007; Kurk et al. 2007, 2009; Wu et al. 2015, green filled circles), and z $\sim$ 7 (De Rosa et al. 2014; Venemans et al. 2015, blue empty squares). All $M_{\rm BH}$ of these high redshift quasars were estimated using Mg II emission lines. The regions with constant Eddington ratio, $L_{\rm Bol}/L_{\rm Edd}$ = 0.01, 0.1, and 1, are plotted with black solid lines. Our sources are plotted with the red empty diamonds. Since only the C IV emission line is available for ID0099, we plotted the $M_{\rm BH}$ using $M_{\rm BH,MgII}$ for ID0085 and ID0106 and $M_{\rm BH,CIV}$ for ID0099 from the relations from Jun et al. (2015), and $L_{\rm Bol}(3000)$ for ID0085 and ID0106 and $L_{\rm Bol}(1350)$ for ID0099. We can see that the low redshift samples occupy different regions of the parameter space to the high redshift sample: the average Eddinton ratios of these high redshift quasars is significantly larger than the low redshift samples. The Eddignton ratio of our two quasars at z $\sim$ 5.5 is 0.91$\pm$0.61, near a value of 1, suggesting that these quasars are growing vigorously. The vigorous growth seems to continue till $z \sim 4$. We note that the Eddington ratio of ID0099, which is an exception, was estimated from $M_{\rm BH,CIV}$ and $L_{\rm Bol}(1350)$, which is less reliable than $M_{\rm BH,MgII}$ and $L_{\rm Bol}(3000)$, respectively.

6.9 Summary

We measured the physical properties of three IMS quasars at z $\sim$ 5, including α_ν, FWHM, and λL_λ, based on the optical and NIR spectra, via spectral modeling of continuum and emission lines. Then we estimated $M_{\rm BH}$ using the line width of broad emission lines such as C IV and/or Mg II, and the continuum luminosity at $\lambda = 1350\mathring{A}$ and/or $3000\mathring{A}$. The discrepancy of $M_{\rm BH}$ derived from different mass

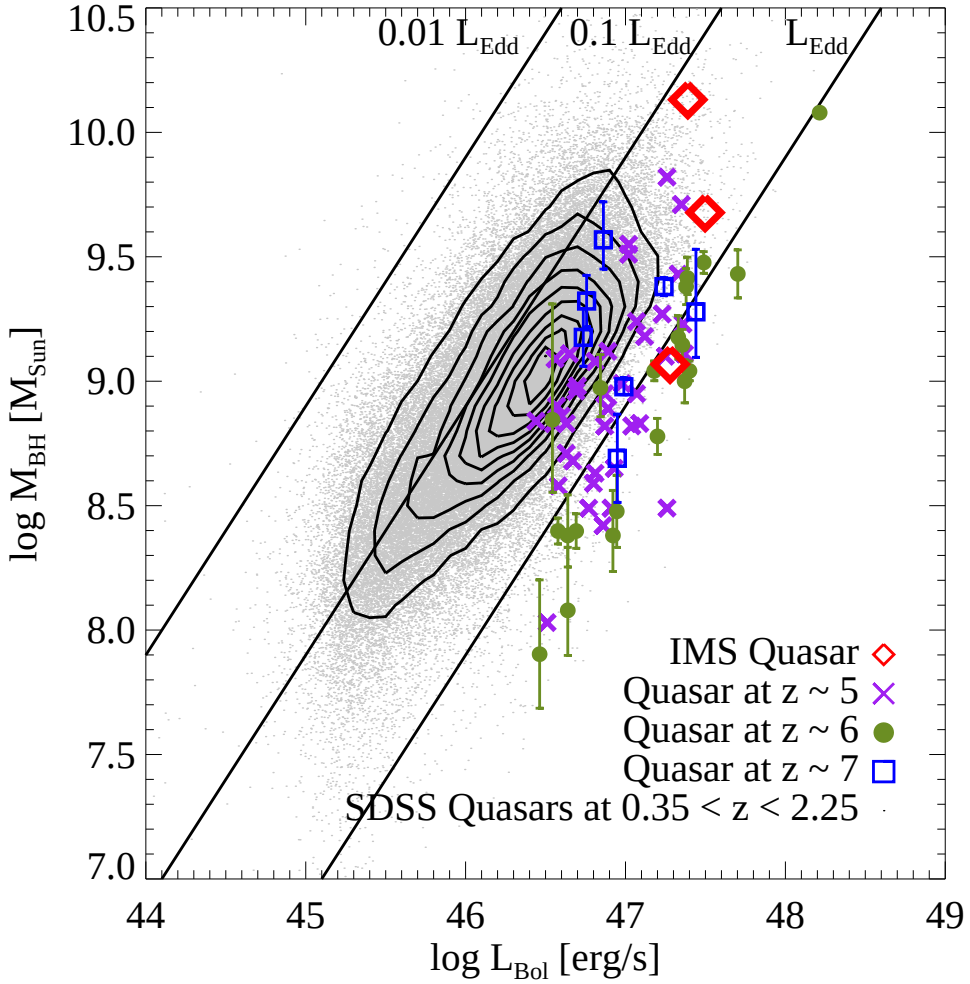

Figure 6.7 $M_{\rm BH}$ as a function of the $L_{\rm Bol}$. Red empty diamonds: our sources, purple crosses: quasars z $\sim$ 5 (Trakhtenbrot et al. 2011), green filled circles: quasars at z $\sim$ 6 (Jiang et al. 2007; Kurk et al. 2007, 2009; Wu et al. 2015), blue empty squares: quasars z $\sim$ 7 (De Rosa et al. 2014; Venemans et al. 2015), and gray points and black contours: a sample of SDSS quasars at $0.35 < z < 2.25$ (Shen et al. 2011) are plotted. The regions with constant Eddington ratio, $L_{\rm Bol}/L_{\rm Edd} = 0.01$, 0.1, and 1, are plotted with black solid lines.

Table 6.1. Power-law slopes, line widths, and continuum luminosities estimated from the NIR spectra

ID	$\alpha_{\nu,\mathrm{CIV}}$	$\alpha_{\nu,\mathrm{MgII}}$	$\mathrm{FWHM_{CIV}}$ (km s^{-1})	$\mathrm{FWHM_{MgII}}$ (km s^{-1})	$\lambda L_\lambda(1350)$ (10^{46} erg s^{-1})	$\lambda L_\lambda(3000)$ (10^{46} erg s^{-1})
ID0085	1.34 ± 0.60	-0.42 ± 0.78	6074 ± 304	2656 ± 277	6.93 ± 2.22	3.69 ± 0.35
ID0099	-0.71 ± 0.85	$\cdots$	8136 ± 802	$\cdots$	6.44 ± 0.48	$\cdots$
ID0106	$\cdots$	-1.57 ± 0.31	6243 ± 312	4205 ± 159	5.91 ± 0.08	6.11 ± 0.64

Table 6.2. Black hole masses estimated from the different mass estimators and relations

ID	$M_{\mathrm{BH,CIV}}$ V06[a] (10^9 $\mathrm{M_\odot}$)	$M_{\mathrm{BH,CIV}}$ J15[b] (10^9 $\mathrm{M_\odot}$)	$M_{\mathrm{BH,MgII}}$ M04[c] (10^9 $\mathrm{M_\odot}$)	$M_{\mathrm{BH,MgII}}$ J15[b] (10^9 $\mathrm{M_\odot}$)
ID0085	5.01±0.99	7.60± 1.55	0.70±0.15	1.17±0.31
ID0099	8.65±1.74	13.53±2.87	$\cdots$	$\cdots$
ID0106	4.86±0.49	7.38±0.78	2.41±0.24	4.76±0.52

[a]Relation from Vestergaard & Peterson (2006)

[b]Relation from Jun et al. (2015)

[c]Relation from McLure & Jarvis (2004)

Table 6.3. $L_{\rm Bol}$, $L_{\rm Edd}$, and $L_{\rm Bol}/L_{\rm Edd}$ estimated from the different mass estimators and relations

ID	$L_{\rm Bol}(1350)$ (10^{46} erg/s)	$L_{\rm Bol}(3000)$ (10^{46} erg/s)	$L_{\rm Edd}$(CIV, V06[a]) (10^{46} erg/s)	$L_{\rm Edd}$(CIV, J15[b]) (10^{46} erg/s)	$L_{\rm Edd}$(MgII, M04[c]) (10^{46} erg/s)	$L_{\rm Edd}$(MgII, J15[b]) (10^{46} erg/s)
ID0085	26.40± 8.45	18.99± 1.80	63.13±12.43	95.78±19.58	8.85± 1.92	14.74± 3.84
ID0099	24.54± 1.83	···	108.96±21.91	170.51±36.14	···	···
ID0106	22.50± 0.31	31.48± 3.30	61.28± 6.14	93.01± 9.83	30.33± 3.03	59.93± 6.53

[a]Relation from Vestergaard & Peterson (2006)

[b]Relation from Jun et al. (2015)

[c]Relation from McLure & Jarvis (2004)

Table 6.4. Eddington ratios estimated from the different mass estimators and relations

ID	Edd. ratio (1350, CIV, V06[a])	Edd. ratio (1350, CIV, J15[b])	Edd. ratio (3000, MgII, M04[c])	Edd. ratio (3000, MgII, J15[b])
ID0085	0.42±0.16	0.28±0.16	2.15±0.51	1.29±0.60
ID0099	0.23±0.05	0.14±0.05	···	···
ID0106	0.37±0.04	0.24±0.04	1.04±0.15	0.53±0.16

[a]Relation from Vestergaard & Peterson (2006)

[b]Relation from Jun et al. (2015)

[c]Relation from McLure & Jarvis (2004)

estimators and relations mainly results the intrinsic scatters of the relations. We computed $L_{\rm Bol}$, $L_{\rm Edd}$, and Eddington ratios from each emission line and continuum luminosity. These values do not agree with each other, which is caused by the the uncertainties of the bolometric correction and $M_{\rm BH}$ estimators. Since it is known that $M_{\rm BH,CIV}$ values are in general less accurate than $M_{\rm BH,MgII}$ values, we consider Mg II-based estimates to be more reliable. We compared Eddington ratios of our sources to those of low and high redshift quasars, and found that the Eddington ratio of our quasars at z $\sim$ 5 have values close to 1. These results, characterized by high luminosities ($M_{1450} < -27$ mag), black hole masses of $> 10^9\,{\rm M}_\odot$, and Eddington limit luminosities, support the hypothesis of the rapid growth of their black holes in the early universe.

Chapter 7

Discussion

7.1 Expected Quasar Number from Our Surveys

We calculated the expected number of quasars from our survey, using the luminosity function of z $\sim$ 6 quasars. The quasar luminosity function, $\Phi(M, z)$, is parameterized by a double power-law (e.g., Fan et al. 2001; Willott et al. 2010a):

$$\Phi(M, z) = \frac{10^{k(z-6)}\Phi(M^*,\, z=6)}{10^{0.4(\alpha+1)(M-M^*)} + 10^{0.4(\beta+1)(M-M^*)}}, \tag{7.1}$$

where α is the faint end slope, β the bright end slope, M the absolute magnitude, M^* the break magnitude, and $\Phi(M^*,\, z=6)$ the space density of quasars at $z=6$ with a magnitude M^*. Willott et al. (2010a) derived the best-fit parameters of this luminosity function using a sample of 40 quasars at z $\sim$ 6: $\Phi(M^*_{1450}) = 1.14 \times 10^{-8}\,\mathrm{Mpc}^{-3}\,\mathrm{mag}^{-1}$, $M^*_{1450} = -25.13$ and $\beta = -2.81$, fixing the faint end slope to $\alpha = -1.5$, based on the quasar luminosity function at low redshift (e.g., Croom et al. 2004).

The 10^{kz} factor accounts for the decline in number density. We adopted two values of k, from Willott et al. (2010a) ($k = -0.47$) and from McGreer et al. (2013) ($k = -0.71$). Willott et al. (2010a) reported $k = -0.47$ from quasars at z $\sim$ 6 by

comparison with the luminosity function of quasars at $3 < z < 6$, whereas McGreer et al. (2013) derived a steeper decline ($k = -0.71$) in the number density evolution with $M_{1450} < -25.5$ for quasars at $4.9 < z < 6$. Venemans et al. (2013) reported that their best-fit k values with the 1σ confidence interval is $k = -0.49^{+0.28}_{-0.74}$, using 3 quasars at $z > 6.5$ from their discovery from the VIKING survey. Although this k is close to the $k = -0.47$ from Willott et al. (2010a), $k = -0.71$ from McGreer et al. (2013) is still within the range of k from Venemans et al. (2013).

Assuming that the quasar luminosity function evolves with constant parameters, with the redshift evolution only considered by the 10^{kz} factor, we extrapolated the luminosity function of $z \sim 6$ to $z \sim 5$ and $z \sim 7$, and derived the expected number of quasars from our survey. For example, we expect 0.0072 quasars per deg^2 for $k = -0.47$ down to $M_{1450} = -27.0$ at $4.60 < z < 5.40$ and 0.0139 quasars per deg^2 for $k = -0.71$.

Table 7.1 shows our quasar selection with different color cuts (column 1), survey area (column 2), redshift range (column 3) for each completeness cut (column 4), and M_{1450} limit with completeness $> 50\%$ (column 5). Figure 7.1 shows luminosity functions of quasars at $z = 5$, 6, and 7 using the best-fit parameters from Willott et al. (2010a), for both cases of $k = -0.47$ (red solid line) and -0.71 (blue solid line). For the uncertainties of these luminosity functions, we considered the uncertainties caused by M^*_{1450} and β from Willott et al. (2010a), using their χ^2 confidence region at 1σ confidence level. The values and uncertainties of the two parameters are $M^*_{1450} = -25.13 \pm 0.8$ and $\beta = -2.81 \pm 0.3$. The 1σ confidence level of Φ by these uncertainties are plotted with the red and blue dashed lines for $k = -0.47$ and $k = -0.71$, respectively. The ranges of M_{1450} from our survey are denoted with shaded regions for each luminosity function. We also plotted the number of quasars per deg^2 as a function of M_{1450} in five redshift ranges in column 3 of Table 7.1 with our survey limits of M_{1450} in Figure 7.2.

The ranges of expected number of quasars for each quasar selection are listed in columns 6 and 7 in Table 7.1 considering their 1σ uncertainties, for the case of $k = -0.47$ and $k = -0.71$, respectively. We only considered the completeness from our color cuts, and assumed that the efficiency of each selection in its redshift range (column 3) and the M_{1450} limit (column 5) is 100%, except the z $\sim$ 7 quasar selection using IR bands, which has 60% completeness.

Our quasar survey discovered 30 quasars including 6 new quasars at $4.7 <$ z < 5.4, and 9 quasars including 2 new quasars at $5.9 <$ z < 6.1. These number satisfy the luminosity functions for each redshift range. However we cannot find any quasar using the $Is - Iz - J$ color-color diagram. Our reasoning for this is illustrated in Chap. 3.8.2 and 3.8.3.

Figure 7.3 shows an evolution of quasar number density per Gpc^3 as a function of redshift. This number density is calculated for a survey depth of $M_{1450} < -27.0$ and $M_{1450} < -24.0$ in (a) and (b), respectively, corresponding to our quasar selection at z $\sim$ 5 and 7 (Table 7.1). The vertical purple bar indicates the number density at z = 6 with the 1σ uncertainty based on the luminosity function from Willott et al. (2010a). Then, we plotted the evolution of the quasar number density for both $k = -0.47$ and $k = -0.71$ to z $\sim$5 (Figure 7.3 (a)) and 7 (Figure 7.3 (b)). In (a), the evolution of the number density from z = 6 to the two redshift ranges in Table 7.1, for the two selection methods of z $\sim$ 5 quasars, are plotted. The vertical red bar at z = 5.0 with the red error bar is the number density of quasars at $4.60 <$ z < 5.40 which can be selected from the $r - i - z - J - K$ and $r - Is - Iz$ selection method when we assume $k = -0.47$, and the vertical blue bar at z = 5.0 with the blue error bar is for $k = -0.71$. Comparing the number density of the two colored bars to the purple bar at z = 6, the blue bar (corresponding to $k = -0.71$) shows a steeper decline toward higher redshift. The numbers of quasars at $5.55 <$ z < 6.05 corresponding to the selection using $r - i - z - J - K$ and $Is - Iz - J$ are

also plotted at z = 5.8 for both each k values. On the other hands, Figure 7.3 (b) shows number density evolution with a survey depth of $M_{1450} < -24.0$, from z $\sim$ 6 to z $\sim$ 7. Similar to (a), we plotted the purple bar at z = 6 and two number density at the range of 6.60 < z < 8.90 and 6.55 < z < 7.45, corresponding to the $z - J - Ch1 - Ch2$ selection and $z - Y - J$ selection, respectively, estimated from the luminosity function of z = 6 for each k value.

We plotted quasar number densities estimated from our discovery, considering the completeness of each survey. The quasar number selected from the survey for 4.60 < z < 5.40 is 30 including our newly discovered 6 quasars. We plotted these number density at z = 5.0 with the black circle. The error bar along the y-axis of this value was calculated assuming Poisson errors. Since we could not find any quasars at 5.55 < z < 6.05, 6.60 < z < 8.90, and 6.55 < z < 7.45 from our data set, we plotted the upper limits of the number density for each redshift range. We estimate the k value comparing the number density from our sources at 4.60 < z < 5.40 to the number density at z = 6, and found that $k = -0.54^{+0.20}_{-0.23}$. We can see that the number density estimated from our sources at z = 5 shows gradual slope, close to the $k = -0.47$. However, $k = -0.71$ is still well within the range of our k uncertainty. The upper limit at z = 5.8 shows a low value comparing to the number density calculated from these three k values, indicating the low selection efficiency when we use $r - i - z - J - K$ and $Is - Iz - J$ colors. In (b), the upper limit of our number density at z = 7 shows a low number density comparing to the expected values from the luminosity function. Therefore we conclude that the quasar number density at z $\sim$ 7 declines toward higher redshift, steeper than the expected k values from Willott et al. (2010a) and McGreer et al. (2013). To summarize, quasar number density evolutions estimated from our surveys shows a gradual slope similar to literature from z = 5 to 6, and a steeper slope that literature from z = 6 to 7.

Table 7.1. Summary of our Survey

Selection Method (col. 1)		Area [deg^2] (col. 2)	Redshift Range (col. 3)	Efficiency [%] (col. 4)	M_{1450} Limit (col. 5)	Expected Number (col. 6)[a]	(col. 7)[b]	Selected Number
z $\sim$ 5	$r - Is - Iz$	3,400	4.60 – 5.40	> 80	-27.0	6.5 – 92.1	12.6 – 178.5	30
	$Is - Iz - J$	3,400	5.55 – 6.05	> 80	-27.0	1.5 – 21.0	1.7 – 24.5	0
z $\sim$ 6		3,400	5.85 – 6.30[c]	> 80[c]	-26.0[c]	5.6 – 50.4	5.6 – 50.2	9
z $\sim$ 7	IR bands	28.4	6.60 – 8.90[c]	> 60[c]	-24.0[c]	0.7 – 2.2	0.5 – 1.5	0
	Y-band	78.3	6.55 – 7.45[c]	> 80[c]	-24.0[c]	1.9 – 5.8	1.2 – 3.8	0

[a] For $k = -0.47$

[b] For $k = -0.71$

[c] When we use the large selection boxes for each seletion method.

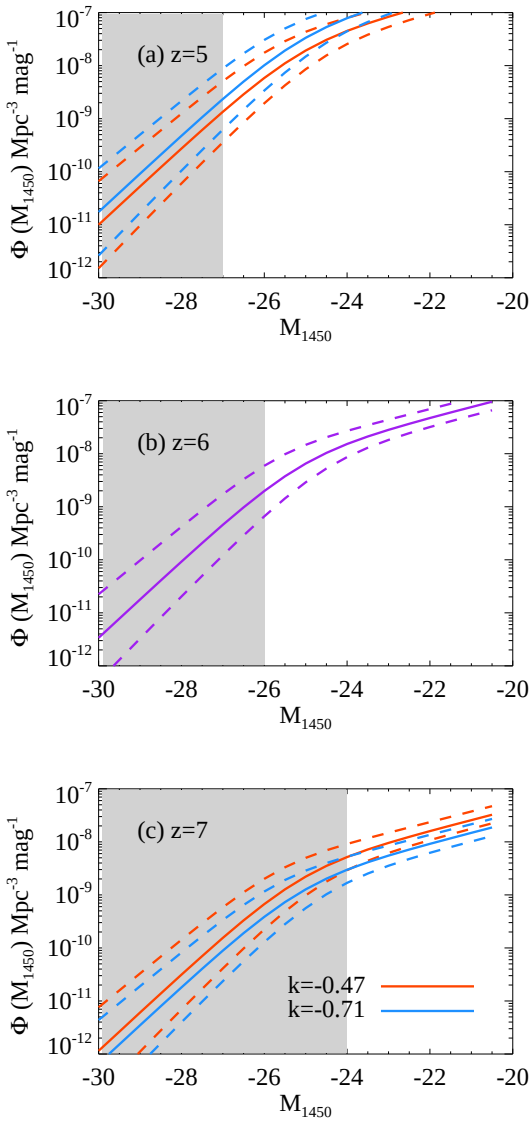

Figure 7.1 Luminosity functions of quasars at z = 5, 6, and 7 using the best-fit parameters from Willott et al. (2010a), for both case of $k = -0.47$ (red solid line) and -0.71 (blue solid line). The 1σ confidence level of Φ are plotted with the red and blue dashed lines for each k value. The coverages from our surveys are denoted with shaded regions for each luminosity function.

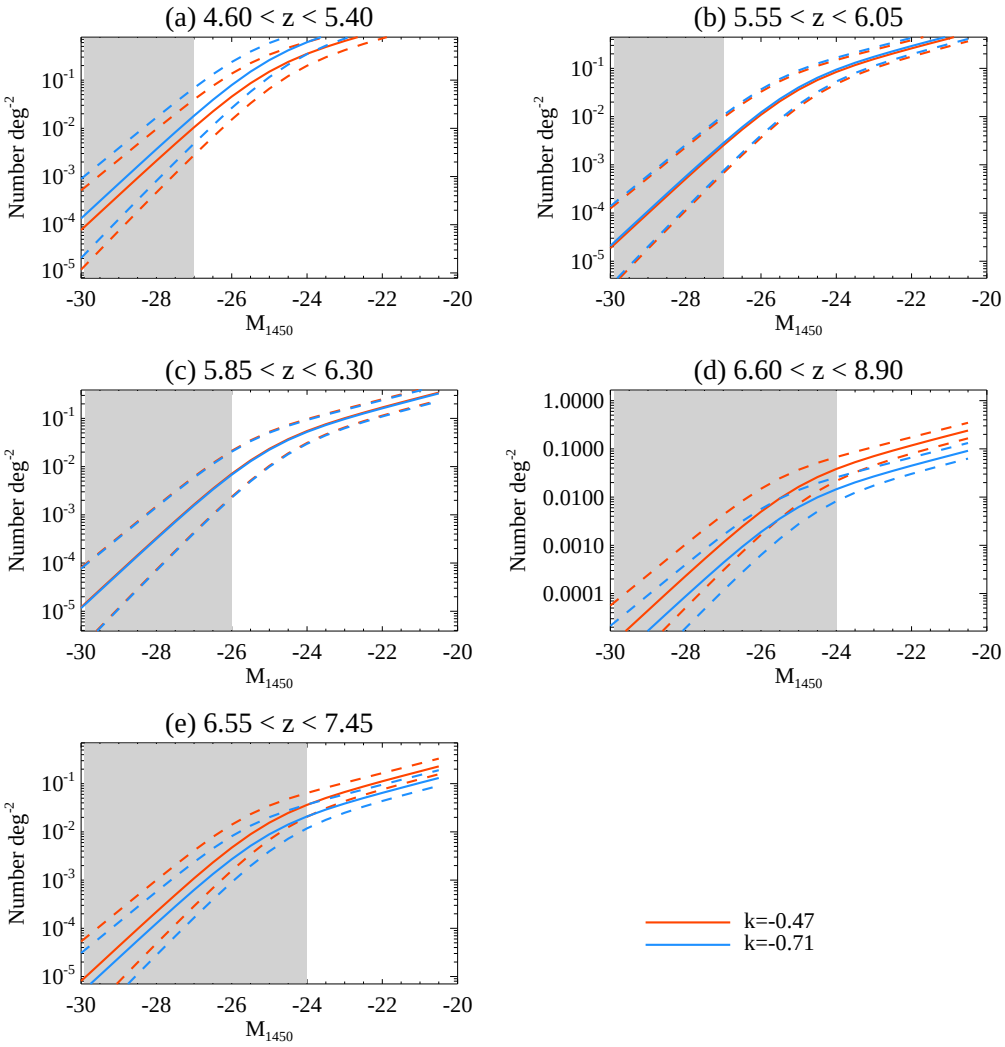

Figure 7.2 Plots similar to Figure 7.1. We plotted the number of quasars per deg^2 as a function of M_{1450} in five redshift ranges with our survey limits of M_{1450}.

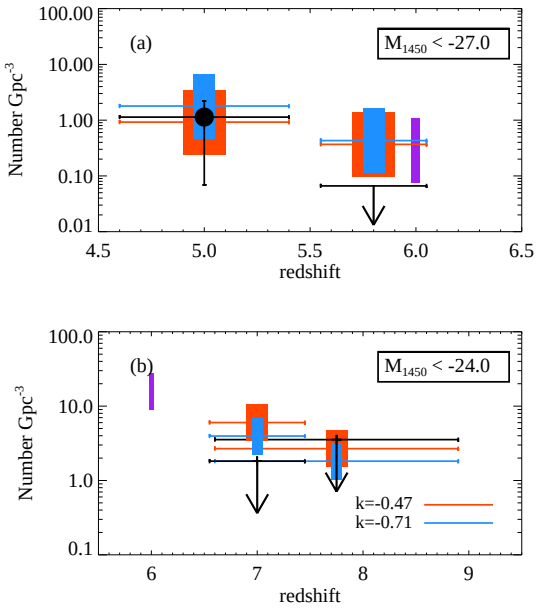

Figure 7.3 Evolution of quasar number density per Gpc^3 as a function of redshift for each our quasar selection. The vertical purple bar indicates the number density at z = 6 considering the 1σ uncertainty based on the luminosity function from Willott et al. (2010a), with a survey depth of $M_{1450} < -27.0$ and $M_{1450} < -24.0$ in (a) and (b), respectively. We plotted evolution of quasar number density for both $k = -4.7$ (red vertical bar) and $k = -0.71$ (blue vertical bar), at the lower or higher redshift comparing to the number density at z = 6. The number density of quasars corresponding to $4.60 < z < 5.40$ and $5.55 < z < 6.05$ are plotted in (a), at z = 5.0 and z = 5.8, respectively. (b) is a similar plot to (a), but it shows number density evolution with $M_{1450} < -24.0$, from $z \sim 6$ to $z \sim 7$. We plotted the purple bar at z = 6 and two number density at the range of $6.60 < z < 8.90$ and $6.55 < z < 7.45$. We plotted the quasar number density selected from our data set at z = 5.0 with the black circle. The error bar along the y-axis of this value was calculated assuming Poison error. Also the upper limit at $5.55 < z < 6.05$, $6.60 < z < 8.90$, and $6.55 < z < 7.45$ are plotted.

7.2 Quasar Number Density Evolution and Black Hole Accretion Activities

To justify our steeper evolution from z = 7 to 6, we compared quasar number density and the black hole accretion activities. Due to accretion activities of black holes, masses of SMBHs evolve with time, and therefore, their Eddington luminosities evolve. Then, for a fixed Eddington ratio, the bolometric luminosities also evolve with time. Assuming a set of SMBHs with a specific luminosity function, the evolution of their luminosities leads to the evolution of the luminosity function. Therefore, the evolution of quasar number densities can be explained in terms of the black hole accretion activities.

The mass growth of black holes with time can be expressed with Eq. 1.1. Using a typical value of $\epsilon = 0.1$, we estimated the mass growth of SMBHs with different Eddington ratios and converted the mass evolution to the number density evolution. Figure 7.4 shows the number density evolution when the Eddington ratio is 1.0 (dotted line) and 0.1 (dashed line). We assumed evolutions to a specific luminosity function at z = 6. Two cases of the different k values from literature are also plotted with red ($k = -0.47$) and blue ($k = -0.71$) solid lines. The evolution estimated from our survey is denoted with a black solid line and an arrow. The two case from literature correspond to the Eddington ratio of 0.3, and our evolution is for the Eddington ratio greater than 0.6. As we can see in Chap. 6.8, quasars at high redshift show drastic mass growth with Eddington limited accretion. Therefore our steeper evolution in the quasar number density is a possible result if we consider the Eddington limited growth, rather than the gradual evolutions from literature.

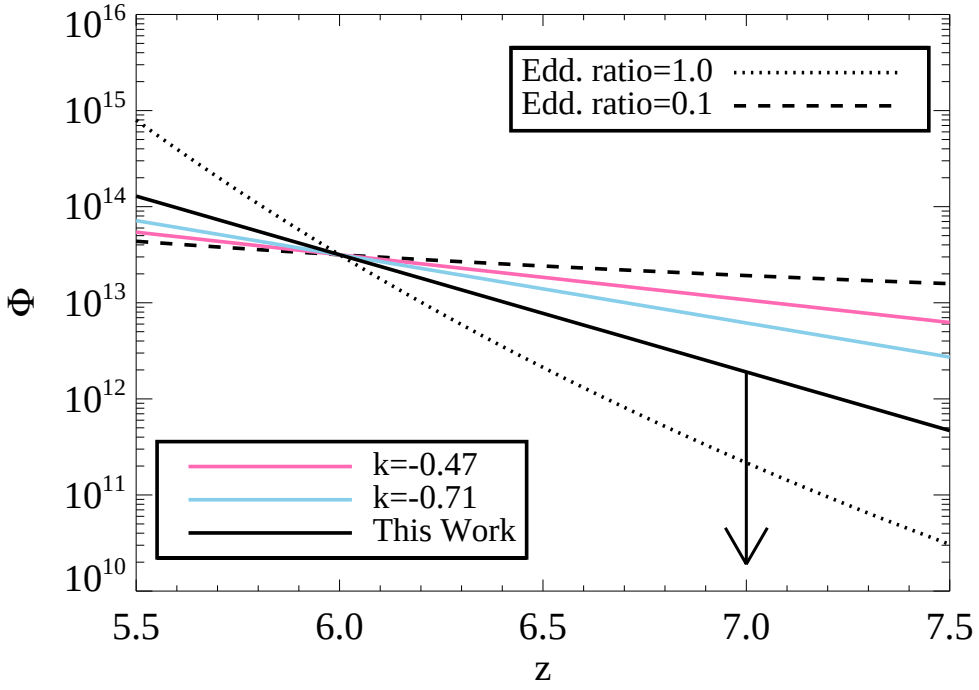

Figure 7.4 Quasar number density evolution as a function of redshift. The black dotted and dashed lines denote evolution when we assume the Eddington ratios 1.0 and 0.1, respectively. Two evolutions with different k values from literature are plotted with red and blue solid lines. We plot our work with the black solid line and arrow. The y-axis is arbitrary numbers.

7.3 Search for Quasars using Other Datasets

7.3.1 Selection of Quasars at z $\sim$ 6 with IMS and UKIDSS DXS

IMS provides J-band data with a depth of J = 22.9 AB. Including UKIDSS DXS with a depth of $21.8 < J$ [AB] < 23.3, we can select quasars at z $\sim$ 6 using 2.5 mag deeper than the UKIDSS LAS data. Table 7.2 summarizes the IMS and DXS fields, which are available for quasar selection at $\sim$ 6. These fields are covered by deep i and z-band data, provided from CFHTLS (depths of i = 24.8 AB and z = 23.9 AB). Because other 3 IMS fields, Lockman Hole, ELAIS-N1, and ELAIS-N2 do not have CFHT MegaCam i-band data, they were excluded from the list. Considering the survey area, we estimated the expected number of quasars using these data.

First, we constructed the completeness distribution from the $i - z - J$ color selection (Figure 3.5 (a)), as a function of redshift and M_{1450} in Figure 7.5. We adopted same method described in Chap. 3.8.1 to estimate the completeness. Considering the survey depth, J = 22.7 AB, which is the average depth between IMS and DXS, we can see that this selection covers a redshift range of $5.85 <$ z < 6.30 with $M_{1450} < -24.0$. In this case, the expected number of quasars is 3.1 – 9.7 for IMS area and 0.5 – 1.5 for DXS area, adopting the luminosity function from Willott et al. (2010a). These quasars can be used to construct the faint end slope of luminosity function of z = 6 quasars at $M_{1450} < -24$, where the uncertainty of the the luminosity function is relatively larger than that of the bright end slope.

7.3.2 Selection of Quasars at z $\sim$ 6 with the *AKARI* NEP-Wide Survey

The *AKARI* space telescope had performed a deep near and mid-infrared imaging survey in the North Ecliptic Pole (NEP) region (e.g., Matsuhara et al. 2006; Lee et al. 2009), covering 5.4 deg^2, so called *AKARI* NEP-Wide survey. For this field,

Table 7.2. IMS and UKIDSS DXS fields available for quasar selection at z $\sim$ 6

Field	RA / Dec	Opical Data	J-band Area [deg^2]	
			IMS	UKIDSS DXS
XMM-LSS	02 : 18 : 00 − 07 : 00 : 00	CFHTLS-W1	6.8	5.3
CFHTLS-W2	08 : 57 : 49 − 03 : 19 : 00	CFHTLS-W2	25.0	···
EGS	14 : 17 : 54 + 54 : 30 : 31	CFHTLS-W3	47.0	···
SA22	22 : 13 : 18 + 01 : 19 : 00	CFHTLS-W4	15.8	9.0
	Total Area		94.5	14.3
	Expected Number		3.1 – 9.7	0.5 – 1.5

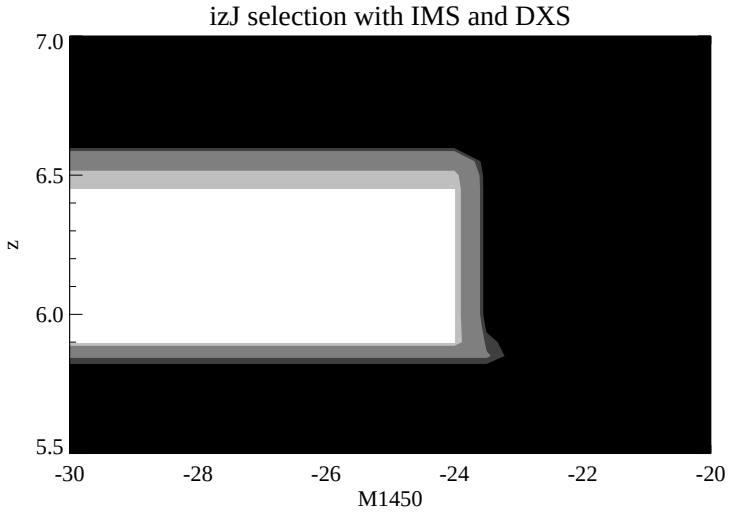

Figure 7.5 Completeness from the $i - z - J$ color selection as a function of redshift and M_{1450} using the IMS and UKIDSS DXS data.

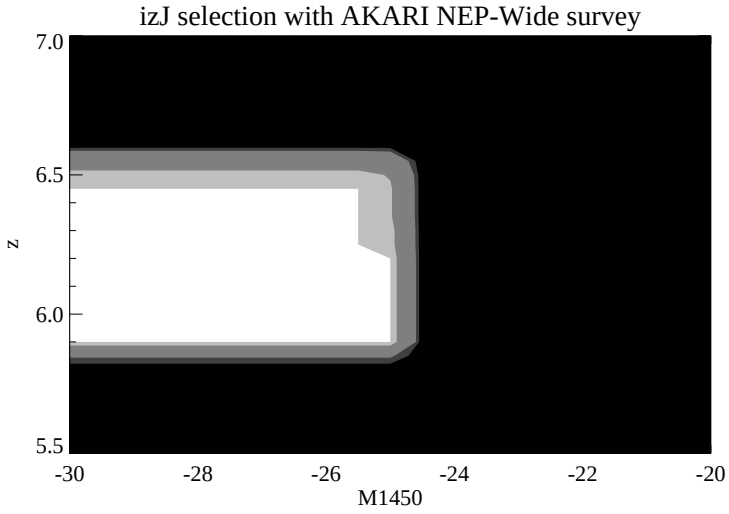

Figure 7.6 Completeness from the $i - z - J$ color selection as a function of redshift and M_{1450} using the *AKARI* NEP-Wide survey data.

a considerable amount of ground-based ancillary datasets have been obtained. For optical counterpart of *AKARI* IR data, Hwang et al. (2007) observed 2 deg^2 of the central region of the NEP-Wide field with CFHT MegeCam *ugriz* filters, with depth of $i = 24.6$ and $z = 23.7$ AB. In NIR wavelengths, Jeon et al. (2014, Appendix B) obtained J and H-band data using KPNO 2-m telescope and FLAMINGOS with a depth of $J = 21.6$ AB, covering the whole NEP-Wide area.

Combining these optical and NIR data, we calculated the expected number of quasars at z $\sim$ 6 among the 2 deg^2 area, using the method similar to Chap. 7.3.1. We note that the depths of optical i and z-bands are deep enough to select i-dropout objects compared to the J-band depth. From the completeness in Figure 7.6, this survey with $J = 21.6$ AB depth covers $M_{1450} < -24.5$ with a redshift range of $5.85 < z < 6.30$. From the luminosity function at z $\sim$ 6 (Willott et al. 2010a), the expected number of quasars at z $\sim$ 6 in 2 deg^2 is only 0.03 – 0.13. Although this NEP-Wide field have relatively deep J-band data, quasar survey for z $\sim$ 6 is

impossible due to its small area coverage. Another optical imaging (Jeon et al. 2010, Appendix A) from Maidanak 1.5-m telescope and SNUCAM cover the outside of the CFHT MegaCam data, expanding the optical counterpart data coverage to 4.9 $\deg^2$. However they only provide BRI band data, which is not suitable for the quasar selection at z $\sim$ 6. Although the Hyper SuprimeCam are conducting imaging survey with $grizy$ bands (Goto & the AKARI NEP team 2015), the survey area is still limited to 5.1 $\deg^2$, where the J-band data exist. In this case, the expected number of quasars is 0.09 – 0.35.

Chapter 8

New Selection Strategy Using Medium-Band Observation

8.1 Introduction

As explained in Chap. 3.1, there exist redshift gaps at $4.8 < z < 5.7$. Although many quasar surveys (e.g., Zheng et al. 2000; Sharp et al. 2001; Schneider et al. 2001; Fan et al. 2003, 2006a; Mahabal et al. 2005; Cool et al. 2006; Willott et al. 2007, 2010a; Jiang et al. 2008, 2009, 2015; Wu & Jia 2010; Matute et al. 2013; McGreer et al. 2013) were performed at $z \sim 5$ or $z \sim 6$, their discovered quasars are limited to $z < 4.7$ or $z > 5.7$ due to limitations of current filter systems employed by these surveys.

To discover quasars at $5 \leq z \leq 6$, in Chap. 3, we planned a survey using Camera for QUasars in EArly uNniverse (CQUEAN; Park et al. 2012), with custom-designed Is and Iz filters that compensate the previous filter systems. Since the central wavelengths of these filters are located between r and i, and between i and z, respectively, it was expected that these filters will be effective to select high redshift quasars at $5 \leq z \leq 6$, where SDSS or other filter sets cannot explore. The quasar

candidates were selected from r-dropout objects of $z < 19.5$ mag over 3,400 deg^2 using multi-wavelength data such as SDSS, the United Kingdom Infrared Telescope Infrared Deep Sky Survey (UKIDSS) Large Area Survey (LAS; Lawrence et al. 2007), and the Two Micron All Sky Survey (2MASS). About 3,500 r-dropouts have the Is/Iz imaging follow-up observations that are on-going (Chap. 3.3). Also we included the photometry from the Wide-Field Infrared Survey Explorer (*WISE*), and found bright candidates in the $W1$ band. So far, 6 r-dropouts, and 2 i-dropouts that were found using different color cuts, were confirmed as quasars with our optical spectroscopic observations; these are referred to as Infrared Medium-deep Survey (IMS) quasars.

However only two targets were discovered after the selection from the Is/Iz photometry; the other 4 targets among the 6 r-dropouts were discovered before the Is/Iz follow-up observations using *WISE* photometry. The expected number of quasars at $5 \leq \mathrm{z} \leq 6$ is about 30 calculated from the luminosity function of Willott et al. (2010a) for the limiting magnitude of $z < 19.5$ mag over 3,400 deg^2 (Chap. 7.1). The first reason of the low efficiency is that the adopted color cuts cannot remove contaminants such as late type stars or dwarf stars well enough. We adopted $r - i$ and $z - J$ color cut to remove these contaminants. Although the dwarf stars can be rejected relatively efficiently using these color cuts (color differences between the dwarf stars and the selection box are $\geq$ 1 mag), the late type stars still prevail (even with an additional $J - K$ cut) because the color differences between the late type stars and the selection box are too small (barely few tenths of a magnitude). As a result (which can also be seen in Richards et al. (2002); Ikeda et al. (2012); Wu & Jia (2010); McGreer et al. (2013) and McGreer et al. (2013)), the SDSS and UKIDSS LAS are incapable of selecting quasars at $5 \leq \mathrm{z} \leq 6$ efficiently. The second reason is due to the variability of quasars. Since the $r - Is$ or $Is - Iz$ selection boxes are too close to other contaminants (e.g. late type/dwarf stars), the quasars,

whose variability can be observed as high as 0.1 mag MacLeod et al. (2012), can be classified as stars, or their low priorities make that they cannot have a chance for the spectroscopic observations. Therefore, we need a new filter system, or a new technique, for the quasar selection.

Matute et al. (2013) adopted an SED fitting method and discovered a faint quasar at z = 5.41 from Advance Large Homogeneous Area Medium Band Redshift Astronomical (ALHAMBRA; Moles et al. 2008) survey over $\sim$1 deg^2. Their survey included a filter sets composed of 20 optical medium-band and 3 broad-band $J/H/Ks$ near infrared (NIR) filters, and an extensive library of SEDs including those of active galaxies. Despite the high redshift quasars contaminated by many low redshift galaxies and late type stars, they were able to select the quasar at z = 5.41 via SED fitting. If we adopt photometry from current large area surveys to increase the survey area, and conduct additional photometry with medium-bands, more quasars can be discovered with higher efficiency.

As an attempt to improve the selection of high redshift quasars, we devised a set of 9 medium-band filters to better trace the SED shapes of various sources and installed these filters to SED camera for QUasars in EArly uNiverse (SQUEAN) on the 2.1 m Otto Struve Telescope at the McDonald Observatory. We explored the potential of selecting high redshift quasars using our medium-band filters. Its results are based on the SQUEAN observational data we took in November 2014 and February 2015. Section 2 describes the overview of our new medium-band filters and two test observations. In Section 3, we describe the performance from the result of medium-band photometry, and in Section 4, we discuss an observational strategy for 2-m class telescopes with these medium-band filters. We summarize our results in the final section. Throughout this paper, we use a cosmology with $\Omega_M = 0.3, \Omega_\Lambda = 0.7$, and $H_0 = 70$ km s^{-1}Mpc^{-1}. We use the AB magnitude system.

8.2 Observations

8.2.1 SQUEAN Medium-band Filters

SQUEAN medium-band filters consist of nine filters, $m625$, $m675$, $m725$, $m775$, $m825$, $m875$, $m925$, $m975$, and $m1025$. With central wavelength from 625 to 1025nm, their bandwidths are 50nm. In addition, SQUEAN has a $m925n$ filter, whose bandwidth is 25nm and has the same central wavelength as $m925$. The response curves are similar to a top-hat filter function. Compared to SDSS r/i and Large Synoptic Survey Telescope (LSST) z/Y bands which has been used in CQUEAN, these filters are finer than r/i by a factor of three, and than z/Y by a factor of two. Figure 8.1 shows filter transmission curves of the medium-band filters (thin solid lines) and other SQUEAN filters (dashed lines) with the detector quantum efficiency (QE; thick solid line) taken into account. The medium-band filters were first installed in November 2014 to SQUEAN on the 2.1m telescope at McDonald Observatory and the first test observation was conducted to characterize the performance of medium-band filters.

8.2.2 Quasar and Dwarf Star Samples

We used IMS quasars to test the medium-band filters. IMS quasars were selected from r-dropout objects using multi-wavelength data such as SDSS, UKIDSS LAS, 2MASS, and *WISE*, and were confirmed as quasars with the optical spectroscopic observations. The redshifts of the targets were estimated from the redshifted Lyman α (Lyα) emission lines, and their errors were calculated considering the resolutions of each spectroscopic instrument. In the case of ID0176, Jiang et al. (2015) discovered it independently and provided a more accurate redshift. We use the redshift from Jiang et al. (2015) in this paper. For comparison, we observed 5 dwarf stars that were spectroscopically identified from Chap. 3. The z-band magnitudes of these

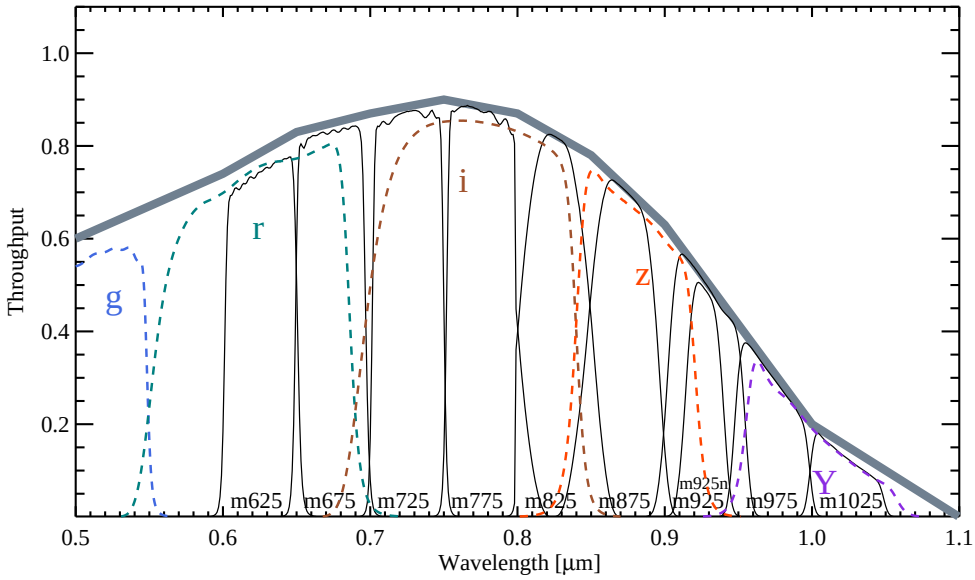

Figure 8.1 The QE of the camera (thick solid line) and the combined response function of the detector QE and filters. The thin solid lines are for our medium-band filters and the dashed lines are for the CQUEAN $g/r/i/z/Y$. The filter names of medium-bands indicate at the position of the central wavelengths.

targets and the spectroscopic redshifts (z_{spec}) of the quasars are listed in Table 8.1.

8.2.3 SQUEAN Medium-band Observations and Data Reduction

Following the first observation in November 2014, we carried out the second test observation in February 2015. During the two observations, we observed 6 quasars and 5 dwarf stars (Table 8.1) with 5 filters; $m675$, $m725$, $m775$, $m825$ and $m875$. The observations were carried out under mostly clear sky conditions. However, both observations were executed proceeded in bright time, and seeing values varied from $1.3''$ to $4.0''$.

The preprocessing, such as bias subtraction, dark subtraction and flat fielding was conducted with usual data reduction procedures using the IRAF[1] `noao.imred.ccdred` package. Then we average-combined images of each field and each filter. We used `ccmap` of IRAF task and SCAMP (Bertin 2006) to derive astrometric solutions. SExtractor (Bertin & Arnouts 1996) was used for the source detection and photometry. We derived auto-magnitudes which are taken as the total magnitude.

We estimated the limiting magnitude for each medium-band filter for $m675$, $m725$, $m775$, $m825$ and $m875$ (Table 8.2). We used the data taken from 8th February 2015. Although the observation was conducted on a bright night with the full moon, the weather was clear and the seeing was less than $1.5''$, which was the best observing condition during the test observations. The photometric depth of Table 8.2 is defined as the 5σ detection limit of a point source with 1 hour integration time. The detection limits were determined from the sky background sigma, within an aperture with a diameter of 2 times the full width at half maximum (FWHM) value. For the $m625$, $m925$, $m925n$, $m975$, and $m1025$, we estimated limiting mag-

[1]IRAF is distributed by the National Optical Astronomy Observatory, which is operated by the Association of Universities for Research in Astronomy, Inc., under cooperative agreement with the National Science Foundation.

Table 8.1. Information of the targets

Type	ID	Name	z [AB]	z_{spec}	Integration Time[a][s]	Seeing[b][″]	z_{phot}
Quasar	ID0085	IMSJ0324+0426	19.15±0.06	4.712±0.039	360, 360, 360, 180, 180	1.6, 1.6, 1.3, 1.3, 1.6	4.640±0.085
Quasar	ID0106	IMSJ0122+1216	19.27±0.06	4.857±0.039	1200, 1200, 1200, 600, 600	3.7, 4.0, 4.0, 1.7, 1.7	4.870±0.115
Quasar	ID0719	IMSJ1437+0708	19.10±0.06	4.967±0.049	360, 360, 360, 180, 180	1.6, 1.6, 1.6, 1.6, 1.6	4.810±0.150
Quasar	ID0308	IMSJ2225+0330	19.47±0.10	5.350±0.049	600, 600, 600, 600, 600	2.6, 2.3, 2.8, 1.7, 1.7	5.280±0.125
Quasar	ID0099	IMSJ0155+0415	19.26±0.06	5.386±0.039	360, 360, 360, 360, 600	2.4, 2.1, 1.9, 1.6, 1.4	5.330±0.135
Quasar	ID0176	IMSJ0148+0600	19.29±0.06	5.993±0.013[c]	720, 720, 720, 360, 360	2.1, 1.9, 1.6, 1.6, 1.3	5.940±0.070
Dwarf Stars	DW2050	IMSJ2322+0638	18.99±0.06	···	600, 600, 600, 600, 600	3.7, 3.7, 3.4, 1.7, 1.7	···
Dwarf Stars	DW0148	IMSJ0054+0651	19.30±0.09	···	1200, 1200, 1200, 600, 600	2.8, 3.1, 2.6, 1.7, 1.7	···
Dwarf Stars	DW0025	IMSJ0116+0529	19.35±0.09	···	1200, 1200, 1200, 600, 600	2.6, 3.7, 3.7, 1.7, 1.7	···
Dwarf Stars	DW0941	IMSJ0330+0014	19.17±0.11	···	810, 720, 720, 360, 360	2.1, 2.1, 2.1, 1.9, 2.1	···
Dwarf Stars	DW0120	IMSJ0316+0557	19.37±0.06	···	360, 360, 360, 180, 180	1.3, 1.3, 1.3, 1.3, 1.6	···

[a]Integration times of the $m675, m725, m775, m825$, and $m875$ filters for the test observations, respectively

[b]Seeings of the $m675, m725, m775, m825$, and $m875$ filters for the test observations, respectively

[c]Jiang et al. (2015) provided the more accurate redshift, $z_{spec} = 5.923 \pm 0.003$

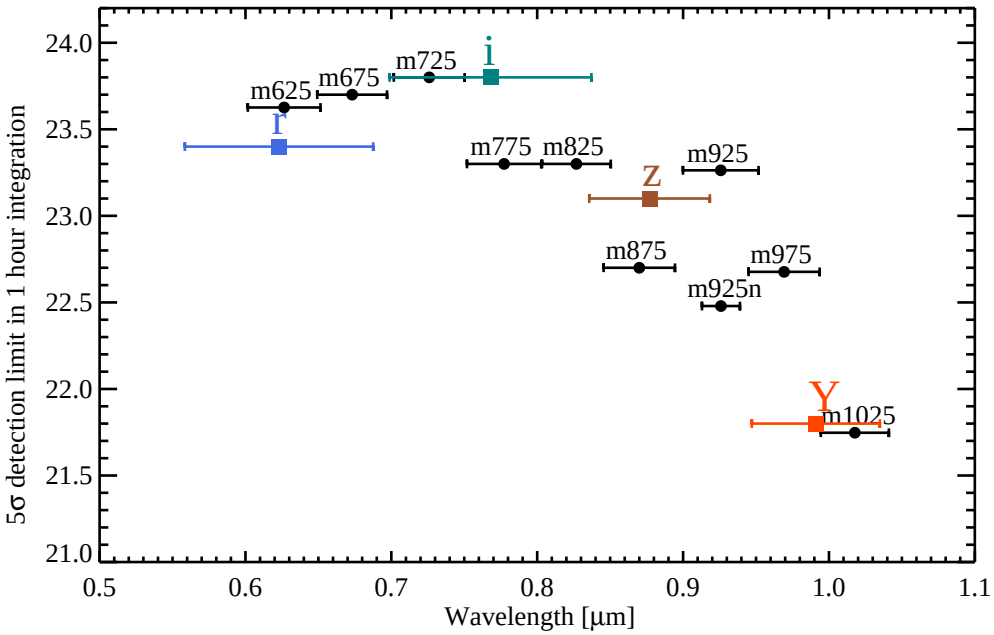

Figure 8.2 Detection limits of the medium-band filters (circles) as well as the $r/i/z/Y$ bands (squares) of CQUEAN.

nitudes using the filter response curves, assuming that the area of each filter curve is proportional to the limiting flux. We compared the $r/i/z/Y$ depths of CQUEAN against these medium-band depths in Figure 8.2. We used the magnitude limit information for bright time from Park et al. (2012). Note that their seeing condition and sky transparency may differ from those of our test observations. We can see that the $m725$ depth is nearly as deep as the i band limit and the depths of the other bands are located between those of i and Y bands.

8.2.4 Photometric Calibration

For the photometric calibration, we used stellar objects that have SDSS photometry and are in the same field as our target. Using the $r/i/z$ band magnitude of a

Table 8.2. Filter characteristic

Filter Name	Central Wavelength [nm]	Effective Wavelength [nm]	FWHM [nm]	Depth[a] [AB]
$m625$	625	626.50	49.81	23.6[b]
$m675$	675	673.12	47.84	23.7
$m725$	725	725.97	48.55	23.8
$m775$	775	777.31	50.95	23.3
$m825$	825	826.84	47.11	23.3
$m875$	875	869.98	48.92	22.7
$m925$	925	925.83	51.87	23.3[b]
$m925n$	925	925.96	26.03	22.5[b]
$m975$	975	969.26	48.76	22.7[b]
$m1025$	1025	1017.75	46.66	21.7[b]

[a] 5σ detection limit of a point source within an aperture with a diameter of 2 times FWHM with 1 hour integration time

[b] Estimated values using the filter response curves

stellar object, we did a χ^2 fitting to the SED of the object to find the best spectral template among stellar spectral templates. We used the stellar templates from Gunn & Stryker (1983), that contain 175 spectra with various stellar types. From the best-fit template, we calculated model magnitudes for each medium-band filter using their filter transmission curves and defined these values as their standard magnitudes (M_{std}) of each filter. Figure 8.3 shows examples of the χ^2 fitting of stars, with their $r/i/z$ magnitudes (boxes) and the best-fit templates (solid lines). Then, the standard magnitudes of the stellar sources were compared with their instrument magnitudes (m_{ins}; $m_{ins} = -2.5\log(\mathrm{DN})$), and the differences between the M_{std} and the m_{ins} were used to estimate the zero-point (Zp). During the calculation, faint objects or objects with large χ^2 values were rejected for the estimation. We chose stars of $\chi^2 < 0.1$ and magnitude error < 0.05 mag. Figure 8.4 shows an example of the Zp calculations, in the case of ID0719, for each filter. The crosses are for all sources in each field and the boxes are sources which satisfy the conditions above. After 3σ clipping, we calculated the Zp as the average value of the magnitude differences. For the Zp uncertainty, we used a standard deviation value of the scatters. The average zero-point error is about 0.05 mag. The standard magnitudes of our targets were calculated with a formula of $M_{std} = Zp + m_{ins}$.

This calibration technique was compared to results from the standard star observations. We used standard star data from the observation of February 5th 2015. BD+33 2642 ($\alpha = 15^h51^m59.86^s$, $\delta = +32^\circ56'54.8''$) was observed with the 5 filters for two different airmasses. To calculate the standard magnitudes of the star for each filter, we used its spectrum obtained from Oke (1990), and the filter transmission curves. We checked the differences between two calibration methods and found that the two Zp values were consistent within the errors calculated using the SDSS stars.

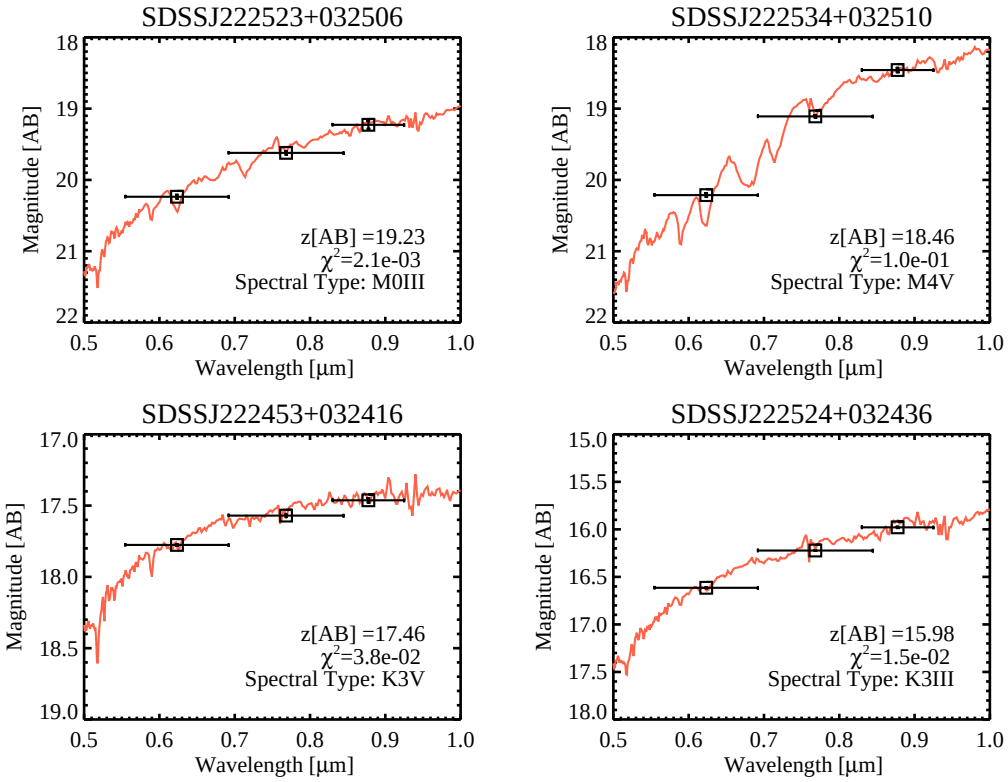

Figure 8.3 Examples of the χ^2 fitting of SDSS stars. The solid line is the best-fit template and the boxes are the SDSS $r/i/z$ photometry.

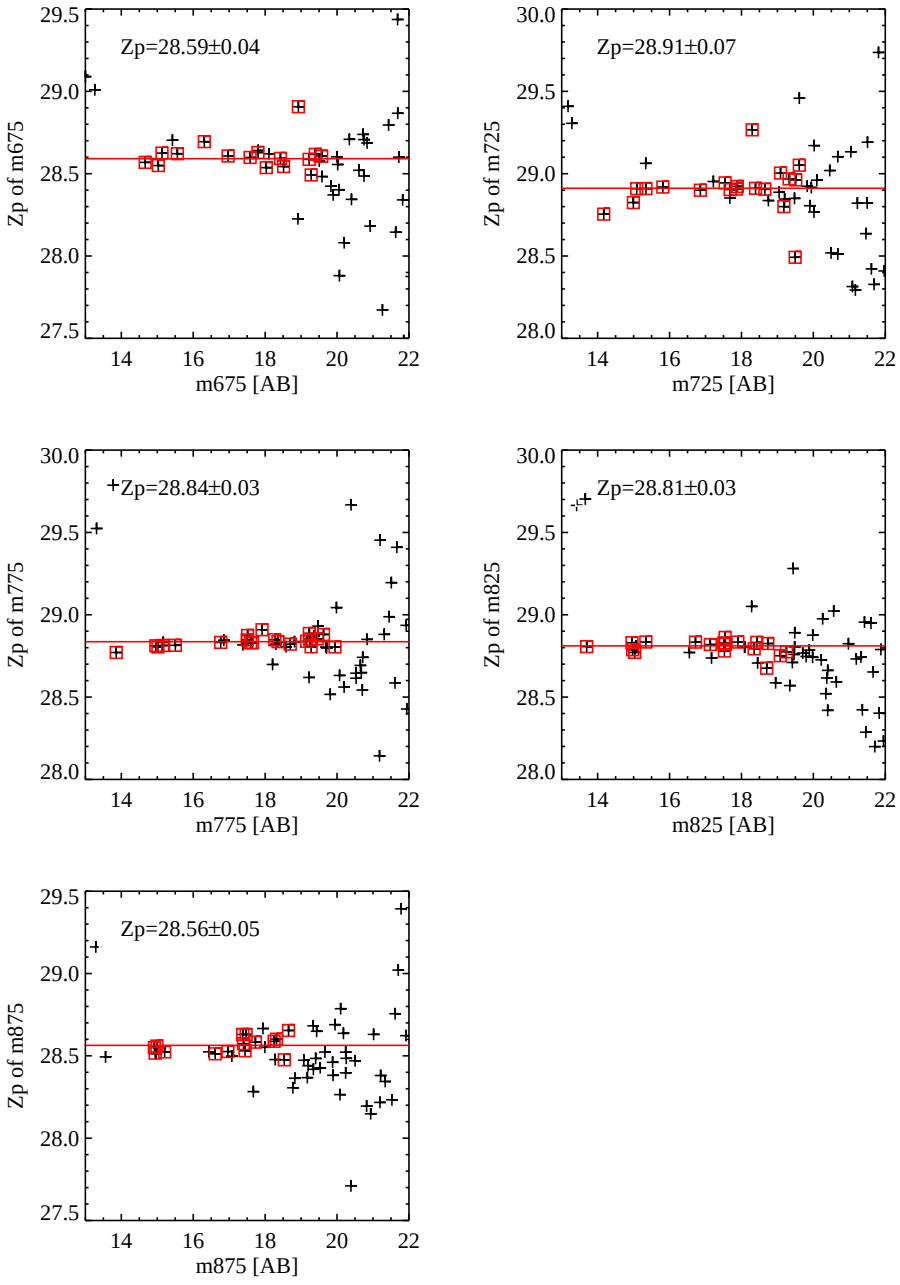

Figure 8.4 *Zp* calculations for ID0719. The crosses are for all sources in each field and the boxes are sources that satisfy the conditions described at Chap. 8.2.4.

8.3 Results

8.3.1 Filter Response Curves with Quasar Spectra

We plot the filter response curves of medium-band filters (thin solid lines) with various high redshift quasar templates (thick solid lines) in Figure 8.5. We used a median composite spectrum of SDSS quasars from Vanden Berk et al. (2001) and adopted the IGM attenuation model from Madau et al. (1996). We also plot the model magnitudes of each filter with squares. We can notice that the Lyα emission line is located in $m725$ band at z=5.0, in $m775$ at z=5.5 and between $m825$ and $m875$ at z=6.0 and they show a sharp drop in flux of the shortward of these filters. Comparing to the dwarf spectra from Burrows et al. (2006) in Figure 8.6, these drops are the distinct features of quasars. We can see that the photometry with these medium-bands trace the SED of sources, similar to doing a spectroscopy with a resolution R$\sim$15.

8.3.2 Magnitude and Colors of Targets

Table 8.3 and 8.4 lists the measured magnitudes of our targets, SDSS and UKIDSS LAS photometry as well as the medium-band filters. The magnitude errors of the medium-band filters are computed by combing the standard SE estimates based on Poison statistic and the zero-point errors from Chap. 8.2.4. Figure 8.7 shows three color composite images for the quasars with 3 color images, Red, Green, Blue. We used 3 filters, $m775$ for Red, $m725$ for Green, and $m675$ for Blue for the color composites, except ID0176. For the ID0176, we used $m875$ for Red, $m825$ for Green, and $m775$ for Blue to show the red color from $m775$ to $m875$. The quasars at z $>$ 5.0 show extreme red colors, showing the Lyα dropouts at the Red while the quasars at z $<$ 5.0 show colors of Red & Green combinations.

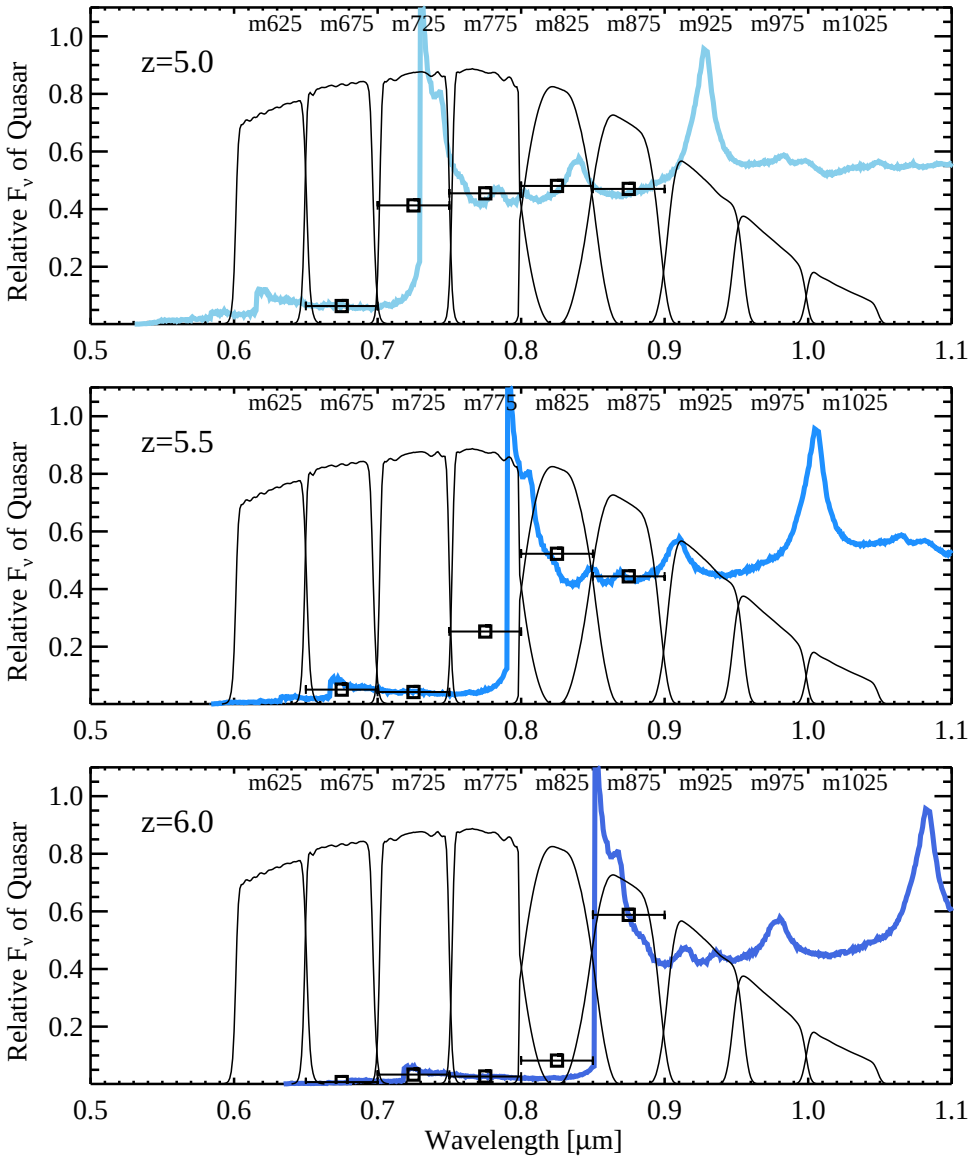

Figure 8.5 Filter response curves (thin solid lines) with quasar spectra (thick solid lines). The model magnitudes of each filter trace the SEDs of the sources similar to a spectroscopy with R $\sim$ 15.

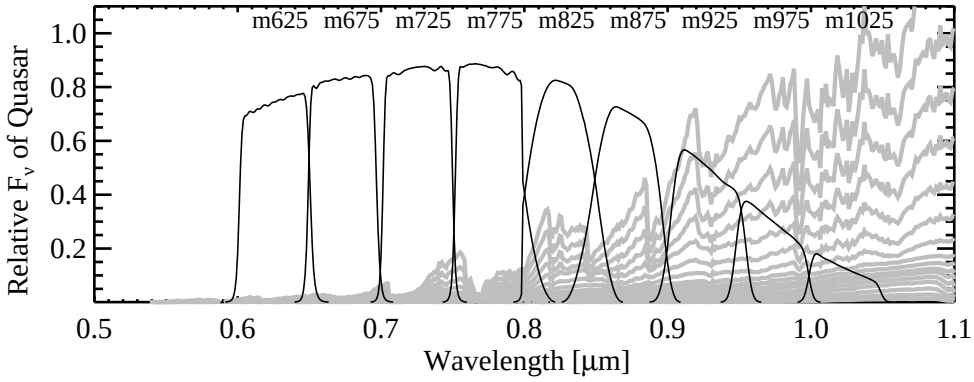

Figure 8.6 Filter response curves (black solid lines) with dwarf spectra (gray solid lines).

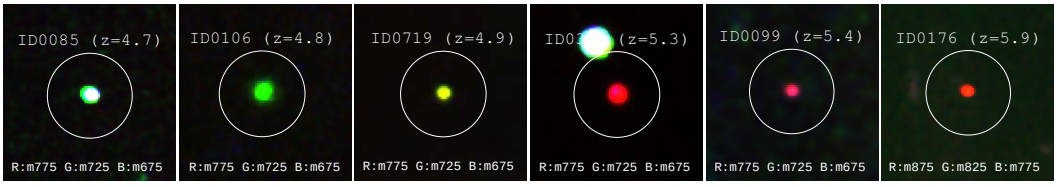

Figure 8.7 Three color composition images of the quasars.

Table 8.3. SDSS and UKIDSS LAS photometric information of the targets

ID	u	g	r	i	z	Y	J	H	K
ID0085	25.50±0.72	23.95±0.39	20.39±0.04	19.03±0.03	19.15±0.06	19.39±0.05	19.23±0.05	18.96±0.05	18.83±0.05
ID0106	23.43±0.59	24.29±0.37	22.35±0.14	19.37±0.03	19.27±0.06	19.12±0.04	18.92±0.04	18.56±0.04	18.50±0.04
ID0719	23.87±1.03	25.02±0.72	20.71±0.04	19.20±0.02	19.10±0.06	19.40±0.05	19.39±0.08	19.01±0.06	18.99±0.08
ID0308	24.06±1.02	25.67±0.68	22.01±0.14	20.02±0.05	19.47±0.10	19.48±0.06	19.33±0.06	19.04±0.10	18.99±0.08
ID0099	24.59±1.04	24.07±0.38	21.81±0.10	19.98±0.03	19.26±0.06	19.66±0.07	19.28±0.06	19.00±0.06	18.91±0.06
ID0176	24.73±0.98	24.95±0.64	24.70±0.57	22.27±0.19	19.29±0.06	19.54±0.06	19.30±0.06	19.10±0.07	19.03±0.07
DW0025	26.21±0.44	24.30±0.46	22.71±0.19	20.14±0.04	18.99±0.06	18.68±0.03	18.99±0.06	18.34±0.04	18.26±0.04
DW0120	24.69±0.75	25.06±0.62	22.99±0.25	20.28±0.07	19.30±0.09	19.53±0.07	19.22±0.07	18.91±0.05	18.93±0.07
DW0148	23.32±0.81	24.96±0.70	22.22±0.18	20.33±0.07	19.35±0.09	19.33±0.04	19.01±0.04	18.78±0.06	18.80±0.07
DW0941	25.20±1.88	24.72±1.02	22.52±0.31	20.51±0.07	19.17±0.11	19.39±0.04	19.04±0.03	18.94±0.04	18.94±0.07
DW2050	23.68±1.05	23.75±0.35	22.97±0.27	20.60±0.05	19.37±0.06	19.34±0.05	19.11±0.05	18.90±0.06	18.91±0.07

Table 8.4. Medium band photometric information of the targets

ID	$m675$	$m725$	$m775$	$m825$	$m875$
ID0085	19.82±0.07	19.30±0.05	19.49±0.05	19.48±0.05	19.12±0.06
ID0106	23.07±0.28	19.08±0.08	20.42±0.13	19.39±0.04	19.57±0.08
ID0719	21.34±0.13	19.06±0.07	19.44±0.05	19.17±0.06	19.03±0.08
ID0308	21.61±0.15	22.27±0.20	19.30±0.09	20.06±0.09	19.52±0.06
ID0099	21.12±0.19	22.08±0.24	19.37±0.12	19.52±0.13	19.55±0.07
ID0176	23.60±0.96	22.26±0.27	22.93±0.47	20.57±0.14	19.05±0.09
DW0025	22.68±0.22	20.82±0.13	20.43±0.11	19.54±0.04	19.22±0.10
DW0120	22.37±0.23	21.12±0.12	20.56±0.12	20.28±0.09	19.86±0.18
DW0148	···	21.02±0.16	20.58±0.12	19.80±0.07	···
DW0941	22.75±0.25	21.36±0.07	20.72±0.08	20.15±0.08	20.57±0.12
DW2050	···	21.64±0.15	20.73±0.12	19.89±0.07	19.68±0.07

8.3.3 SEDs

The medium-band filters trace SEDs of high redshift quasars and dwarf stars differently (Figure 8.8; gray lines are redshifted quasar templates from Vanden Berk et al. (2001) with IGM attenuation, red squares are the 5 medium-band magnitudes, and blue crosses are SDSS $r/i/z$ magnitudes). The quasars show noticeable dropouts near the Lyα emission lines at specific filters. On the other hand, dwarf stars show a smooth continuum shape that is characteristic of stars. Such a difference in SED cannot be identified from $r/i/z$ broad-band photometry unambiguously. Drastic magnitude drop at a redshifted Lyα is a key to distinguish high redshift quasars and dwarf stars and the medium-band filters offer enough resolution for such a purpose. These dropouts can be also checked in color-color diagram.

8.3.4 Color-color Diagrams

Figure 8.9 shows 7 color-color diagrams from combinations of all nine medium-band filters (black lines are the quasar redshift tracks with a specific redshift range, light green triangles are the model magnitudes of dwarf stars from Burrows et al. (2006), dark green boxes with error bars or arrows are our dwarf stars, and red circles with error bars or arrows are our quasars). Figure 8.9 (a) is for $m625 - m675$, vs. $m675 - m725$, (b) is for $m675 - m725$, vs. $m725 - m775$, (c) is for $m725 - m775$ vs. $m775 - m825$, (d) is for $m775 - m825$ vs. $m825 - m875$, (e) is for $m825 - m875$ vs. $m875 - m925$, (f) is for $m875 - m925$ vs. $m925 - m975$, and (g) is for $m925 - m975$ vs. $m975 - m1025$. Figure 8.9 (b), (c), and (d) contain the medium-band colors from our observations. From Figure 8.9 (b), we can denote that the $m675$-dropout is found for ID0106 (z=4.9) and ID0719 (z=5.0). On the other hand, it is difficult to select ID0085 (z=4.7) as a high redshift quasar, because its Lyα drop locates at $m675$ and the magnitudes of 3 filters are similar each other. For a similar reason, in Figure 8.9 (c), ID0308 (z=5.3) and ID0099 (z=5.4) also show red $m725 - m775$ colors against

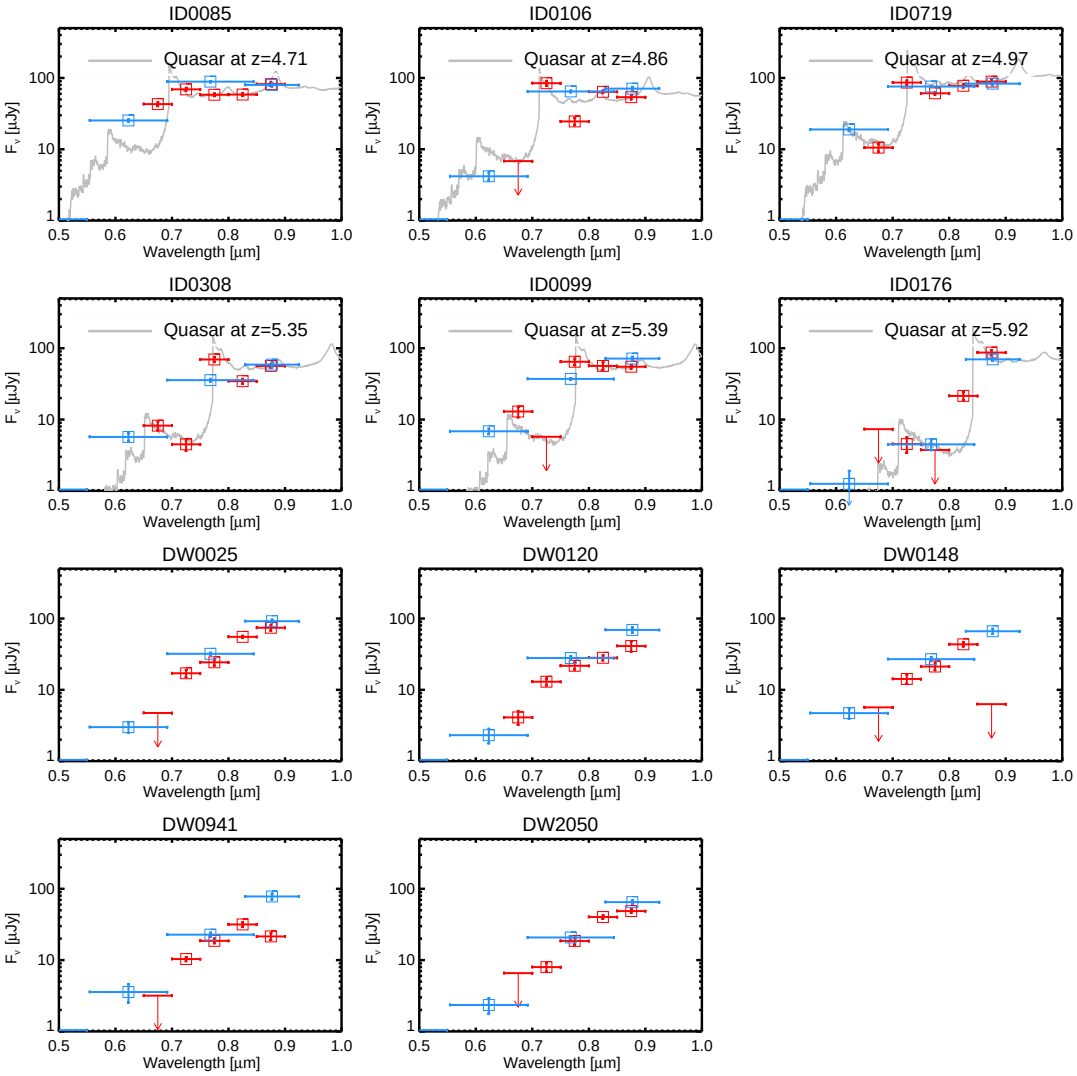

Figure 8.8 Photometry from the SDSS $r/i/z$ (blue crosses) and the medium-band filters (red squares), and redshifted quasars templates (gray lines).

ID0085 (z=4.7), ID0106 (z=4.9), and ID0719 (z=5.6) due to the $m725$-dropout. In the case of quasars at z > 6 (Figure 8.9 (d)), they can be separated from dwarf stars with this color-color diagram considering the redshift track. However, for ID0176 (z=5.9) in Figure 8.9 (d), since its Lyα emission line moves from $m775$ to $m875$, the Lyα-dropout between $m775$ and $m825$ or $m825$ and $m875$ is not strong as other quasars, and thus, ID0176 (z=5.9) shows similar $m775 - m825$ and $m825 - m875$ colors with dwarf stars of temperatures less than 1,300K (T dwarf stars). We can see that the all color-color diagram can be used for the high redshift quasar selections at $4.8 < z < 5.5$ and $z > 6.0$ because the positions of the quasars are definitely different from those of the dwarf stars, apart than > 1 mag from the quasar tracks. On the other hand, quasar selection at $5.5 < z < 6.0$ is yet impossible using these medium-band colors. For Figure 8.9 (d), (e), (f), and (g), the quasars at z > 6 can be separated from dwarf stats clearer than the other color-color diagrams, because color differences between quasars and dwarf stars are more than 2 mag. Although it is difficult for our 2.1-m telescope to observe quasar candidates at z > 6, other large mirror telescopes can be conducted for the imaging observations using these medium-band filters. The magnitudes from these observations can help to separate quasars from dwarf stars more efficiently due to the large color differences between two objects.

For comparison, we plot various color-color diagrams including SDSS and UKIDSS LAS filters. Since the r band has a similar wavelength with $m675$ and z has a similar wavelength with $m875$, we plot $r - m725$, vs. $m725 - m775$ and $m775 - m825$ vs. $m825 - z$ color-color diagram in Figure 8.10 (a) and (b), respectively. We can see that $m775 - m825$ vs. $m825 - z$ is similar with the color-color diagram of Figure 8.9 (c). However, differently with the color-color diagram of Figure 8.9 (b), the colors from the quasar redshift track at $4.6 < z < 5.1$ are not different with those of dwarf stars in $r - m725$, vs. $m725 - m775$ color-color diagram in Figure 8.10 (a). It is

because the difference of the wavelength coverage between r and $m675$ bands. Since r filter covers the Lyβ emission line of a quasar at the redshift range of $4.6 < z < 5.0$ and lead to a larger flux than $m675$, the magnitude different between r and $m725$ is smaller than that between $m675$ and $m725$ and, therefore, the dropout effect from r and $m725$ is not strong enough to distinguish quasars from dwarf stars. To check the possibility to select quasars at $z \sim 6$ with our medium-band and near-infrared bands, we adopted the Y or J bands ((c) and (d) of Figure 8.10). The $z-Y$ or $z-J$ colors of $z \sim 6$ quasars are different with those of dwarf stars, which is a traditional selection method to select $z \sim 6$ quasars such as $i-z$ vs. $z-J$ color-color diagram. Using these two diagrams (c and d), we also select quasars at $z \sim 6$ separating from the dwarf stars. For the selection of quasars at $z > 6.5$, one can use longer passbands (Choi et al. 2012).

8.3.5 Photometric Redshifts of Quasars from SED Fitting

Using these medium-band filters, we can estimate photometric redshifts (z_{phot}) via the χ^2 fitting. Figure 8.11 shows the reduced χ^2 distributions for each quasars along the redshifts. The z_{phot}s are estimated from a redshift where the reduced χ^2 has a minimum value. The red dotted lines indicate the spectroscopic redshifts (z_{spec}) from the spectroscopic observations and the blue solid lines are for the z_{phot}s. The uncertainties of z_{phot}s ($\Delta\ z_{phot}$) are estimated from the 1σ deviations (confidence level of 68.3%) of the reduced χ^2 distribution, where the reduced χ^2 takes on a value one greater than its minimum. The errors of the z_{phot}s (blue) and z_{spec}s (red) are denoted in the gray boxes on each plot. We can see that the z_{phot}s agree with the z_{spec}s within the $\Delta\ z_{phot}$. The $\Delta\ z_{phot}$ is less than 0.15, which shows the power of the medium-band photometry to select the high redshift quasars via the χ^2 fitting of the SEDs. The z_{phot}s and their errors are provided in Table 8.1.

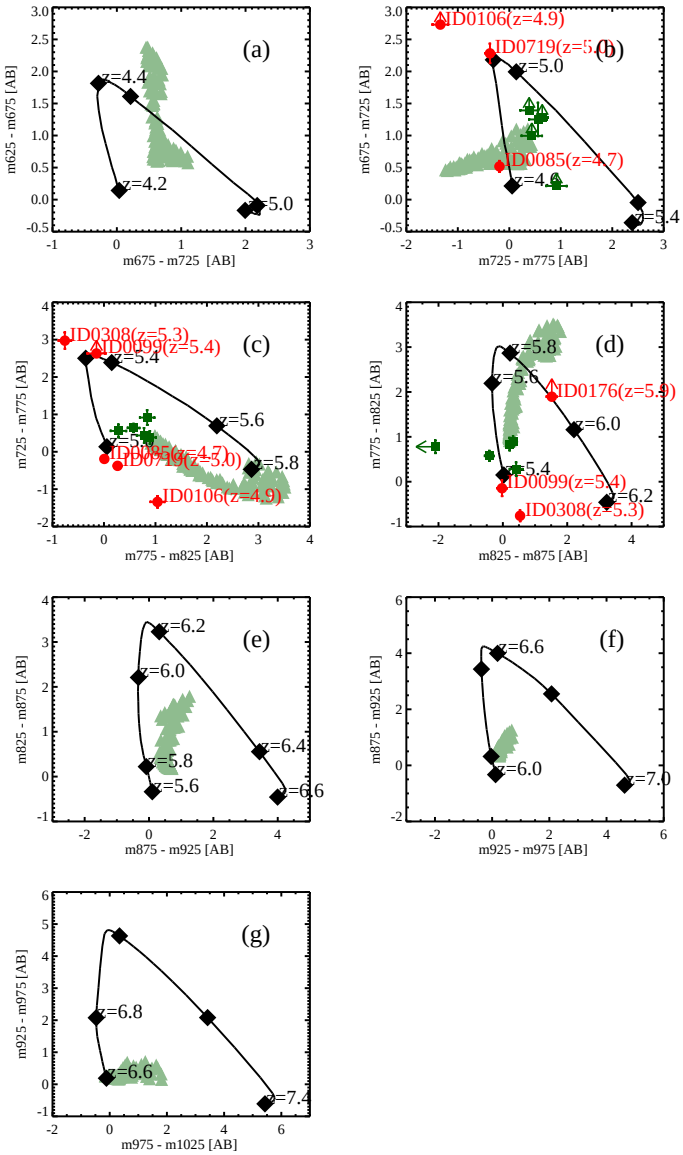

Figure 8.9 Color-color diagrams from combinations of nine medium-band filters. The black lines are the quasar redshift tracks with the diamond symbols of $\Delta z = 0.2$, light green triangles are the model magnitudes of dwarf stars, dark green boxes with error bars or arrows are our dwarf stars, and red circles with error bars or arrows are our quasars.

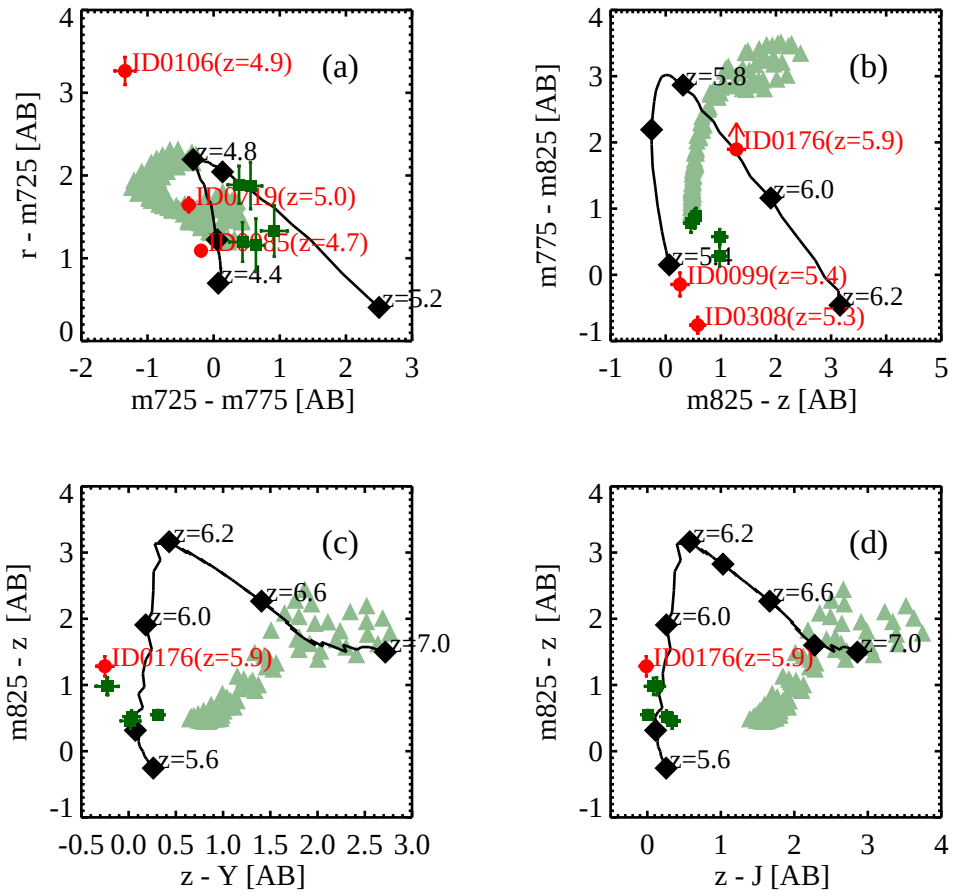

Figure 8.10 Similar with Figure 8.9, but including SDSS and UKIDSS LAS filters.

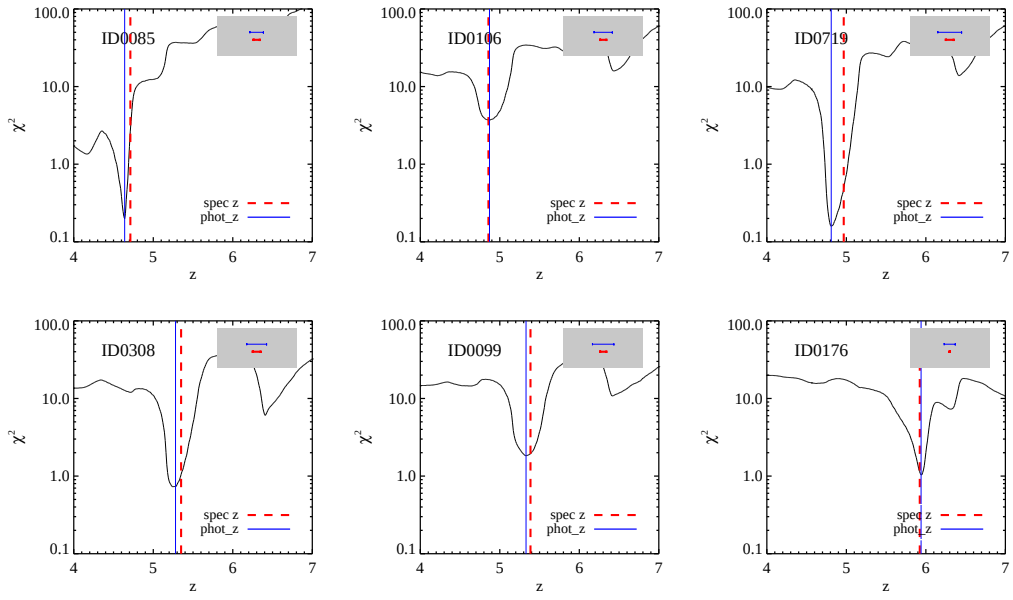

Figure 8.11 Reduced χ^2 distributions for each quasar along the redshifts when we use Filterset1. The red dotted lines indicate the z_{spec}s and the blue solid lines are for the z_{phot}s. The errors of the z_{phot}s (blue) and z_{spec}s (red) are denoted in the gray boxes.

8.3.6 χ^2 Fitting with Different Filter Sets

We calculated the reduced χ^2 values between our photometry for a specific filter set and the quasar templates with various redshifts. We defined available filter sets combining our medium-bands and SDSS filters as follows:

Filterset1=$\{m675, m725, m775, m825, m875\}$

Filterset2=$\{r, m725, m775, m825, m875\}$

Filterset3=$\{m675, m725, m775, m825, z\}$

Filterset4=$\{r, m725, m775, m825, z\}$

Filterset5=$\{r, i, z\}$

After finding the best quasar template for each target, we compared the best-fit χ^2 values from quasars and dwarf stars. Figure 8.12 shows the reduced χ^2 distributions for a quasar and a dwarf with Filterset4 and Filterset5. We used ID0719 and DW0120 as an example. The red dotted lines indicate the z_{spec} of the quasar and the blue solid lines are for the z_{phot}s of the sources. We can see that the best-fit χ^2 values for the quasar and the dwarf stars using Filterset4 (upper two panels) are certainly different (0.63 for the quasar and 3.30 for the dwarf star). On average, for Filterset1–4, which include 3 medium-bands that substitute the i-band wavelengths ($m725, m775, m825$), the reduced χ^2 values for the quasars are about 3–5 times smaller than those for the dwarf stars. Therefore the χ^2 fitting using filter sets including these 3 medium-band filters can be used for quasar selections. On the other hand, in case of Filterset5 (lower two panels), which contains only $r/i/z$ bands without medium-bands, the best-fit χ^2 value of the dwarf star is rather smaller than that of the quasar. Therefore we might misestimated dwarf stars as actual quasars via χ^2 fitting if we use photometry only from $r/i/z$ bands. Here, we showed that photometric information from $m725, m775$ and $m825$ filters, combined with SDSS r/z magnitudes, are sufficient to use SED χ^2 fitting to separate quasars from dwarf stars. Therefore we can select robust quasar candidates using SED fitting including

medium-band photometry from large sample selected from broad-band photometry.

8.4 Observation Strategy

Among the quasar candidates selected from broad-band photometry, it is important to reduce the number of other contamination and list robust candidates, and we showed that our medium-band photometry is useful to separate quasars from dwarf stars. We estimated expected observing time by the most efficient way, reducing total exposure time and reaching the depth we aim. We can see that, at least, three medium-bands ($m725, m775$, and $m825$ filters) are enough to remove dwarf stars through the SED fitting if SDSS photometric information is provided. Considering the depths of medium-bands and the average magnitude of our candidates (i = 19.9 mag and z = 19.3 mag), we need 6, 6, and 3 min for $m725$, $m775$, and $m825$ band observations with the McDonald 2.1-m telescope with SQUEAN, respectively, to reach a S/N $\sim$ 25 (corresponding photometric error of 0.04 mag) for detection and a 5σ depth less than 6μJy for dropouts. In this case we need 15 minutes per target for photometry in these three medium-bands. Additionally, 6 and 3 min are needed for $m675$ and $m875$ bands. Therefore totally 24 min is required for all five filters. Generally, similar integration time is needed for the 2-m class telescopes with red-sensitive CCDs.

8.5 Discussion and Summary

We showed the results from the medium-band observations of the 6 high redshift quasars at $4.7 < z < 6.0$ and the 5 dwarf stars. The SEDs of the quasars and dwarf stars from the medium-band photometry show different shapes, and the positions on various color-color digrams can clearly separate quasars from dwarf stars. The best-fit χ^2 values of quasars and dwarf stars are quite different if we have information of

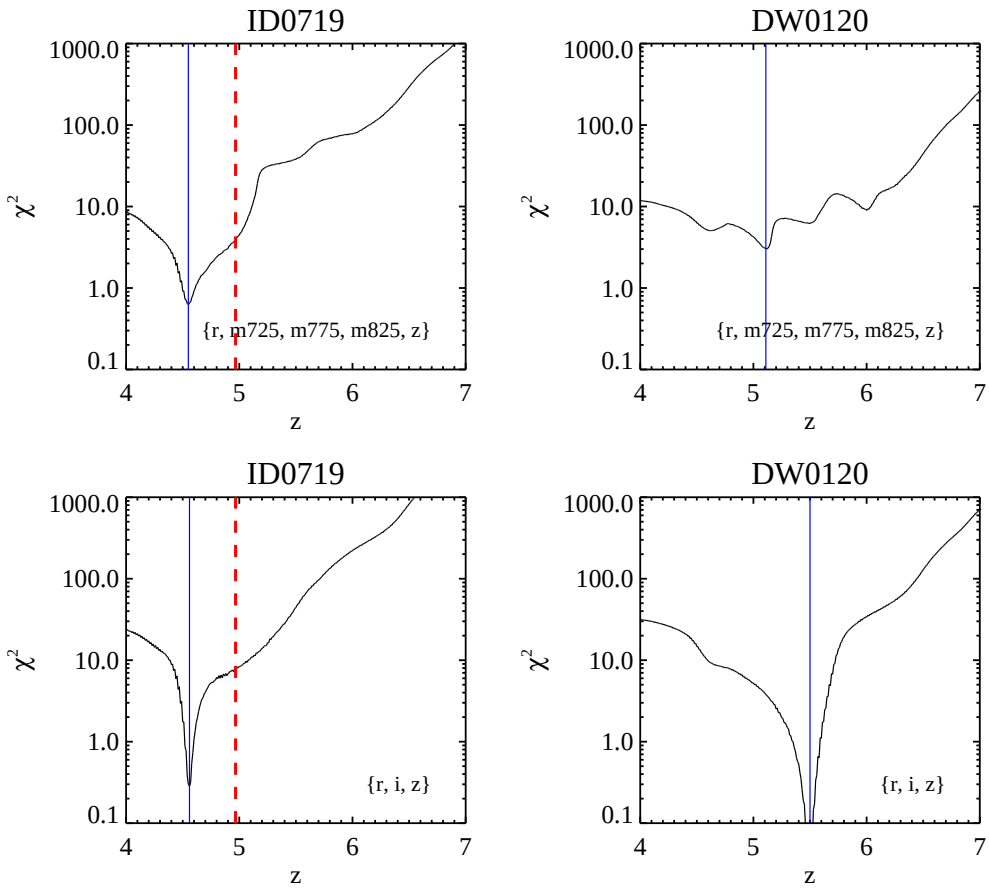

Figure 8.12 Similar with the Figure 8.11, but for the ID0719 and DW0120 with Filterset4 and Filterset5.

only 3 medium-bands and SDSS photometry. These three results from the medium-bands cannot be produced by the SDSS photometry. Also the χ^2 fitting of the SEDs can estimate accurate z_{phot}s within a $\Delta\ z_{phot} = 0.15$ if we use 5 medium-band filters. The previous quasar surveys cannot cover the redshift range between 5 and 6 due to the limitations of the previous filter sets. Our new technique using the medium-bands will be the powerful selection method for the high redshift. The 2-m class telescopes such as the McDonald 2.1-m telescope with SQUEAN can conduct imaging follow-up observations of the high redshift quasar candidates of $z < 19.3$ mag in these 3 medium-band filters within 15 min per target. For higher redshift quasars, larger telescopes are able to carry on quasar survey at $z > 6$ using longer bandpass medium-band filters with a high efficiency to reduce contamination.

Chapter 9

Conclusion

High redshift quasars are key probes to investigate the early universe. Since high redshift quasars are rare, their discovery requires special data and a new selection technique. In this thesis, we presented new selection methods for high redshift quasars at different redshift ranges.

First, we designed a quasar survey for z $\sim$ 5 (4.6 $<$ z $<$ 6.0). This redshift range belongs to the redshift gap that previous studies could not cover, due to the limitations of traditional filter sets and selection techniques. We conducted a quasar selection using multi-wavelength data covering a wide area (3,400 deg^2), with development of a new selection method to eliminate as many contaminants as possible. For this purpose we adopted custom-design filters, Is and Iz, and carried out imaging follow-up observations. After optical spectroscopic observations, we discovered 6 new quasars, also re-discovered 24 quasars at $z \sim 5$. To measure their physical properties, we carried out NIR spectroscopy. From the NIR spectra, we estimated black hole masses and Eddington ratios and compared these values to those of low and high redshift quasars. We found that the Eddington ratios of our quasars at z $\sim$ 5 have values close to 1, which indicates vigorous mass growth through accretion. However, the selection efficiency of quasars at 5.5 $<$ z $<$ 6.0 is still

low even with the Is and Iz photometry, compared to the expected quasar number calculated from the quasar luminosity function. Another selection technique, in addition to the ones discussed in this thesis, is desirable for higher efficiency.

To improve the quasar identification efficiency, we devised a new selection method of high redshift quasar survey using imaging follow-up observations with medium-band filters. From the medium-band observations of our high redshift quasars and dwarf stars, we show that the color-color diagram consisting of these medium-bands can clearly separate high redshift quasars at specific redshift ranges from dwarf stars, which was difficult with previous filter sets. We can identify quasars by comparing the χ^2 estimates of quasars and dwarfs, fitted from the medium-band photometry, and the χ^2 estimates allow us to calculate photometric redshifts within a 1σ error of 0.15. For higher redshift quasars, larger telescopes can carry out the quasar survey at higher redshifts (z $>$ 6) using longer bandpass medium-band filters, with a high efficiency in reducing the contamination.

The second sub-survey is for bright quasars at z $\sim$ 6 (5.8 $<$ z $<$ 6.3). We developed a new selection criterion in addition to previous selection methods, and found that our new method eliminates 94% of contaminants. Also imaging follow-up observations removed all interlopers and we confirmed two quasars at z $\sim$ 6 via spectroscopic observations. The quasar selection at z $\sim$ 6 can also be conducted using deeper datasets, for example IMS data, and the discovered quasars can be used to constrain the faint end slope of the quasar luminosity function.

The third selection is for quasars at z $\sim$ 7, which is the most challenging survey. We carried out NIR imaging survey for these faint and rare objects, covering $\sim$120 deg^2 area with a detection limit of $Y = 22.3$ Vega and $J = 22.0$ Vega. Seven extragalactic fields with multi-wavelength data were selected as IMS fields, and we provide catalogs containing photometric information of $\sim 7 \times 10^6$ sources in these fields. We developed a new selection technique for z $\sim$ 7 quasars combining NIR and

IR wavelength data to supplement the previous selection techniques, and conducted the quasar selection over an area of ∼110 deg^2 area. So far, we have yet found any z ∼ 7 quasars, and the upper limit on the quasar number density estimated from this value is ∼3 times lower than the expected number density from the quasar luminosity function of z ∼ 6 in literature, even after assuming various types of evolution of the quasar number density. We conclude that the quasar number density at z ∼ 7 declines toward higher redshift, at a rate faster than the empirically determined number of quasars at lower redshifts.

To summarize, from this study, we

i) provided new deep NIR imaging data with Y and J-bands of seven IMS fields. They have pre-existing multi-wavelength data from X-ray to radio, which make the IMS fields some of the most popular extragalactic regions. These data have been used to select high redshift quasar candidates.

ii) developed effective selection techniques for quasar selection at high redshifts using multi-wavelength photometric data, and suggested a new selection strategy for quasars at z ∼ 5.

iii) estimated physical properties, such as black hole masses and Eddington ratios, of our newly discovered high redshift quasars. These results show that high redshift quasars are shining at near the Eddington limit, and that their number density is rapidly evolving toward higher redshift. We find that the universe at z > 5 to be an era where SMBHs are emerging rapidly through AGN activities.

Bibliography

Bañados, E., Venemans, B. P., Morganson, E., et al. 2014, AJ, 148, 14

Bañados, E., Venemans, B. P., Morganson, E., et al. 2015, ApJ, 804, 118

Baldwin, J. A., Phillips, M. M., & Terlevich, R. 1981, PASP, 93, 5

Barnett, R., Warren, S. J., Banerji, M., et al. 2015, A&A, 575, A31

Barth, A. J., Pancoast, A., Thorman, S. J., et al. 2011, ApJ, 743, L4

Baskin, A., & Laor, A. 2005, MNRAS, 356, 1029

Becker, G. D., Rauch, M., & Sargent, W. L. W. 2007, ApJ, 662, 72

Begelman, M. C., Blandford, R. D., & Rees, M. J. 1984, Reviews of Modern Physics, 56, 255

Begelman, M. C., Volonteri, M., & Rees, M. J. 2006, MNRAS, 370, 289

Bellovary, J., Volonteri, M., Governato, F., et al. 2011, ApJ, 742, 13

Bentz, M. C., Walsh, J. L., Barth, A. J., et al. 2010, ApJ, 716, 993

Bertin, E., & Arnouts, S. 1996, A&AS, 117, 393

Bertin, E., Mellier, Y., Radovich, M., et al. 2002, Astronomical Data Analysis Software and Systems XI, 281, 228

Bertin, E. 2006, Astronomical Data Analysis Software and Systems XV, 351, 112

Blandford, R. D., & McKee, C. F. 1982, ApJ, 255, 419

Bower, R. G., Benson, A. J., Malbon, R., et al. 2006, MNRAS, 370, 645

Bromm, V., & Loeb, A. 2003, ApJ, 596, 34

Bruzual, G., & Charlot, S. 2003, MNRAS, 344, 1000

Burrows, A., Sudarsky, D., & Hubeny, I. 2006, ApJ, 640, 1063

Cardelli, J. A., Clayton, G. C., & Mathis, J. S. 1989, ApJ, 345, 245

Carilli, C. L., Wang, R., Fan, X., et al. 2010, ApJ, 714, 834

Casali, M., Adamson, A., Alves de Oliveira, C., et al. 2007, A&A, 467, 777

Choi, C., Im, M., Jeon, Y., & Ibrahimov, M. 2012, Journal of Korean Astronomical Society, 45, 7

Cool, R. J., Kochanek, C. S., Eisenstein, D. J., et al. 2006, AJ, 132, 823

Croom, S. M., Smith, R. J., Boyle, B. J., et al. 2004, MNRAS, 349, 1397

Croton, D. J., Springel, V., White, S. D. M., et al. 2006, MNRAS, 365, 11

Davis, S. W., Woo, J.-H., & Blaes, O. M. 2007, ApJ, 668, 682

De Rosa, G., Decarli, R., Walter, F., et al. 2011, ApJ, 739, 56

De Rosa, G., Venemans, B. P., Decarli, R., et al. 2014, ApJ, 790, 145

Devecchi, B., & Volonteri, M. 2009, ApJ, 694, 302

Djorgovski, S. G., Volonteri, M., Springel, V., Bromm, V., & Meylan, G. 2008, The Eleventh Marcel Grossmann Meeting On Recent Developments in Theoretical and Experimental General Relativity, Gravitation and Relativistic Field Theories, 340

Dye, S., Warren, S. J., Hambly, N. C., et al. 2006, MNRAS, 372, 1227

Fan, X., Strauss, M. A., Schneider, D. P., et al. 1999, AJ, 118, 1

Fan, X., White, R. L., Davis, M., et al. 2000, AJ, 120, 1167

Fan, X., Narayanan, V. K., Lupton, R. H., et al. 2001, AJ, 122, 2833

Fan, X., Strauss, M. A., Schneider, D. P., et al. 2003, AJ, 125, 1649

Fan, X., Hennawi, J. F., Richards, G. T., et al. 2004, AJ, 128, 515

Fan, X., Strauss, M. A., Richards, G. T., et al. 2006a, AJ, 131, 1203

Fan, X., Strauss, M. A., Becker, R. H., et al. 2006b, AJ, 132, 117

Fan, X. 2006c, New Astronomy Reviews, 50, 665

Ferland, G. J., Korista, K. T., Verner, D. A., et al. 1998, PASP, 110, 761

Ferrarese, L., & Merritt, D. 2000, ApJ, 539, L9

Ferrarese, L. 2002, ApJ, 578, 90

Fine, S., Croom, S. M., Hopkins, P. F., et al. 2008, MNRAS, 390, 1413

Frey, S., Gurvits, L. I., Paragi, Z., & Gabanyi, K. 2012, Resolving The Sky - Radio Interferometry: Past, Present and Future, 41

Gebhardt, K., Bender, R., Bower, G., et al. 2000, ApJ, 539, L13

Gehrels, N., Ramirez-Ruiz, E., & Fox, D. B. 2009, ARA&A, 47, 567

Ghez, A. M., Klein, B. L., Morris, M., & Becklin, E. E. 1998, ApJ, 509, 678

Gillessen, S., Eisenhauer, F., Trippe, S., et al. 2009, ApJ, 692, 1075

Goto, T. 2006, MNRAS, 371, 769

Goto, T., & the AKARI NEP team 2015, arXiv:1505.00012
25

Grier, C. J., Peterson, B. M., Pogge, R. W., et al. 2012, ApJ, 755, 60

Gunn, J. E., & Peterson, B. A. 1965, ApJ, 142, 1633

Gunn, J. E., & Stryker, L. L. 1983, ApJS, 52, 121

Hamuy, M., Walker, A. R., Suntzeff, N. B., et al. 1992, PASP, 104, 533

Hamuy, M., Suntzeff, N. B., Heathcote, S. R., et al. 1994, PASP, 106, 566

Hartman, J. D., Bakos, G. Á., Noyes, R. W., et al. 2011, AJ, 141, 166

Hewett, P. C., Warren, S. J., Leggett, S. K., & Hodgkin, S. T. 2006, MNRAS, 367, 454

Hopkins, P. F., Somerville, R. S., Hernquist, L., et al. 2006, ApJ, 652, 864

Hwang, N., Lee, M. G., Lee, H. M., et al. 2007, ApJS, 172, 583

Ikeda, H., Nagao, T., Matsuoka, K., et al. 2012, ApJ, 756, 160

Im, M. 2009, AKARI, a Light to Illuminate the Misty Universe, 418, 227

Irwin, M. J., Lewis, J., Hodgkin, S., et al. 2004, Proc. SPIE, 5493, 411

Jang, M., Im, M., Lee, I., et al. 2011, ApJ, 741, L20

Jeon, Y., Im, M., Ibrahimov, M., et al. 2010, ApJS, 190, 166

Jeon, Y., Im, M., Kang, E., Lee, H. M., & Matsuhara, H. 2014, ApJS, 214, 20

Jiang, L., Fan, X., Vestergaard, M., et al. 2007, AJ, 134, 1150

Jiang, L., Fan, X., Annis, J., et al. 2008, AJ, 135, 1057

Jiang, L., Fan, X., Bian, F., et al. 2009, AJ, 138, 305

Jiang, L., Fan, X., Brandt, W. N., et al. 2010, Nature, 464, 380

Jiang, L., McGreer, I. D., Fan, X., et al. 2015, AJ, 149, 188

Juarez, Y., Maiolino, R., Mujica, R., et al. 2009, A&A, 494, L25

Jun, H. D., Im, M., Lee, H. M., et al. 2015, ApJ, 806, 109

Kaiser, N., Aussel, H., Burke, B. E., et al. 2002, Proc. SPIE, 4836, 154

Kaiser, N., Burgett, W., Chambers, K., et al. 2010, Proc. SPIE, 7733, 77330E

Kashlinsky, A., Arendt, R. G., Mather, J., & Moseley, S. H. 2005, Nature, 438, 45

Kaspi, S., Smith, P. S., Netzer, H., et al. 2000, ApJ, 533, 631

Kim, D., Im, M., Kim, J. H., et al. 2015, ApJS, 216, 17

Kirkpatrick, J. D., Reid, I. N., Liebert, J., et al. 1999, ApJ, 519, 802

Kuhn, O., Elvis, M., Bechtold, J., & Elston, R. 2001, ApJS, 136, 225

Kurk, J. D., Walter, F., Fan, X., et al. 2007, ApJ, 669, 32

Kurk, J. D., Walter, F., Fan, X., et al. 2009, ApJ, 702, 833

Laor, A., & Davis, S. W. 2011, MNRAS, 417, 681

Latif, M. A., Schleicher, D. R. G., Schmidt, W., & Niemeyer, J. 2013, MNRAS, 433, 1607

Lawrence, A., Warren, S. J., Almaini, O., et al. 2007, MNRAS, 379, 1599

Lee, H. M., Kim, S. J., Im, M., et al. 2009, PASJ, 61, 375

Leipski, C., Meisenheimer, K., Walter, F., et al. 2014, ApJ, 785, 154

Lodato, G., & Natarajan, P. 2006, MNRAS, 371, 1813

MacLeod, C. L., Ivezić, Ž., Sesar, B., et al. 2012, ApJ, 753, 106

Madau, P., Ferguson, H. C., Dickinson, M. E., et al. 1996, MNRAS, 283, 1388

Madau, P., & Rees, M. J. 2001, ApJ, 551, L27

Madau, P., Haardt, F., & Dotti, M. 2014, ApJ, 784, L38

Magorrian, J., Tremaine, S., Richstone, D., et al. 1998, AJ, 115, 2285

Mahabal, A., Stern, D., Bogosavljević, M., Djorgovski, S. G., & Thompson, D. 2005, ApJ, 634, L9

Malkan, M. A., & Sargent, W. L. W. 1982, ApJ, 254, 22

Marconi, A., & Hunt, L. K. 2003, ApJ, 589, L21

Massey, P., & Gronwall, C. 1990, ApJ, 358, 344

Matsuhara, H., Wada, T., Matsuura, S., et al. 2006, PASJ, 58, 673

Matute, I., Masegosa, J., Márquez, I., et al. 2013, A&A, 557, A78

McGreer, I. D., Mesinger, A., & Fan, X. 2011, MNRAS, 415, 3237

McGreer, I. D., Jiang, L., Fan, X., et al. 2013, ApJ, 768, 105

McLure, R. J., & Jarvis, M. J. 2002, MNRAS, 337, 109

McLure, R. J., & Jarvis, M. J. 2004, MNRAS, 353, L45

Menci, N., Fontana, A., Giallongo, E., Grazian, A., & Salimbeni, S. 2006, ApJ, 647, 753

Moles, M., Benítez, N., Aguerri, J. A. L., et al. 2008, AJ, 136, 1325

Morganson, E., De Rosa, G., Decarli, R., et al. 2012, AJ, 143, 142

Mortlock, D. J., Patel, M., Warren, S. J., et al. 2009, A&A, 505, 97

Mortlock, D. J., Warren, S. J., Venemans, B. P., et al. 2011, Nature, 474, 616

Netzer, H., Lira, P., Trakhtenbrot, B., Shemmer, O., & Cury, I. 2007, ApJ, 671, 1256

Oke, J. B. 1990, AJ, 99, 1621

Park, W.-K., Pak, S., Im, M., et al. 2012, PASP, 124, 839

Park, D., 2012, Master Thesis, Seoul National University

Patten, B. M., Stauffer, J. R., Burrows, A., et al. 2006, ApJ, 651, 502

Peterson, B. M. 1993, PASP, 105, 247

Peterson, B. M., Ferrarese, L., Gilbert, K. M., et al. 2004, ApJ, 613, 682

Polsterer, K. L., Zinn, P.-C., & Gieseke, F. 2013, MNRAS, 428, 226

Richards, G. T., Fan, X., Newberg, H. J., et al. 2002, AJ, 123, 2945

Richards, G. T., Lacy, M., Storrie-Lombardi, L. J., et al. 2006, ApJS, 166, 470

Schlegel, D. J., Finkbeiner, D. P., & Davis, M. 1998, ApJ, 500, 525

Schmidt, M. 1963, Nature, 197, 1040

Schneider, D. P., Fan, X., Strauss, M. A., et al. 2001, AJ, 121, 1232

Shapiro, S. L. 2005, ApJ, 620, 59

Sharp, R. G., McMahon, R. G., Irwin, M. J., & Hodgkin, S. T. 2001, MNRAS, 326, L45

Shen, Y., Greene, J. E., Strauss, M. A., Richards, G. T., & Schneider, D. P. 2008, ApJ, 680, 169

Shen, Y., Richards, G. T., Strauss, M. A., et al. 2011, ApJS, 194, 45

Shen, Y., & Liu, X. 2012, ApJ, 753, 125

Springel, V., Di Matteo, T., & Hernquist, L. 2005, MNRAS, 361, 776

Stark, D. P., Ellis, R. S., & Ouchi, M. 2011, ApJ, 728, L2

Stoughton, C., Lupton, R. H., Bernardi, M., et al. 2002, AJ, 123, 485

Trakhtenbrot, B., Netzer, H., Lira, P., & Shemmer, O. 2011, ApJ, 730, 7

Trakhtenbrot, B., & Netzer, H. 2012, MNRAS, 427, 3081

Treister, E., & Urry, C. M. 2012, Advances in Astronomy, 2012, 516193

Tsuzuki, Y., Kawara, K., Yoshii, Y., et al. 2006, ApJ, 650, 57

Urry, C. M., & Padovani, P. 1995, PASP, 107, 803

Vanden Berk, D. E., Richards, G. T., Bauer, A., et al. 2001, AJ, 122, 549

Venemans, B. P., McMahon, R. G., Warren, S. J., et al. 2007, MNRAS, 376, L76

Venemans, B. P., Findlay, J. R., Sutherland, W. J., et al. 2013, ApJ, 779, 24

Venemans, B. P., Bañados, E., Decarli, R., et al. 2015, ApJ, 801, L11

Vestergaard, M., & Wilkes, B. J. 2001, ApJS, 134, 1

Vestergaard, M., & Peterson, B. M. 2006, ApJ, 641, 689

Vestergaard, M., Fan, X., Tremonti, C. A., Osmer, P. S., & Richards, G. T. 2008, ApJ, 674, L1

Vestergaard, M., & Osmer, P. S. 2009, ApJ, 699, 800

Volonteri, M., & Rees, M. J. 2005, ApJ, 633, 624

Volonteri, M. 2010, A&A Rev., 18, 279

Volonteri, M. 2012, Science, 337, 544

Volonteri, M., & Bellovary, J. 2012, Reports on Progress in Physics, 75, 124901

Walter, F., Riechers, D., Cox, P., et al. 2009, Nature, 457, 699

Wang, R., Wagg, J., Carilli, C. L., et al. 2011, AJ, 142, 101

Wang, R., Wagg, J., Carilli, C. L., et al. 2013, ApJ, 773, 44

Wang, J.-M., Du, P., Li, Y.-R., et al. 2014, ApJ, 792, L13

Willott, C. J., Delfosse, X., Forveille, T., Delorme, P., & Gwyn, S. D. J. 2005, ApJ, 633, 630

Willott, C. J., Delorme, P., Omont, A., et al. 2007, AJ, 134, 2435

Willott, C. J., Delorme, P., Reylé, C., et al. 2009, AJ, 137, 3541

Willott, C. J., Delorme, P., Reylé, C., et al. 2010a, AJ, 139, 906

Willott, C. J., Albert, L., Arzoumanian, D., et al. 2010b, AJ, 140, 546

Woo, J.-H., Schulze, A., Park, D., et al. 2013, ApJ, 772, 49

Wu, X.-B., & Jia, Z. 2010, MNRAS, 406, 1583

Wu, X.-B., Wang, F., Fan, X., et al. 2015, Nature, 518, 512

Wyithe, J. S. B., & Loeb, A. 2012, MNRAS, 425, 2892

Xie, X., Shen, S., Shao, Z., & Yin, J. 2015, ApJ, 802, L16

Zhang, Z. H., Pokorny, R. S., Jones, H. R. A., et al. 2009, A&A, 497, 619

Zheng, W., Tsvetanov, Z. I., Schneider, D. P., et al. 2000, AJ, 120, 1607

Zier, C., & Biermann, P. L. 2002, A&A, 396, 91

Appendix A

Optical Images and Source Catalog of *AKARI* NEP-Wide Survey Field

Publication: The Astrophysical Journal Supplement, Volume 190, Issue 1, pp. 166-180 (2010)

ABSTRACT

We present the source catalog and the properties of the $B-, R-$, and $I-$band images obtained to support the *AKARI* North Ecliptic Pole - Wide (NEP-Wide) survey. The NEP-Wide is an *AKARI* infrared imaging survey of the North Ecliptic Pole covering 5.8 deg^2 area over 2.5 – 6 micron wavelengths. The optical imaging data were obtained at the Maidanak Observatory in Uzbekistan using the Seoul National University 4k × 4k Camera (SNUCAM) on the 1.5m telescope. These images cover 4.9 deg^2 where no deep optical imaging data are available. Our $B-, R-$, and $I-$band data reach the depths of ∼23.4, ∼23.1, and ∼22.3 magnitudes (AB)

at 5σ, respectively. The source catalog contains 96,460 objects in $R-$band, and the astrometric accuracy is about $0.15''$ at 1σ in each RA and Dec direction. These photometric data will be useful for many studies including identification of optical counterparts of the infrared sources detected by *AKARI*, analysis of their spectral energy distributions (SEDs) from optical through infrared, and the selection of interesting objects to understand the obscured galaxy evolution.
Key words: catalogs — galaxies: evolution — galaxies: photometry — surveys

A.1 INTRODUCTION

Recently, the observational study of the cosmic star formation history has been at the center of our efforts to understand the evolution and the formation of galaxies. This is because the observational data play a key role in constraining physical processes governing the evolutionary history of galaxies on which outcomes of the theoretical predictions are strongly dependent. Many studies have been carried out to derive star formation rates in distant galaxies (e.g., Goto et al. 2010; Le Borgne et al. 2009; Le Floc'h et al. 2009; Reddy et al. 2008; Shim et al. 2007; Im 2005), however, there is a major obstacle in such efforts - the dust extinction of the light coming from star formation.

Since the discovery of ultra-luminous infrared galaxies (ULIRGs) and luminous infrared galaxies (LIRGs) by the InfraRed Astronomical Satellite (IRAS), it has been recognized that a significant portion of the light from the star formation is missing in the optical/ultraviolet but emitted in infrared (IR). Therefore, statistical studies of infrared luminous galaxies to reveal the hidden cosmic star formation activities were major themes of the more recent infrared space telescope missions such as the Infrared Space Observatory (ISO), the *Spitzer* Space Telescope, and the *AKARI* Space Telescope. Such studies found that the star formation at higher redshifts ($z \sim 1$) are more obscured than at $z \sim 0$ (e.g., Le Floc'h et al. 2005; Bell et

al. 2007; Goto et al. 2010) underlining the importance of infrared-based studies of galaxies. However, due to the lack of efficient coverage between 10 to 20 μm in the *Spitzer* imaging, comparison of the same rest-frame mid-infrared (MIR) quantities over a wide redshift range is not possible to further examine the usefulness of the MIR star formation indicators at various redshifts and the correlation between the star formation and the relative strengths of MIR spectroscopic features made by molecules such as PolyAromatic Hydrocarbon (PAH) and silicates. The additional MIR coverage at 10 to 20 μm is also advantageous in studying the MIR-excess emission in early-type galaxies (Ko et al. 2009; Shim et al. 2010), and the identification of Active Galactic Nuclei (AGN; e.g., Lee et al. 2007; Huang et al. 2009).

The *AKARI* satellite is an infrared space telescope launched in February 2006. By offering a contiguous, wide-field imaging capability in the wavelength range between 2.5 and 26μm, *AKARI* complements the capability of the *Spitzer* space telescope, and provides an unprecedented view of the universe, especially at 11 and 15μm. Because of the Sun-synchronous orbit of *AKARI*, deep observations can be done only at the North and the South ecliptic poles. Therefore, the North Ecliptic Pole (NEP) survey is one of the important extragalactic surveys of *AKARI*. The NEP survey has two major programs, NEP-Wide and NEP-Deep surveys. The NEP-Wide field covers 5.8 deg^2 centered at NEP, whereas the NEP-Deep field covers 0.38 deg^2 with deeper exposures than the NEP-Wide. Due to the wide field, the contiguous MIR wavelength coverage, and the low extinction value of $E(B-V) = 0.047$ at the center of NEP (Schlegel et al. 1998), the NEP-Wide field is unique for the studies of the extragalactic objects like infrared luminous galaxies and AGNs. For further information about NEP surveys, the readers can refer to Matsuhara et al. (2006), Wada et al. (2007), and Lee et al. (2007, 2009).

Optical imaging data can enhance the value of the unique *AKARI* NEP survey. Since *AKARI* has a low spatial resolution (the full width at half maximum

(FWHM) of the point spread function (PSF) is about $6''$ at 15μm), the optical imaging with a higher resolution can help improving the astrometric accuracy and help deblending confused objects. Also, the optical bands are important to construct multi-wavelength spectral energy distributions (SEDs) of infrared sources such as galaxies and AGNs to understand their properties. There already exist deep optical data covering 2 deg^2 of the central region of the NEP-Wide field, obtained by the Canada-France-Hawaii Telescope (CFHT) with u^*, g', r', i', and z' filters (Hwang et al. 2007). However, there is no deep optical data for the remaining NEP-Wide area. The Digitized Sky Survey images are available, but neither their depths nor spatial resolutions are sufficient (the depth is about 20 mag at R and the seeing is about $3''$ with pixel scale of $1.0''$ at the NEP area) for identifying optical counterparts of many infrared sources. Hence, we observed this remaining NEP-Wide area in optical B, R, and I filters. The BRI filters were chosen because we needed a multiple color set at least three colors to construct the optical part of the SED of galaxy; one blue part, one red part, and a middle part between red and infrared bands. Also, those Bessell filters are wider than the Sloan Digital Sky Survey (SDSS) filters, enabling us to achieve a higher signal to noise ratio (S/N) per unit exposure time than the SDSS filters.

Throughout the paper, we use a cosmology with $\Omega_M = 0.3, \Omega_\Lambda = 0.7$, and $H_0 =$ 70 km s^{-1}Mpc^{-1} (e.g., Im et al. 1997). We also use the AB magnitude system.

A.2 OBSERVATIONS

The *AKARI* NEP-Wide field is centered at $\alpha = 18^h00^m00^s, \delta = +66°36'00''$ covering a circular area of 5.8 deg^2. Our optical BRI imaging survey covers 4.9 deg^2 outside the central 2 deg^2 area of the *AKARI* NEP-Wide. Figure A.1 shows the field coverage of different components of the NEP-Wide survey. The thick, solid circle indicates the *AKARI* NEP-Wide (5.8 deg^2) coverage. The dashed squares are the CFHT

optical survey area. The small squares show the Maidanak optical imaging area. It consists of 70 subfields, each of them having an $18' \times 18'$ field of view. These Maidanak fields are grouped into 4 different sections, East (8 fields), West (7 fields), North (23 fields), and South (32 fields), and we name each subfield with E01–E08, W01–W08, N01–N23, and S01–S32. The names of the subfields and their central positions are listed in Table A.1.

The images were obtained in Bessell B, R, and I filters from 2007 June 12 to August 5 at the Maidanak Observatory in Uzbekistan, using the Seoul National University 4k $\times$ 4k Camera (SNUCAM) on the 1.5 m Richey-Chretien, AZT-22 telescope (Im et al. 2010). The CCD camera has a 4096 $\times$ 4096 format and a pixel scale of $0.266''$ at f/7.75. We used the four amplifier mode for the CCD image readout.

Twilight flats were taken at the start and the end of each night when possible. Since the $I-$band images are found to have complicated fringe patterns, all of the $I-$band images were dithered by $\sim 20''$ in random directions. These dithered images were used to construct the master fringe image. For photometric calibration, we observed photometric standard fields from Landolt (1992) at two different altitudes at least. In most subfields, standard star images were obtained on the same night, but in a few cases no corresponding standard star observations were carried out due to bad weather. In such cases, the photometric calibration was done using a different way, as described in section B.3.3.

Table A.2 summarizes our observations. For each filter, typical total exposure times are 21 min in B, 30 min in R, and 20 min in I filter. The images for a given subfield and a given filter were obtained mostly on a single night so that images are in homogeneous quality at least for a single filter of a given subfield. There are a few exceptions to this rule (3 subfields for $B-$band and 13 subfields for $I-$band). This happened when we needed to take images of a given subfield and a given filter

over two nights due to observational constraints such as the lack of the observing time (e.g., the night was ending before finishing all the images of the subfield), or a rapidly deteriorating weather or seeing. In some cases, the total exposure times and the number of images of each subfield were adjusted to the weather conditions. For example, when there were thin clouds in the sky, the exposure time or the number of images were increased to compensate for the loss of the S/N. The frame times for individual exposures were also adjusted. Shorter exposure times (2 minutes) were used when there were no guide stars, or the weather condition was varying too rapidly. The $B-$ and $R-$band images were mostly taken during the same nights under dark/grey sky to provide images with similar seeing values, but the $I-$band images were taken mostly during the bright time since the depth of $I-$band images is the least influenced by the presence of the moon among the BRI filters. The seeing condition for each subfield was determined as the median value of FWHM of non-saturated point sources with the magnitudes between 13 and 15 mag. In general, the seeing FWHM values of the stacked $R-$band and $I-$band images are stable at $\sim 1.2''$ and $\sim 1.1''$, respectively, but there were more variations in the seeing conditions in $B-$band and the $B-$band images have the worst seeing FWHM values in general among the BRI filters. The maximum and the minimum seeing values among the BRI filter images of a given subfield differ by a factor of 1.5 in median, but in extreme cases, the difference could be as large as a factor of $\sim$2 due to deteriorated seeing conditions in the $B-$band. The 5σ detection limits of each subfield were determined from the sky background sigma, within an aperture diameter of 3 times FWHM value. The detection limits vary from subfield to subfield, but the median 5σ detection limit in $R-$band is 23.1 mag. Table A.3 lists the seeings and 5σ depths for each subfield. Figure A.2 shows the seeing and the 5σ detection limit of the three filters for each subfield.

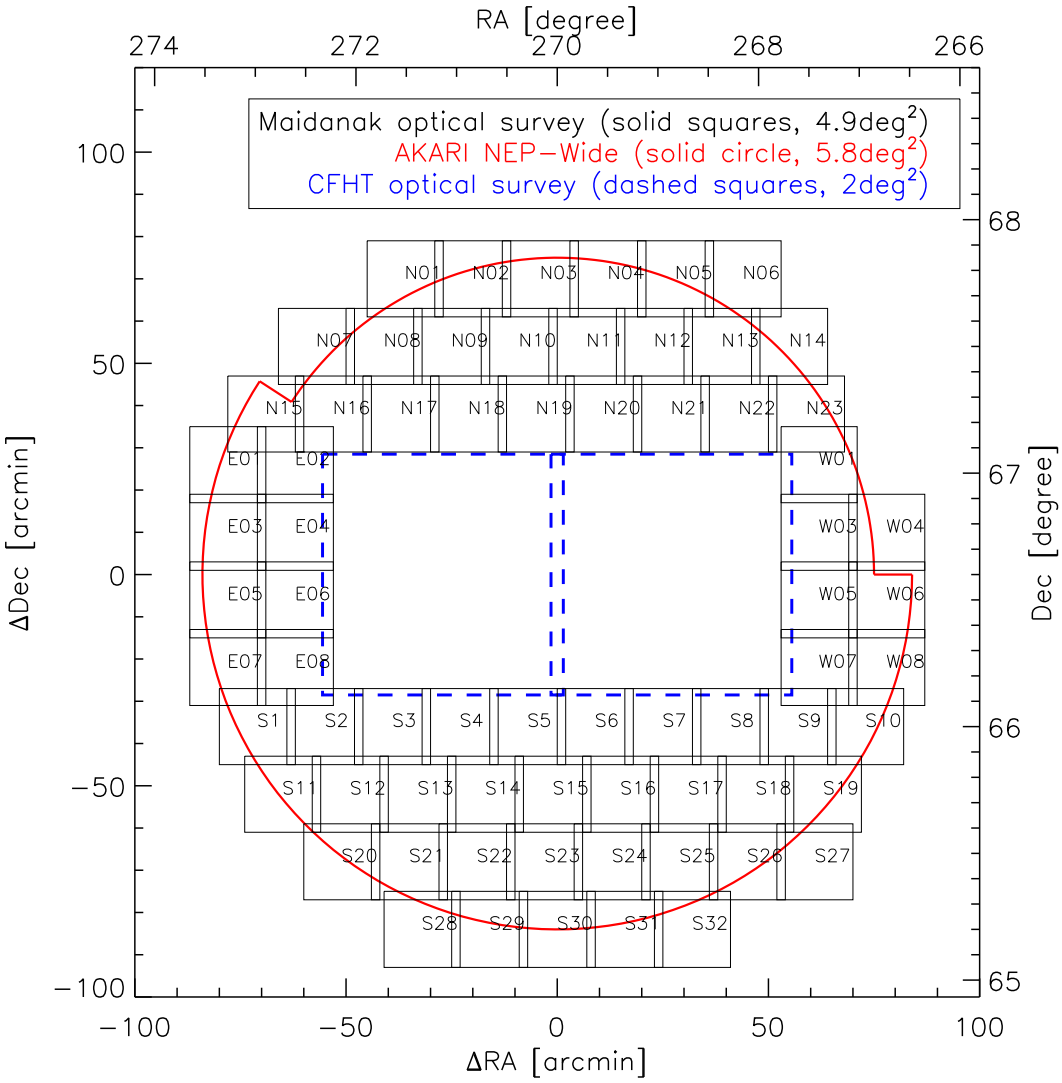

Figure A.1 Field coverage of the NEP-Wide optical survey. The center of the image corresponds to the NEP at $\alpha = 18^h00^m00^s, \delta = +66°36'00''$. Our *BRI* imaging data (4.9 deg^2) are indicated with small squares, while the thick, solid circle and the dashed squares indicate *AKARI* (5.8 deg^2) and CFHT (2 deg^2) coverage, respectively. The *BRI* images consist of 70 fields. The names of the subfields and their central positions are listed in Table A.1.

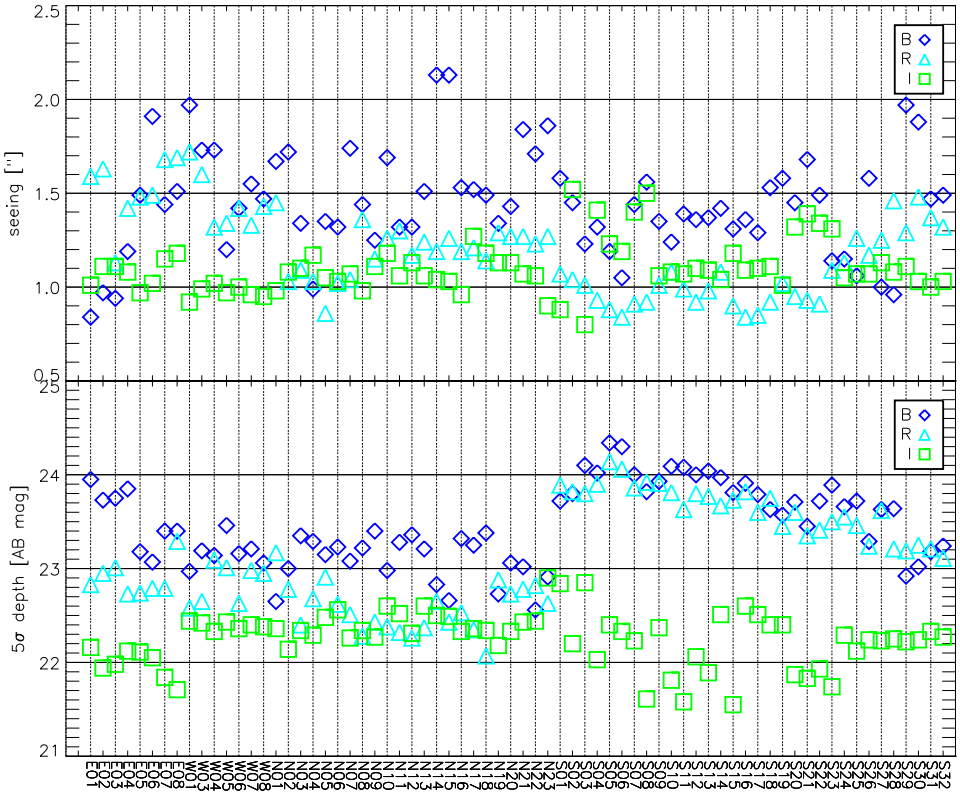

Figure A.2 The upper and the lower panels show the seeing FWHMs and the 5σ detection limits for each subfield, respectively (the diamonds for B, the triangles for R, and the squares for $I-$band).

Table A.1. Names of each subfield in Figure A.1 and their central positions.

Field	RA	Dec	Field	RA	Dec
E01	18:12:44.2	66:59:38.6	N21	17:55:28.5	67:08:38.6
E02	18:10:23.5	66:59:38.6	N22	17:52:47.6	67:08:38.6
E03	18:12:44.2	66:43:38.6	N23	17:50:06.7	67:08:38.6
E04	18:10:23.5	66:43:38.6	S01	18:11:54.0	65:58:38.6
E05	18:12:44.2	66:27:38.6	S02	18:09:13.1	65:58:38.6
E06	18:10:23.5	66:27:38.6	S03	18:06:32.2	65:58:38.6
E07	18:12:44.2	66:11:38.6	S04	18:03:51.3	65:58:38.6
E08	18:10:23.5	66:11:38.6	S05	18:01:10.4	65:58:38.6
W01	17:49:36.5	67:01:38.6	S06	17:58:29.5	65:58:38.6
W03	17:49:36.5	66:45:38.6	S07	17:55:48.6	65:58:38.6
W04	17:47:15.8	66:45:38.6	S08	17:53:07.7	65:58:38.6
W05	17:49:36.5	66:29:38.6	S09	17:50:26.8	65:58:38.6
W06	17:47:15.8	66:29:38.6	S10	17:47:45.9	65:58:38.6
W07	17:49:36.5	66:13:38.6	S11	18:10:53.6	65:44:38.6
W08	17:47:15.8	66:13:38.6	S12	18:08:12.7	65:44:38.6
N01	18:06:22.1	67:40:38.6	S13	18:05:31.8	65:44:38.6
N02	18:03:41.2	67:40:38.6	S14	18:02:51.0	65:44:38.6
N03	18:01:00.3	67:40:38.6	S15	18:00:10.1	65:44:38.6
N04	17:58:19.4	67:40:38.6	S16	17:57:29.2	65:44:38.6
N05	17:55:38.5	67:40:38.6	S17	17:54:48.3	65:44:38.6
N06	17:52:57.7	67:40:38.6	S18	17:52:07.4	65:44:38.6
N07	18:10:03.4	67:24:38.6	S19	17:49:26.5	65:44:38.6
N08	18:07:22.5	67:24:38.6	S20	18:09:23.1	65:30:38.6
N09	18:04:41.6	67:24:38.6	S21	18:06:42.2	65:30:38.6
N10	18:02:00.7	67:24:38.6	S22	18:04:01.3	65:30:38.6
N11	17:59:19.8	67:24:38.6	S23	18:01:20.4	65:30:38.6
N12	17:56:38.9	67:24:38.6	S24	17:58:39.6	65:30:38.6
N13	17:53:58.0	67:24:38.6	S25	17:55:58.7	65:30:38.6
N14	17:51:17.1	67:24:38.6	S26	17:53:17.8	65:30:38.6
N15	18:11:33.9	67:13:38.6	S27	17:50:36.9	65:30:38.6
N16	18:08:53.0	67:08:38.6	S28	18:05:21.8	65:16:38.6
N17	18:06:12.1	67:08:38.6	S29	18:02:40.9	65:16:38.6
N18	18:03:31.2	67:08:38.6	S30	18:00:00.0	65:16:38.6
N19	18:00:50.3	67:08:38.6	S31	17:57:19.1	65:16:38.6
N20	17:58:09.4	67:08:38.6	S32	17:54:38.2	65:16:38.6

Table A.2. Observation summary.

Filter	Total exposure time [min]	Exposure time per image [min]	Seeing [″]	5σ depth [AB mag]	50% Completeness [AB mag]
B	20–45 (21)	2–15	0.8–2.1 (1.4)	22.56–24.34 (23.40)	22.05–23.86 (22.98)
R	18–40 (30)	2–10	0.8–1.7 (1.2)	22.07–24.14 (23.09)	21.75–23.57 (22.60)
I	16–64 (20)	2	0.8–1.5 (1.1)	21.55–22.90 (22.33)	21.16–22.37 (21.85)

Note. — The values in the parentheses are the median values.

Table A.3. Photometric zero-point, seeing, 5σ detection limit, magnitude of the completeness 50%, and magnitude of the reliability 99% for each subfield.

	$B-$band					$R-$band					$I-$band				
Field	Z_p[a] [mag]	Seeing [″]	Depth[b] [mag]	comp50%[c] [mag]	relia99%[d] [mag]	Z_p[a] [mag]	Seeing [″]	Depth[b] [mag]	comp50%[c] [mag]	relia99%[d] [mag]	Z_p[a] [mag]	Seeing [″]	Depth[b] [mag]	comp50%[c] [mag]	relia99%[d] [mag]
E01	22.88	0.84	23.95	23.63	23.62	23.42	1.59	22.83	22.25	22.87	23.32	1.01	22.16	21.79	21.53
E02	22.90	0.97	23.73	23.37	23.73	23.39	1.63	22.95	22.29	23.17	23.32	1.11	21.94	21.61	21.53
E03	22.90	0.94	23.75	23.38	23.71	23.21	1.13	23.01	22.48	22.67	23.32	1.11	21.98	21.69	21.12
E04	22.87	1.19	23.85	23.51	23.45	23.36	1.42	22.73	22.10	22.92	23.32	1.09	22.12	21.81	21.02
E05	22.85	1.49	23.18	22.80	23.54	23.32	1.48	22.74	22.31	22.70	23.32	0.97	22.11	21.66	20.91
E06	22.84	1.91	23.07	22.56	23.00	23.34	1.49	22.79	22.30	22.66	23.32	1.02	22.05	21.79	20.82
E07	22.86	1.44	23.40	22.88	23.22	23.28	1.68	22.79	22.04	22.82	23.32	1.15	21.84	21.16	20.78
E08	22.85	1.52	23.40	22.98	23.57	23.42	1.69	23.29	22.82	23.03	23.32	1.18	21.71	21.29	20.79
W01	22.88	1.97	22.97	22.41	22.89	23.40	1.72	22.58	22.02	22.31	23.37	0.92	22.44	21.97	21.72
W03	22.87	1.73	23.19	22.89	22.80	23.39	1.60	22.65	22.28	22.45	23.37	1.00	22.42	21.88	21.41
W04	22.84	1.73	23.14	22.77	22.81	23.39	1.32	23.09	22.57	22.78	23.37	1.02	22.33	21.84	21.55
W05	22.81	1.20	23.46	23.08	23.00	23.39	1.34	23.01	22.70	22.53	23.37	0.97	22.43	21.96	21.73
W06	22.78	1.42	23.16	22.81	23.01	23.41	1.42	22.63	22.23	22.74	23.36	1.00	22.36	21.75	21.48
W07	22.84	1.55	23.21	22.81	23.09	23.41	1.33	22.98	22.55	22.13	23.36	0.96	22.40	22.11	21.26
W08	22.82	1.47	23.06	22.75	22.28	23.40	1.43	22.95	22.60	22.16	23.36	0.95	22.38	22.11	21.54
N01	22.80	1.67	22.65	22.23	22.02	23.40	1.45	23.17	22.75	22.95	23.36	0.98	22.36	22.04	21.63
N02	22.76	1.71	23.00	22.48	22.79	23.39	1.03	22.78	22.34	21.87	23.36	1.08	22.14	21.79	21.52
N03	22.68	1.34	23.35	22.95	23.11	23.39	1.09	22.40	21.92	22.01	23.40	1.10	22.34	21.84	21.95
N04	22.65	0.99	23.29	23.06	22.41	23.38	1.03	22.68	22.02	21.35	23.40	1.17	22.29	21.83	21.79
N05	22.61	1.35	23.15	22.82	23.17	23.38	0.86	22.91	22.32	21.80	23.40	1.05	22.48	22.03	21.91
N06	22.57	1.32	23.23	22.91	22.58	23.37	1.02	22.62	22.31	21.37	23.40	1.03	22.56	22.23	21.98
N07	22.71	1.74	23.08	22.57	22.95	23.36	1.04	22.51	22.19	21.46	23.40	1.07	22.26	21.85	21.96
N08	22.69	1.44	23.22	22.79	22.72	23.32	1.36	22.28	21.81	21.19	23.40	0.98	22.34	21.82	22.08
N09	22.80	1.25	23.40	22.88	23.36	23.31	1.15	22.43	21.79	21.17	23.40	1.11	22.27	21.89	21.45
N10	22.78	1.69	22.98	22.51	23.24	23.31	1.26	22.38	21.89	20.77	23.38	1.18	22.60	22.09	22.11
N11	22.74	1.32	23.28	22.95	22.96	23.30	1.30	22.32	21.92	20.86	23.38	1.06	22.52	22.11	22.17
N12	22.70	1.32	23.36	23.03	22.99	23.29	1.17	22.26	21.78	20.34	23.38	1.13	22.31	21.87	22.22
N13	22.84	1.51	23.21	22.75	23.20	23.30	1.24	22.37	21.93	21.77	23.38	1.06	22.60	22.25	22.38

Table A.3 (cont'd)

	$B-$band					$R-$band					$I-$band				
Field	Z_p[a] [mag]	Seeing [″]	Depth[b] [mag]	comp50%[c] [mag]	relia99%[d] [mag]	Z_p[a] [mag]	Seeing [″]	Depth[b] [mag]	comp50%[c] [mag]	relia99%[d] [mag]	Z_p[a] [mag]	Seeing [″]	Depth[b] [mag]	comp50%[c] [mag]	relia99%[d] [mag]
N14	22.80	2.13	22.83	22.30	22.71	23.34	1.19	22.65	22.26	22.00	23.38	1.04	22.50	22.00	21.84
N15	22.77	2.13	22.66	22.05	22.79	23.34	1.26	22.43	21.75	21.77	23.31	1.03	22.49	22.23	21.82
N16	22.85	1.52	23.32	22.84	23.29	23.33	1.19	22.53	22.15	21.34	23.31	0.96	22.33	22.02	21.26
N17	22.80	1.52	23.25	22.85	22.70	23.32	1.21	22.35	21.84	21.75	23.37	1.27	22.36	21.74	21.23
N18	22.81	1.49	23.38	23.05	23.15	23.31	1.14	22.07	21.76	21.46	23.34	1.18	22.34	21.74	21.71
N19	22.72	1.34	22.73	22.36	21.52	23.34	1.29	22.88	22.31	22.45	23.33	1.13	22.18	21.87	21.46
N20	22.72	1.43	23.06	22.76	22.70	23.33	1.27	22.73	22.25	22.40	23.37	1.13	22.33	22.10	20.99
N21	22.77	1.84	23.02	22.54	23.31	23.33	1.27	22.78	22.31	22.06	23.37	1.07	22.43	21.97	21.46
N22	22.77	1.71	22.56	22.17	22.43	23.32	1.23	22.82	22.42	21.90	23.36	1.06	22.44	22.13	20.61
N23	22.77	1.86	22.91	22.45	22.96	23.31	1.27	22.63	22.19	21.79	23.39	0.90	22.90	22.23	21.96
S01	22.96	1.58	23.72	23.18	23.76	23.54	1.07	23.89	23.48	23.16	23.42	0.88	22.84	22.37	20.77
S02	22.94	1.45	23.80	23.28	23.82	23.55	1.04	23.82	23.26	23.65	23.14	1.52	22.20	21.79	21.93
S03	23.10	1.23	24.10	23.43	24.18	23.55	1.01	23.80	23.04	23.61	23.43	0.80	22.85	21.94	19.94
S04	22.96	1.32	24.02	23.62	23.62	23.55	0.93	23.90	23.28	23.78	23.12	1.41	22.03	21.52	21.36
S05	23.09	1.19	24.34	23.86	23.10	23.56	0.88	24.14	23.53	23.19	23.42	1.23	22.40	21.78	21.39
S06	23.10	1.05	24.30	23.77	24.16	23.56	0.84	24.06	23.38	23.82	23.12	1.18	22.33	21.76	21.53
S07	23.10	1.44	24.00	23.56	24.12	23.56	0.91	23.86	23.14	23.85	23.06	1.40	22.23	21.81	21.60
S08	22.99	1.55	23.82	23.34	24.12	23.56	0.92	23.92	23.57	23.86	23.03	1.50	21.61	21.28	21.25
S09	23.00	1.35	23.93	23.44	24.18	23.55	1.01	23.91	23.37	23.72	23.14	1.06	22.37	22.09	21.97
S10	23.00	1.24	24.09	23.75	23.96	23.55	1.08	23.81	23.23	23.60	23.03	1.08	21.81	21.57	21.55
S11	23.00	1.39	24.08	23.71	23.78	23.48	0.99	23.63	23.18	23.30	22.73	1.07	21.58	21.28	20.86
S12	23.00	1.36	24.00	23.36	24.03	23.48	0.92	23.80	23.27	23.70	22.68	1.10	22.06	21.78	20.73
S13	23.00	1.37	24.04	23.48	23.50	23.48	0.98	23.77	23.04	23.61	22.78	1.09	21.89	21.35	19.30
S14	23.00	1.41	23.97	23.62	23.96	23.45	1.08	23.67	23.25	23.17	23.29	1.04	22.51	22.08	21.58
S15	22.98	1.31	23.81	23.37	23.97	23.45	0.90	23.73	23.17	23.50	22.18	1.18	21.55	21.21	20.28
S16	22.97	1.36	23.91	23.44	23.61	23.45	0.84	23.82	23.37	23.50	23.28	1.09	22.60	22.24	21.77
S17	22.98	1.29	23.79	23.41	23.68	23.45	0.85	23.60	23.14	23.45	23.27	1.10	22.51	21.86	21.00
S18	22.98	1.53	23.63	23.19	23.98	23.45	0.92	23.75	23.23	23.11	23.21	1.11	22.40	22.00	21.51

A.3 DATA REDUCTION

A.3.1 Preprocessing

We used IRAF[1] `noao.imred.ccdred` package to process raw images. The data were processed with usual reduction procedures such as bias subtractions using a combined bias image and flat-field correction using twilight flat of each night. Dark correction was unnecessary since there is virtually no dark current in the images taken with our CCD camera.

Because the bias subtraction and the flat fielding could not remove the amplifier bias level variations perfectly due to small temporal variations in the bias level, some of the preprocessed images show slightly different bias levels in different quadrants, each representing a section of image read by a single amplifier. To remove this pattern, we determined the background values of the 4 quadrants, and subtracted the differences between the background levels of the 4 quadrant images from each quadrant. Then the background levels are normalized to the background level of a quadrant with the lowest background value.

We removed the fringe pattern in $I-$band following the steps below. First, we created a master fringe image combining all $I-$band images (716 images) in median. Then, before subtracting the master fringe frame, we re-scaled the master fringe frame by an appropriate factor. This scaling factor is taken as the ratio of the median background value of each science image to the master fringe frame background value. Finally, we subtracted the re-scaled master fringe frame from each $I-$band image. We checked the difference in image quality before and after the fringe removal. Before the fringe pattern removal, the large scale fringe pattern varies $\pm 3\%$ of the background level which is comparable to the sky sigma value per

[1]IRAF is distributed by the National Optical Astronomy Observatory, which is operated by the Association of Universities for Research in Astronomy, Inc., under cooperative agreement with the National Science Foundation.

Table A.3 (cont'd)

Field	$B-$band					$R-$band					$I-$band				
	Z_p[a] [mag]	Seeing [″]	Depth[b] [mag]	comp50%[c] [mag]	relia99%[d] [mag]	Z_p[a] [mag]	Seeing [″]	Depth[b] [mag]	comp50%[c] [mag]	relia99%[d] [mag]	Z_p[a] [mag]	Seeing [″]	Depth[b] [mag]	comp50%[c] [mag]	relia99%[d] [mag]
S19	22.97	1.59	23.57	23.11	23.44	23.44	1.02	23.45	23.06	23.35	23.21	1.01	22.40	21.98	21.64
S20	22.97	1.45	23.71	23.30	23.55	23.38	0.95	23.60	23.01	23.24	23.16	1.32	21.87	21.36	21.40
S21	22.96	1.68	23.45	22.96	23.35	23.37	0.93	23.35	22.93	23.15	23.24	1.39	21.83	21.32	21.51
S22	23.05	1.49	23.72	23.26	23.72	23.37	0.91	23.41	22.94	22.91	23.33	1.34	21.93	21.51	21.82
S23	23.04	1.14	23.89	23.34	23.87	23.38	1.09	23.50	22.92	23.51	23.04	1.32	21.74	21.29	21.30
S24	22.91	1.15	23.66	23.26	23.98	23.38	1.13	23.55	23.22	23.18	23.35	1.05	22.29	21.75	21.55
S25	22.89	1.06	23.72	23.31	23.66	23.37	1.26	23.46	23.03	23.08	23.36	1.07	22.12	21.77	21.63
S26	22.62	1.58	23.29	22.87	23.01	23.38	1.17	23.24	22.82	22.74	23.36	1.07	22.24	21.94	21.23
S27	22.83	1.00	23.63	23.23	23.36	23.47	1.25	23.62	22.99	23.40	23.36	1.13	22.23	21.78	21.04
S28	22.82	0.96	23.64	23.28	23.50	23.33	1.46	23.21	22.59	23.19	23.36	1.08	22.25	21.95	21.39
S29	22.98	1.97	22.92	22.41	23.57	23.37	1.29	23.19	22.83	23.08	23.36	1.11	22.22	21.92	21.26
S30	22.52	1.88	23.02	22.42	23.07	23.48	1.48	23.25	22.76	23.47	23.35	1.03	22.24	21.93	21.40
S31	22.94	1.47	23.18	22.82	22.81	23.34	1.37	23.21	22.64	23.25	23.35	1.00	22.33	21.80	21.61
S32	22.92	1.49	23.24	22.87	22.42	23.42	1.32	23.11	22.65	22.85	23.35	1.03	22.27	21.95	21.58

[a]The apparent magnitude is $M = Z_p - 2.5 \log\,(DN/sec)$.

[b]The 5σ detection limit for a circular aperture with diameter of 3 times FWHM

[c]The magnitude corresponding to the completeness 50%

[d]The magnitude corresponding to the reliability 99%

pixel. After the fringe subtraction, the large scale variation is reduced to $< 0.5\%$ of the background or more than 6 times less than the sky sigma value, showing that the fringe pattern is removed successfully well below the sky sigma values.

After the fringe correction and the registration, all images were combined in median. Cosmic rays are removed during the stacking of multiple images with a sigma clipping adopting +3-sigma for rejecting outlier pixels.

A.3.2 Astrometry

To derive astrometry solutions, we used a software named SCAMP which finds astrometry solution by cross-matching automatically an input reference catalog containing a set of accurate RA and Dec values of sources against a list of object positions obtained from an input FITS image (Bertin 2006). In our case, we used USNO-B1 catalog (Monet et al. 2003) as the reference catalog for the astrometry calibration. Astrometry solutions were derived for all the stacked, subfield images in each filter separately. The degree of the polynomial for distortion correction is adopted to be 4, since it gave the best solution among other options. SCAMP can refine the astrometry solution by comparing positions of objects in overlapping images, but the procedure does not apply to our case.

To check the accuracy of the astrometry solution, we compared our catalog with the USNO-B1 catalog stars that had the positional errors of $< 0.2''$ and the apparent magnitudes of $14 < B1 \text{ mag} < 19$. Figure A.3-(a) shows the distribution of the differences in position between the USNO-B1 stars and the corresponding objects in our catalog in RA and Dec directions. Figures A.3-(b) and (c) show the histograms of the astrometric differences between our catalog and USNO-B1 catalog of RA and Dec, respectively. To derive the astrometry error, we fit the histogram of the astrometric differences with Gaussian functions. The dotted lines indicate the best-fit Gaussian function to the distributions. After the fitting, we find that the 1σ

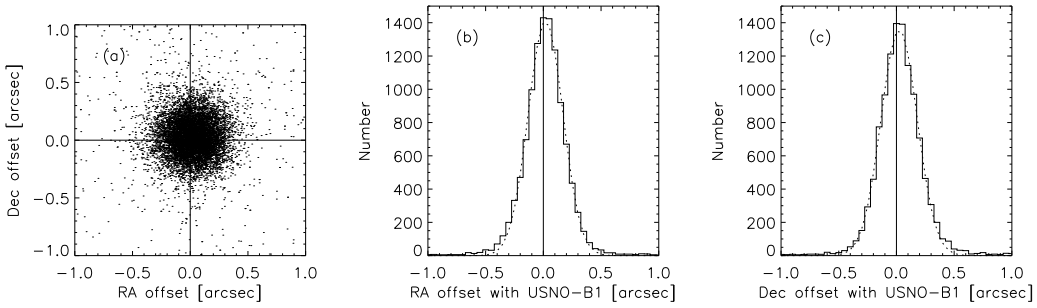

Figure A.3 Distribution (a) of the astrometry differences between our catalog and USNO-B1 catalog, and the histograms of the differences in RA (b) and Dec (c) directions. In (b) and (c), the dotted lines indicate the best-fit Gaussian functions to the histograms of the distribution. From the Gaussian function, the 1σ astrometric errors are $0.16''$ for RA and $0.15''$ for Dec.

astrometric errors are $0.16''$ for RA and $0.15''$ for Dec.

A.3.3 Photometric Calibration

We carried out the photometry calibration using three methods depending on the availability of the standard star data. The first method uses the Landolt standard stars (Landolt 1992). This procedure applies to 25 fields in $B-$band, 25 fields in $R-$band, and 18 fields in $I-$band, where the standard star data were taken at two different altitudes at the least. The adopted standard calibration formula is $m_{ins} - M_{std} = k_0 + k_1 X$, where m_{ins} is an instrumental magnitude ($m_{ins} = 25 - 2.5$ log (DN/sec)), M_{std} is a standard magnitude, k_0 is a zero point, k_1 is an airmass coefficient, and X is an airmass. The instrumental magnitudes were measured within an aperture of a $12''$ diameter on the standard stars. We checked with growth curves that this aperture is large enough to contain virtually all photons from the star irrespective of the seeing of our data. We chose the standard stars that have similar

colors for deriving the coefficients of the above formula. To confirm the effect of not including the color terms, we checked the difference between the listed magnitudes of standard stars with various colors (those not included in the derivation of the photometric zero-points) and the magnitudes of these standard stars derived with our photometry solutions. We find that the rms difference is less than 0.05 mag. That is, the magnitudes derived with our photometry solutions are independent of the color terms well within the error 0.05 mag. This is consistent with the expected variation in the photometric zero points due to neglecting the color term, based on an observational campaign of photometry standards using the SNUCAM at Maidanak (Lim et al. 2009). Therefore we decided to neglect the color term of the formula. We found k_0 and k_1 values for each night and each filter, and derived the standard magnitudes of the objects using these values. The k_0 has the values in the range of 1.67 $\pm$ 0.13 at $B-$band, 1.70 $\pm$ 0.11 at $R-$band, and 2.07 $\pm$ 0.08 at $I-$band. Also, the k_1 have the values of 0.33 $\pm$ 0.05 at $B-$band, 0.10 $\pm$ 0.03 at $R-$band, and 0.04 $\pm$ 0.01 at $I-$band. These values are consistent with values derived from a campaign observation of standard stars (Lim et al. 2009). The zero-point errors were estimated from the rms magnitude differences between the known magnitudes of the standard stars and the magnitudes of the same standard stars derived from our zero-point solution. The zero-point error is about 0.032 mag using this method.

The second photometric calibration method is adopted for the data taken during the nights which have only one altitude data for standard stars (34, 40, and 27 fields at $B-$, $R-$, and $I-$band, respectively.). In such cases, we used other night's k_1 value since the night-to-night variation in k_1 is not significant. This produces an additional zero-point error of 0.028 mag, at most. Consequently, the total error associated with the zero-point determination of the second photometric calibration method is less than 0.040 mag.

The third method of the photometric calibration is applied to the subfields with-

out associated standard star observations. For such fields (11, 5, and 25 fields in $B-$, $R-$, and $I-$band, respectively.), we used photometry of sources in the overlapping area of a neighbor subfield. The corresponding sources that have magnitudes between 12 and 16 mag were used to measure the photometric zero-point. For this method, the zero-point error was derived from the standard deviation of the magnitude offset between the sources in the field where we want to determine the photometric zero-point and the matched sources in the neighbor fields. In this case, the zero-point error is about 0.045 mag with respect to the photometry of the neighbor field. Therefore, the total error in the zero-point for the third method is about 0.032–0.045 mag, depending on the method used for the photometry calibration of the neighbor field.

We checked the consistency of our photometric calibration using an overlap area between two neighboring fields (those that were not used for the photometric calibration of the other field). In the case of the first method, the mean photometry differences are $-0.006\pm$ 0.028 mag in B (30 fields for overlaps), 0.002 $\pm$ 0.033 mag in R (23 fields for overlaps), and 0.001 $\pm$ 0.017 mag in I magnitudes (17 fields for overlaps). In the case of the second method, the mean photometry differences are about 0.002 $\pm$ 0.030 mag in B (37 fields for overlaps), $-0.006\pm$ 0.040 mag in R (44 fields for overlaps), and $-0.022\pm$ 0.035 mag in I magnitudes (20 fields for overlaps). Note that the consistency of our photometric calibration between different nights are well below 0.05 mag for all filters which is expected from the zero-point errors.

The Z_p for each subfield are listed in Table A.3. For the nights which have the k_0 and the k_1 values, the Z_p means $25-(k_0+k_1X)$, i.e. the zero point for converting DN per exposure time to magnitude, including the airmass correction. Therefore we can determine the apparent magnitude M, through $M = Z_p - 2.5\log{(DN/sec)}$. The Z_p can be used for the purpose of checking the depth of each subfield. Figure A.4 shows several depths of each subfield for the three filters. For each subfield, the

depth are checked using the 5σ detection limit, the 50% completeness (see section A.4.4), the 99% reliability (see section A.4.5), or the Z_p, as well as the total exposure time.

A.4 CATALOGS

A.4.1 Object Detection and Photometry

SExtractor (Bertin & Arnouts 1996) was used for the detection and the photometry of objects in the images. We stacked $B-, R-$, and $I-$band images together, and used the BRI stacked image as our object detection image. After many trials of SExtractor parameter sets and examining the detected and the non-detected sources by eye, we chose a set of 1.2σ for DETECT_THRESH, 5 connected pixels for DETECT_MINAREA, DEBLEND_NTHRESH of 64, DEBLEND_MINCONT of 0.005, 200 for BACK_SIZE, and 3 for BACK_FILTERSIZE as the optimal set of detection parameters. Lowering the detection limit produced too many spurious detections and increasing the detection limit tend to miss obvious sources. The adopted detection limit corresponds to the S/N of about 4.5 which is usually an optimal S/N limit for detection of objects (e.g., Shim et al. 2006).

To cross-identify and perform the photometry of objects in each band, we used the ASSOC parameter in SExtractor with a matching radius of $0.658''$, 3σ value of the astrometric error. The above process may miss faint objects which are brighter in a particular filter than the others. To supplement the above source detection, we also ran SExtractor on images in each filter separately. This process reveals faint sources detected in a single filter image, but not detected in the BRI stacked image. These sources detected in a single filter image were also matched with detections in other single filter images with the matching radius of $0.658''$. Adding these faint sources, we detected 63,333 for B, 96,460 for R and 70,492 sources for I filter

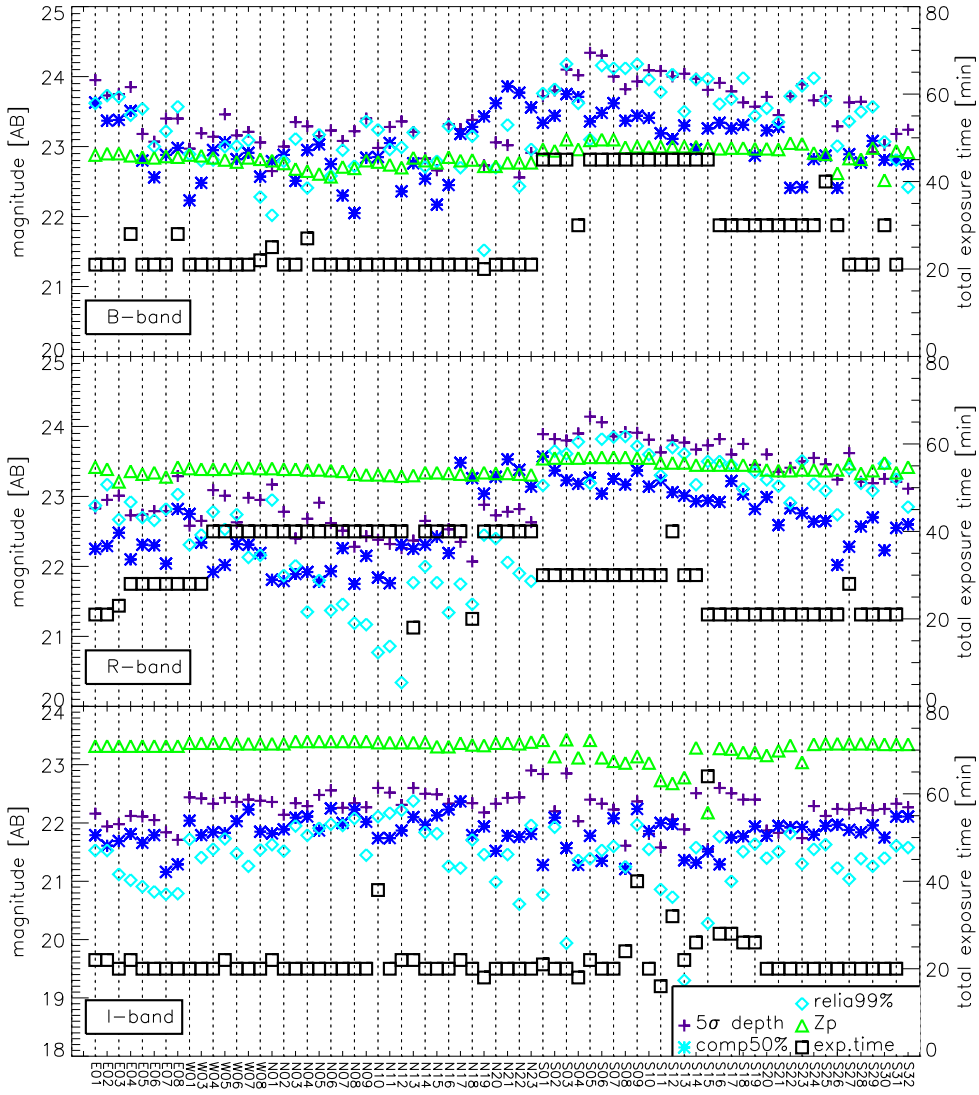

Figure A.4 The figure shows several measures of the image quality and the depth of each subfield, such as the 5σ depth (the cross symbols), the 50% completeness (the asterisks; see section A.4.4), the 99% reliability (the diamonds; see section A.4.5), the photometric zero point, Z_p (the triangles), and the total exposure time (the squares).

over the reliability of 99% (see section A.4.5). Among these objects, 16% in B, 33% in R, and 15% in I are detected only in the single filter images. We derived aperture magnitudes using an aperture of diameter of 3 times FWHM and auto magnitudes with Kron-like elliptical apertures (Kron 1980) which are taken as the total magnitudes . The aperture correction value is 0.10 ± 0.02 mag for all the filters and all the subfields.

The magnitude errors are computed by combining the standard SExtractor estimates and the zero-point errors we estimated. The standard SExtractor error estimates are based on the Poisson statistics, and could underestimate the noise values when the sky noises in adjoining pixels are correlated due to the stacking of the dithered frames (Gawiser et al. 2006). Using a similar procedure described in Gawiser et al. (2006), we calculated how the error within a square aperture of $N \times N$ pixels, σ_N, changes as a function of N. In the case where each pixel noise is uncorrelated with each other, $\sigma_N \propto N$. When the noise is correlated, the exponent of N is greater than 1. In our data, we find $\sigma_N \propto N^{1.14}$. For a magnitude measured within an aperture with $3.0''$ diameter (3 times a typical FWHM of our image), there are about 110 pixels (or $N \simeq 10$). Therefore, the photometric errors of faint objects ($R \gtrsim 22$ mag) could be underestimated by as much as about a factor of 1.4. For the brighter objects ($R \lesssim 20$ mag), the photometric errors are not affected by this effect, since their errors are dominated by the object noise.

For the same object that exist on two or more fields in the overlapping areas, we chose an object that had the smallest FLAGS value from SExtractor (the FLAGS has a nonzero value if the object is blended, saturated, and/or truncated at an edge of a image) and the smallest photometric error. Among the same objects, we only included the one with a better S/N or image quality in the final catalog. The examples of such cases are objects on the edge of an image or objects elongated due to astigmatism near the edge of the CCD in one image, but do not suffer such a

problem in the other. At the bright end, the photometry is free from saturation and non-linearity above $R \simeq 12$ mag. We cut off the faint sources over the magnitude of false detection rate 1% (see section A.4.5).

We found spurious detections due to the reflection halos caused by the bright objects and due to faint, uncorrected fringe patterns in $R-$band images. In case of the reflection halos around bright stars, we divided the bright stars into three classes, and set a radius to define the region where spurious detections lie within it ($120''$ at $8 \leq B$ mag < 10 , $80''$ at $10 \leq B$ mag < 12 , $40''$ at $12 \leq B$ mag < 14). We flag detections inside these radii as 'near_bright_obj', since they are likely to be spurious detections or their photometry are not reliable. We also found many spurious detections in the outer regions of stacked $R-$band images, thus we flag objects that are not matched with $B-$ or $I-$band catalogs and exist within $30''$ from the edge as 'near_edge'. We found 5,186 (5%) of 'near_bright_obj' at $R-$band and 14,833 (15%)of 'near_edge' sources, and checked those spurious sources by eyes. These flags are included in the BRI merged catalog. Also we flag non-stellar sources as 'galaxy' (see, section B.4.4). The flags are marked at the last column of the catalog (Table A.4).

A.4.2 Star-Galaxy Separation

To distinguish stellar sources from other extragalactic sources, we used a $B - H$ vs. $H - N2$ color-color diagram and the SExtractor stellarity index. Here, the stellarity indices measure the likelihood of a source being a point source or an extended source, with the value of 1 for a perfect point source, and 0 for a diffuse, extended source. The stellarities are measured from the single-filter stacked images. However, when we determine whether a source is point-like or extended, we adopted the stellarity value measured in a stacked image in the filter where the photometric error of the source is the smallest. Note that the stellarity values are nearly identical among

Table A.4. $B-, R-$, and $I-$ band merged catalog.

ID	RA	Dec	B_{AUTO}	Error	B_{APER}	Error	R_{AUTO}	Error	R_{APER}	Error	I_{AUTO}	Error	I_{APER}	Error	Stellarity	A_B	A_R	A_I	flags
E01_00001	18:11:06.3	+66:57:11.5	22.88	0.12	23.00	0.10	99.00	99.00	99.00	99.00	99.00	99.00	99.00	99.00	0.89	0.18	0.11	0.08	
E01_00002	18:11:08.9	+66:51:35.9	21.67	0.10	22.35	0.08	99.00	99.00	99.00	99.00	99.00	99.00	99.00	99.00	0.00	0.18	0.11	0.08	
E01_00003	18:11:09.3	+67:07:40.4	23.07	0.16	23.32	0.14	99.00	99.00	99.00	99.00	99.00	99.00	99.00	99.00	0.03	0.19	0.12	0.08	near_bright_obj
E01_00004	18:11:09.3	+66:51:19.9	23.59	0.33	24.10	0.27	99.00	99.00	99.00	99.00	99.00	99.00	99.00	99.00	0.18	0.18	0.11	0.08	galaxy
E01_00005	18:11:09.6	+67:07:54.8	23.39	0.25	23.96	0.24	99.00	99.00	99.00	99.00	99.00	99.00	99.00	99.00	0.64	0.19	0.12	0.08	near_bright_obj
E01_00006	18:11:09.6	+66:51:22.9	23.03	0.21	24.02	0.25	99.00	99.00	99.00	99.00	99.00	99.00	99.00	99.00	0.69	0.18	0.11	0.08	galaxy
E01_00007	18:11:10.2	+67:07:32.0	20.85	0.08	22.52	0.09	99.00	99.00	99.00	99.00	99.00	99.00	99.00	99.00	0.00	0.19	0.12	0.08	near_bright_obj
E01_00008	18:11:10.5	+67:07:51.7	21.90	0.11	23.19	0.13	99.00	99.00	99.00	99.00	99.00	99.00	99.00	99.00	0.01	0.19	0.12	0.08	near_bright_obj
E01_00009	18:11:11.2	+67:05:29.6	22.82	0.18	23.59	0.18	99.00	99.00	99.00	99.00	99.00	99.00	99.00	99.00	0.32	0.19	0.12	0.08	
E01_00010	18:11:11.2	+66:50:56.2	99.00	99.00	99.00	99.00	22.15	0.12	22.21	0.12	99.00	99.00	99.00	99.00	0.36	0.18	0.11	0.08	near_edge
E01_00011	18:11:11.3	+66:50:53.4	99.00	99.00	99.00	99.00	21.91	0.11	22.04	0.12	99.00	99.00	99.00	99.00	0.47	0.18	0.11	0.08	near_edge
E01_00012	18:11:11.4	+67:05:27.2	22.35	0.14	23.33	0.15	99.00	99.00	99.00	99.00	99.00	99.00	99.00	99.00	0.21	0.19	0.12	0.08	galaxy
E01_00013	18:11:11.4	+67:07:10.7	20.55	0.06	20.60	0.06	99.00	99.00	99.00	99.00	99.00	99.00	99.00	99.00	0.98	0.19	0.12	0.08	near_bright_obj
E01_00014	18:11:11.4	+66:50:51.2	99.00	99.00	99.00	99.00	22.77	0.16	22.27	0.14	99.00	99.00	99.00	99.00	0.46	0.18	0.11	0.08	near_edge
E01_00015	18:11:11.5	+66:51:19.2	99.00	99.00	99.00	99.00	22.69	0.17	22.46	0.16	99.00	99.00	99.00	99.00	0.43	0.18	0.11	0.08	near_edge
E01_00016	18:11:11.6	+67:05:27.1	22.95	0.17	23.66	0.19	99.00	99.00	99.00	99.00	99.00	99.00	99.00	99.00	0.71	0.19	0.12	0.08	
E01_00017	18:11:11.7	+67:07:12.8	20.50	0.06	20.62	0.06	99.00	99.00	99.00	99.00	99.00	99.00	99.00	99.00	0.96	0.19	0.12	0.08	near_bright_obj
E01_00018	18:11:11.7	+66:51:04.3	99.00	99.00	99.00	99.00	22.81	0.19	22.53	0.18	99.00	99.00	99.00	99.00	0.40	0.18	0.11	0.08	near_edge
E01_00019	18:11:11.9	+67:07:22.9	23.59	0.79	23.24	0.14	99.00	99.00	99.00	99.00	99.00	99.00	99.00	99.00	0.00	0.19	0.12	0.08	near_bright_obj
E01_00020	18:11:12.1	+66:53:23.3	99.00	99.00	99.00	99.00	18.10	0.05	19.19	0.05	99.00	99.00	99.00	99.00	0.03	0.18	0.11	0.08	

Note. — (1) The identification number of the source. Each ID consists of the subfield name (Figure A.1) and number in the order of their RA.

(2) and (3) The J2000.0 right ascension (RA) and the declination (Dec) of a source in a sexigesimal.

(4)–(15) are the total magnitudes, its magnitude errors, aperture magnitudes and its magnitude errors of a source in the $B-, R-$, and $I-$band. The aperture magnitudes are obtained with the aperture diameter of 3 times FWHM. The magnitudes are not corrected for the extinctions.

(16) The stellarity index of a source from SExtractor. See Figure A.6 for the distribution of this index.

(17–19) The galactic extinction values of $B-, R-$, and $I-$band from extinction map of Schlegel et al. (1998).

(20) The flags parameter. 'near_bright_obj' for the spurious detection near bright stars, 'near_edge' for the spurious detection near the edge of a single image, or 'galaxy' for the non-stellar sources classified at section B.4.4.

different filter images when an object is sufficiently bright ($R < 19$ mag). We also note that the stellarity values are determined from the $R-$band images for most of the objects, since the $R-$band images generally have the highest S/N among the three filters.

The $H-$band magnitudes come from the catalog made from the $J-$ and $H-$band images of the NEP-Wide field which were took with FLAMINGOS on the 2.1m telescope at Kitt Peak National Observatory (Jeon et al., in preparation), and the $N2$ magnitudes come from the *AKARI* observation, of which the effective wavelength is 2.43μm (Lee et al. 2007). We matched the objects detected in $H-$ and $N2-$band with the objects detected in $B-, R-$, and $I-$band using a matching radius of $1.5''$ (for $H-$band) and $3''$ (for $N2-$band), respectively.

Figure A.5 shows the $B - H$ vs. $H - N2$ diagram. Barkhouse and Hall (2001) used $B - J$ vs. $J - K$ colors to distinguish quasars from stars. Instead of $J - K$ color, we used a similar selection method using $H - N2$. On the left panel of Figure A.5, the dots and the contours are made from the object detected in $B-$band with the magnitude error less than 0.1 and matched with H and $N2$ detections. We can notice that there is a stellar locus at $H - N2 \simeq -0.5$ mag with $0 < B - H < 5$. Because most of stars have similar slopes at wavelength greater than 1μm on their SEDs, stars have $H - N2 \sim -0.5$ mag. We checked the stellar locus using stars (the crosses of the right panel of Figure A.5) in NEP-Wide field which had the stellarity greater than 0.8 and the magnitude of $10 < H < 13$. Most of the stars are located at the stellar locus with a few exceptions.

We also checked the location of galaxies using redshift tracks of galaxies. The dashed line is for a star-forming galaxy, M51 (Silva et al. 1998) and the dotted line is for a passively evolving galaxy (see figure caption for the model used for this). We considered the intergalactic medium (IGM) attenuation (Madau et al. 1996) for all redshift tracks. Most of the galaxy track lie in the area of $H - N2$ greater than

-0.2 mag, but galaxies with z $\lesssim 0.1$ lie at $H - N2 < -0.2$ mag. The PSF of galaxy at low redshift (z < 0.1) is in general larger than that of star, so such sources can be identified as extended sources in the image. However, if the low redshift galaxies are faint and small, they may get misclassified as stars with the color cut.

Since the magnitude limit of the H and $N2-$band are different from those in the optical, this method can be applied only to a relatively bright magnitude limit. Also, in order to identify bright, extended sources (namely, low redshift galaxies) in the stellar region on the color-color plot, we apply a stellarity cut where stellarity index has a value between 1 (point sources) and 0 (extended sources).

In summary, we define stellar sources as the following:

Objects with $H - N2 < -0.2$ mag and the stellarity index > 0.2 or
Objects with $H - N2 \geq -0.2$ mag and the stellarity index > 0.8 or
if there is no $H - N2$ color available, stellarity index > 0.8

The first condition weeds out extended objects at low redshift, while the second condition allows us to select clear, point sources in the region of galaxies on the color-color magnitude. The third criterion applies to a small number of objects near the detection limit of optical images, since H and $N2$ images show detections of 98% and 77% of objects brighter than the magnitude cut of the catalog at 50% completeness limit.

A.4.3 Catalog Format

The $B-, R-$, and $I-$band merged catalog is presented in Table A.4. The catalog contains objects that are deemed to be reliable above 99% confidence where the confidence values are derived independently for each subfield in each filter (see section A.4.5). Our catalog contains each object's identification number (ID), RA, Dec, the total magnitude and its error in each band, the aperture magnitude within a circular aperture with a diameter of 3 times FWHM and its error in each band,

the stellarity value from SExtractor, the galactic extinction value from the extinction map of Schlegel et al. (1998) for each band, and the flags described in section A.4.1. Note that the listed magnitudes are not corrected for the galactic extinction. The conversion formulas of Vega to AB magnitudes are $B(\mathrm{Vega}) = B(\mathrm{AB}) + 0.09$, $R(\mathrm{Vega}) = R(\mathrm{AB}) - 0.22$ and $I(\mathrm{Vega}) = I(\mathrm{AB}) - 0.45$. The offset values between Vega and AB magnitude are computed from the Vega spectrum (Bohlin & Gilliland 2004) and B, R, and I filter response functions (Bessell 1990) coupled with the CCD quantum efficiency curve. The magnitude error is the square root of the quadratic summation of the photometric measurement error and the zero-point error from the photometric calibration. We use a dummy value of 99.00 for non-detection.

Figure A.6 shows the stellarity distribution (the left three panels) and the photometric error distribution (the right three panels) for all sources detected in $B-, R-$, and $I-$ band images. The white lines on the right panels show the mode values for each magnitude bins, with the 25% and 75% quartiles indicated with error bars. The spread of the data points in the magnitude versus error plots are caused mainly by varying depths of the data from different subfields. On average, the photometric error is less than 0.1 mag at $B \lesssim 22.5$ mag, $R \lesssim 22$ mag, and $I \lesssim 21$ mag.

A.4.4 Completeness

Since the source detection near the detection limit is dominated by the detections performed on the single filter image ($\simeq 90\%$ of the faintest sources of $R-$band are detected only in the single filter image) rather than the BRI stacked images, we computed the completeness using the $B-$, $R-$, and $I-$band single filter images of each subfield, to examine the completeness of the source detection. To estimate the completeness, we created artificial objects for each magnitude bin from 12 to 23.5 mag and placed them randomly in the background regions of the single filter images. The artificial objects are made of 100 point sources and 100 extended sources where

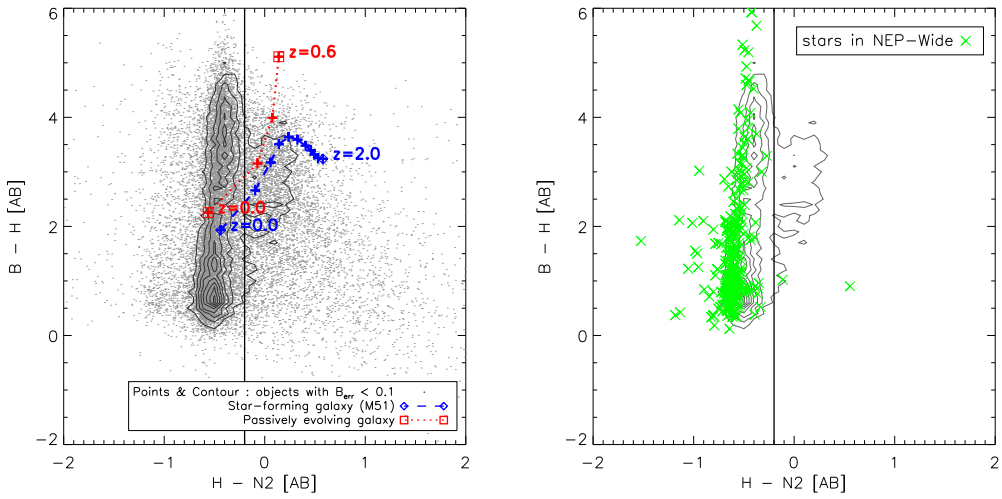

Figure A.5 $B-H$ vs. $H-N2$ color-color diagrams and the density contours of sources detected in B, H, and $N2$. The points and the contours in both figures are made with objects that have $B-$band magnitude errors less than 0.1 mag. The dashed line is a redshift track of a star-forming galaxy (M51) and the dotted line is for a passively evolving galaxy made with the Bruzual & Charlot (2003) model of a passively evolving 5 Gyr-old galaxy with spontaneous burst, metallicity of Z=0.02, and the Salpeter IMF. We use the vertical line as a boundary that distinguishes stellar sources against galaxies and AGNs. In the right panel, we overlay stars in the NEP-Wide field (crosses) to indicate the effectiveness of the color-cut in separating stars from galaxies.

the elliptical galaxies account for 40% of the extended sources. These artificial objects are created using the `noao.artdata` package of the IRAF. After performing detection and photometry of these artificial sources with the same parameter setting as those applied to the actual images, we calculated the completeness, which is defined as the ratio of the number of detected artificial sources to the number of input objects for each magnitude bin. Figure A.7 shows the completeness of $B-$, $R-$,

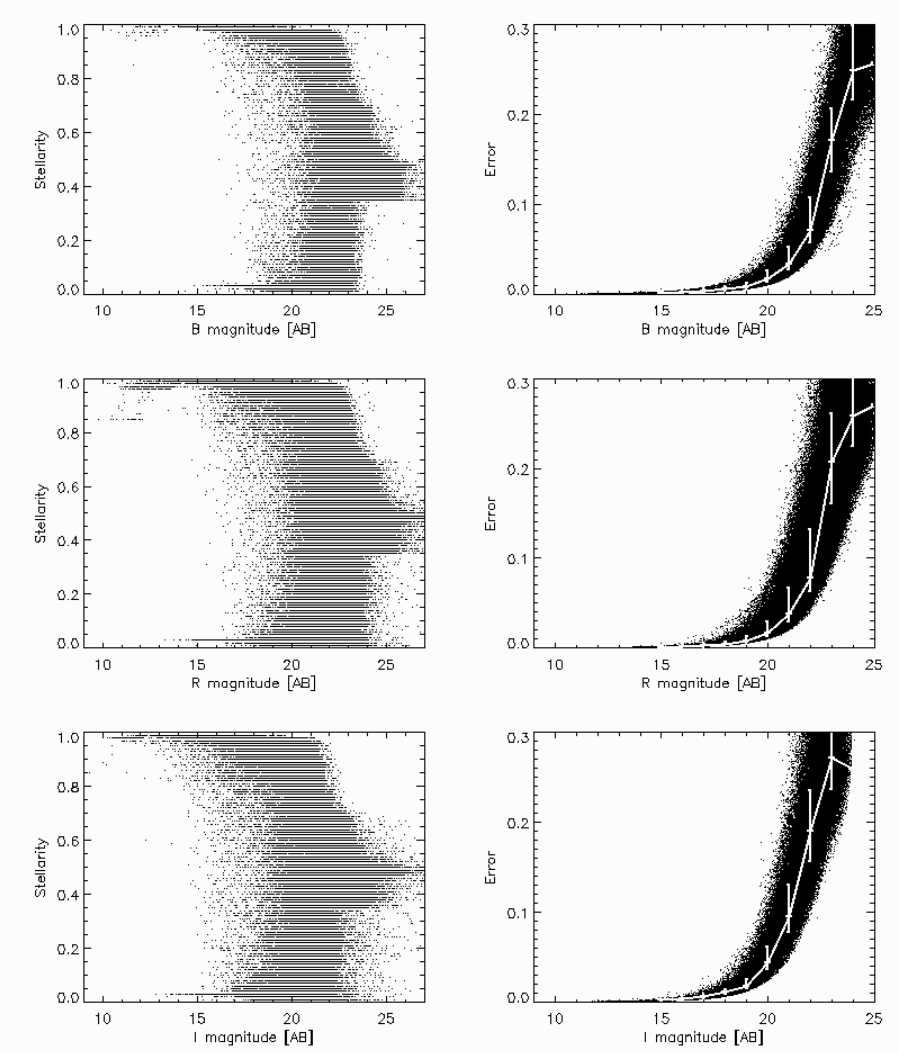

Figure A.6 SExtractor stellarity distribution and the photometric error distribution for all sources detected in $B-$, $R-$, and $I-$ band images, respectively. The stellarity index has a value between 1 (point sources) and 0 (extended sources). In the right panel, we calculated the mode values of photometric error for each magnitude bin and let the 25% and 75% quartiles of the distributions as the error for each point. For $B \lesssim 22.5$ mag, $R \lesssim 22$ mag, and $I \lesssim 21$ mag, the photometric error is less than 0.1 mag.

and $I-$ band data. The gray solid lines in Figure A.7 represent the completeness of all the subfields calculated with this method. We overploted the deepest (S05 in B, S05 in R and N23 in I) and the shallowest (N22 in B, N18 in R, and S15 in I) fields in the 5σ depths with the black solid lines. The galaxy number counts (see section B.5.1) after the corrections based on these completeness result match the number counts from deeper surveys, meaning that our completeness estimates are reasonable. Figure A.4 shows the 50% completeness as the asterisks for each subfield, as well as the 5σ depth, the 99% reliability (see section A.4.5), the Z_p, and the total exposure time. The magnitudes of completeness 50% for each subfield are presented in Table A.3. We can see that the magnitudes at 50% completeness are brighter than the ones of 5σ detection limits by a few tenths of magnitude.

A.4.5 Reliability

We examined the reliability of our detections using false detection rates for each filter and for each subfield. Here, we define false detection rate as the ratio of the number of objects detected in a negative image to the number of objects detected in the original image at a given magnitude bin. The negative image means the original image multiplied by -1. By this definition, an image with noises only would have the false detection rate of 1, while an image containing objects but with no noise would have the false detection rate of 0. When estimating the false detection rates, we excluded areas where objects are marked with 'near_edge', since the inclusion of such area could disproportionately overestimate the false detection rate in the other areas which occupy most of the image.

Figure A.8 shows the false detection rates of $B-, R-$, and $I-$band data. The magnitude of the false detection rates 1% (or the reliability 99%) of all the subfields are indicated in Table A.3. Also, Figure A.4 shows the 99% reliability as diamond symbols for each subfield, as well as the 5σ depth, 50% completeness, the Z_p, and

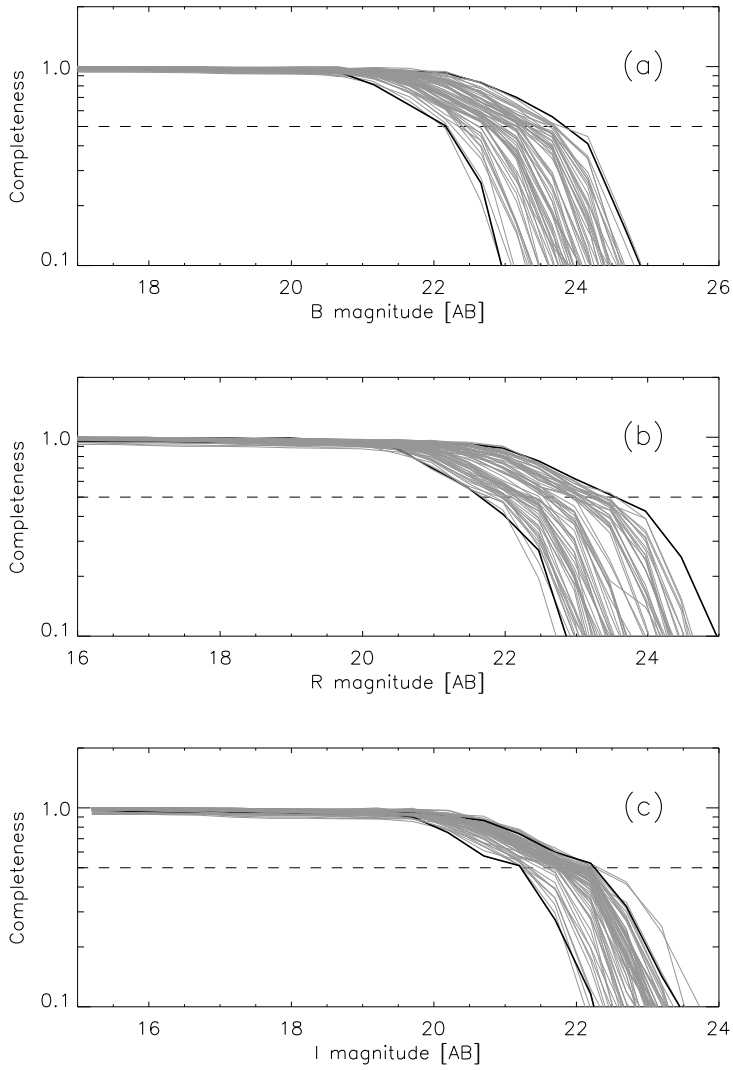

Figure A.7 Completeness for $B-, R-$, and $I-$band. The gray solid lines are the completeness of all subfields from the simulation method, especially for the deepest fields (S05 for B, S05 for R, and N23 for I;the upper black solid lines) and the shallowest fields (N22 for B, N18 for R, and S15 for I;the lower black solid lines) in the 5σ depths. The horizontal dashed line is for 50% completeness cut. The magnitudes of completeness 50% for each subfield are shown in Table A.3.

the total exposure time. Figure A.4 show that the magnitude limit of reliability 99% is greater than the 50 % completeness limit for $B-$ and $R-$band, except $\simeq$20 fields. The 99% reliability limit in $I-$band is consistently brighter than the 50% completeness limit by 0.3 mag. The systematic trend arises from false detections of the fringe patterns left in $I-$band image even after the fringe subtraction. Field-to-field variations of false detection rates and the completeness limits are much larger for R-band than the other filters. It is due to the large difference of the image depths of each subfield in $R-$band, where some fields (from N02 to N23) have relatively small depth with the 5σ limit < 22.5. It is because of the moon phase since these images were taken during full moon phase (29 July – 1 August).

As a separate exercises, we examined the magnitude distribution of objects marked as 'near_edge' or 'near_bright_obj'. Note that most of these objects are likely to be spurious detections. 80% of these sources are found to be fainter than the magnitude limit of the 99% reliability. The 99% reliability cut of the catalog removes most of the spurious detections, but we note that objects marked with 'near_edge' or 'near_bright_obj' should be treated with caution.

A.5 PROPERTIES OF THE DATA

A.5.1 Galaxy Number Counts

To obtain the depth and homogeneity of this survey, we show the galaxy number count as a function of magnitude. The total area in which we used the galaxy number count of bright galaxies is about 3.8 deg^2 where $H-$ and $N2-$band data are also available. We take the Poisson error as the error estimate of number counts.

We calculated the number of galaxies per square degree at each magnitude bin. Since the depth of each subfield is different from another, the combined number counts of all the NEP survey fields were computed following the steps below. First,

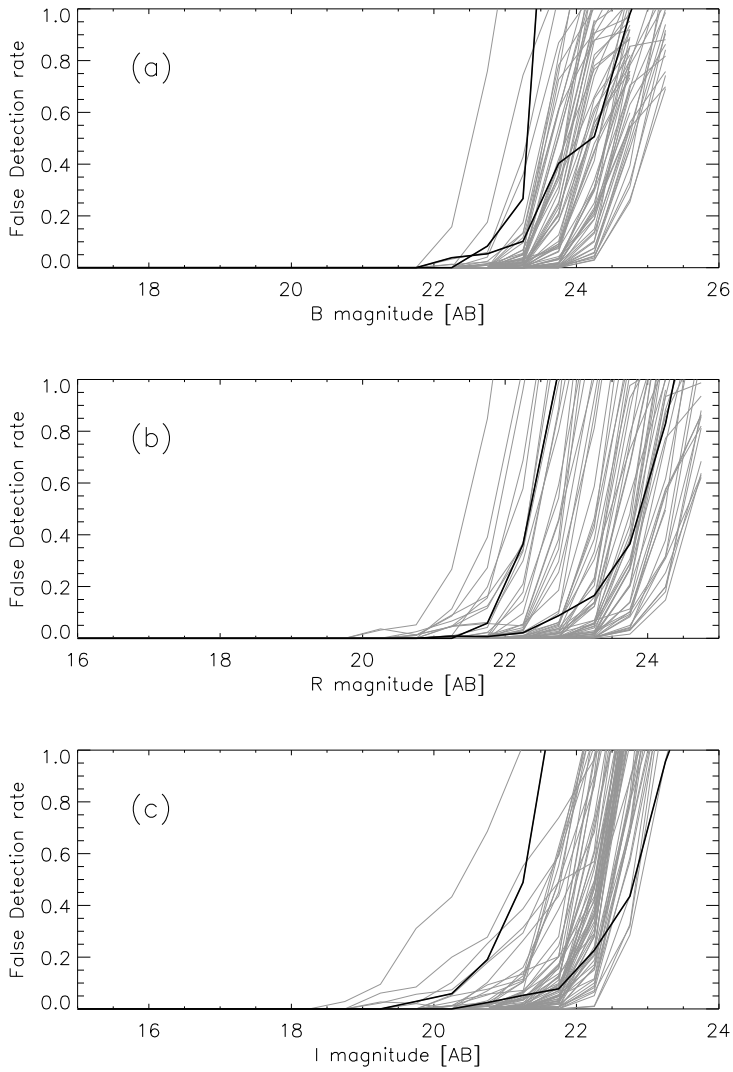

Figure A.8 False detection rate (the ratio of the number of objects detected in the negative image to the number of objects detected in the original image for each magnitude bin) of all subfields in $B-, R-$, and $I-$band. The black solid lines are for the deepest or the shallowest fields as same as Figure A.7. The magnitudes of false detection rate 1% for each field are shown in Table A.3.

the number count was computed for each subfield up to the completeness limit of 50% as determined in section A.4.4. Then, the completeness correction was applied to the number count of each subfield. Finally, we combined the number counts from all the subfields to derive the final number count result. With this method, the bright end of the number counts, usually susceptible to field-to-field variations, include the data from all the 70 fields, while the deepest number counts include the data from the deepest subfields only. We also calculated the number count of stars using the stellar objects of magnitude brighter than the completeness limit of $\sim 50\%$.

Figure A.9 displays the galaxy and the stellar number counts in $B-, R-$, and $I-$band. The lower solid line with crosses represents raw number count and the upper solid line with crosses is the number count after applying correction for the completeness. The solid line with asterisks shows the number count of stars. Also we compare our number counts with those in the literature (Arnout et al. 1999, 2001; Bertin & Dennefeld 1997; Capak et al. 2004; Couch et al. 1993; Hogg et al. 1997; Infante et al. 1986; Jones et al. 1991; Kron 1978; Kummel & Wagner 2001; Lilly et al. 1991; Mamon 1998; McCracken et al. 2003; Metcalfe et al. 1995, 2001; Picard 1991; Postman et al. 1998; Smail et al. 1995; Stevenson et al. 1986; Tyson 1988; Yasuda et al. 2001). Since some of the filter systems in the literature are slightly different from ours, we applied the magnitude transformation by Metcalfe et al. (1995, 2001) to the literature values. We can see that our number counts match with others. The galaxies and stars number count data are provided in Table A.5.

A.5.2 Color-Magnitude Diagram

Figure A.10 displays the color-magnitude diagrams of R vs. $B-R$ (left) and its histograms (right). The upper panel shows the diagram for galaxies with R magnitude error less than 0.1, and the lower panel shows for the stars as the same conditions

Table A.5. Galaxy and stellar number counts.

	$B-$band				$R-$band				$I-$band			
mag	galaxy number	error	corrected number	star number	galaxy number	error	corrected number	star number	galaxy number	error	corrected number	star number
15.75	3.68E+00	9.85E-01	3.68E+00	1.46E+02	1.13E+01	1.73E+00	1.13E+01	2.24E+02	9.21E+00	1.56E+00	9.21E+00	2.72E+02
16.25	3.42E+00	9.49E-01	3.42E+00	1.74E+02	1.71E+01	2.12E+00	1.71E+01	2.96E+02	1.76E+01	2.15E+00	1.76E+01	3.35E+02
16.75	6.58E+00	1.32E+00	6.58E+00	2.19E+02	2.58E+01	2.61E+00	2.58E+01	3.27E+02	3.30E+01	4.28E+00	3.31E+01	4.03E+02
17.25	1.26E+01	1.82E+00	1.26E+01	2.49E+02	4.24E+01	3.34E+00	4.24E+01	3.91E+02	5.93E+01	5.91E+00	5.95E+01	5.04E+02
17.75	2.13E+01	2.37E+00	2.13E+01	2.92E+02	8.58E+01	4.75E+00	8.58E+01	4.58E+02	1.03E+02	9.62E+00	1.03E+02	5.84E+02
18.25	2.97E+01	2.80E+00	2.97E+01	3.42E+02	1.15E+02	8.29E+00	1.15E+02	5.25E+02	1.95E+02	1.42E+01	1.97E+02	7.06E+02
18.75	5.55E+01	3.82E+00	5.55E+01	3.73E+02	2.19E+02	1.27E+01	2.20E+02	5.99E+02	3.34E+02	3.08E+01	3.38E+02	7.96E+02
19.25	8.05E+01	4.60E+00	8.05E+01	3.91E+02	3.73E+02	2.81E+01	3.78E+02	7.24E+02	5.07E+02	7.27E+01	5.30E+02	8.81E+02
19.75	1.27E+02	5.77E+00	1.27E+02	4.78E+02	6.00E+02	5.98E+01	6.20E+02	8.28E+02	7.29E+02	1.02E+02	7.87E+02	9.12E+02
20.25	1.99E+02	2.62E+01	2.02E+02	5.38E+02	9.25E+02	9.37E+01	9.78E+02	9.36E+02	1.08E+03	1.24E+02	1.24E+03	9.83E+02
20.75	3.76E+02	5.74E+01	3.89E+02	6.09E+02	1.26E+03	1.20E+02	1.38E+03	1.02E+03	1.54E+03	1.49E+02	2.01E+03	1.05E+03
21.25	6.59E+02	8.96E+01	7.10E+02	7.69E+02	1.48E+03	1.38E+02	1.73E+03	1.00E+03	2.02E+03	1.70E+02	3.12E+03	9.80E+02
21.75	9.65E+02	1.12E+02	1.11E+03	8.38E+02	1.71E+03	1.47E+02	2.21E+03	8.55E+02	...	...	...	...
22.25	1.41E+03	1.35E+02	1.88E+03	9.24E+02	2.36E+03	1.71E+02	3.37E+03	7.24E+02	...	...	...	...
22.75	2.01E+03	1.58E+02	2.97E+03	9.31E+02	3.37E+03	2.02E+02	5.56E+03	6.31E+02	...	...	...	...
23.25	3.13E+03	1.95E+02	5.09E+03	7.14E+02	6.12E+03	2.73E+02	1.12E+04	3.98E+02	...	...	...	...

Note. — Units of the galaxy and stellar number densities and their errors are Numbers $0.5\mathrm{mag}^{-1}$ deg^{-2}.

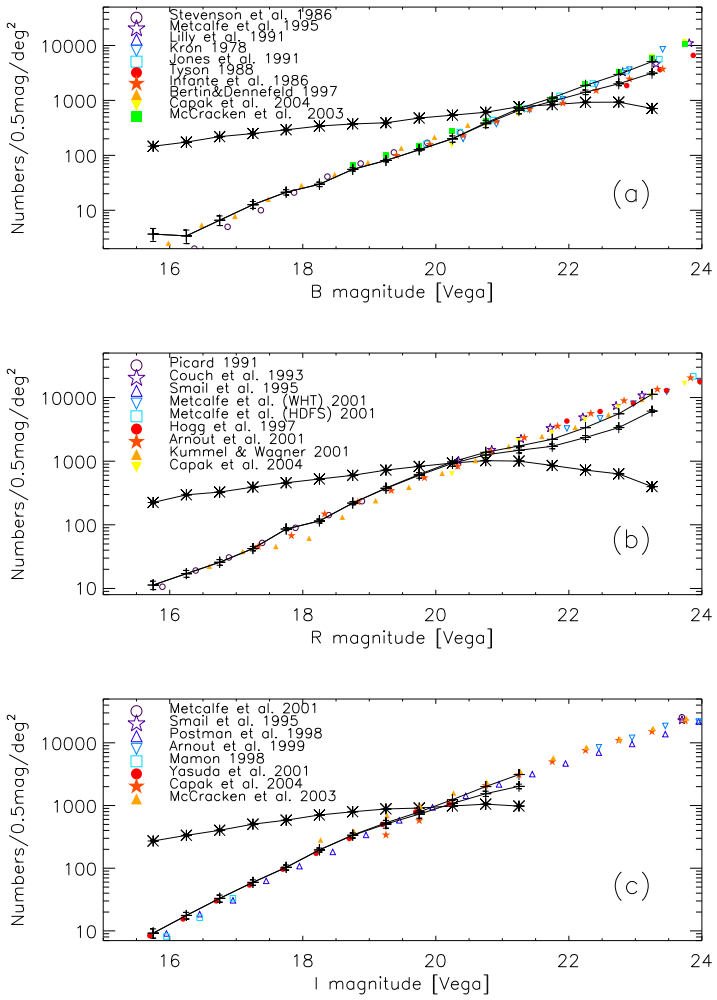

Figure A.9 Galaxy and stellar number counts of $B-, R-$, and $I-$band (two solid lines with crosses). The error estimates of number counts are the Poisson errors. The lower solid line is for galaxy number count without completeness correction, and the upper solid line is from the galaxy number count corrected using the completeness. We compare our number counts with the number counts in the literature (other symbols). The solid lines with asterisks are for the number count of stars. The galaxy and stellar number count data are provided in Table A.5.

with galaxies in the upper panel. We checked positions of galaxies on the color-magnitude diagram traced by the redshifts. The dotted line represents a redshift track of a star-forming galaxy, M51 (Silva et al. 1998), and the dashed line is for a passively evolving galaxy. The SED of a passively evolving galaxy is for a 5 Gyr old stellar population, created with the Bruzual & Charlot (2003) model, assuming a spontaneous burst of single stellar population with metallicity of Z=0.02 and the Salpeter IMF. We included the attenuation of galaxy light due to the IGM when computing the colors (Madau et al. 1996). Two different lines represent galaxies with characteristic absolute magnitudes: for an early type galaxy, the characteristic absolute magnitude, $M^*(r^*)$, is taken as $-20.75+5\log h$, and for a late type galaxy, $-20.30+5\log h$ is adopted for $M^*(r^*)$ (Nakamura et al. 2003). To convert the r^*-band magnitude to the $R-$band magnitude, we used the magnitude transformation relation of Jester et al. (2005), and $g-r\simeq 0.8$ as the mean color of galaxies. The k corrections are calculated from the templates of two galaxies in a standard manner. The $B-R$ colors of elliptical and spiral galaxies are 1–1.5 mag at z=0.1. For $0.2\leq$ z ≤ 0.6, the elliptical galaxies have the $B-R$ values of 1.5–3 mag and the spiral galaxies have the $B-R$ values of 1–1.5 mag. The color-magnitude plot shows that our B and $R-$band images detect galaxies at $z=0$ through $z=0.6$, and galaxies brighter than $M^*(r^*)$ to higher redshifts ($z\sim 1$). On the other hand, we find bimodality in the color-magnitude diagrams of stellar objects (bottom plot, Figure A.10). The bimodality originates from G dwarfs that dominate the color at $B-R\simeq 0.5$ and M Giant stars at $B-R\simeq 2$. Figure A.11 displays the color-magnitude diagrams in I vs. $R-I$ (left) and its histograms (right) with the sources of the I magnitude error less than 0.1. The symbols and the tracks are the same as in Figure A.10. The $R-I$ color of elliptical and spiral galaxies is 0.3–0.5 at z $\lesssim 0.2$ and 0.5–0.9 at z $\simeq 0.5$. Like Figure A.10, the distribution of objects in the I versus $R-I$ plot confirm that $I-$band images have the depth similar to the $R-$band

images in terms of detecting galaxies at different redshifts. We can notice that the model colors of $B-R$ and $R-I$ are consistent with the distributions of galaxies. We expect that the combination of the optical data and the *AKARI* infrared data to provide a unique view on the evolution of galaxies, such as the morphological transformation process through studying MID excess emission in early-type galaxies (Ko et al. 2009).

A.6 DISCUSSION

Here, we investigate how our data compare with other similar optical datasets, and explore the potential of selecting high redshift galaxies and quasars using the data.

First, many extragalactic surveys have been performed with various depths and area coverage. The 5.8 deg^2 coverage of the NEP-Wide survey is wider than that of the Cosmic Evolution Survey (COSMOS, Scoville et al. 2007), or other deeper surveys such as DEEP2 (Davis et al. 2003) and the Great Observatories Origins Deep Survey (GOODS, Dickinson et al. 2003). On the other hand, the area coverage is smaller than that of the *Spitzer* Wide-Area Infrared Extragalactic Survey (SWIRE) survey (Lonsdale et al. 2003) by a factor of 10 with a similar depth in infrared as well as optical ancillary datasets. In terms of the depth and area coverage, our survey is most similar to the *Spitzer* First Look Survey (FLS, Fadda et al. 2004). Our infrared depth is a bit shallower than those of the FLS, while we provide a contiguous wavelength coverage including 11 to 15 micron. Consequently, our optical imaging depths are designed to match the infrared survey depths, thus about a magnitude shallower than the $R-$band depth of the FLS ancillary data.

Next, we discuss the usefulness of our datasets for selecting high redshift objects such as Lyman Break Galaxies (LBGs) and quasars. Figure A.12 shows color-color diagrams in $B-R$ vs. $R-I$. We plotted sources with R and I magnitude errors less than 0.07 mag as gray points which correspond to objects with $R \lesssim 21.0$–23.0

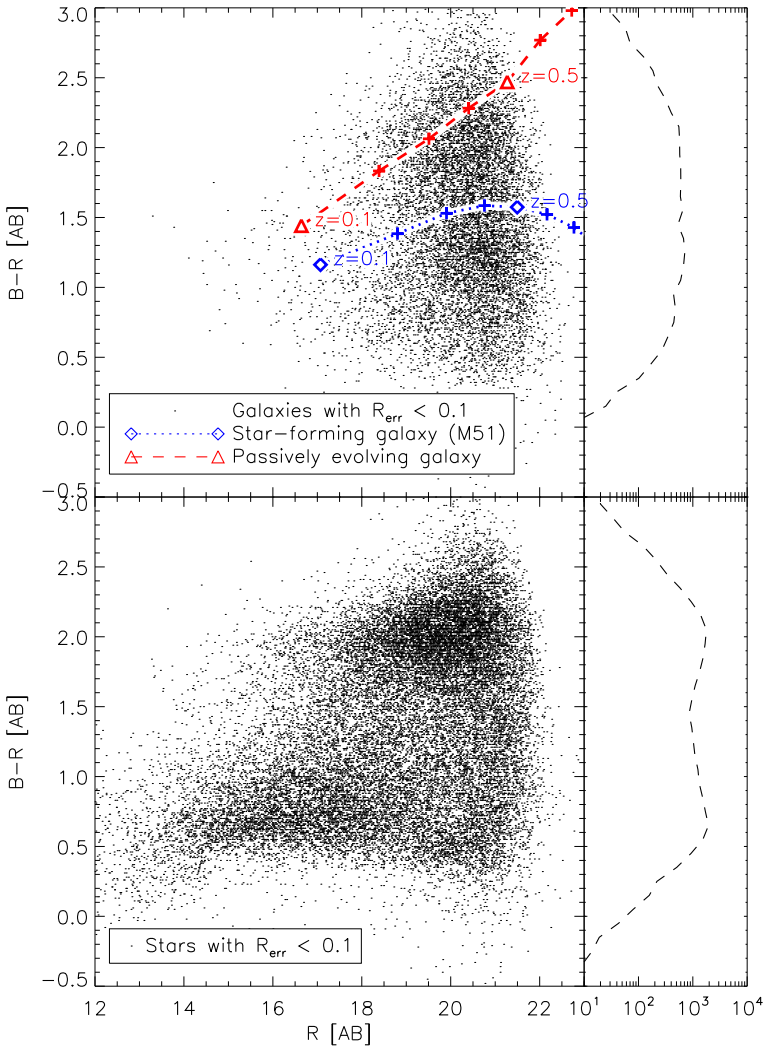

Figure A.10 The color-magnitude diagram of R vs. $B-R$ (left) and histograms showing the distribution $B-R$ colors (right). The upper panel shows the galaxies with R magnitude error less than 0.1. The dotted line is a redshift track for a star-forming galaxy (M51) and the dashed line is for a passively evolving galaxy. The redshift track is for galaxies with the characteristic absolute magnitudes (see the text). The lower panel shows the stars of the same conditions in the upper panel.

mag, and $I \lesssim 20.4$–21.8 mag. The dashed line with diamonds represents a redshift track for a star-forming galaxy (M51, Silva et al. 1998) and the dotted line with squares is a redshift track of a median composite spectrum of SDSS quasars from Vanden Berk et al. (2001). The attenuation of the source light below Lyman α due to IGM is calculated using the model of Madau et al. (1996). Using the redshift tracks as a guide, we define a selection box in the color-color diagram where objects at z $>$ 3.5 can be found ($B-$band dropouts; e.g., Steidel et al. 1999; Giavalisco et al. 2004; Kang & Im 2009; Glikman et al. 2010). The selection box is defined with the following equations:

$$B - R \geq 2 \tag{A.1}$$

$$B - R \geq 4(R - I) + 0.8 \tag{A.2}$$

Although LBGs could be found in this selection box in principle, the expected number of the $B-$dropout galaxies in our data is very low. Extrapolating the surface number density of z $\sim$ 4 LBGs from Steidel et al. (1999) assuming an exponential decrease of the brightest objects as in the Schechter function, we expect about one or less than one $B-$dropout galaxies at $I < 21.5$ mag. On the other hand, the number density could be higher by a factor of 10 or so, if the bright end of the luminosity function flattens due to AGN contribution as seen in the luminosity functions of $U-$band dropout objects at $z \sim 3$ (e.g., Hunt et al. 2004; Shim et al. 2007). In our data, we identify $\sim$800 $B-$dropout candidates in the selection box, but we believe that most of these are interlopers such as stars and low redshift galaxies due to the large mismatch with the expected number.

The expected number of quasars over the 4.9 deg^2 is $\lesssim$ 10 at $I < 20$ mag (Richards et al. 2006), or 10 and 20 at $R < 21.5$ mag and 22.5 mag, respectively (Glikman et al. 2010). After inspecting images of the B-dropout candidates visually and examining their multi-wavelength SEDs from the optical through the MIR

11μm-band of *AKARI*, we identify at least several objects that have the SED shapes consistent with those of high redshift quasars. Judging from the shapes of the SEDs, most of the interlopers are low redshift galaxies or late-type stars. The selection of quasar candidates at $z > 3.5$ is ongoing, and we expect that the identification of z $\sim$ 4 quasars at these magnitude limits will be valuable for constraining the faint-end slope of quasars at high redshift (e.g., Glikman et al. 2010).

A.7 SUMMARY

We have shown the characteristics of $B-, R-$, and $I-$band data at Maidanak Observatory from the follow-up imaging observation of the *AKARI* NEP-Wide field. Using the SNUCAM on the 1.5m telescope, we covered 4.9 deg^2 with the 5σ depth of $\sim$23.4, $\sim$23.1, and $\sim$22.3 magnitudes (AB) at $B-, R-$, and $I-$band, respectively. We detected 63,333 sources in $B-$band, 96,460 objects in $R-$band, and 70,492 in $I-$band. These data are now being used to identifying optical counterparts for accurate astrometry of infrared sources and deblending of confused sources. Also, our data provide a multi-wavelength coverage of the NEP-Wide field, enabling detailed SED analysis. Through these SEDs, we can get key physical properties such as stellar mass and photometric redshifts, and select interesting objects such as high redshift quasars. Spectroscopic follow-up surveys are being conducted on infrared luminous objects using the information gathered from this imaging survey.

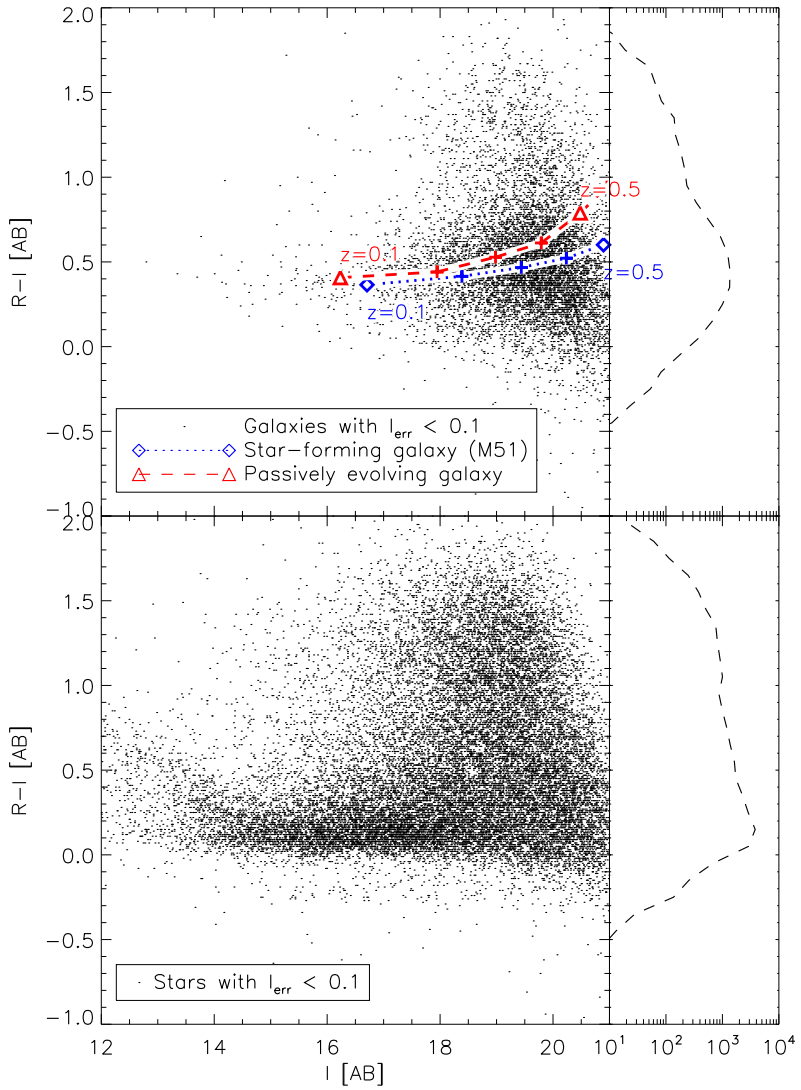

Figure A.11 I vs. $R-I$ color-magnitude diagrams (left) and the distribution of $R-I$ colors (right) with the sources of I magnitude error less than 0.1. The upper panel is for the galaxies and the lower panel is for the stars. The symbols are the same as those in the Figure A.10.

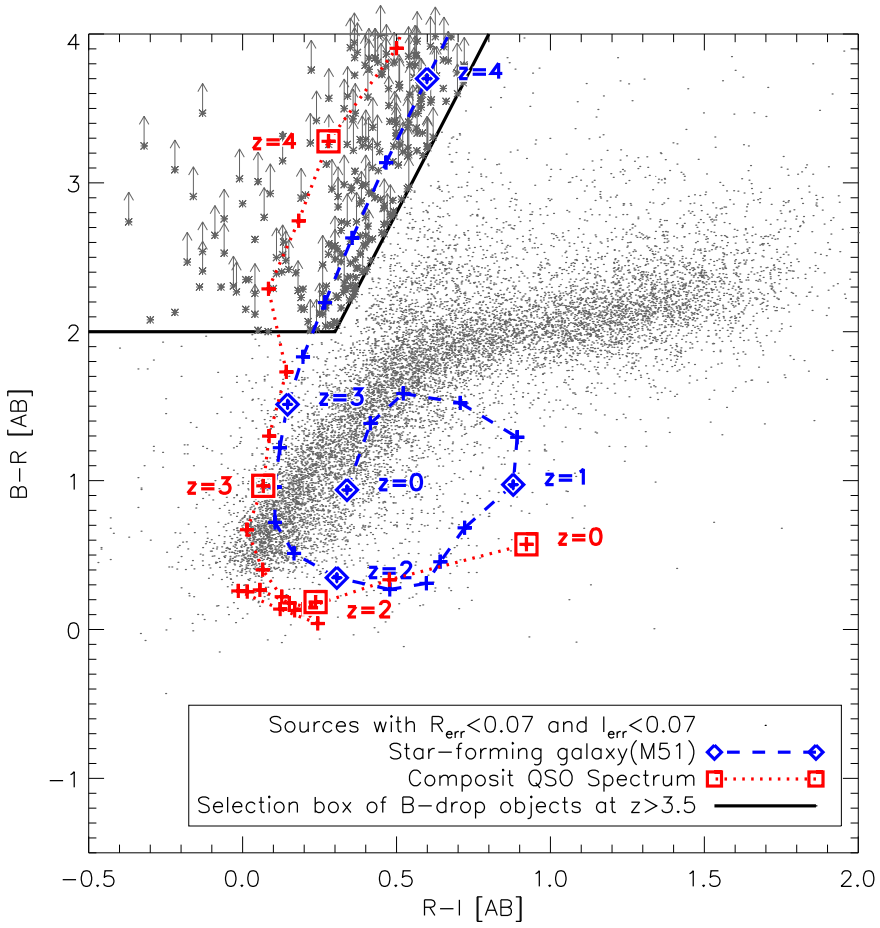

Figure A.12 The color-color diagrams of $B-R$ vs. $R-I$ and the redshift tracks of a star-forming galaxy and a quasar. The gray points are sources with R and I magnitude errors less than 0.07. The dashed line with diamond points represents a track for M51, and the dotted line with squares is for a redshift track made from a median composite spectrum of SDSS quasars from Vanden Berk et al. (2001). The black boxed area in the upper-left corner defines the selection region for high redshift objects at z $>$ 3.5. The asterisks show the sources in this area and the asterisks with arrows indicate objects with 2σ lower limits for $B-R$ colors, when the object was not detected in $B-$band.

Bibliography

Arnouts, S., et al. 2001, A&AS, 379, 740

Arnouts, A., DOdorico, S., Cristiani, S., Zaggia, S., Fontana, A., & Giallongo, E., 1999, A&AS, 341, 641

Barkhouse, W. A. & Hall, P. B. 2001, AJ, 121, 2843

Bell, E. F., Zheng, X. Z., Papovich, C., Borch, A., Wolf, C., & Meisenheimer, K. 2007, ApJ, 663, 834

Bertin, E. 2006, Astronomical Data Analysis Software and Systems XV, 351, 112

Bertin, E. & Arnouts, S. 1996, A&AS, 117, 393B

Bertin, E. & Dennefeld, M., 1997, A&AS, 317, 43

Bessell, M. S. 1990, PASP, 102, 1181

Bohlin, R. C. & Gilliland, R. L. 2004, AJ, 127, 3508

Bruzual, G., & Charlot, S. 2003, MNRAS, 344, 1000

Capak, P., et al. 2004, AJ, 127, 180

Couch, W.J., Jurcevic, J., & Boyle, B.J., 1993, MNRAS, 260, 241

Davis, M., et al. 2003, Proc. SPIE, 4834, 161

Dickinson, M., & Giavalisco, M. 2003, The Mass of Galaxies at Low and High Redshift, ed. R. Bender & A. Renzini (New York: Springer), 324

Fadda, D., Jannuzi, B. T., Ford, A., & Storrie-Lombardi, L. J. 2004, AJ, 128, 1

Gawiser, E., et al. 2006, ApJS, 162, 1

Giavalisco, M., et al. 2004, ApJ, 600, L93

Glikman, E., Bogosavljević, M., Djorgovski, S. G., Stern, D., Dey, A., Jannuzi, B. T., & Mahabal, A. 2010, ApJ, 710, 1498

Goto, T., et al. 2010, A&A, 514, A6

Hogg, D.W., Pahre, M.A., McCarthy, J.K., Cohen, J.G., Bland-ford, R., Smail, I., & Soifer, B.T., 1997, MNRAS, 288, 404

Huang, J.-S., et al. 2009, ApJ, 700, 183

Hunt, M. P., Steidel, C. C., Adelberger, K. L., & Shapley, A. E. 2004, ApJ, 605, 625

Hwang, N. et al. 2007, ApJS, 172, 583

Im, M., Griffiths, R. E., & Ratnatunga, K. U. 1997, ApJ, 475, 457

Im, M. 2005, J. Korean Astron. Soc, 38, 135

Im, M., Ko, J., Cho, Y., Choi, C., Jeon, Y., Lee, I., & Ibrahimov, M. 2010, J. Korean Astron. Soc, 43, 75

Infante, L., Pritchet, C., & Quintana, H., 1986, AJ, 91, 217

Jester, S. et al. 2005, AJ, 130, 873

Jones, L.R., Fong, R., Shanks, T., Ellis, R.S., & Peterson, B.A., 1991, MNRAS, 249, 481

Kang, E., & Im, M. 2009, ApJ, 691, L33

Ko, J., et al. 2009, ApJ, 695, L198

Kron, R. G. 1980, ApJS, 43, 305

Kron, R. G. 1978, PhD thesis, University of California at Berkeley.

Kummel, M. W. & Wagner, S. J., 2001, A&AS, 370, 384K

Landolt, A. U. 1992, AJ, 104, 340

Lee, H. M. et al. 2007, PASJ, 59S, 529

Lee, H. M. et al. 2009, PASJ, 61, 375

Le Floc'h, E., et al. 2005, ApJ, 632, 169

Le Floc'h, E., et al. 2009, ApJ, 703, 222

Le Borgne, D., Elbaz, D., Ocvirk, P., & Pichon, C. 2009, A&A, 504, 727

Lim, B. et al. 2009, JKAS, 42, 161

Lilly, S.J., Cowie, L.L., & Gardner, J.P., 1991, ApJ, 369, 79

Lonsdale, C. J., et al. 2003, PASP, 115, 897

Madau, P., Ferguson, H. C., Dickinson, M. E., Giavalisco, M., Steidel, C. C., & Fruchter, A. 1996, MNRAS, 283, 1388

Mamon, Gary A. 1998, in Wide Field Surveys in Cosmology, ed., S. Colombi, Y. Mellier, & B. Raban (Gif-sur-Yvette : Editions Frontie‘res), 323

Matsuhara, H. et al. 2006, PASJ, 58, 673

McCracken, H. J. et al. , 2003, A&AS, 410, 17

Metcalfe, N., Shanks, T., Campos, A., McCracken, H. J., & Fong, R. 2001, MNRAS, 323, 795

Metcalfe, N., Shanks, T., Fong, R., & Roche, N. 1995, MNRAS, 273, 257

Monet, D. G. et al. 2003, AJ, 125, 984

Nakamura, O. et al. 2003, AJ, 125, 1682N

Picard, A., 1991, AJ, 102, 445

Postman, M., Lauer, T.R., Szapudi, I., & Oegerle, W., 1998, ApJ, 506, 33

Reddy, N. A., Steidel, C. C., Pettini, M., Adelberger, K. L., Shapley, A. E., Erb, D. K., & Dickinson, M. 2008, ApJS, 175, 48

Richards, G. et al. 2006, AJ, 131, 2766

Schlegel, D. J., Finkbeiner, D. P., & Davis, M. 1998, ApJ, 500, 525

Scoville, N., et al. 2007, ApJS, 172, 1

Shim, H., Im, M., Pak, S., Choi, P., Fadda, D., Helou, G., & Storrie-Lombardi, L. 2006, ApJS, 164, 435

Shim, H., Im, M., Choi, P., Yan, L., & Storrie-Lombardi, L. 2007, ApJ, 669, 749

Shim, H. et al. 2010, ApJ, submitted

Silva, L. et al. 1998, ApJ, 509, 103

Smail, I., Hogg, D.W., Yan, L., & Cohen, J.G., 1995, ApJ, 449, L105

Steidel, C. C., Adelberger, K. L., Giavalisco, M., Dickinson, M., & Pettini, M. 1999, ApJ, 519, 1

Stevenson P. R. F., Shanks T., & Fong R., 1986, in Chiosi C., Renzini A., eds, Spectral Evolution of Galaxies. Reidel, Dordrecht p. 439

Tyson, J.A., 1988, AJ, 96, 1

Vanden Berk, D. E. 2001, AJ, 122, 549

Wada, T. et al. 2007, PASJ, 59S, 515

Yasuda, N. et al. 2001, AJ, 122, 1104

Appendix B

J and *H*-band Imaging of *AKARI* North Ecliptic Pole Survey Field

Publication: The Astrophysical Journal Supplement, Volume 214, Issue 2, article id. 20, 15 pp. (2014)

ABSTRACT

We present the J and $H-$band source catalog covering the *AKARI* North Ecliptic Pole field. Filling the gap between the optical data from other follow-up observations and mid-infrared (MIR) data from *AKARI*, our near-infrared (NIR) data provides contiguous wavelength coverage from optical to MIR. For the J and $H-$band imaging, we used the FLoridA Multi-object Imaging Near-ir Grism Observational Spectrometer (FLAMINGOS) on the Kitt Peak National Observatory 2.1m telescope covering a 5.1 deg^2 area down to a 5σ depth of $\sim$21.6 mag and $\sim$21.3 mag (AB) for J and $H-$band with an astrometric accuracy of $0.14''$ and $0.17''$ for 1σ in

R.A. and Decl. directions, respectively. We detected 208,020 sources for $J-$band and 203,832 sources for $H-$band. This NIR data is being used for studies including analysis of the physical properties of infrared sources such as stellar mass and photometric redshifts, and will be a valuable dataset for various future missions.
catalogs — galaxies: evolution — galaxies: photometry — infrared: galaxies — surveys

B.1 INTRODUCTION

AKARI is an infrared (IR) space telescope launched in 2006 (Murakami et al. 2007) which has conducted an all-sky survey in far-IR (FIR) as well as imaging observations of regions of special interest from near-IR (NIR) to FIR. Since *AKARI* was placed on a Sun-synchronous orbit, it conducted deep observations only toward the north and the south ecliptic poles. Observing these areas in the contiguous nine passbands between 2.4 and 26μm covering NIR to mid-IR (MIR), *AKARI* provided valuable NIR to MIR imaging survey data where the *Spitzer Space Telescope* has limitations, especially at the 11, 15, and 18μm bands.

Taking the advantage of the Sun-synchronous orbit, *AKARI* carried out deep surveys with nine filters of the InfraRed Camera (IRC) that cover from 2 to 26 μm contiguously toward the region around the North Ecliptic Pole (NEP; Matsuhara et al. 2006; Wada et al. 2007; Lee et al. 2007, 2009). The NEP survey is composed of two main programs, NEP-Wide and NEP-Deep surveys. The NEP-Wide survey (Lee et al. 2009; Kim et al. 2012) covers the entire 5.4 deg^2 to the depths of 20.9 (AB mag) to 17.8 (AB mag) from 2.4 to 24 μm (5σ point-source sensitivity), whereas the NEP-Deep survey (Wada et al. 2008; Takagi et al. 2012) covers a 0.67 deg^2 area with exposures 3–10 times longer than the NEP-Wide survey. With its continuous MIR wavelength range and wide field of view, *AKARI* NEP survey provides a unique dataset for the study of galaxy evolution, and it has been used to unveil the link

between the star formation and the active galactic nucleus activity of distant galaxies (Karouzos et al. 2014; Hanami et al. 2012), the cosmic star formation history beyond z > 1 (Goto et al. 2010), the properties of polycyclic aromatic hydrocarbons luminous galaxies (Takagi et al. 2010; Ohyama et al. 2007), the environmental dependence of star formation activities of galaxies in a supercluster and MIR-excess of early-type galaxies (Ko et al. 2012), and the nature of sources in 11 and 15 μm limited samples (Lee et al. 2007; Matsuhara et al. 2007; Pearson et al. 2010). Derivation of the accurate local luminosity functions in MIR is under progress (Kim et al., in preparation), by utilizing the subsequent spectroscopic survey data (Shim et al. 2013).

For the *AKARI* NEP field, a considerable amount of ground-based ancillary datasets have been obtained. Figure B.1 shows the filter response curves of the multi-wavelength datasets used in the *AKARI* NEP field survey. Follow up imaging data observed by the MegaCam of the Canada-France-Hawaii Telescope (CFHT) with u^*, g', r', i', and z' filters covers 2 deg^2 of the central region of the NEP field (Hwang et al. 2007, thick dotted blue lines in Figure B.1). Also for the remaining area, Jeon et al. (2010) provided optical data of B, R, and $I-$band covering 4.9 deg^2 (thick gray lines in Figure B.1) using the Seoul National University 4k × 4k Camera (SNUCAM; Im et al. 2010) on the 1.5m Ritchey-Chrétian, AZT-22 telescope at the Maidanak observatory. Spectroscopic data of 1796 sources were obtained using Hectospec of MMT and Hydra of the WIYN telescope (Shim et al. 2013). The radio data were taken with the Westerbork Radio Synthesis Telescope (WSRT) over a 1.7 deg^2 area around NEP (White et al. 2010), and ultraviolet (UV) imaging data were obtained with the *Galaxy Evolution Explorer (GALEX)* at Far-UV and Near-UV (Malkan et al., in preparation). More recently, the entire *AKARI* NEP field has been covered by the Spectral and Photometric Imaging Receiver (SPIRE; Griffin et al. 2010) and a part of the NEP area is covered by the Photoconductor Array Camera

and Spectrometer (PACS; Poglitsch et al. 2010) of the *Herschel Space Observatory* (Serjeant et al. 2012). In addition, the NEP-Deep area has been observed for optical/NIR images with the Subaru telescope and the CFHT (Oi et al. 2014) and in optical spectroscopy with the DEep Imaging Multi-Object Spectrograph (DEIMOS) on the Keck telescope (Takagi et al., in preparation). We summarized the information of the multi-wavelength surveys for the optical, NIR and MIR bands in Table B.1 for NEP-Wide and Table B.2 for NEP-Deep.

The *AKARI* data (Kim et al. 2012, thin solid red lines and thin dashed red lines in Figure B.1) covers a wavelength range from 2.4 to 24μm with nine filters ($N2, N3, N4, S7, S9W, S11, L15, L18W$, and $L24$, where the number indicates the central wavelength of the filter in μm), while the ground-based imaging data offering the coverage at $\lambda < 0.9$ μm. However there is a gap in the wavelength coverage between the optical $I-$band (0.85μm) and the shortest *AKARI* band (2.4μm). Filling this gap in the spectral energy distribution (SED) will significantly enhance the value of the NEP dataset in many ways. First, by adding the NIR data, characterization of the SEDs with a contiguous wavelength range from NIR to MIR will increase the accuracy in estimating stellar masses of low redshift galaxies, because the shorter (or longer) wavelength data may be contaminated by star formation and dust content. Second, the NIR coverage can help improve the photometric redshift estimation by sampling crucial wavelengths at which some prominent features, such as the 1.6μm bump or the 4000Å break, may reside for low redshift or high redshift galaxies, respectively.

The NEP field has served as a major survey field for extragalactic astronomy for *AKARI*, and *Herschel* missions, but it is also poised to do so in future missions such as *Euclid* (Laureijs et al. 2011), Space Infrared Telescope for Cosmology and Astrophysics (*SPICA*; Serjeant et al. 2012), Cosmic Infrared Background Experiment (*CIBER*; Bock et al. 2013), extended ROentgen Survey with an Imaging Telescope

Array (eROSITA; Merloni et al. 2012), and LOw-Frequency ARray (LOFAR; van Haarlem et al. 2013). In order to fill the gap in the wavelength coverage and to enhance the scientific value of the *AKARI* NEP survey, we conducted an imaging observation of the entire NEP survey area in J, and H-band (thick black lines in Figure B.1). Here, we present the J and $H-$band data of the *AKARI* NEP field. This paper is organized as follows. In Section B.2, we describe the details of the observations. In Section B.3, data reduction processes are explained. In Section B.4, we describe the source detection and photometry along with the properties of the data and provide the J and $H-$band merged catalog. In Section B.5, we provide the result from our data such as source number counts and color-magnitude diagrams. We summarize our results in the final section. Throughout this paper, we use a cosmology with $\Omega_M = 0.3, \Omega_\Lambda = 0.7$, and $H_0 = 70$ km s^{-1}Mpc^{-1}. We use the AB magnitude system.

B.2 OBSERVATIONS

The *AKARI* NEP field is centered at $\alpha = 18^h00^m00^s, \delta = +66°33'38''$ and our NIR data cover the entire *AKARI* 's NEP field area. Figure B.2 (left) shows tiling components of our NIR data (small empty green squares; each of them has a $21' \times 21'$ field of view.) as well as the field coverage of the *AKARI* NEP surveys (solid red circles) and its multi-wavelength follow-up observations. The two dashed blue squares show the coverage of the CFHT observation ($u^*g'r'i'z'-$bands) and the gray area is for the Maidanak observation ($BRI-$bands). The four filled orange squares have J and K_s-band imaging data introduced in Imai et al. (2007) covering only the NEP-Deep area. The right panel of Figure B.2 shows the same field coverage as the left one, but shows the field name for each subfield of our NIR data. From FLM01 to FLM66, 65 tiles constitute the NEP NIR area. Three subfields, FLM64 to FLM66, have only $H-$band data from our observation, because this area overlaps

Table B.1. Information of the multi-wavelength survey for the optical, NIR and MIR bands in NEP-Wide survey.

Instrument	Area (deg^2)	Pixel Size ($'' \ pix^{-1}$)	Filter	Effective Wavelength (μm)	Sensitivity (5σ, AB mag)	Reference
MegaCam (CFHT)	2	0.19	$u*$	0.37	25.8	Hwang et al. (2007)
			g'	0.49	25.9	
			r'	0.63	25.4	
			i'	0.77	24.6	
			z'	0.89	23.7	
SNUCAM (Maidanak 1.5m)	4.9	0.27	B	0.44	23.4	Jeon et al. (2010)
			R	0.64	23.1	
			I	0.79	22.3	
FLAMINGOS (KPNO 4m)	5.1	0.30	J	1.25	21.6	This work
			H	1.64	21.3	
IRC (AKARI)	5.4	1.46×1.46	$N2$	2.4	20.9	Kim et al. (2012)
			$N3$	3.2	21.1	
			$N4$	4.1	21.1	
		2.34×2.34	$S7$	7.0	19.5	
			$S9W$	9.0	19.3	
			$S11$	11.0	19.0	
		2.51×2.39	$L15$	15.0	18.6	
			$L18W$	18.0	18.7	
			$L24$	24.0	17.8	

Table B.2. Same as Table B.1 but in NEP-Deep survey.

Instrument	Area (deg^2)	Pixel Size ($'' \ pix^{-1}$)	Filter	Effective Wavelength (μm)	Sensitivity (5σ, AB mag)	Reference
MegaCam (CFHT)	1	0.19	$u*$	0.37	24.6	Takagi et al. (2012)
			g'	0.49	26.5	Oi et al. (2014)
			r'	0.63	25.7	
			i'	0.77	24.9	
			z'	0.89	23.9	
SuprimeCam (Subaru)	0.255	0.2	B	0.43	28.4	Takagi et al. (2012)
			V	0.54	28.0	
			R	0.65	27.4	
			i'	0.80	27.0	
			z'	0.91	26.2	
WIRCam (CFHT)	0.6	0.3	Y	1.02	23.2	Oi et al. (2014)
			J	1.25	22.8	
			K_s	2.15	22.5	
FLAMINGOS (KPNO 4m)	0.2	0.61	J	1.25	21.9	Imai et al. (2007)
			K_s	2.15	21.0	
IRC (AKARI)	0.67	1.46×1.46	$N2$	2.4	21.5	Takagi et al. (2012)
			$N3$	3.2	21.7	
			$N4$	4.1	22.1	
		2.34×2.34	$S7$	7.0	19.7	
			$S9W$	9.0	19.5	
			$S11$	11.0	19.3	
		2.51×2.39	$L15$	15.0	18.7	
			$L18W$	18.0	18.7	
			$L24$	24.0	17.8	

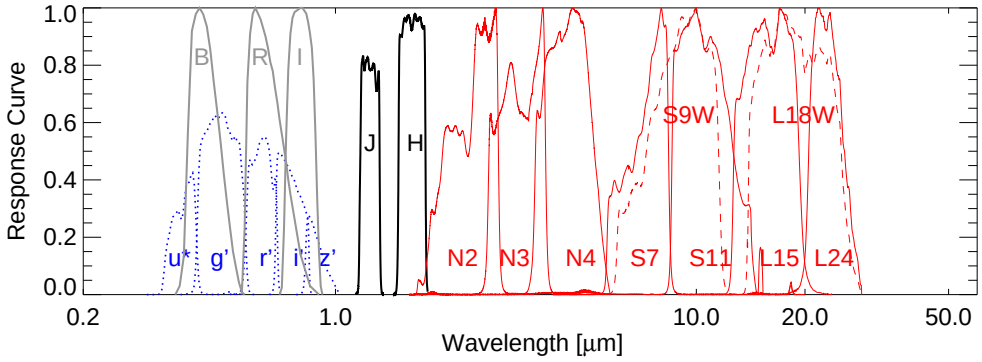

Figure B.1 Filter response curves of multi-wavelength data covering the NEP field. The thick dotted blue lines represent the u^*, g', r', i', and z' band filters from MegaCam of CFHT. The thick gray lines are for the B, R, and $I-$band filters from Maidanak observatory. The thin solid red lines and thin dashed red lines are for the *AKARI* IR band filter coverage ($N2, N3, N4, S7, S9W, S11, L15, L18W$, and $L24$). The thick black lines are for our J and $H-$band filters, which make the wavelength coverage between the optical data and the *AKARI* data continuous. Table B.1 lists the information of multi-wavelength data for the filters, shown here.

with Imai et al. (2007)'s J and K_s-band data. The tile names are used for the target ID (Section B.4.5). The names of each subfield and their central positions are listed in Table B.3.

The NIR imaging observation was done with J and H filters from 2008 June 13 to 23 at Kitt Peak National Observatory (KPNO) using the FLoridA Multi-object Imaging Near-ir Grism Observational Spectrometer (FLAMINGOS; Elston et al. 2006), which is an NIR camera attached to the Cassegrain focal plane of the 2.1m telescope. It uses a Hawaii II 2048x2048 HgCdTe array, divided into four quadrants with 8 amplifiers each. It provides a $21' \times 21'$ field of view, with a pixel scale of $0.606''$ pix^{-1}.

The observation was carried out under mostly clear sky conditions. The observations followed a standard sequence which consists of a 5 × 5 dither pattern with $20''$ offsets to make the sky frame for the sky subtraction. Each subfield overlaps with neighboring subfields for regions of width $4'$ to avoid the low efficiency parts on the edges of each chip. The total exposure time for each subfield is ∼36 minutes for $J-$band and ∼21 minutes for $H-$band, and the data reach 5σ depths of ∼21.6 mag and ∼21.3 mag, respectively. We used 1.5 minutes as an exposure time per frame for $J-$band throughout the observations. However, for the $H-$band observations, we employed exposure times between 0.5 and 1.0 minutes per frame to adjust the background level. The seeing values for each subfield were determined as the median values of full width at half maximum (FWHM) of non-saturated point sources with magnitudes between 15 and 19. The seeing values of the stacked J and $H-$band images are determined to be $\sim 1.8''$ and $\sim 1.7''$, respectively. To determine the limiting magnitude, we used the aperture size corresponding to a diameter of 3 times the FWHM following the definition introduced in Section B.4.1. Tables B.4 and B.5 show the observation summary including the total on-source exposure time, the exposure time per frame, the median seeing size, 5σ detection limit, and 50% completeness magnitude (see Section B.4.6) for each filter. We plot the values of seeing size and 5σ detection limits for all subfields for both filters in Figure B.3. The figure can be used to check the subfield variance of the values. Also to determine the quality of the images, we show plots of the magnitudes for the 5σ detection limits (crosses), 50% completeness (see Section B.4.6), 99% reliability (see Section B.4.7) and photometric zeropoints Z_p (see Section B.3.3) for each subfield in Figure B.4. The total exposure times for each subfield are plotted on the right axis.

Table B.3. Names of each subfield in Figure B.1 and their central positions.

Field	R.A.	Decl.	Field	R.A.	Decl.
FLM01	18:04:18.09	+67:32:00.71	FLM66	17:56:29.34	+66:28:38.50
FLM02	18:01:30.29	+67:36:38.52	FLM34	17:53:58.87	+66:28:38.50
FLM03	17:58:39.75	+67:36:38.52	FLM35	17:51:28.40	+66:28:38.50
FLM04	17:55:49.22	+67:36:38.52	FLM36	17:48:57.93	+66:28:38.50
FLM05	18:07:08.92	+67:15:36.93	FLM37	18:11:22.13	+66:11:38.51
FLM06	18:04:18.63	+67:16:45.62	FLM38	18:08:51.66	+66:11:38.51
FLM07	18:01:30.29	+67:19:38.53	FLM39	18:06:21.19	+66:11:38.51
FLM08	17:58:39.75	+67:19:38.53	FLM40	18:03:48.46	+66:10:45.92
FLM09	17:55:49.22	+67:19:38.53	FLM41	18:01:18.11	+66:10:23.74
FLM10	17:52:58.68	+67:19:38.53	FLM42	17:58:49.78	+66:11:38.51
FLM11	18:10:39.67	+66:59:10.18	FLM43	17:56:19.31	+66:11:38.51
FLM12	18:07:51.48	+67:02:38.51	FLM44	17:53:48.84	+66:11:38.51
FLM13	18:05:00.95	+67:02:38.51	FLM45	17:51:18.37	+66:11:38.51
FLM14	18:02:10.41	+67:02:38.51	FLM46	17:48:47.90	+66:11:38.51
FLM15	17:59:19.88	+67:02:38.51	FLM47	18:10:11.92	+65:54:38.52
FLM16	17:56:29.34	+67:02:38.51	FLM48	18:07:21.38	+65:54:38.52
FLM17	17:53:38.81	+67:02:38.51	FLM49	18:04:30.85	+65:54:38.52
FLM18	17:50:48.27	+67:02:38.51	FLM50	18:01:40.31	+65:54:38.52
FLM19	18:11:49.59	+66:43:31.48	FLM51	17:58:49.78	+65:54:38.52
FLM20	18:09:21.76	+66:45:38.52	FLM52	17:55:59.25	+65:54:38.52
FLM21	18:06:51.28	+66:45:38.52	FLM53	17:53:08.72	+65:54:38.52

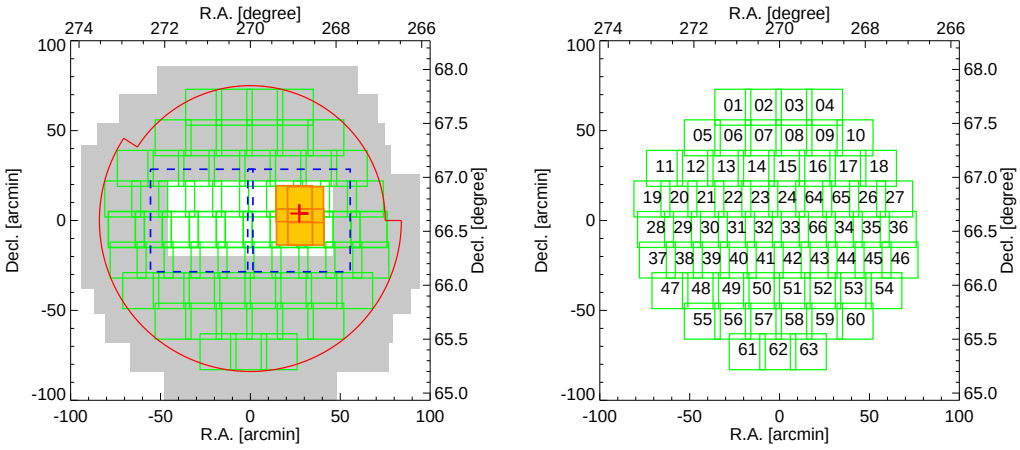

Figure B.2 Field coverage of the *AKARI* NEP multi-wavelength data. The center is the NEP whose coordinates are $\alpha = 18^h00^m00^s, \delta = +66°33'38''$. Our J and $H-$band survey (5.1 deg^2) is indicated with small empty green squares on both panels (65 subfields). The names of the subfields are marked with numbers on the right panel. The names and central positions for each subfield are listed in Table B.3. The solid red circles and the two dashed blue squares indicate *AKARI* (5.4 deg^2) and CFHT MegaCam (2 deg^2) coverage, respectively. The gray area represents the *BRI* imaging survey (4.9 deg^2) from Maidanak observatory. The thick red cross indicates the center of NEP-Deep field (0.67 deg^2). The J and K_s band coverage from Imai et al. (2007) (750 arcmin^2) are marked with four filled orange squares centered at the NEP-Deep field.

Table B.3 (cont'd)

Field	R.A.	Decl.	Field	R.A.	Decl.
FLM22	18:04:20.82	+66:45:38.52	FLM54	17:50:18.18	+65:54:38.52
FLM23	18:01:50.35	+66:45:38.52	FLM55	18:07:11.35	+65:37:38.53
FLM24	17:59:19.88	+66:45:38.52	FLM56	18:04:20.82	+65:37:38.53
FLM64	17:56:49.40	+66:45:38.52	FLM57	18:01:30.29	+65:37:38.53
FLM65	17:54:18.93	+66:45:38.52	FLM58	17:58:39.75	+65:37:38.53
FLM26	17:51:48.46	+66:45:38.52	FLM59	17:55:49.22	+65:37:38.53
FLM27	17:49:18.00	+66:45:38.52	FLM60	17:52:58.68	+65:37:38.53
FLM28	18:11:32.17	+66:28:38.50	FLM61	18:03:00.56	+65:20:38.51
FLM29	18:09:01.69	+66:28:38.50	FLM62	18:00:10.03	+65:20:38.51
FLM30	18:06:31.22	+66:28:38.50	FLM63	17:57:19.50	+65:20:38.51
FLM31	18:03:58.38	+66:27:09.87			

B.3 DATA REDUCTION

B.3.1 Preprocessing

For the data reduction, we first carried out i) linearity correction, ii) dark subtraction and flat fielding, iii) distortion correction, iv) sky subtraction, v) bad pixel and cosmic ray masking, and vi) image alignment and combining. All these steps are performed using IRAF[1].

To correct the nonlinearity of the NIR detector, we used the IRAF `irlincor`

[1]IRAF is distributed by the National Optical Astronomy Observatory, which is operated by the Association of Universities for Research in Astronomy (AURA) under cooperative agreement with the National Science Foundation.

Table B.4. Observation summary.

Filter	Total exposure time [minutes]	Exposure time per image [minutes]	Seeing [$''$]	5σ detection limits [AB mag]	50% Completeness [AB mag]
J	28.5 – 52.5 (36)	1.5	1.4 – 2.4 (1.8)	20.88 – 21.94 (21.63)	20.11 – 21.01 (20.65)
H	11.3 – 34.0 (21.3)	0.5 – 1.0 (0.7)	1.4 – 2.6 (1.7)	20.42 – 21.72 (21.29)	19.44 – 20.81 (20.35)

Note. — The values in the parentheses are the median values.

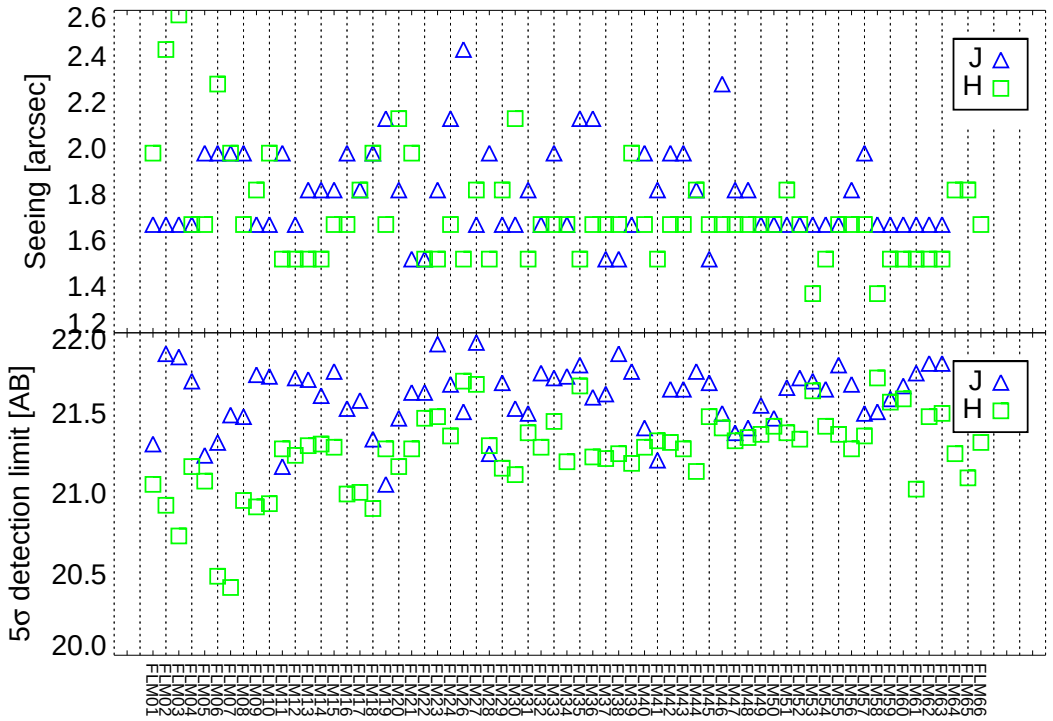

Figure B.3 Seeing and 5σ detection limits for each subfield. (Triangles for J and squares for $H-$band)

task. For FLAMINGOS, the linearity correction can be expressed as a third-order polynomial[2]:

$$y = x \times (a + b \times (x/32767) + c \times (x/32767)^2),$$

where x is the raw signal, y is the linearity corrected signal in ADU, and the coefficients are $a = 1.00425, b = -0.03323, c = 0.04489$.

We used a standard method for dark subtraction and flat fielding with the IRAF `noao.imred.ccdred` package. Master dark frames were created by combining dark frame image for each night and exposure time. We subtracted the master dark image

[2]http://www.noao.edu/kpno/manuals/flmn/flmn.user.html

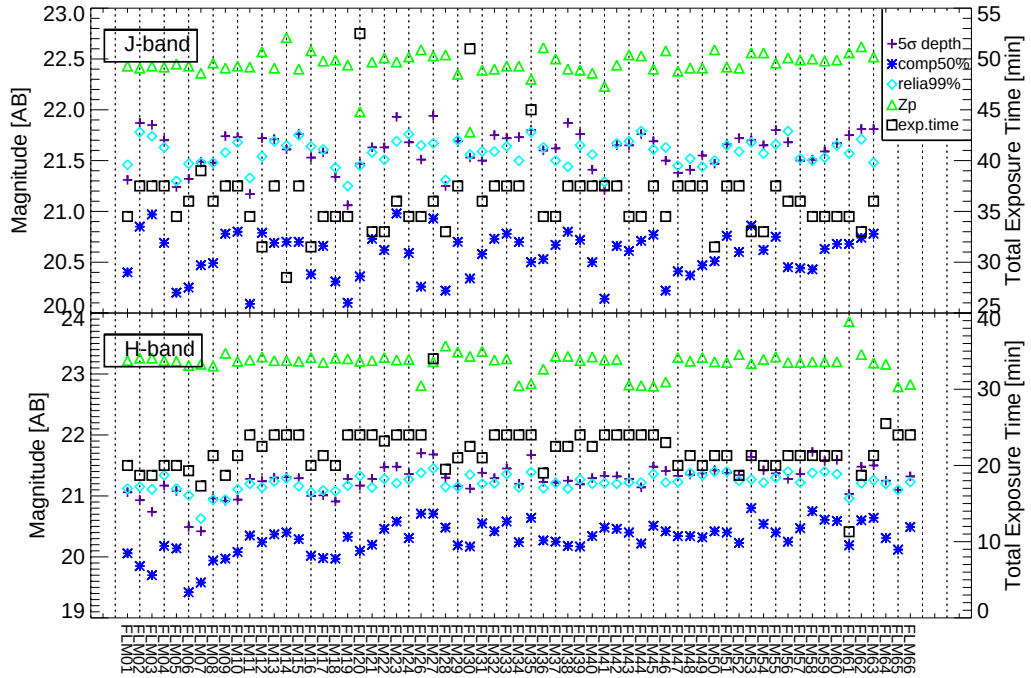

Figure B.4 Several measures of the image quality and depth of each subfield, such as the 5σ detection limit (crosses), the 50% completeness (asterisks; see Section B.4.6), the 99% reliability (diamonds; see Section B.4.7), the photometric zeropoint Z_p (triangles; see Section B.3.3), and the total exposure time (squares).

from each science image. These dark subtracted science images, typically 250 frames with a background count of 3000 DNs, were combined in median after scaling them to a reference image by the mode pixel value to construct master sky flat images for each night. We compared this master sky flat image with flat frames taken from dome dimming lights and found that the master sky flat can remove ring structures in the center of science images more efficiently. The flat fielding was done by dividing dark subtracted images by the normalized master sky flat image for each night. We removed satellite tracks on the images using the IRAF `satzap` task.

The distortion correction[3] was performed using a distortion map constructed from pinhole data. We used the IRAF `geotran` task for the correction. Among the various distortion maps, we used the most resent one, KP2m04.map, obtained in July 2003. The distortion map doubles the number of pixels in each axis and sets the pixel scale to $0.303''$ pix^{-1}. We compared the astrometric accuracy before and after the distortion correction (see Section B.3.2 for more details about the astrometry). We used the FLM14 $J-$band field as a test field. The astrometric accuracy was improved by up to $\sim$5% after the distortion correction.

To subtract the sky, mask bad pixels and cosmic rays, and align and combine the sky subtracted individual images, we used the Experimental Deep Infrared Mosaicing Software (`XDIMSUM`; Stanford et al. 1995) package of IRAF. Six adjacent frames were used for making the sky image to subtract the sky. The mask images were created using the master dark images and master sky flat images for each night, excluding bad pixels which have unusual values compared with the normal distribution of the pixel values. Cosmic rays are removed with a 3σ clipping method while combining the images.

B.3.2 Astrometry

We employed SCAMP (Bertin 2006) which finds astrometric solution by cross matching between positions of input catalog created from a science image without astrometry calibration and a reference catalog containing a set of accurate R.A. and Decl. values. The Two Micron All Sky Survey Point Source Catalog (2MASS PSC) was used as the reference catalog. The astrometric solution was derived for each subfield and each filter separately. We tried to find the best parameter value for the degree of the polynomial for distortion correction between 3, 4, 5, and 6 and found that a 5^{th}-order polynomial gave the best astrometric accuracy among other options.

[3]http://flamingos.astro.ufl.edu/DistortionFiles/index.html

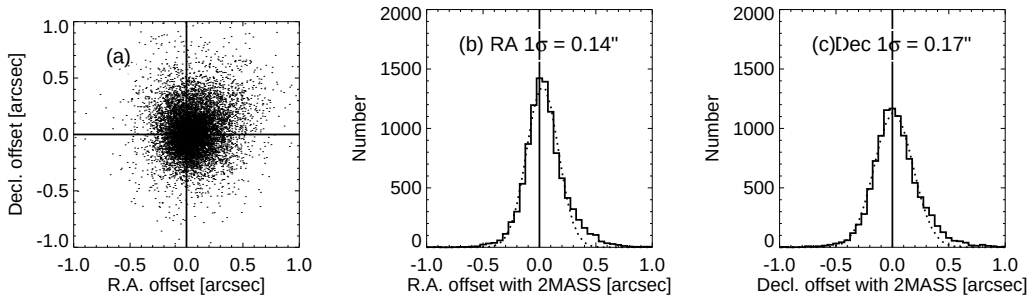

Figure B.5 (a): Distribution of the differences in position between our sources and the corresponding 2MASS sources in R.A. and Decl. directions. (b) and (c): Histograms of the distributions in R.A. and Decl. directions, respectively. The dotted lines indicate the best fitted Gaussian function for the histograms. From the Gaussian function, the 1σ astrometry errors are $0.14''$ for R.A. and $0.17''$ for Decl..

Therefore we set the degree of the polynomial to 5.

To check the astrometric accuracy, 2MASS point sources with 1σ position uncertainty less than $0.2''$ are compared with our catalog. Figure B.5 (a) shows the distributions of the positional differences between our sources and the corresponding 2MASS sources in R.A. and Decl. directions, and (b) and (c) show the histogram of the position differences in the two directions, respectively. We fit the histograms with a Gaussian function (dotted lines) and take the 1σ value of the best fitted Gaussian function as the 1σ astrometric errors in R.A. and Decl. direction. Here, the 1σ errors are around $0.16''$ for both directions. Combining the rms scatter in both directions in quadrature, we get the absolute positional accuracy of $0.17''$. Considering that the astrometry error of the 2MASS sources is about $0.2''$, our astrometric accuracy is quite good, and most of the uncertainty in the astrometry seems to originate from the 2MASS catalog.

B.3.3 Photometric Calibration

For the photometric calibration, we also used stellar objects in the 2MASS PSC. We restricted the photometric reference stars to have the color $-0.9 < J_{2MASS} - K_{2MASS} < 0.1$ ($0 < J_{2MASS} - K_{2MASS} < 1$ for the Vega system; see Section B.4.5), photometric error less than 0.05 mag, and magnitude fainter than 11.9 mag (11 mag for the Vega system). For each field, we derived the difference between the 2MASS and instrumental magnitudes of each source in the field and computed the average value of the difference to define the zeropoint (Z_p). The zeropoint error was derived from the standard deviation of the magnitude offset. The average zeropoint error is $\sim$0.05 mag for both J and $H-$band. The Z_p for each subfield is listed in Table B.5 for the purpose of checking the depth of each field. The Z_p is used for converting the DN per exposure time to magnitudes, i.e. $M = Z_p - 2.5 \log (DN/sec)$. Figure B.4 shows the distribution of several depth indicators for each field. The depths are checked using the 5σ detection limit, the 50% completeness (see Section B.4.6), the 99% reliability (see Section B.4.7), and the Z_p (triangles), as well as the total exposure time.

To check the photometric accuracy, we compare the magnitudes of 2MASS sources with our sources. Figure B.6 shows the magnitude differences between our sources and the corresponding 2MASS sources as a function of magnitude for J (left panel) and H (right panel) band. We used the 2MASS point sources of same color and photometric error properties that we used for the Z_p calculation. The magnitude offsets show very small systematic differences (0.002 for $J-$band and 0.001 for $H-$band). For the brightest sources (J and $H \lesssim 13.5$), however, they show offsets of $\sim$0.05 for both filters. Since the halo region near a very bright star has a dark background, it causes the flux of the bright star to be overestimated. The dark halos are induced by the sky subtraction during preprocessing because bright stars in the dithered images overestimate the sky values. The scatter of the magnitude difference

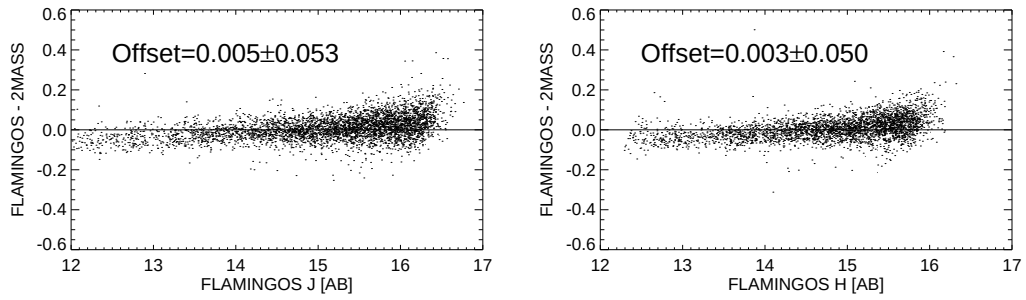

Figure B.6 Photometric difference between our sources and the corresponding 2MASS sources as a function of magnitude to check the photometric accuracy. Although the systematic offset is very small, the bright sources show average offsets of ∼0.05 for both filters. The scatter of the magnitude difference is larger for fainter sources, which may be caused by the photometric uncertainties for the sources. The dispersion of the magnitude difference are ∼0.05 mag. These values are corresponding with the zeropoint uncertainty.

is larger for fainter sources, which may be caused by the photometric uncertainties for the sources. We calculated the variances of the offsets for both filters using the standard deviation of the offsets. They have values of ∼0.05, which coincide with the zeropoint uncertainties. Therefore the magnitudes of our catalog are accurate to ∼0.05 mag.

Table B.5. Photometric zeropoint, seeing, 5σ detection limit, magnitude of 50% completeness, and magnitude of 99% reliability for each subfield.

	$J-$band					$H-$band				
Field	Z_p[a] (mag)	Seeing ($''$)	detection limits[b] (mag)	comp50%[c] (mag)	relia99%[d] (mag)	Z_p[a] (mag)	Seeing ($''$)	detection limits[b] (mag)	comp50%[c] (mag)	relia99%[d] (mag)
FLM01	22.43	1.67	21.31	20.40	21.46	23.22	1.98	21.06	20.06	21.12
FLM02	22.41	1.67	21.87	20.85	21.78	23.26	2.43	20.93	19.85	21.15
FLM03	22.43	1.67	21.85	20.97	21.74	23.26	2.58	20.74	19.70	21.11
FLM04	22.42	1.67	21.70	20.69	21.63	23.22	1.67	21.17	20.18	21.34
FLM05	22.45	1.98	21.24	20.20	21.30	23.21	1.67	21.08	20.14	21.12
FLM06	22.43	1.98	21.32	20.25	21.47	23.14	2.28	20.49	19.42	21.01
FLM07	22.36	1.98	21.49	20.47	21.48	23.16	1.98	20.42	19.58	20.63
FLM08	22.46	1.98	21.48	20.49	21.48	23.13	1.67	20.96	19.94	20.94
FLM09	22.41	1.67	21.74	20.78	21.58	23.34	1.82	20.92	19.97	20.94
FLM10	22.43	1.67	21.73	20.80	21.68	23.21	1.98	20.94	20.08	21.11
FLM11	22.42	1.98	21.17	20.09	21.33	23.23	1.52	21.28	20.35	21.20
FLM12	22.57	1.67	21.72	20.79	21.54	23.28	1.52	21.24	20.24	21.14
FLM13	22.41	1.82	21.71	20.69	21.69	23.22	1.52	21.30	20.37	21.24
FLM14	22.71	1.82	21.61	20.70	21.65	23.22	1.52	21.31	20.40	21.29
FLM15	22.40	1.82	21.76	20.70	21.75	23.21	1.67	21.29	20.29	21.16
FLM16	22.58	1.98	21.53	20.38	21.64	23.27	1.67	21.00	20.02	21.06
FLM17	22.48	1.82	21.58	20.66	21.61	23.19	1.82	21.01	19.98	21.09
FLM18	22.49	1.98	21.34	20.31	21.43	23.26	1.98	20.91	19.97	21.08
FLM19	22.44	2.13	21.06	20.10	21.25	23.25	1.67	21.28	20.33	21.17
FLM20	21.98	1.82	21.47	20.36	21.45	23.21	2.13	21.17	20.10	21.33
FLM21	22.47	1.52	21.63	20.73	21.58	23.22	1.98	21.28	20.20	21.14
FLM22	22.51	1.52	21.63	20.62	21.51	23.27	1.52	21.47	20.46	21.28
FLM23	22.47	1.82	21.93	20.98	21.69	23.23	1.52	21.48	20.58	21.21
FLM24	22.52	2.13	21.68	20.59	21.76	23.24	1.67	21.36	20.31	21.27
FLM26	22.59	2.43	21.51	20.26	21.65	22.81	1.52	21.70	20.71	21.38
FLM27	22.53	1.67	21.94	20.93	21.67	23.20	1.82	21.68	20.71	21.45
FLM28	22.54	1.98	21.25	20.22	21.31	23.46	1.52	21.30	20.48	21.15
FLM29	22.35	1.67	21.69	20.70	21.70	23.36	1.82	21.16	20.19	21.15

Table B.5 (cont'd)

Field	$J-$band					$H-$band				
	Z_p[a] (mag)	Seeing ($''$)	detection limits[b] (mag)	comp50%[c] (mag)	relia99%[d] (mag)	Z_p[a] (mag)	Seeing ($''$)	detection limits[b] (mag)	comp50%[c] (mag)	relia99%[d] (mag)
FLM30	21.78	1.67	21.53	20.34	21.56	23.29	2.13	21.12	20.17	21.35
FLM31	22.39	1.82	21.50	20.58	21.59	23.37	1.52	21.38	20.55	21.20
FLM32	22.40	1.67	21.75	20.73	21.59	23.23	1.67	21.29	20.42	21.21
FLM33	22.43	1.98	21.72	20.78	21.64	23.25	1.67	21.45	20.58	21.36
FLM34	22.43	1.67	21.73	20.70	21.50	22.81	1.67	21.20	20.24	21.14
FLM35	22.30	2.13	21.80	20.50	21.78	22.84	1.52	21.67	20.64	21.39
FLM36	22.61	2.13	21.60	20.53	21.63	23.08	1.67	21.23	20.27	21.13
FLM37	22.50	1.52	21.62	20.67	21.50	23.29	1.67	21.22	20.25	21.21
FLM38	22.40	1.52	21.87	20.80	21.44	23.29	1.67	21.25	20.18	21.12
FLM39	22.39	1.67	21.76	20.72	21.65	23.22	1.98	21.19	20.17	21.27
FLM40	22.36	1.98	21.41	20.50	21.56	23.28	1.67	21.29	20.34	21.20
FLM41	22.23	1.82	21.21	20.14	21.29	23.23	1.52	21.33	20.48	21.21
FLM42	22.44	1.98	21.65	20.66	21.67	23.24	1.67	21.32	20.46	21.20
FLM43	22.54	1.98	21.65	20.61	21.69	22.82	1.67	21.28	20.40	21.22
FLM44	22.53	1.82	21.76	20.71	21.79	22.81	1.82	21.14	20.22	21.22
FLM45	22.40	1.52	21.69	20.77	21.61	22.80	1.67	21.48	20.51	21.36
FLM46	22.58	2.28	21.50	20.22	21.63	22.87	1.67	21.41	20.42	21.22
FLM47	22.38	1.82	21.38	20.41	21.45	23.27	1.67	21.33	20.34	21.23
FLM48	22.41	1.82	21.41	20.37	21.52	23.21	1.67	21.35	20.34	21.38
FLM49	22.41	1.67	21.55	20.47	21.44	23.27	1.67	21.37	20.32	21.34
FLM50	22.59	1.67	21.47	20.51	21.50	23.20	1.67	21.42	20.42	21.40
FLM51	22.42	1.67	21.66	20.76	21.65	23.19	1.82	21.38	20.40	21.40
FLM52	22.41	1.67	21.72	20.60	21.59	23.32	1.67	21.34	20.23	21.25
FLM53	22.56	1.67	21.70	20.86	21.68	23.17	1.37	21.64	20.80	21.27
FLM54	22.56	1.67	21.65	20.62	21.57	23.24	1.52	21.42	20.54	21.22
FLM55	22.46	1.67	21.80	20.75	21.66	23.28	1.67	21.37	20.40	21.30
FLM56	22.51	1.82	21.68	20.45	21.79	23.19	1.67	21.28	20.25	21.40
FLM57	22.49	1.98	21.50	20.44	21.52	23.19	1.67	21.36	20.47	21.22

B.4 CATALOGS

B.4.1 Object Detection and Photometry

To detect sources and conduct photometry, we employed SExtractor (SE; Bertin & Arnouts 1996).

We found optimal parameters for SE to obtain high completeness while not sacrificing reliability of the detection (Sections B.4.6 and B.4.7) for all magnitude bins. To do so, we made artificial objects using the IRAF `noao.artdata` package and they are placed randomly at the background regions of the images. We performed detections and photometry with various parameter settings. After many trials with varying SE parameters, we chose the following set of detection parameters for SE: DETECT_MINAREA=20, DETECT_THRESH=1.1, DEBLEND_NTHRESH=64, DEBLEND_MINCONT=0.005, BACK_SIZE=500, BACK_FILTERSIZE=2. The adopted detection parameters corresponds to $S/N = 5$.

We detected 208,020 sources and 203,832 sources for J and $H-$band, respectively, at the magnitude limits brighter the 99% reliability (see Section B.4.7). Among these objects, 28.3% in J and 30.8% in H are detected only in a single filter image. Most of the sources detected only in a single filter image are those at near the magnitude limits, suggesting that they are missed in an image in the other band due to the detection limit. The reason for the percentage of sources detected only in $J-$band being slightly higher is the deep $J-$band catalog from Imai et al. (2007). If a bright object of $J < 19$ mag or $H < 20$ mag has no counterpart in the other band, we find that they are a crosstalk or cosmic ray. We derived auto magnitudes with Kron-like elliptical aperture (Kron 1980), which are assumed to be total magnitudes. For the aperture magnitudes, we set the aperture diameter size to 3 times the FWHM. We found a diameter of 3 times the FWHM to be an optimal diameter which can contain the majority of the flux from an object but is

Table B.5 (cont'd)

Field	$J-$band					$H-$band				
	Z_p[a] (mag)	Seeing ($''$)	detection limits[b] (mag)	comp50%[c] (mag)	relia99%[d] (mag)	Z_p[a] (mag)	Seeing ($''$)	detection limits[b] (mag)	comp50%[c] (mag)	relia99%[d] (mag)
FLM58	22.50	1.67	21.51	20.43	21.50	23.20	1.37	21.72	20.75	21.38
FLM59	22.48	1.67	21.59	20.63	21.53	23.20	1.52	21.57	20.61	21.40
FLM60	22.49	1.67	21.67	20.68	21.65	23.20	1.52	21.59	20.59	21.36
FLM61	22.56	1.67	21.75	20.68	21.57	23.86	1.52	21.03	20.19	20.96
FLM62	22.62	1.67	21.81	20.74	21.71	23.32	1.52	21.48	20.60	21.21
FLM63	22.52	1.67	21.81	20.78	21.48	23.18	1.52	21.50	20.64	21.26
FLM64	...	...	...	...	...	23.16	1.82	21.25	20.31	21.20
FLM65	...	...	...	...	...	22.79	1.82	21.10	20.12	21.10
FLM66	...	...	...	...	...	22.83	1.67	21.32	20.49	21.23

[a] The apparent magnitude is $M = Z_p - 2.5 \log (DN/sec)$.

[b] The 5σ detection limit for a circular aperture with diameter of 3 times FWHM

[c] The magnitude corresponding to the 50% completeness

[d] The magnitude corresponding to the 99% reliability

not affected by the local fluctuation in the sky background. This has been checked by growth curves of objects with various magnitudes. The magnitude errors are computed by combining the standard SE errors based on Poisson statistics and the zeropoint errors. At the bright end, the photometry is free from saturation above $J \sim$10 mag and $H \sim$11 mag.

Since the stacking of the dithered frames with sub-pixels during preprocessing causes poor measurement of pixel-by-pixel rms for the correlated neighboring pixels, the errors from SE, which only consider the Poisson noise, can be underestimated. To improve the accuracy of the estimated errors, we adopted the method in Gawiser et al. (2006) and Jeon et al. (2010), calculating the noise rate induced by the pixel-by-pixel correlated noise. We place ∼3000 apertures of a given size randomly located in the background area. The aperture has an area of n_{pix} and an effective diameter of $N = n_{pix}^{1/2}$. The background rms fluctuations are derived from a Gaussian curve fit to the histogram of fluxes inside each aperture. The noise calculated from the rms fluctuations for a given effective diameter is expressed as $\sigma_N \propto N^{\beta}$. If the noise is only dependent on the Poisson noise, it is independent from one pixel to another. Therefore for this case, $\sigma_N \propto N$. However, for the adjoining pixels, the sky noise has $\beta > 1$. For our data, we find $\sigma_N \propto N^{1.4}$. For an aperture with $5.4''$ diameter (3 times the typical FWHM of our images), there are about 250 pixels (or $N \simeq 16$). Therefore, the photometric errors of faint objects ($J \gtrsim 18$ mag) may be underestimated by a maximum factor of 3. For the brighter objects ($J \lesssim 16$ mag), the photometric errors are not affected by this effect, since their errors are dominated by noises from the source.

The detection and photometry of the sources are carried out for each subfield image, rather than a single mosaic of all the subfields, since there is a variation in the weather condition among subfields. Catalogs from individual subfields are then merged together to form a master catalog for each filter. However, since each sub-

field image overlaps with a neighboring images, catalogs created from each subfield image contain duplicate entries in the overlap region. To deal with the duplicate entries during the merging process of all the subfield catalogs, we set the criterion for choosing the entry with the smallest FLAGS values from SE and smallest photometric errors for multiple entries with positional offsets less than $1.5''$. Only the object chosen with the above criterion, and its SE output values derived from the chosen subfield are included in the final catalog.

When we merged the J and $H-$band catalogs, we used a $1.5''$ radius. Every row, regardless of whether they have information in both bands, is included in the final catalog. Regarding the stellarity from SE, we chose a single stellarity value for the final catalog where the photometric error of the source is smaller between the two filters.

B.4.2 Crosstalk Flagging

The FLAMINGOS chip exhibits crosstalk artifacts between amplifiers on both sides of a bright source[4], where the crosstalk signals can be identified as doughnut-shaped signals at every 128 pixels, which corresponds to the width of one amplifier, from the position of a bright source. The strength of the crosstalk signal is stronger for a brighter source, and it decreases as the distance from the bright source increases. We examined the magnitude of the source that generates crosstalks and the positions of the crosstalks. The crosstalks start to be seen on both sides of a bright source at a magnitude of $J \sim 15.0$ mag and $H \sim 15.5$ mag in the stacked image. For sources that are about 3 magnitudes brighter than that limit, the crosstalks continue to the end of a quadrant. The bright sources create the crosstalk signal at distances of multiples of 256 pixels in our stacked image whose pixel sizes are a half of the pixel size of the raw image. The direction in which the crosstalks appeared depends on

[4]http://flamingos.astro.ufl.edu/DetQE/index.html

the readout direction and where the object is located, but it is predictable. Using these properties, we predicted the positions of the crosstalks and included the flag information for objects at these points in our merged catalog that the object is a potential crosstalk signal or its photometry is affected by the crosstalk.

B.4.3 Data from Imai et al. (2007)

The J and K_s-band imaging was conducted in 2004, covering 750 arcmin^2 near the center of NEP-Deep by Imai et al. (2007), where we avoided duplicate observation in $J-$band. To construct a continuous area coverage of the $J-$band imaging in the NEP field, we included the $J-$band images from Imai et al. (2007) when creating a catalog of $J-$band sources. For consistency in the final catalog, we conducted new detections and photometry using our own method (see Section B.4.1). Their flux calibration was done using standard stars listed in Persson et al. (1998), resulting in uncertainties in the flux calibration up to 0.1 mag. We were able to reduce the errors to less than 0.05 mag using our flux calibration method (see Section B.3.3). We added this catalog to the final catalog to fill the gap in the NEP field from our $J-$band survey. The average depths of images of Imai et al. (2007) are $\sim$0.3 mag deeper than those of our data.

B.4.4 Star-Galaxy Separation

We used the same method as Jeon et al. (2010) to separate galaxies from stars. Since most stars have similar slopes at wavelengths greater than 1μm on their SEDs, NIR colors of stars lie in narrow range while those of distant galaxies are more diverse due to redshifted SED. Figure B.7 shows the $B-H$ versus $H-N2$ color-color diagram. The stellar locus can clearly be seen by the clouded gray points and overlapping contour ($H-N2 \sim 0.5$). Also the redshift tracks of two types of galaxies are shown to check the location of galaxies. The dashed line is a redshift track of a star-

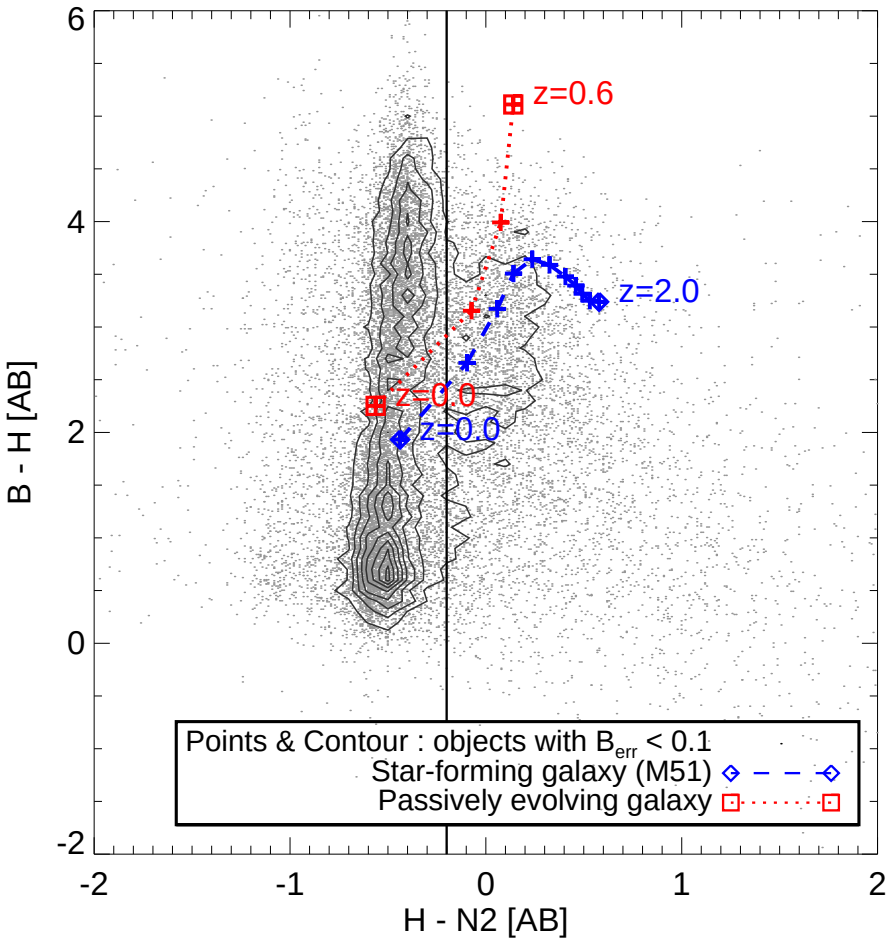

Figure B.7 $B-H$ versus $H-N2$ color-color diagram and the density contours of sources detected in B, H, and $N2-$band. The points and the contours are made with objects that have $B-$band magnitude errors less than 0.1 mag. The dashed line is a redshift track of a star-forming galaxy (M51) and the dotted line is for a passively evolving galaxy made with the Bruzual & Charlot (2003) model of a passively evolving 5 Gyr-old galaxy with a spontaneous burst, a metallicity Z=0.02, and the Salpeter IMF. We use the vertical line as a boundary that distinguishes stellar sources against galaxies.

forming galaxy (M51) and the dotted line is that of a passively evolving 5 Gyr-old galaxy with a spontaneous burst, a metallicity Z=0.02, and the Salpeter initial mass function (IMF) created with the Bruzual & Charlot (2003) model. As indicated in Figure B.7, we find that the galaxies and stars can be separated effectively with a color cut at $H - N2 = -0.2$ mag, where objects with $H - N2 < -0.2$ are mostly stars. However, galaxies at z $\sim$ 0 also have $H - N2 < -0.2$ mag, and there are also stars with peculiar colors with $H - N2 > -0.2$. To deal with such case, we also use the stellarity parameter from SE of objects in the optical catalog (Jeon et al. 2010; Hwang et al. 2007) since the optical images offer better spatial resolution ($\sim 1''$). The SE stellarity parameter has a value between 1 (point source) and 0 (extended source). For the galaxies with $H - N2 < -0.2$ mag, they can be selected using the criterion stellarity ≤ 0.8. Likewise, point sources with stellarity > 0.8 with $H - N2 > -0.2$ mag are classified as stars. This method was applied only to objects brighter than the 50% completeness magnitude, which corresponds to $R < 20$ mag or $r < 22$ (see Figure 6 in Jeon et al. (2010) and Figure 2 in Hwang et al. (2007)), since the 50% completeness magnitude is the limit for which the stellarity parameter can be used to separate the extended sources from the point sources. Near the detection limit, all objects fainter than the magnitude of 50% completeness are considered as galaxies.

B.4.5 Catalog Format

Table B.6 shows a part of the J and $H-$band merged catalog. The catalog contains objects whose detection reliability is higher than 99%. The magnitude cut was computed independently for each field in each filter (see Section B.4.7). The catalog contains 15 columns; identification number (ID), the right ascension (R.A.) and declination (Decl.), J and $H-$band magnitudes and errors, stellarity, galactic extinction values for each filter, and the information about the crosstalk. The

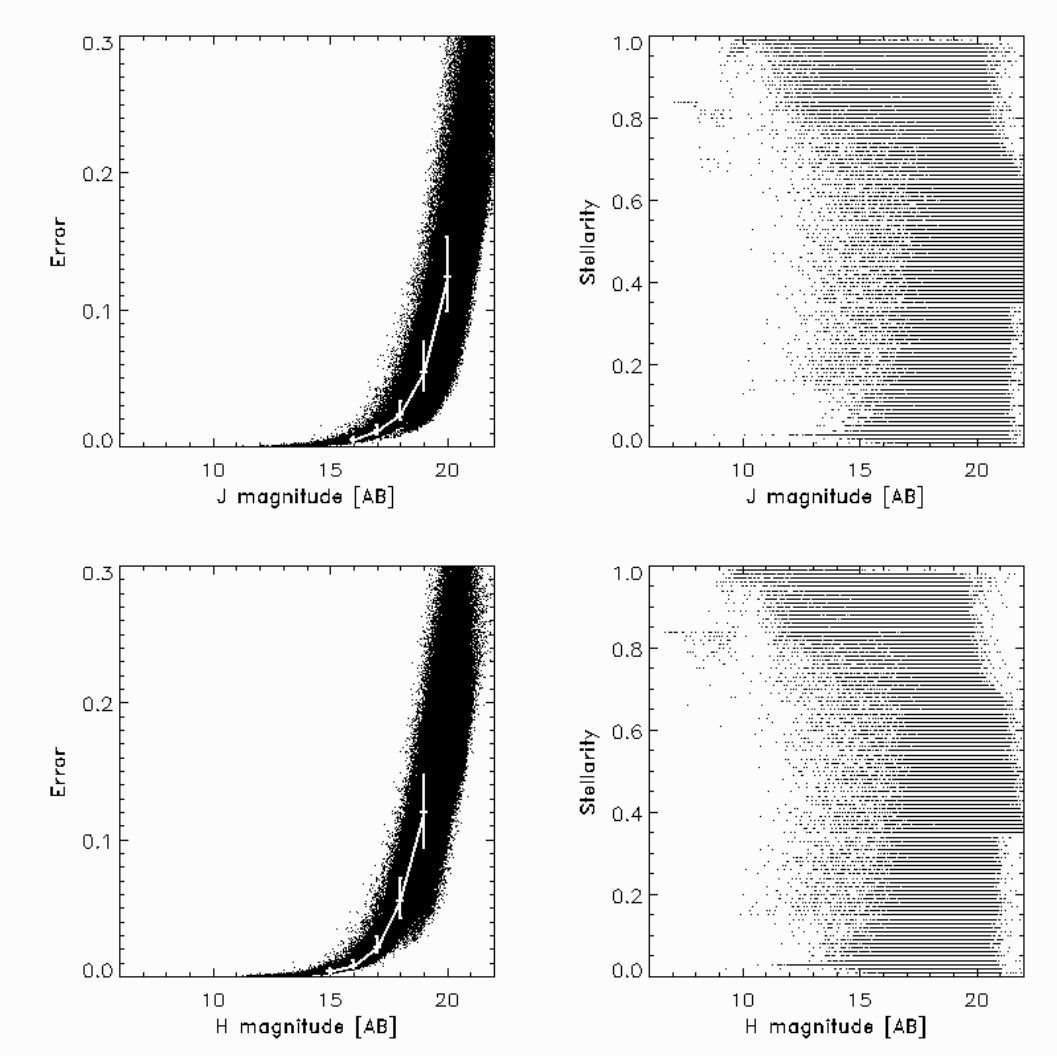

Figure B.8 The photometric error distribution and the stellarity distribution.

object IDs consist of their field name and number in the order of their R.A. for each field. For both J and $H-$band, we provide two kinds of magnitudes; auto magnitude (J_{AUTO} and H_{AUTO}) using Kron-like elliptical aperture and aperture magnitude (J_{APER} and H_{APER}) within a circular aperture with a diameter of three times FWHM. The magnitude errors are computed from the square root sum of the

Poisson noise from the source and the zeropoint error from the photometric calibration. The zeropoint errors have values less than 0.05 mag. The distributions of the errors are shown in Figure B.8. The large dispersions of the errors are induced by the different depths of each field. The stellarities have values between 0 (extended source) and 1 (point source), and the distributions of the stellarities are also shown in Figure B.8. The galactic extinction values are from the extinction map of Schlegel et al. (1998). Since the color excess $E(B-V)$ has values of 0.034 – 0.058, $A_J \sim 0.04$ and $A_H \sim 0.03$, which are both smaller than the photometric zeropoint errors. Note that the magnitudes in the final catalog are not corrected for the galactic extinction. The final column contains information regarding the crosstalks; the *crt* means that the object is located on a crosstalk position. We used a dummy value of 99.999 for non-detections. If the object has only single filter data, we used *NaN* for the other filter information.

Using the filter response curve data of FLAMINGOS[5] and the Vega spectrum from Bohlin & Gilliland (2004), we computed the conversion factor between AB and Vega magnitude. The conversion formulae from Vega to AB magnitudes are as follows:

$$J(Vega) = J(AB) - 0.926$$

$$H(Vega) = H(AB) - 1.367$$

$$K_s(Vega) = K_s(AB) - 1.798$$

We apply this method to the 2MASS filter system (J_{2MASS} and H_{2MASS}) and found that they have values similar to those of the FLAMINGOS filter system, 0.910 for J_{2MASS} and 1.383 for H_{2MASS}.

[5]http://flamingos.astro.ufl.edu/Filter_Info/index.html

Table B.6. J and $H-$band merged catalog.

ID	R.A.	Decl.	J_{AUTO}	Error	J_{APER}	Error	H_{AUTO}	Error	H_{APER}	Error	Stellarity	A_J	A_H	flag
(1)	(2)	(3)	(4)	(5)	(6)	(7)	(8)	(9)	(10)	(11)	(12)	(13)	(14)	(15)
FLM01_00651	18:03:16.74	+67:32:13.20	20.911	0.136	20.966	0.168	20.885	0.177	21.299	0.276	0.65	0.045	0.029	
FLM01_00652	18:03:16.75	+67:41:18.77	*NaN*	*NaN*	*NaN*	*NaN*	20.838	0.202	20.746	0.172	0.47	*NaN*	0.027	
FLM01_00653	18:03:16.81	+67:22:15.77	21.172	0.199	21.199	0.200	99.999	99.999	99.999	99.999	0.48	0.045	*NaN*	
FLM01_00654	18:03:16.88	+67:37:10.82	20.198	0.074	20.109	0.092	99.999	99.999	99.999	99.999	0.67	0.042	*NaN*	
FLM01_00655	18:03:16.91	+67:36:12.73	99.999	99.999	99.999	99.999	20.715	0.158	20.921	0.199	0.49	*NaN*	0.027	
FLM01_00656	18:03:16.92	+67:30:57.40	20.254	0.086	20.342	0.106	20.400	0.112	20.464	0.137	0.89	0.046	0.029	
FLM01_00657	18:03:16.96	+67:33:30.66	20.399	0.103	20.524	0.120	19.795	0.100	19.798	0.087	0.16	0.044	0.028	
FLM01_00658	18:03:16.97	+67:26:35.22	20.136	0.072	20.265	0.101	99.999	99.999	99.999	99.999	0.90	0.046	*NaN*	
FLM01_00659	18:03:17.05	+67:27:24.29	99.999	99.999	99.999	99.999	21.049	0.177	21.198	0.253	0.61	*NaN*	0.030	
FLM01_00660	18:03:17.05	+67:37:27.81	20.610	0.184	20.866	0.155	99.999	99.999	99.999	99.999	0.55	0.042	*NaN*	
FLM01_00661	18:03:17.09	+67:36:35.88	21.122	0.187	21.149	0.195	99.999	99.999	99.999	99.999	0.58	0.042	*NaN*	
FLM01_00662	18:03:17.10	+67:37:22.53	21.117	0.217	21.255	0.214	99.999	99.999	99.999	99.999	0.65	0.042	*NaN*	
FLM01_00663	18:03:17.15	+67:38:35.97	20.786	0.155	20.829	0.151	99.999	99.999	99.999	99.999	0.51	0.041	*NaN*	
FLM01_00664	18:03:17.17	+67:29:08.37	19.167	0.070	19.209	0.066	19.016	0.067	19.050	0.065	0.89	0.046	0.030	
FLM01_00665	18:03:17.19	+67:41:50.41	*NaN*	*NaN*	*NaN*	*NaN*	18.020	0.058	18.138	0.057	0.17	*NaN*	0.027	
FLM01_00666	18:03:17.22	+67:34:37.53	20.523	0.148	20.908	0.160	99.999	99.999	99.999	99.999	0.34	0.043	*NaN*	
FLM01_00667	18:03:17.23	+67:32:17.26	20.957	0.135	21.282	0.219	20.929	0.197	20.760	0.174	0.40	0.045	0.029	
FLM01_00668	18:03:17.23	+67:33:04.26	20.589	0.161	20.984	0.170	99.999	99.999	99.999	99.999	0.47	0.044	*NaN*	
FLM01_00669	18:03:17.24	+67:37:29.69	99.999	99.999	99.999	99.999	19.754	0.106	20.266	0.118	0.49	*NaN*	0.026	
FLM01_00670	18:03:17.26	+67:39:22.08	21.222	0.188	21.120	0.191	99.999	99.999	99.999	99.999	0.65	0.042	*NaN*	
FLM01_00671	18:03:17.31	+67:45:01.33	*NaN*	*NaN*	*NaN*	*NaN*	20.456	0.114	20.455	0.136	0.37	*NaN*	0.028	

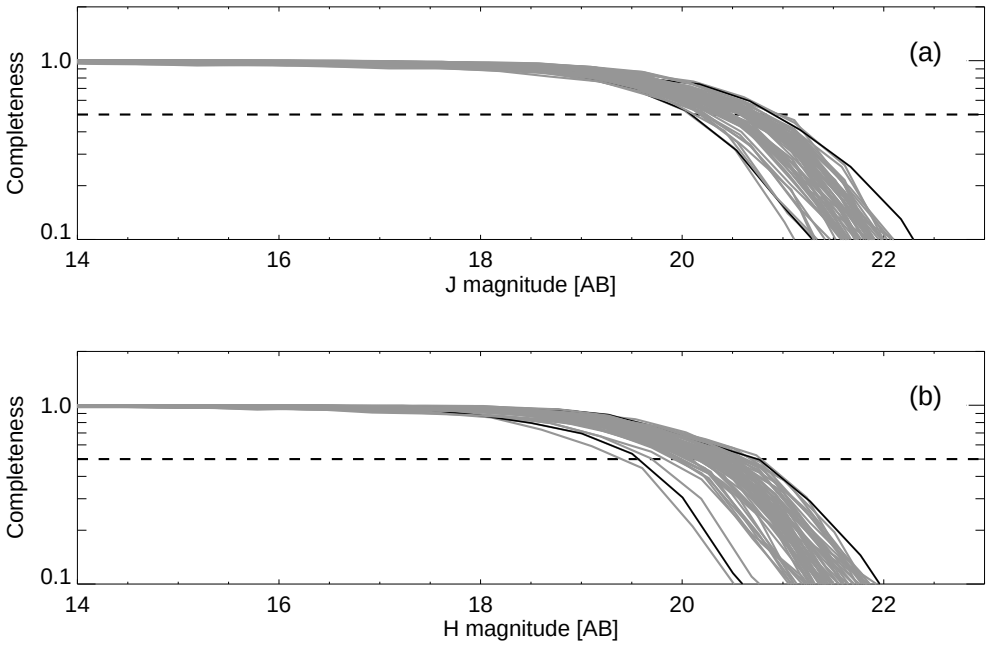

Figure B.9 Completeness (the ratio of the number of detected artificial sources to the number of input objects in a given magnitude bin) for J and $H-$band. The gray solid lines are the completeness of all subfields from the simulation method, especially for the deepest fields (FLM27 in J and FLM58 in H; the upper black solid lines) and the shallowest fields (FLM19 in J and FLM07 in H; the lower black solid lines) in the 5σ detection limits. The horizontal dashed line is for 50% completeness cut. The magnitudes of 50% completeness for each subfield are shown in Table B.5.

B.4.6 Completeness

To estimate the completeness for each field, we used artificial objects from the `noao.artdata` package of IRAF. The artificial objects are created with magnitude between 11 and 25 and they are placed randomly in the background regions of the images. The number of point sources and extended sources created are 100 each.

Table B.6 (cont'd)

ID	R.A.	Decl.	J_{AUTO}	Error	J_{APER}	Error	H_{AUTO}	Error	H_{APER}	Error	Stellarity	A_J	A_H	flag
(1)	(2)	(3)	(4)	(5)	(6)	(7)	(8)	(9)	(10)	(11)	(12)	(13)	(14)	(15)
FLM01_00672	18:03:17.35	+67:40:17.33	21.132	0.146	21.319	0.226	99.999	99.999	99.999	99.999	0.49	0.042	*NaN*	
FLM01_00673	18:03:17.42	+67:35:23.47	21.448	0.142	23.891	2.331	99.999	99.999	99.999	99.999	0.52	0.042	*NaN*	
FLM01_00674	18:03:17.52	+67:23:31.96	20.646	0.077	20.710	0.137	99.999	99.999	99.999	99.999	0.70	0.045	*NaN*	
FLM01_00675	18:03:17.58	+67:34:33.18	20.243	0.142	20.824	0.150	99.999	99.999	99.999	99.999	0.65	0.043	*NaN*	
FLM01_00676	18:03:17.60	+67:35:51.45	19.728	0.079	20.022	0.088	99.999	99.999	99.999	99.999	0.97	0.042	*NaN*	*crt*
FLM01_00677	18:03:17.61	+67:30:59.62	99.999	99.999	99.999	99.999	21.111	0.144	22.253	0.654	0.49	*NaN*	0.029	
FLM01_00678	18:03:17.62	+67:33:00.44	99.999	99.999	99.999	99.999	21.034	0.162	21.097	0.231	0.54	*NaN*	0.028	
FLM01_00679	18:03:17.63	+67:30:23.69	21.848	0.234	22.219	0.503	20.091	0.111	20.073	0.103	0.52	0.046	0.029	
FLM01_00680	18:03:17.67	+67:39:53.53	17.777	0.061	18.106	0.059	17.814	0.058	17.948	0.056	0.30	0.042	0.027	

Note. — (1) The identification number of the source (ID). Each ID consists of the subfield name (Figure B.2) and number in the order of their R.A..

(2) and (3) The J2000.0 R.A. and Decl. of a source in a sexigesimal.

(4)–(11) are the total magnitude, its magnitude error, aperture magnitude and its magnitude error of a source in the J and $H-$band. The aperture magnitudes are obtained with the aperture diameter of 3 times FWHM. The magnitudes are not corrected for the galactic extinctions. We used a dummy value of 99.999 for non-detections. If the object has only single filter data, we used *NaN* for the other filter information.

(12) The stellarity index of a source from SE. See Figure B.8 for the distribution of this index.

(13–14) The galactic extinction values of J and $H-$band from extinction map of Schlegel et al. (1998).

(15) The flag parameter. It contains the crosstalk information (*crt*). See section B.4.2 for details .

Among the extended sources, 40% are elliptical galaxies while the others are disk galaxies, with a minimum redshift of z $\sim$ 0.01. The angular sizes of the galaxies, which are equivalent to the half-flux diameters of the model objects, are set to be the FWHM values for each image. We performed detections and photometry with the same parameter settings of SE which were applied for the actual images. We define the completeness as the ratio of the number of detected artificial sources to the number of input objects in a given magnitude bin. Figure B.9 represents the completeness of J and $H-$band data as a function of magnitude. The gray lines represent the completeness for each subfield. The thick, black lines are for the deepest (FLM27 in J and FLM58 in H) and the shallowest (FLM19 in J and FLM07 in H) fields according to the 5σ detection limits. In Figure B.4, we compared the magnitude of 50% completeness (asterisks) for each field with the 5σ detection limit, the 99% reliability (see Section B.4.7), the Z_p, and the total exposure time. The magnitudes of 50% completeness for each field are listed in Table B.5. We can see that the magnitudes of 50% completeness are $\sim$1 mag brighter than the 5σ detection limits.

B.4.7 Reliability

To examine the reliability of our source detection, we used the false detection rate for each field and filter. The false detection rate is defined as the ratio of the number of objects detected in a negative image to the number of objects detected in the original image in a given magnitude bin. The negative images were created by multiplying -1 to the original images. If an image has only noise, its false detection rate would be 1. We performed detections and photometry on the negative image with the same parameter settings of SE which were applied for the actual images. Figure B.10 represents the false detection rates of J and $H-$band data as a function of magnitude. The gray lines represent the false detection rates for each

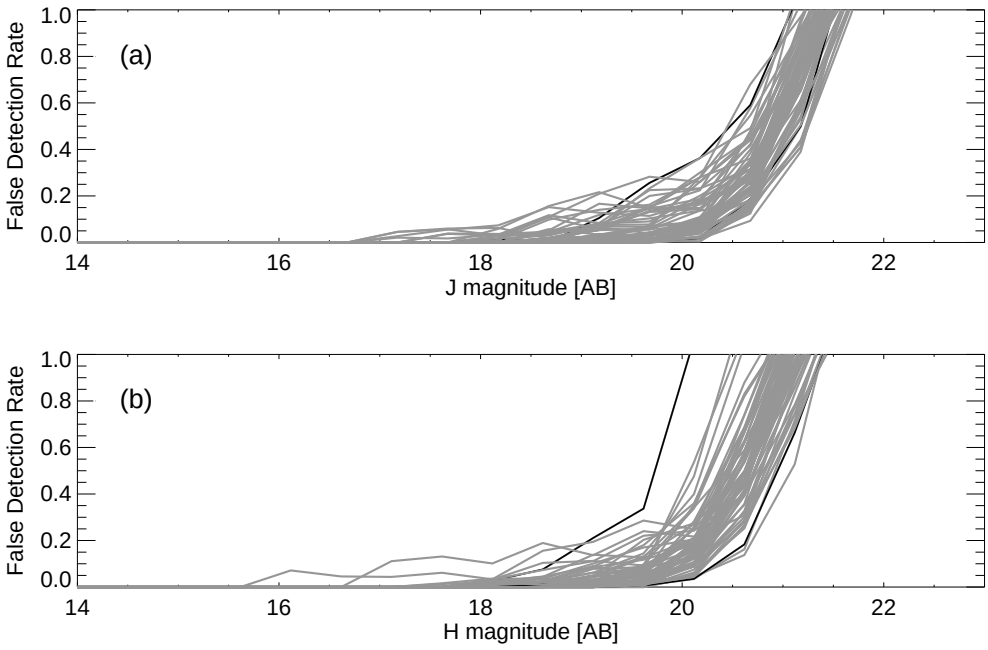

Figure B.10 False detection rate (the ratio of the number of objects detected in the negative image to the number of objects detected in the original image for each magnitude bin) of all subfields in J, and $H-$band. The black solid lines are for the deepest or the shallowest fields as same as Figure B.9. The magnitudes of false detection rate 1% for each field are shown in Table B.5.

subfield. The thick, black lines are for the deepest (FLM27 in J and FLM58 in H) and the shallowest (FLM19 in J and FLM07 in H) fields according to the 5σ detection limits. In Figure B.4, we compared the magnitude of 1% false detection rates (equivalent to 99% reliability) (diamonds) for each field with the 5σ detection limit, 50% completeness, the Z_p, and the total exposure time. The magnitude of 99% reliability for each field are presented in Table B.5. We can see that the magnitudes of 99% reliability are similar with the 5σ detection limits.

B.5 PROPERTIES OF THE DATA

B.5.1 Source Number Counts

The galaxy number count as a function of magnitude is a quantity used in investigating galaxy evolution. Due to the contamination of dust extinction and star formation, the galaxy number counts in NIR bands provide more accurate information of galaxy evolution than those using the optical bands. Here, we show the galaxy number count as a function of magnitude for representation of depth and homogeneity of our survey. The total area used in calculating the galaxy number count is 4.98 $\deg^2$, where the optical data (Jeon et al. 2010; Hwang et al. 2007) and the *AKARI* IR data overlap.

Using the galaxies defined so in Section B.4.4, we calculated the number of galaxies per square degree for each magnitude bin. Since the depth of each subfield is different from another, we computed the number count for each subfield down to the 99% reliability magnitudes limit. Then the completeness correction was applied to the number counts for each subfield. Finally, we combined the number counts from all the subfields to derive the final number count result. We also calculated the number count of stars up to the 99% reliability magnitude. The errors from the number counts are computed from the Poisson errors.

Figure B.11 shows the galaxy and star number counts in J and $H-$band. The lower solid line with crosses represents the raw number counts and the upper solid line with crosses shows the number counts after applying the completeness correction. We compared our number counts with those in the literature (Yan et al. 1998; Saracco et al. 1999, 2001; Martini 2001; Chen et al. 2002; Iovino et al. 2005; Frith et al. 2006; Metcalfe et al. 2006; Cristóbal-Hornillos et al. 2009; Keenan et al. 2010). Since the filter systems in the literature do not exactly match with that of our survey and also due to the cosmic variance, some offsets may exist. For example, Metcalfe

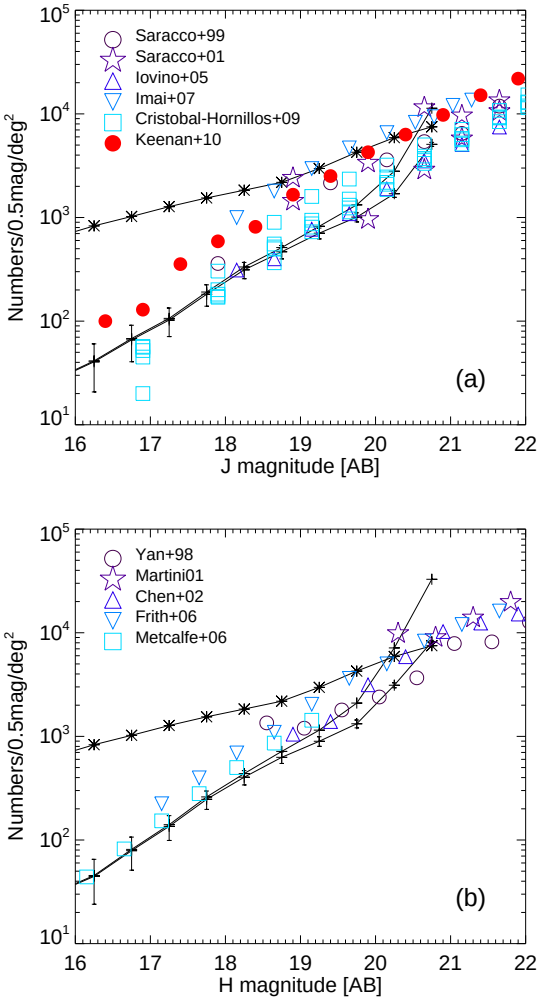

Figure B.11 Galaxy (two solid lines with crosses) and stellar (solid lines with asterisks) number counts of J and $H-$band. The error estimates of number counts are from the Poisson errors. The lower solid line is for galaxy number count without completeness correction, and the upper solid line is from the galaxy number count corrected using the completeness. We compare our number counts with the number counts in the literature (other symbols). The galaxy and stellar number count data are provided in Table B.7.

Table B.7. Galaxy and stellar number counts.

	$J-$band				$H-$band			
mag	Galaxy Number	Error	Corrected Number	Star Number	Galaxy Number	Error	Corrected Number	Star Number
16.25	4.05e+01	1.98e+01	9.94e-01	8.31e+02	4.45e+01	2.05e+01	9.94e-01	8.31e+02
16.75	6.59e+01	2.54e+01	9.85e-01	1.02e+03	7.89e+01	2.78e+01	9.87e-01	1.02e+03
17.25	1.02e+02	3.15e+01	9.78e-01	1.27e+03	1.35e+02	3.64e+01	9.78e-01	1.27e+03
17.75	1.82e+02	4.23e+01	9.67e-01	1.54e+03	2.47e+02	4.98e+01	9.63e-01	1.54e+03
18.25	3.13e+02	5.59e+01	9.52e-01	1.84e+03	4.04e+02	6.37e+01	9.37e-01	1.84e+03
18.75	4.67e+02	6.84e+01	9.25e-01	2.18e+03	6.28e+02	7.99e+01	8.90e-01	2.18e+03
19.25	7.06e+02	8.45e+01	8.71e-01	2.97e+03	8.96e+02	9.54e+01	7.94e-01	2.97e+03
19.75	1.01e+03	1.01e+02	7.73e-01	4.27e+03	1.31e+03	1.15e+02	6.42e-01	4.27e+03
20.25	1.64e+03	1.27e+02	6.17e-01	5.89e+03	3.00e+03	1.70e+02	4.42e-01	5.89e+03
20.75	4.96e+03	2.23e+02	4.54e-01	7.50e+03	8.11e+03	2.87e+02	2.52e-01	7.50e+03

Note. — Units of the galaxy and stellar number densities and their errors are numbers 0.5 mag^{-1} deg^{-2}.

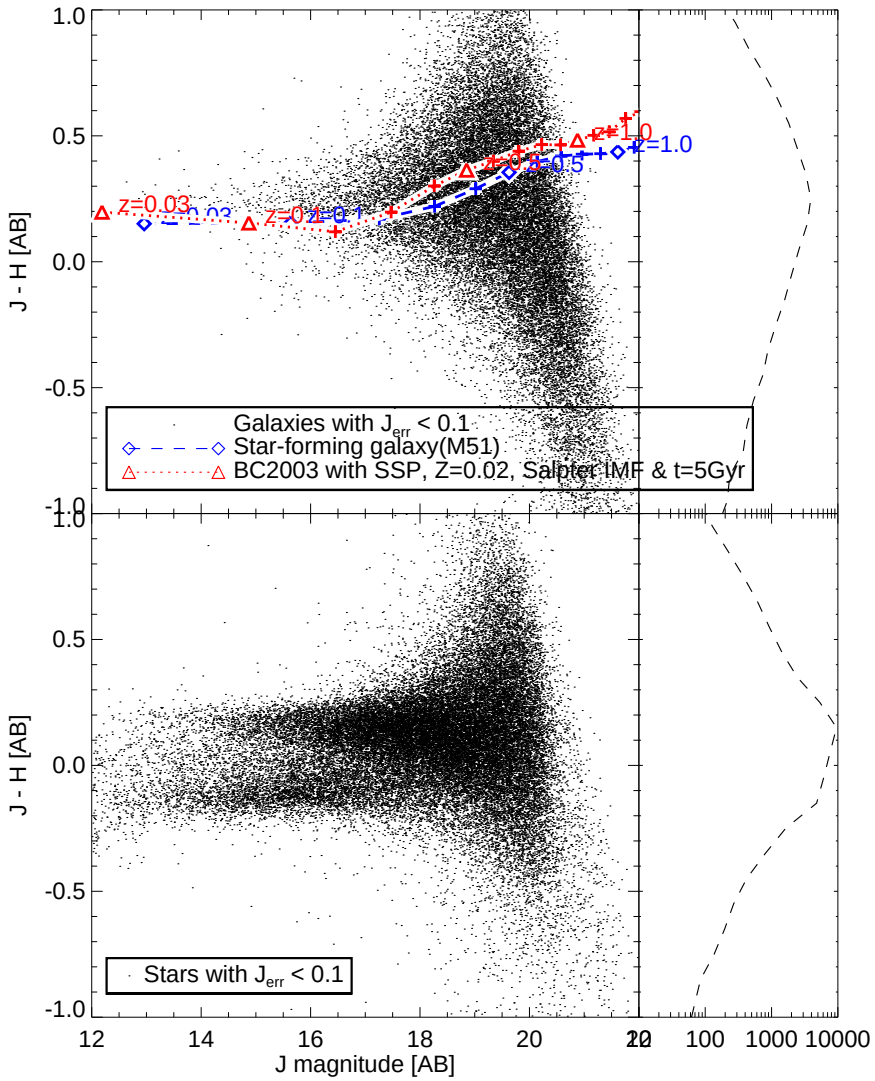

Figure B.12 Color-magnitude diagram of J versus $J-H$ (left) and histograms showing the distribution of $J-H$ colors (right). The upper panel shows the galaxies with J magnitude error less than 0.1 mag. We used same condition of galaxy redshift track at Section B.4.4. The redshift track is for galaxies with the characteristic absolute magnitudes. The lower panel shows the distribution and histogram of the stars of the same conditions in the upper panel.

et al. (2006) mention that their number counts, covering only 0.95×0.95 arcmin^2, can be uncertain by up to a factor of 2 due to the cosmic variance. We can see that our number counts are consistent with other results. The solid line with asterisks shows the number counts of stars. The galaxy and star number count data are provided in Table B.7.

B.5.2 Color-Magnitude Diagram

Figure B.12 shows the color-magnitude diagram of J versus $J-H$ and its histogram. The upper panel shows the distribution for galaxies with $J-$band magnitude error less than 0.1 mag, and the lower panel shows that for stars with the same condition as galaxies in the upper panel. We used the redshift track to check the position of galaxies on the color-magnitude diagram. We used the same conditions for the galaxy redshift track as used in Section B.4.4. These redshift tracks represent galaxies with characteristic absolute magnitude M^*. We adopt $M^* - 5\log h$ for $J-$band as -22.85 ± 0.04 from Jones et al. (2006). We calculated the k-correction values in a standard manner (Hogg et al. 2002). The $J-H$ colors of the star forming galaxies and passive evolving galaxies are similar to each other up to redshift $\sim$1. Therefore the galaxies on Figure B.12 are those within the redshift range 0 to 1, and those at higher redshift with magnitude brighter than M^*.

B.6 SUMMARY

We have presented the properties of sources using J and $H-$band data from FLAMINGOS on the KPNO 2.1m telescope, a set of follow-up imaging observations of the *AKARI* NEP field. We cover 5.1 deg^2 with 5σ depth of $\sim$21.6 mag and $\sim$21.3 mag (AB) for J and $H-$band, respectively. We detected 208,020 sources for $J-$band and 203,830 sources for $H-$band. Our NIR data provides multi-wavelength coverage for

the *AKARI* NEP sources along with the optical and the MIR data, enabling detailed SED analysis. Through these SEDs, we can obtain key physical properties such as stellar mass and photometric redshifts, and select interesting objects such as high redshift galaxies.

Bibliography

Bertin, E. & Arnouts, S. 1996, A&AS, 117, 393B

Bertin, E. 2006, Astronomical Data Analysis Software and Systems XV, 351, 112

Bock, J., Sullivan, I., Arai, T., et al. 2013, ApJS, 207, 32

Bohlin, R. C. & Gilliland, R. L. 2004, AJ, 127, 3508

Bruzual, G., & Charlot, S. 2003, MNRAS, 344, 1000

Chen, H.-W., McCarthy, P. J., Marzke, R. O., et al. 2002, ApJ, 570, 54

Cristóbal-Hornillos, D., Aguerri, J. A. L., Moles, M., et al. 2009, ApJ, 696, 1554

Elston, R. J., Gonzalez, A. H., McKenzie, E., et al. 2006, ApJ, 639, 816

Frith, W. J., Metcalfe, N., & Shanks, T. 2006, MNRAS, 371, 1601

Gawiser, E., van Dokkum, P. G., Herrera, D., et al. 2006, ApJS, 162, 1

Goto, T., Takagi, T., Matsuhara, H., et al. 2010, A&A, 514, A6

Griffin, M. J., Abergel, A., Abreu, A., et al. 2010, A&A, 518, L3

Hanami, H., Ishigaki, T., Fujishiro, N., et al. 2012, PASJ, 64, 70

Hogg, D. W., Baldry, I. K., Blanton, M. R., & Eisenstein, D. J. 2002, arXiv:astro-ph/0210394

Hwang, N. et al. 2007, ApJS, 172, 583

Im, M., Ko, J., Cho, Y., et al. 2010, Journal of Korean Astronomical Society, 43, 75

Imai, K., Matsuhara, H., Oyabu, S., et al. 2007, AJ, 133, 2418

Iovino, A., McCracken, H. J., Garilli, B., et al. 2005, A&A, 442, 423

Jeon, Y., Im, M., Ibrahimov, M., et al. 2010, ApJS, 190, 166

Jones, D. H., Peterson, B. A., Colless, M., & Saunders, W. 2006, MNRAS, 369, 25

Karouzos, M., Im, M., Trichas, M., et al. 2014, ApJ, 784, 137

Keenan, R. C., Trouille, L., Barger, A. J., Cowie, L. L., & Wang, W.-H. 2010, ApJS, 186, 94

Kim, S. J., Lee, H. M., Matsuhara, H., et al. 2012, A&A, 548, A29

Ko, J., Im, M., Lee, H. M., et al. 2012, ApJ, 745, 181

Kron, R. G. 1980, ApJS, 43, 305

Laureijs, R., Amiaux, J., Arduini, S., et al. 2011, arXiv:1110.3193

Lee, H. M. et al. 2007, PASJ, 59S, 529

Lee, H. M. et al. 2009, PASJ, 61, 375

Martini, P. 2001, AJ, 121, 2301

Matsuhara, H. et al. 2006, PASJ, 58, 673

Matsuhara, H., Wada, T., Pearson, C. P., et al. 2007, PASJ, 59, 543

Merloni, A., Predehl, P., Becker, W., et al. 2012, arXiv:1209.3114

Metcalfe, N., Shanks, T., Weilbacher, P. M., et al. 2006, MNRAS, 370, 1257

Murakami, H., Baba, H., Barthel, P., et al. 2007, PASJ, 59, 369

Ohyama, Y., Onaka, T., Matsuhara, H., et al. 2007, PASJ, 59, 411

Oi, N., Matsuhara, H., Murata, K., et al. 2014, arXiv:1403.7934

Pearson, C. P., Oyabu, S., Wada, T., et al. 2010, A&A, 514, A8

Persson, S. E., Murphy, D. C., Krzeminski, W., Roth, M., & Rieke, M. J. 1998, AJ, 116, 2475

Poglitsch, A., Waelkens, C., Geis, N., et al. 2010, A&A, 518, L2

Saracco, P., D'Odorico, S., Moorwood, A., et al. 1999, A&A, 349, 751

Saracco, P., Giallongo, E., Cristiani, S., et al. 2001, A&A, 375, 1

Schlegel, D. J., Finkbeiner, D. P., & Davis, M. 1998, ApJ, 500, 525

Serjeant, S., Buat, V., Burgarella, D., et al. 2012, arXiv:1209.3790

Shim, H., Im, M., Ko, J., et al. 2013, ApJS, 207, 37

Stanford, S. A., Eisenhardt, P. R. M., & Dickinson, M. 1995, ApJ, 450, 512

Takagi, T., Ohyama, Y., Goto, T., et al. 2010, A&A, 514, A5

Takagi, T., Matsuhara, H., Goto, T., et al. 2012, A&A, 537, A24

van Haarlem, M. P., Wise, M. W., Gunst, A. W., et al. 2013, A&A, 556, A2

Wada, T. et al. 2007, PASJ, 59S, 515

Wada, T., Matsuhara, H., Oyabu, S., et al. 2008, PASJ, 60, 517

White, G. J., Pearson, C., Braun, R., et al. 2010, A&A, 517, A54

Yan, L., McCarthy, P. J., Storrie-Lombardi, L. J., & Weymann, R. J. 1998, ApJ, 503, L19

요 약

고 적색편이 퀘이사들은 초기 우주의 진화를 연구하는 데에 매우 중요한 천체이다. 하지만 기존의 연구로부터 밝혀진 퀘이사들은 개수가 매우 적고 (약 70 개) 대부분 적색편이 6 근처에 편중되어 있다. 초거대질량 블랙홀의 초기 질량 증가와 우주 재이온화의 마지막 상태를 이해하기 위해서는 다양한 물리적 성질의, 통계적으로 유의미한 수의 퀘이사 표본을 확보하는 것이 중요하다. 이에 우리는 새로운 퀘이사 탐사를 제시한다. 이 탐사는 적색편이의 범위에 따라서 3가지의 하위 탐사로 나눠진다.

SDSS와 UKIDSS LAS 자료, 그리고 CQUEAN 후속 관측을 추가하여, 적색편이 5 근처의 퀘이사 탐사를 수행하였다. 이 적색편이 근방의 퀘이사는 기존 연구에서 사용한 필터의 기술적인 한계 때문에 발견하기 어렵다고 알려져 있다. 이를 해결하기 위해 기존 필터들과 차별되는 Is/Iz 필터를 주문 제작하여 측광 후속 관측을 수행하였다. 최종적으로 광학 분광 관측을 통하여 6개의 새로운 퀘이사들을 발견할 수 있었다. 이 중 3개의 퀘이사에 대해 적외선 분광 관측을 하였고 이들의 물리적인 성질을 측정하였다. 이 퀘이사 탐사의 효율을 계산하기 위하여 완전성 테스트를 수행 하였다.

적색편이 6 근처의 퀘이사 탐사는, SDSS와 UKIDSS LAS 자료를 사용하여, 넓은 영역에 걸쳐서 상대적으로 밝은 퀘이사들을 찾는 탐사이다. 우리는 다른 천체들을 제거하기 위하여 새로운 방법을 개발하였고, 이 방법이 다른 천체들을 제거하는 데에 효율적인 것을 확인하였다. 최종 후보들에 대하여 측광과 분광 후속 관측을 수행하였고, 2개의 새로운 퀘이사를 발견하였다. 후속 연구로 IMS 자료를 이용하여 상대적으로 어두운, 적색편이 6 근처의 퀘이사 탐사를 수행 할 수 있을 것이다.

적색편이 7 근처의 퀘이사를 찾기 위하여, 우리는 고유의 적외선 측광 탐사인 IMS를 수행하였다. 이 탐사는 UKIRT와 WFCAM을 이용한 것으로, 5년에 걸쳐서 $\sim$120 deg^2 를 $Y = 22.3$ Vega, $J = 22.0$ Vega 의 5σ 깊이로 관측하였다. 깊은 광학 자료가 있는 7개의 외부은하 필드가 사용되었다. 우리는 이 자료들을 분석하여

$\sim 7 \times 10^6$ 개 천체들의 측광 정보가 담겨있는 카탈로그를 만들었다. 적색편이 7 근처의 퀘이사를 찾기 위하여 2가지 방법을 사용하였다. 깊은 J 필터 자료 (IMS와 UKIDSS DXS) 와 광학 측광 자료를 Y 필터 자료 혹은 적외선 자료, SWIRE와 합쳤다. 이 퀘이사 탐사는 $\sim$110 deg^2 에 걸쳐 수행되었으며 약 30개의 퀘이사 후보를 찾았다. 이 연구는 진행 중이고, 후속 분광 관측을 통하여 퀘이사로 확정하고자 한다.

우리는 새롭게 발견한 퀘이사들의 광학과 근적외선 분광 자료를 이용하여 블랙홀의 질량과 에딩턴 비를 계산하였다. 이 천체들은 작은 적색편이의 퀘이사들과 비교했을 때, 급격한 질량 증가를 통한 성장을 하고 있다고 관찰되어진다. 또한 우리가 발견한 퀘이사들로부터 퀘이사 개수 밀도를 계산하였고, 기존의 알려져 있는 퀘이사 밝기 함수로부터 예상되는 개수 밀도와 비교를 하였다. 적색편이 5 근처의 발견된 퀘이사들의 경우, 개수 밀도가 기존의 연구들과 비슷한 값을 보였다. 하지만 적색편이 7 근처의 퀘이사 개수 밀도는, 개수 밀도의 진화를 고려하더라도 기존의 연구 결과보다 작은 값을 보였다. 이로부터 적색편이 7 근처의 퀘이사 개수 밀도는 이전에 알려진 바 보다 더 급격한 진화를 보이면서 큰 적색편이로 갈수록 감소하는 것을 알 수 있다.

본 연구에서는, 기존 연구와 마찬가지로 $5.5 < z < 6.0$ 의 퀘이사들을 찾지 못하였다. 이를 위하여, 이 적색편이 구간에서 퀘이사를 효율적으로 찾을 수 있는 새로운 방법인 중대역 필터를 이용하는 방법을 제시한다. 이 중대역 필터 측광으로부터의 스펙트럼 에너지 분포를 이용하여 χ^2 핏팅을 수행하였고, 측광 적색편이의 1σ 오차가 0.15 인 것이 측정되었다. 그러므로 이 중대역 필터를 이용한 퀘이사 탐사는 적색편이 5.5 부근의 퀘이사를 찾는 데에 효과적일 것으로 기대된다.

주요어: 카탈로그 – 관측 – 퀘이사: 방출선 – 퀘이사: 일반 – 퀘이사: 초거대질량 블랙홀 – 탐사

학 번: 2007-20438